Author/s:
Gladman, Brendan Robert

Title:
The effect of shear on dewatering of flocculated suspensions

Date:
2005

Citation:
Gladman, B. R. (2005). The effect of shear on dewatering of flocculated suspensions. PhD thesis, Faculty of Engineering, Chemical and Biomolecular Engineering, The University of Melbourne.

Publication Status:
Unpublished

Persistent Link:
https://hdl.handle.net/11343/35262

The Effect of Shear on Dewatering of Flocculated Suspensions

by

Brendan Robert Gladman

B.E Chem. (Hons.)

December 2005

Submitted in total fulfilment of the requirements of the degree of Doctor of Philosophy

Particulate Fluids Processing Centre

Department of Chemical and Biomolecular Engineering

The University of Melbourne

Victoria, Australia 3010

Preface

I hereby declare that this thesis represents solely my own work, except where due reference is made, and is less than 100,000 words in length.

Acknowledgements

First and foremost, I would like to thank my supervisors Prof. Peter Scales and Dr. Murray Rudman. Their guidance and support was a constant source of motivation and inspiration. Thanks especially to Peter, for always having an open door and for encouraging the belief that research should, above all, be fun. Thankyou to Murray, for help with all matters numerical, and for showing an abundance of patience while answering my never-ending questions.

I would also like to thank those people who paved the way before me; in particular Daniel Lester, Shane Usher, Janine Hulston and Ainul Aziz. Thanks Daniel for taking the time to explain the workings behind the various mathermatica codes and Ainul for demonstrating the "art" of flocculation. Thanks are due to Ross de Kretser, for his help with setting up and trouble shooting the filtration rig and for showing an interest in my research. To the more "senior" members of the PFPC; David Boger, Tom Healy, David Dixon, it was a privilege to learn from among the very best. To the rest of the PFPC, Raj, Xavier, and co, thanks for making uni a fine place to be. My office buddies; Adam, Sam, Briony, and next-door neighbours Ian, Dan and Will, who were a source of constant entertainment (and distraction). Special thanks to Will for introducing us to mousebreaker.com – it made the write up a blast! I would like to express my gratitude to Annmaree Sharkey, who managed travel, finances and administrative matters efficiently, without hassle or complaint, and a big thankyou to Kevin and the boys in the workshop who do a fine job, considering the required time frame for work is invariably yesterday. Also, thanks to those

who lent me a hand at various times, and got themselves dirty in the process; Adam and Jonathon, and research students Jack, Kristy and Josephine.

There are many people at CSIRO Minerals who I'd like to thank. Kosta Simic for his supervision, support and efforts to get the tall column up and running and Andy, for fixing anything that broke, as often tended to happen. Furthermore, a big thankyou is extended to everyone at CSIRO Waterford; especially Phil Fawell for the generous offer of time, materials and lab space, while making me feel generally welcome. Thanks Deanne for both putting me up, and putting up with me; and Andrew for proving that Perth actually does have a night life worth leaving home for. Thankyou to the companies sponsoring the AMIRA 266D thickener project for financial support. In particular, Brett Wroth from Iluka Resources, for arranging the site work and being a great help throughout my visit. Thanks to folk at AAAA Trusty Rentals for getting me around; trusty by name, trusty by nature. Closer to home, thanks to Sticks and my fellow Ballhandlers, sorry I bailed this season, I hope you have a win soon. Thanks to Sarah for generously offering her family's holiday home in Wandiligong. Many words penned in this thesis were inspired by the amazing views and equally amazing wine.

I would like to thank my family, Lyndell and Daniel, and especially Mum and Dad, for the love and support they provided me over the years. It's largely because of you that I am where I am today. It's always nice to visit home for Mom's curry where the words "dewatering" and "compressive yield stress" are rarely, if ever, spoken! Finally to Jo, words cannot possibly express my gratitude for the love, support and understanding you have shown over the past three years. Thanks for the late night pickups from uni when I was too tired to walk, and for knowing the right time for peppermint tea. Thanks for helping with my "always at the last minute" packing, and for listening when I needed to talk and

for single handedly shifting all our possessions twice in the space of six weeks. Above all else, thanks for being a friend. This thesis is dedicated to you.

List of Publications

P.J Scales, A.A.A Aziz and B.R Gladman "The compressional rheology of suspensions" Proceedings from XIVth International Congress on Rheology, Seoul Korea (2004)

B Gladman, RG deKretser, M Rudman and PJ Scales, 'Effect of shear on particulate suspension dewatering,' Trans IChemE Part A, 83 (A7): 1-4 (2005).

S.P. Usher, B.R Gladman and P.J. Scales "New Techniques for Understanding Settler/Clarifier Behaviour" American Filtration Society Conference (2005)

Farrow, JB, Rudman, M, Nguyen, T, Simic, K, Fawell, PD, Mittoni, L, Baldacchino, FA, Bell, RA, Bui, A, Heath, AR, Koh, P, Labbett, DM, Livk, I, Owen, AT, Paterson, D, Scales, PJ, Sutalo, I, Swift, JD, Syme, M, White, RB, Estevez, L and Gladman, B (2002), AMIRA P266D Project. Improving Thickener Technology. 2nd Progress Report.

Farrow, JB, Rudman, M, Nguyen, T, Simic, K, Fawell, PD, Mittoni, L, Baldacchino, FA, Brent, AK, Bui, A, Heath, AR, Koh, P, Labbett, DM, Lawton, A, Livk, I, Owen, AT, Paterson, D, Scales, PJ, Sutalo, I, Swift, JD, White, RB, Estevez, L and Gladman, B (2002), AMIRA P266D Project. Improving Thickener Technology. 3rd Progress Report.

Farrow, JB, Rudman, M, Nguyen, T, Simic, K, Fawell, PD, Heath, AH, Austin PJ, Baldacchino, FA, Brent, AK, Bui, A, Francis, NS, Labbett, DM, Lawton, A,

Livk, I, Owen, AT, Paterson, D, Scales, PJ, Sutalo, I, Swift, JD, White, RB, Estevez, L and Gladman, B (2003), AMIRA P266D Project. Improving Thickener Technology. 4th Progress Report.

Farrow, JB, Rudman, M, Nguyen, T, Simic, K, Fawell, PD, Heath, AH, Austin PJ, Baldacchino, FA, Bell, RB, Brent, AK, Bui, A, Francis, NS, Graham, L, Labbett, DM, Lawton, A, Livk, I, Owen, AT, Paterson, D, Scales, PJ, Sutalo, I, Swift, JD, White, RB, Estevez, L and Gladman, B May 2004. AMIRA P266D Project. Improving Thickener Technology. 5th Progress Report

Abstract

The ability to separate a suspension into its respective solid and liquid constituents is an important requirement in the chemical, wastewater and mineral industries. Typically, separation occurs in open, large diameter tanks known variously as thickeners, settlers or clarifiers. The design and operation of these devices have been based, until recently, on kinematic models and macroscopic mass balances. The problem with these approaches is that consolidation in the bed is not described accurately and consequently, the area required for thickening is often grossly overestimated. Recently, Buscall and White [24] proposed a 1−D phenomenological theory of dewatering that encompasses both sedimentation and consolidation, providing a more solid grounding for understanding, simulating and optimising dewatering in a range of devices, including thickeners. This theory identifies two important rheological parameters; a concentration dependent yield stress, $P_y(\phi)$ and hindered settling function, $R(\phi)$.

Despite representing a significant improvement over a kinematical approach, Buscall and White's dewatering theory involves a number of simplifications so that in practise, simulations often underestimate dewatering in full sized thickeners [97, 153]. One aspect of thickening that is poorly understood is the effect of raking. At the base of the thickener, a rake transports the thickened sediment to the outlet. An additional effect from raking is to increase the average solid concentration in the underflow [33, 46]. Raking introduces normal and shear stresses, which cannot be described within a one-dimensional framework.

Therefore, observed differences between predicted and measured thickener underflow concentrations are attributed to the action of the rake.

The aim of this thesis is to develop a better understanding of how shear stresses effect compressional dewatering in both pilot and full scale thickening operations. Before attempting to quantify the effect of shear on dewatering, it was considered necessary to first establish that the 1-D model was capable of predicting dewatering in the absence of shear. Up until now, no known studies have been undertaken to validate the model under controlled conditions. To approximate one-dimensional flow with no shear, a tall narrow column with no moving parts was used. Two solid fluxes and several bed heights were studied, and the outputs from the column were compared with the 1-D model predictions. The results show that under ideal conditions, the model predicted the underflow solid concentration to within 10 %.

The effect of shear on dewatering was investigated using a Couette shear device. Couette geometry was chosen to provide uniform shear. Since in Couette flow, no normal stresses act in the direction of rotation, the mechanism behind dewatering can investigated. These experiments showed that shear caused dewaterability to improve up to a critical shear rate, beyond which dewaterability was adversely affected. The relationship between this critical shear rate and flocculation conditions was investigated by using different flocculant dosages. The shear modified $P_y(\phi,\dot{\gamma})$ and $R(\phi,\dot{\gamma})$ can be input to the 1−D model, thereby incorporating shear indirectly. As a result, the model predicted an order of magnitude increase in solids flux.

The above procedure was used to characterise the dewaterability of a real thickener feed as a function of shear rate. The optimum shear rate was determined by finding the minimum $R(\phi,\dot{\gamma})$. Then, $P_y(\phi)$ and $R(\phi)$ were

input into the thickener model. The predicted underflow concentration could then be compared against plant data.

Even when shear is taken into account, the model still under predicts the performance of the thickener. To understand this result, the pilot column work was revisited since the control over experimental conditions was far greater. To introduce shear, concentric cylinders were installed in the column and rotated at a fixed speed. Thus, the effect of shear and bed height on underflow density were determined at different rates of shear. This showed that the underflow concentration increased with bed height; a result not expected based on the model prediction. The effects of shear on underflow density were secondary to bed height.

The bed height dependence can only be explained if dewatering is not steady but changes over time. For a four metre bed height the residence time is eight times longer than a one metre bed. Improvements in dewatering could be related to time dependent restructuring of aggregates which would result in an associated change in $R(\phi)$. By fluidizing suspensions for times corresponding to the residence times in the tall column, $R(\phi)$ and $P_y(\phi)$ could be determined, as functions of volume fraction and time. Aggregate properties including structure and density were measured before and after fluidization using focussed beam reflectance measurement (FBRM) and floc density analysis (FDA).

Contents

Nomenclature

A	Cross sectional area
Ar	Archimedes number
b	Floc bulkiness $b = \frac{1}{\phi_{floc}}$
c	Concentration
C_D	Drag coefficient
C_f	Mass of solid per unit volume of feed to thickener
d	Size of an aggregate
d_0	Size of primary particle
d_f	Mass fractal dimension
$d_{\lim}$	Limiting diameter of an aggregate when subjected to force
$d_{\max}$	Maximum diameter of thickener
D_T	Stirred tank diameter

D_i	Diameter of impeller in stirred tank
$f(\phi)$	Solids flux function
F	Total force on a particle
F_B	Buoyancy Force
F_c	Cohesive or breakage force between two particles
F_D	Hydrodynamic Drag Force
F_G	Gravitational force
g	Gravitational acceleration constant
G	Globally averaged shear rate in stirred tank
$h(t)$	Height of suspension-supernatant interface as function of time
h_0	Initial height of suspension-supernatant interface
h_∞	Equilibrium height in batch settling
H_b	Height of compression zone in thickener
H_i	Impeller height measured from the stirred tank base
$I(Q)$	Scattered intensity of light

k , $k(\phi)$	Aggregate permeability
K	Hydraulic conductivity
L	Characteristic linear length of an aggregate
L_{AL}	Injection port arm length
L_{FP}	Flocculant injection port length in stirred reactor
$L_{LIQ\ LEV}$	Immersed height in stirred reactor
m	Consistency in Herschel-Bulkley model (chapters 5 and 6) Linear mass (Chapter 8)
M	Mass of an aggregate
n	Flow index parameter in Herschel-Bulkley model
N	Impeller velocity (Chapter 3) Number of particles in an aggregate (Chapter 8)
N_p	Dimensionless impeller power number
N_q	Dimensionless pumping capacity
p	Pressure
pK_a	Acid Dissociation Constant

P	Total stress (Chapter 2) Power dissipation in stirred tank (Chapter 3)
P_e	Effective stress
P_{os}	Osmotic pressure
$P_y(\phi)$	Compressive yield stress (kPa)
$q(t)$	Volume averaged velocity
Q	Scattering wave vector
Q_f	Volumetric solids flux of thickener feed
Q_0	Volumetric solids flux of overflow from thickener
Q_u	Volumetric solids flux of thickener underflow
r	Radial position in Couette
$r(\phi)$	Hindered settling factor
r_p	Particle radius
R	Radius of Couette shear device
$R(\phi)$	Hindered settling function, or interphase drag function
$\mathrm{Re_p}$	Particle Reynolds number

S	Characteristic strength of an aggregate
$S(\phi)$	Solid distribution function
S_B	Particle surface area per unit volume of bed
t	Time
t_c	Fluid circulation time in stirred tank
t_{res}	Solid residence time in thickener
T	Rake torque
u	Pore water pressure
$u(\phi)$	Solid particles hindered settling rate
u_c	Superficial fluid velocity in fluidized bed
u_{mf}	Minimum or incipient fluidization velocity
u_∞	Stokes settling velocity
v	Fluid velocity
v_θ	Angular fluid velocity in Couette
v_∞	Fluid approach velocity

V	Filtrate volume (Chapter 2); Stirred tank volume (Chapter 3)
V_f	Volumetric feed flow rate to thickener
V_p	Volume of a single particle
z	Vertical height in thickener
z_e	Boundary between settling and consolidation zones in thickener
$\alpha(z)$	Shape factor used in thickener modelling
$\alpha(\phi)$	Specific volume cake resistance
β^2	Inverse of the slope of a t vs. V^2 plot, $\left(\frac{dt}{dV^2}\right)^{-1}$
δ	Gap width in Couette
ε	Viscous dissipation rate (Chapter 3)
ϕ_0	Initial solid volume fraction of suspension
ϕ_∞	Solid volume fraction at equilibrium
ϕ_{cp}	Solid volume fraction at close packing
ϕ_f	Solid volume fraction of the feed to the thickener

ϕ_g	Gel point or critical solids concentration
ϕ_u	Solid volume fraction of the thickener underflow
$\dot{\gamma}$	Shear rate (s^{-1})
η_0	Refractive index
η	Intrinsic viscosity (Chapter 3) Non Newtonian fluid viscosity (Chapters 5 and 6)
κ	Dynamic compressibility
λ_0	Wavelength
μ	Newtonian fluid viscosity
ν	Kinematic viscosity
θ	Scattering angle of incident light
ρ	Density
ρ_{eff}	Effective aggregate density or buoyant density
ρ_f	Average density of fluid phase
ρ_{floc}	Density of floc
ρ_s	Average density of solid phase

$\tau_{r\theta}$	Shear stress in cylindrical coordinates
τ_w	Shear stress at wall
τ_y	Shear yield stress
$\boldsymbol{\tau}$	Stress tensor
Γ	Aspect ratio in Couette device
Ω	Rotational rate of cylinder in Couette geometry
$\boldsymbol{\Delta}$	Stretching tensor
ΔP	Applied pressure in filtration
Δu	Excess pore fluid pressure
$\Delta\rho$	Interphase density difference
$\Delta\phi$	Change in average solid volume fraction

List of Figures

List of Tables

Chapter 1

Introduction

1.1 Background to Dewatering

The ability to dewater, or separate suspensions into their respective solid and liquid constituents, is an important requirement in the chemical, wastewater and mineral industries. The volume of waste generated by these industries can be massive. For example, a typical Australian iron ore refinery can generate over 3000 tonnes of waste per hour; a rate sufficient to fill the Melbourne Cricket Ground to 10 metres depth in just two and a half days. Often, solids represent a small fraction of the total mass. In wastewater processing for example, solids settle to concentrations typically less than one percent by weight [77]. Therefore, the potential for water recovery in these industries can be enormous. By dewatering, the volume occupied by solids is decreased while at the same time fluid (usually water) is recovered. The concentrated solids may be processed further, disposed to land fill or incinerated, while the water is recycled back to the process.

The minerals industry is particularly reliant on dewatering since most mineral processing operations (i.e. comminution and beneficiation) occur in an aqueous environment. Traditionally, mine tailings are discharged directly into settling ponds where the solids consolidate over time and surface water is recovered [111]. As mineral deposits become increasingly depleted, greater volumes of ore must be mined to meet demands, producing even greater

quantities of waste. Consequently, the land area required for these disposal sites can be enormous, leading to a host of environmental and economic implications [111, 130]. A further problem, exacerbated in dry climates and high altitudes is water loss due to evaporation. In these contexts, optimizing dewatering has become increasingly essential both to reduce the land requirement and minimise water loss. Obviously, these outcomes translate into considerable financial and environmental benefits [111].

Separation of solid-liquid suspensions, or dewatering, generally occurs in multiple stages [138]. The stages are differentiated by the driving force which could be gravitational, centrifugal or mechanical. The first stage usually involves particles settling under a gravitational field; a process termed thickening. A second dewatering stage may be necessary if the solids are required in a highly concentrated state (e.g. for landfill or incineration purposes). Traditionally, this involved filtration, although centrifugation is increasingly being explored as a lower cost alternative. In all cases dewatering involves the same principal; the flow of fluid through a compressible porous medium. However, with filtration and centrifugation, mechanical or centrifugal forces act in combination with gravity so that considerably higher compressive stresses are achieved, and higher solid volume fractions result. The formation of compacted cakes comes at a premium however, since the costs of purchasing, operating and maintaining filters are significantly higher than gravitational thickeners; an estimate of 100 times has been suggested [77]. Because the efficiency of filtration improves when the feed is highly concentrated and homogenous, thickening is an effective and useful precursor to filtration [10]. Other advantages of thickening include;

- The ability to accommodate highly dilute feeds in which the solid concentration, mineral composition or throughput could fluctuate dramatically.

- Relatively simple to operate and low costs.
- The ability to produce a reasonably dense underflow (an order of magnitude increase in solid volume fraction is typical).

This thesis will focus primarily on gravitational thickening. However, in most cases the results and findings can be applied to dewatering in a range of devices.

1.2 Thickening

The separation of solids from suspending fluid by gravity is an age old process. References dating as early as 500 BC, describe ancient Egyptian practices of digging, washing and settling ores, to recover alluvial gold [22]. Modern gravitational thickening works by the same principle; solid-liquid separation driven by density differences between the solid and liquid phases.

Separation usually occurs in open, large diameter tanks, known as thickeners, settlers or clarifiers. The different names reflect whether it is thickening or clarification that is the most important objective. Clarification refers specifically to the removal of fine dispersed particles from a suspension; this may be needed to comply with statutory regulations, reduce turbidity levels, or recover product. Conventional thickeners (see Figure 1-1) are large, shallow, tanks that may have either a flat or a gently sloping bottom. Thickeners may be operated batch-wise, although continuous operation is more common. Under normal operation, three distinct regions can be identified; clarification, sedimentation and compression zones. These are shown schematically in Figure 1-2. Normally, the objective of thickening is to produce a highly concentrated solid underflow. To meet this objective without compromising throughput, it is often necessary to rake the bed. In general, raking and shear effects improve the rate of sedimentation enabling faster operation. Raking also helps transport thickened material to the discharge

point, ensuring a constant supply of material to the underflow pump. Rake design is important as improper design can result in rat holing or short circuiting of solids which lead quickly to rake torque problems [2].

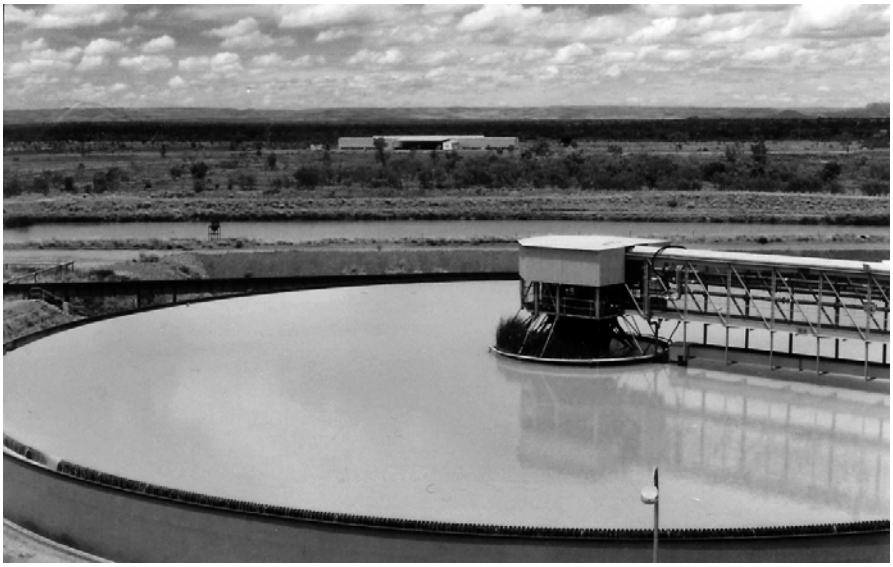

Figure 1-1 Photograph of a conventional thickener

Solids normally enter the thickener via a centrally located feed well. Continuous dewatering of suspensions containing a high proportion of fine colloidal sized particles is difficult because settling rates are prohibitively slow. To circumvent this problem, high molecular weight polymer is often added. Functional groups adsorb to the particles and modify the surface chemistry, promoting the formation of aggregates. The subject of flocculation is considered in Chapter 3. The particles (or flocs) settle under gravity from the feed well and into a sedimentation zone below. As the solid concentration increases, particle-particle interactions slow or hinder the particle's settling rate. Above a critical solids concentration, known as the gel point $\left(\phi_g\right)$, the suspension begins to exhibit solid like properties including a characteristic compressive yield stress, $P_y\left(\phi\right)$.

The compressibility (strength) and permeability (inversely related to a hindered settling function) are important material parameters. Together with the free and hindered settling behaviour of flocs, these form the inputs for thickener modelling. The mechanisms of sedimentation and consolidation are discussed in Chapter 2. To measure these parameters, a series of tests are required, since no single test covers the entire parameter space. Tests include batch sedimentation, gravity permeation, centrifugation and pressure filtration [39, 57, 58, 98, 154]. While not comprehensive, these tests have been shown to provide reproducible material property characterisation for basic thickener, filtration and centrifugation modelling.

Despite the widespread application of thickening, the design and operation of thickeners is still largely empirical. Traditionally, the design of thickeners has been based on kinematical methods [87] in which the solid and liquid fluxes are balanced to ensure that no solids exit via the overflow. This approach is useful for predicting a minimum thickener dimension or a maximum operating solids flux for a given thickener size; however, it gives no indication of the expected solids concentration or the rheology of the underflow material. Kinematic theory and the application to thickener design are discussed in more detail in Appendix 2.

The ability to predicatively design and operate these devices is the key to improving the thickening process. Phenomenological theory provides a solid grounding for understanding, simulating and optimising dewatering in a range of applications, including gravitational thickening. It is essential that such models account for compression effects in the thickener bed, as well as the free settling behaviour identified by Kynch and others [48, 87]. Several equivalent models and their computational solutions can be found in the literature [5, 17, 21, 23, 53, 92, 94, 156]. This thesis will only consider one such model and its specific solution methodology [156]; however, it can be shown that all the above models

derive from the same fundamental basis. The key features (inputs, assumptions and outputs) of the model are outlined in Chapter 4.

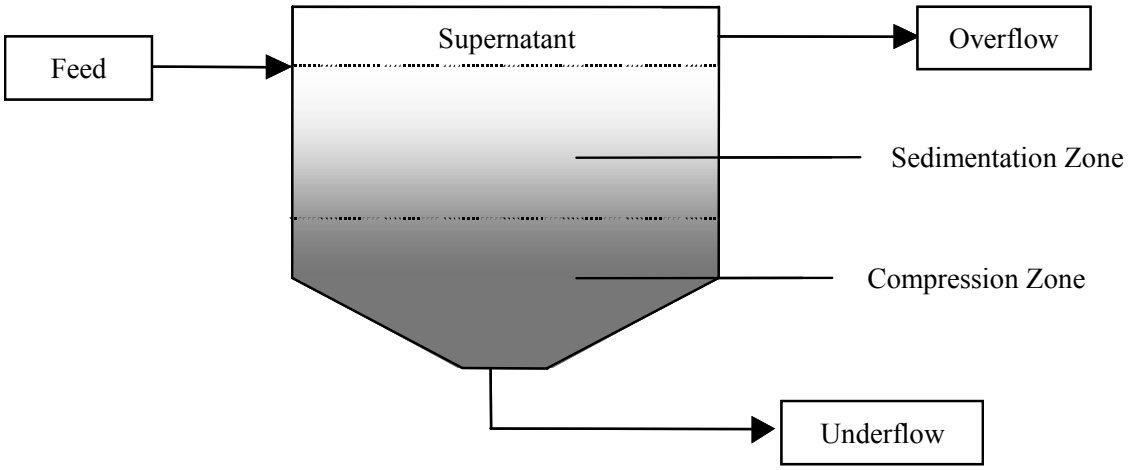

Figure 1-2 Schematic of a continuous thickener showing the different zones

With the development of a thickening model, comparison between prediction and the performance of operating thickeners is possible. The material specific inputs to the model can be either measured in the laboratory or on site. Usher [153, 155] characterised the material in several operating thickeners and with the measured dewatering parameters as inputs, modelled the dewatering behaviour of each thickener. The results are shown in Figure 1-3. The predicted solid flux versus underflow solids concentration reveals that steady state modelling consistently under estimates the true dewatering performance of the thickeners [155]. Detailed analysis of the model data also shows that most thickeners operate in a solids flux range that is limited by the suspension permeability.

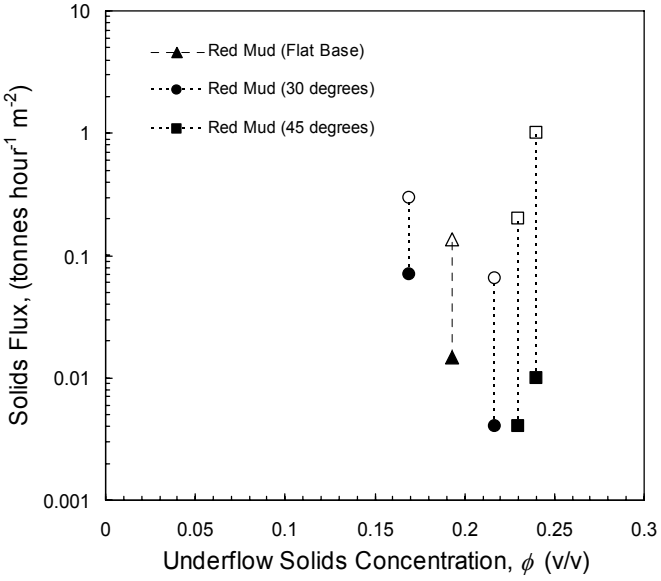

Figure 1-3 Predicted (solid) and measured (hollow) underflow solids concentration for several operating solid fluxes in thickeners with varying cone angles [155]

The results show that the model and plant data can differ anywhere between 2 and 200 fold [123]. To a reader unfamiliar with thickening, this would seem an extremely poor correlation. Indeed, from any modelling perspective, this would be a reasonable conclusion, although this outcome is consistent with other results reported by workers in the same group and reflects the current state of the art [156]. The fact that good correlation of modelling with operations is observed for selected cases implies that the model inputs are the root cause of the discrepancy, not the model.

Careful examination of the results in Figure 1-3 revealed that the differences depended on two factors; the speed of the rake and the slope angle of the conical base [155]. Increasing both rake speed and cone angle led to significant improvements in the measured permeability, while an increased cone angle also

produced a higher underflow density [153, 155]. As material settled and flowed down the sloped wall in a converging base thickener, shear forces are imparted to the flocculated material affecting both sedimentation and consolidation behaviour. This effect has been investigated in the laboratory by conducting settling tests in a conical settling vessel [155]. The results show that predicted settling behaviour (based on dewatering information from an equivalent vertical test) deviates from the observed settling data; with the suspension in a sloped vessel settling faster and achieving a lower equilibrium height. The problem with such an approach is that it is difficult to quantify the shear, and hence comparisons between the laboratory results and full scale thickening are complex.

Several studies in the literature show qualitatively the benefit of raking to the dewaterability of a suspension [33, 46, 71, 77, 112, 157]. To reproduce the effect of raking, it is possible to rotate a variety of implements within a suspension as it settles [155]. However, as with the sloped settling tests mentioned previously, these studies also suffer from quantification issues. The exact mechanism(s) by which rakes or pickets enhance dewatering is not entirely understood. By selecting different rake designs it is possible to investigate several possible dewatering mechanisms including shear failure, channelling and the "squeeze" due to pressure waves generated by the moving rake blade. Vertical pickets, sometimes fixed to the rake arm, are thought to improve dewatering by providing an escape path for the fluid. Rotation of the horizontal blades disturbs or prevents the formation of arch like structures which provide support to the network causing the sediment to collapse irreversibly [33]. Experimental evidence shows that a suspension raked with vertical pickets, in fact dewatered faster than when the same suspension was raked with a horizontal rake [155]. Despite this, the exact role of channelling is still poorly understood and likely to depend on a range of factors including the type of material, its flocculation state, and shear regime. This issue is explored further in Chapter 5.

One approach to understanding the effect of shear on dewatering and hopefully better predict thickening behaviour, is to quantify the effect of shear on dewatering by measuring changes in $P_y(\phi)$ and $R(\phi)$. By measuring these parameters under more representative conditions of full sized thickeners, it is hoped that the predictive capability of thickener modelling will improve. This objective forms the basis for the experimental work appearing in Chapter 5.

Another option is to observe continuous thickeners on an industrial scale and vary operating parameters such as the speed, height, pitch and spacing of the rake blades. Unfortunately, several practical reasons prevent such studies including; a shortage of sites able to accommodate the significant disturbance to operation that such a study would impose; the small range in rake motor speed due to the large torque requirements; and a lack of sensitivity to these changes because of limited control over the operating variables. This last point is a feature of most thickeners operating in the minerals industry. The issues and obstacles of comparing model predictions against operational outputs are discussed in Chapter 6. A pilot scale thickener could provide an alternative. Advantages of pilot scale experiments include lower operational costs, greater control over experimental parameters and the flexibility to vary these parameters as desired. Pilot scale experiments in both the absence and presence of shear are reported in Chapter 4 and Chapter 7 respectively.

A feature of flocculated suspensions is their extreme shear sensitivity. If the compressibility and permeability of a freshly flocculated sample is measured, and the sample is sheared and $P_y(\phi)$ and $R(\phi)$ remeasured, changes are observed. The application of shear reduces the network strength so that the sediment becomes more compressible. More compressible sediments are often less permeable. To explain this result, shear must facilitate the escape of fluid

during the settlement and consolidation of the flocs. The densification of aggregates due to shear is not accounted for in steady state modelling, since the compressibility and permeability are assumed constant with time. In Chapter 8, aggregate restructuring over extended time scales relevant to thickening is considered. The results of this work could explain why steady state thickener models are unable to predict what appears to be a transient and complex problem.

1.3 Research Objectives

The overriding objective of this research is to increase fundamental understanding of thickening and in particular the role of raking in a consolidating bed. The state of the art in this area represents quantitative comparison between un-raked batch laboratory experiments and phenomenological modelling (which gives a generally poor correlation) and empirical observations of improvements in settling performance associated with shear and raking of sediments. To begin to quantify some of the role of shear and raking in dewatering, a number of tasks were undertaken that comprise the key chapters of this thesis. The tasks included:

- To demonstrate that existing method of characterising, analysing and modelling dewatering, *in the absence of shear*, are fundamentally correct by operating a tall pilot scale column under ideal conditions.
- To design a method for quantifying the effect of shear on dewatering and to identify the critical shear rates which produce maximum dewatering and develop a relationship between shear, dewatering and particle flocculation.

- To consider mechanistically how suspensions fail under combined shear and compressive forces. Knowledge of a failure mechanism has important ramifications in multidimensional dewatering analysis when applying computational fluid dynamics methods. Ongoing work on the multi-dimensional modelling of thickening requires quantitative inputs that are currently unavailable.
- To trial the newly developed shear characterisation method on a full-scale raked thickener. The aim was to characterise material freshly sampled from the thickener at different shear rates and simulate thickening performance based on the characterisation. Predictions and actual solid underflows may then be compared.
- To apply the method to characterise flocculated solids feed (calcite) fed to a pilot tall column operated under controlled conditions and a well defined shear rate. The aim is to allow comparison between dewatering in the column at a known constant shear rate and model prediction based on an equivalent shear applied during batch settling.
- To investigate the possibility of shear densification of flocculated particles at solid volume fractions less than the gel point. The aim is to update laboratory techniques to take into account the broad range of solids concentrations typical of thickening and ensure that these techniques produce data that is representative of operational thickeners. It was expected that a new technique would be required in which flocs are agitated by a counter current water flow for a length of time representative of a continuous thickener. Changes in dewatering and the structural properties of flocs can be considered as functions of time, flocculant dose and shear during flocculation.

1.4 Thesis Outline

This thesis has been presented in a chronological format deliberately. Often, the experimental protocols and research direction were dictated by results from earlier chapters, with the overall objective of shear in mind. For example, the shear experiments described in Chapter 5 were designed based on knowledge gained from Chapter 4; specifically that the 1-D model correctly predicted dewatering for certain, idealised cases. Full scale testing of the characterisation method was conducted based on the positive outcomes from the shear experiments of Chapter 5, and so on. Without this logical progression in mind, the significance and reasoning behind the experiments may be lost. The first three chapters are devoted primarily to background information concerning dewatering theory, flocculation and thickener modelling. The information presented in these chapters will be continually drawn upon in the experimental chapters which follow. The remaining chapters provide information regarding procedures, results, and additional theory not covered in the first three chapters.

Chapter 2 presents an overview of modern dewatering theory and its applications to thickening. Topics discussed include a phenomenological description of sedimentation and consolidation, generally valid for any dewatering process. Laboratory methods for measuring the dewatering parameters including transient settling, batch settling and filtration are detailed and dewatering analysis is explained.

Chapter 3 reviews the important theory of particle aggregation. Given the importance of flocculation to efficient dewatering, and the dependence of the experimental results, flocculation is explored in some detail. Mechanisms of particle aggregation, factors influencing flocculation and methods for flocculating in the laboratory are discussed A basic understanding of flocculation is essential

in order to understand the results appearing in later chapters, which consider the effect of flocculation conditions on dewatering as a function of shear rate, for example. In the final section of Chapter 3, the dewatering behaviour of two flocculated systems (calcite and kaolin) is presented using the established characterization and analytical tools introduced in Chapter 2. In this way, flocculation performance is assessed and optimum flocculation conditions identified. Note however, that these characterization tools do not account for shear effects.

Chapter 4 describes the operation of a tall narrow pilot column. In the first instance the column was operated without any externally applied shear (i.e. no moving components or rakes). The compressive rheology of the flocculated calcite feed was characterised using methods discussed in Chapter 2 and model simulation allowed the predicted values to be compared against experimental data. This was done for a range of operating conditions. The objective of this work was to establish that the model accurately predicted dewatering in the absence of shear.

Chapter 5 describes a novel technique for characterising suspension dewatering by applying shear. A Couette geometry was used to accurately quantify shear rates. Dewatering data was measured as a function of shear rate and flocculant dosage so that changes in dewatering due to shear could be quantified and the thickener remodelled. For each flocculant dose it is possible to identify a critical shear rate at which dewatering is optimised. Finally, a comparison between Couette and raked settling tests allowed a postulate for a dominant dewatering mechanism.

Chapter 6 describes the application of shear to characterise a freshly flocculated feed sampled from an industrial operating thickener with a rake. The suspension

rheology, i.e. $P_y(\phi)$ and $R(\phi)$ is determined in both the absence and presence of shear forces and dewatering simulated based on a zero and optimum shear rate (as determined by the Couette shear experiment). It is hoped that by accounting for shear during the characterization, the subsequent modelling efforts will be improved. This is tested by comparing the model prediction incorporating shear to the underflow solids concentration produced by the thickener.

Chapter 7 extends the model validation attempt presented in Chapter 4 by introducing shear into the column. The operation of the column is discussed including improved control methodology. The results from the column and the model prediction accounting for shear are compared.

Chapter 8 considers dewatering of flocculated suspension at solid concentrations less than the gel point, which are subjected to mild shear for an extended period of time. A fluidization technique is developed to keep the solid concentration constant. The flow of water through the fluidized bed gently massages the flocs and changes their structure. Several techniques were employed to measure these structural changes as a result of this gentle shear. The compressive dewatering parameters were measured as a function of flocculation conditions, (flocculant dosage and shear rate) and the time of fluidization. Thus, it is possible to parameterize $R(\phi)$ and $P_y(\phi)$ with time.

Chapter 9 summarizes the key findings and identifies avenues for future research.

Chapter 2

Dewatering; theory, characterisation and analysis

2.1 Introduction

This chapter provides background to dewatering theory by considering the mechanics of sedimentation and consolidation. Mechanically, these processes are similar; both are driven by gravity and resisted by a hydrodynamic drag. They differ only by the presence of a network stress term in the consolidation force balance. Consequently, the same equations (mass and linear momentum balances) apply equally to both sedimentation and consolidation when combined with appropriate constitutive relationships for the interphase drag and solid stress. Experimental methods for determining these relationships are integral to dewatering analysis and any subsequent modelling efforts. These methods and their limitations are outlined.

2.2 Dewatering phenomenology

The phenomenon of dewatering is demonstrated by the simple batch-settling test, shown in Figure 2-1. A cylinder is filled with a suspension of small particles (relative to the cylinder diameter). The suspension is initially homogeneous, with a solid volume fraction ϕ_0. Over time, the particles settle due to a net buoyancy force. Consequently, a shock or discontinuity develops between the particles and supernatant; which is manifest as an interface, $h(t)$ (see Figure 2-1 F-H). The

particles settle until reaching the bottom of the cylinder where a loose bed structure forms. Therefore, at any time three distinct regions can be identified in a sedimentation process; supernatant, hindered settling, and bed zones.

Particles continue to settle from the hindered settling zone until eventually only the bed and supernatant regions remain (Figure 2-1 I). If the particles were force free hard spheres, dewatering will end at this point. However, most flocculated systems are compressible to some extent, and therefore, dewatering will continue as a result due to failure under the weight of the bed. Compressive and shear stresses can cause significant deformation of the bed resulting in volume change; a process termed consolidation (Figure 2-1 J).

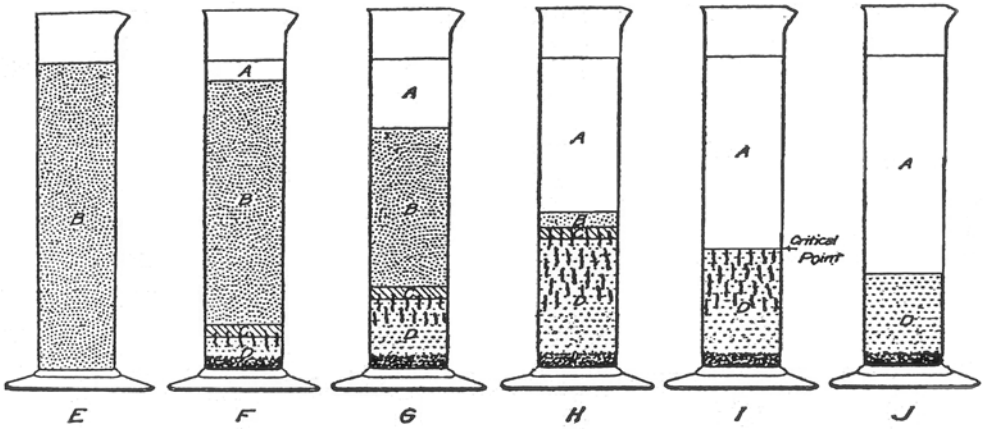

Figure 2-1 Settling of flocculated suspensions from Coe and Clevenger [32] showing the different zones in thickening; **(A)** clarified water zone **(B)** zone of initial concentration (ϕ_0) **(C)** transition zone **(D)** consolidation zone

2.2.1 Sedimentation

Under dynamic equilibrium conditions, sedimentation involves the balance of three forces, namely gravitational, F_G buoyancy, F_B and hydrodynamic drag, F_D;

$$F_G + F_B + F_D = 0 \tag{2.1}$$

The hydrodynamic drag results from fluid flow past the particle and consists of a normal component caused by fluid acceleration and a tangential component arising from surface friction [90]. In 1861, Stokes determined F_D for a single particle settling in an infinite medium. Using the equations of motion, Stokes showed that under creeping flow, F_D is given by the following expression;

$$F_D = 6\pi \mu r_p v_\infty \tag{2.2}$$

where r_p is the particle radius, μ is the fluid viscosity and v_∞ is the fluid approach velocity.

The gravitational force F_G is determined from the weight of the solid particles, while the buoyant force F_B, is the simply the weight of displaced fluid.

$$F_G = \frac{4}{3}\pi r_p{}^3 \rho_s g \tag{2.3}$$

$$F_B = -\frac{4}{3}\pi r_p{}^3 \rho_f g \tag{2.4}$$

where g is the gravitational acceleration, ρ_f is the density of the fluid phase and ρ_s is the density of the solid phase. Substituting equations (2.2), (2.3) and (2.4) into equation (2.1), yields Stokes Law for the terminal velocity of a single particle, u_∞;

$$u_\infty = \frac{d_p{}^2 \Delta\rho g}{18\mu} \tag{2.5}$$

Stokes law applies to the low Reynolds limit i.e. $\mathrm{Re}_p = \frac{\rho_f u d_p}{\mu} << 1$. For $\mathrm{Re}_p \geq 0.2$, inertial terms become significant and an empirical interphase drag coefficient (C_D) is required;

$$F_D = \frac{1}{2} \rho_f u_\infty^2 C_D A \tag{2.6}$$

where A is the cross sectional area of the flow.

2.2.2 Consolidation

Originally, consolidation was of interest primarily to geotechnical and civil engineers concerned about the strength and stability of structural foundations, embankments and tailing dams. Consolidation is the process of reducing the water content of a volume element of soil or sediment by applying a force. In general, an incremental stress increase causes a volume change in one of three ways;

- compression of individual particles,
- compression of fluid
- compression of a particle network

Because fluid and solid particles are significantly less compressible than the particle network, the particle and fluid phases are treated as incompressible. Then, any volume change is due entirely to the failure and realignment of particles within the network.

The mechanics of consolidation can be described by way of an analogy. Consider a cylinder (with cross sectional area A) that contains fluid, a spring and is sealed by a moveable piston with a valve (see Figure 2-2). The spring represents the compressible particle skeleton, the fluid, the interstitial pore water, while the valve diameter corresponds to the permeability of the sediment, which in this model is constant.

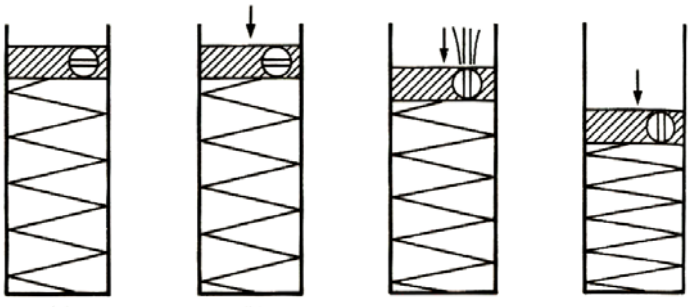

Figure 2-2 Consolidation analogy with loaded spring. Reproduced from Craig [38]

If a force (F) is applied, the volume of the cylinder does not change since the fluid is incompressible. The piston is stationary and no force is transferred to the spring. Instead, the load is borne entirely by the pore water, so that the fluid pressure u increases above a datum by Δu, where Δu is given by $\frac{F}{A}$.

If the valve is suddenly opened, the excess pore pressure forces fluid from the cylinder, so that the piston can now descend and the load is transferred partially to the spring. Fluid continues to drain until the excess pore pressure reduces to zero, at which point the load is entirely supported by the spring. The stress on the spring is the effective solid stress P_e, the load on the piston, the total stress P, and the difference is the excess pore pressure.

$$P = P_e + \Delta u \tag{2.7}$$

2.3 Modern dewatering theory

In 1987, Buscall and White [24] proposed a unified theory describing sedimentation and consolidation of flocculated particles. The theory identifies three important properties governing dewatering; the compressive yield stress, $P_y(\phi)$, hindered settling function, $R(\phi)$ and solid gel point, ϕ_g. Collectively, these constitute the compressional rheology of a suspension. The compressive yield stress is analogous to the shear yield stress, and determines the strength or extent a suspension will dewater. The hindered settling function $R(\phi)$, quantifies the hydrodynamic resistance and thus governs the rate at which water escapes. Thus, $R(\phi)$ is analogous (and inversely related) to the Darcian hydraulic conductivity K. The gel point is the critical solid volume fraction, at which individual particles or aggregates first "touch" to form a continuous load bearing network structure. Thus, the gel point determines the onset of consolidation for compressible flocculated suspensions.

2.3.1 Hindered Settling Function

In a concentrated suspension, long-range hydrodynamic interactions hinder the relative movement of particles through fluid. The interphase drag is a complex entity, depending on fluid viscosity, local solid volume fraction, particle size and shape, and suspension microstructure.

Landman and White [92] account for particle-particle interactions through a concentration dependent parameter, known as the hindered settling factor, $r(\phi)$. The hindered settling factor quantifies the hydrodynamic drag in a volume

element of suspension by correcting for the deviation from single particle settling dynamics, i.e. $r(\phi) = \frac{u_\infty}{u(\phi)}(1-\phi)$. where u_∞ is Stokes settling velocity and $u(\phi)$ is the velocity of particles settling in a suspension with an average solid volume fraction ϕ. A typical plot of $r(\phi)$ (Figure 2-3) displays the following properties;

$$\lim_{\phi \to 0} r(\phi) \to 1$$
$$\lim_{\phi \to 1} r(\phi) \to \infty \tag{2.8}$$

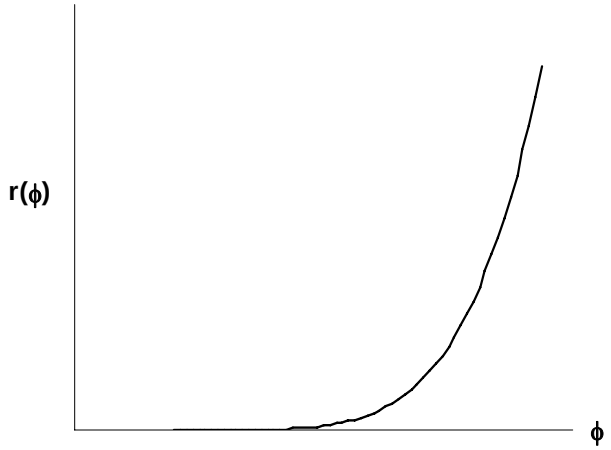

Figure 2-3 Hindered settling function as a function of solid volume fraction

The hindered settling factor therefore quantifies the hydrodynamic drag in a volume element of suspension at local solid fraction ϕ;

$$F_D = -\frac{C_D}{V_P}\frac{\phi}{1-\phi} r(\phi)(u-v) \tag{2.9}$$

where $V_p =$ the volume of a particle while $(u-v)$ is the relative particle-fluid velocity.

The interphase drag coefficient C_D and the particle volume V_p are difficult parameters to determine experimentally, especially for fractal aggregates at concentrations above the gel point. Hence, C_D and V_p are commonly combined with $r(\phi)$, to yield the more convenient hindered settling function, $R(\phi)$ [92]:

$$R(\phi) = \frac{C_D}{V_P} r(\phi) \tag{2.10}$$

For ideal systems, the hindered settling factor can be calculated theoretically. Batchelor [9] for example, calculated $r(\phi)$ for a monodisperse suspension of spheres to first order in ϕ. Higher order approximations are possible, however, microstructural complexities make computing $r(\phi)$ for real systems impractical [97]. Consequently, in practice $R(\phi)$ is determined experimentally. For a variety of suspensions, $R(\phi)$ data has been correlated by the following functional forms;

$$\begin{aligned} R(\phi) &= w(1-\phi)^{-m} \\ R(\phi) &= we^{m\phi} \end{aligned} \tag{2.11}$$

where w and m are constants. The above functions are by no means comprehensive. Efforts to expand upon these functional forms in order to describe a wider body of materials, is an ongoing area of research.

2.3.2 Compressive Yield Stress

The compressive yield stress, $P_y(\phi)$, is an important property characterising the strength of a particle network subject to uniaxial compression. The compressive yield stress is the pressure at which a flocculated suspension, at solid volume fraction ϕ, can no longer support the load elastically. The compressive yield stress is related inherently to the strength, type and density of inter-particle bridging forces. The strength of flocs and therefore $P_y(\phi)$ can be modified at constant ϕ, either by changing the type of flocculant or increasing the flocculant dosage.

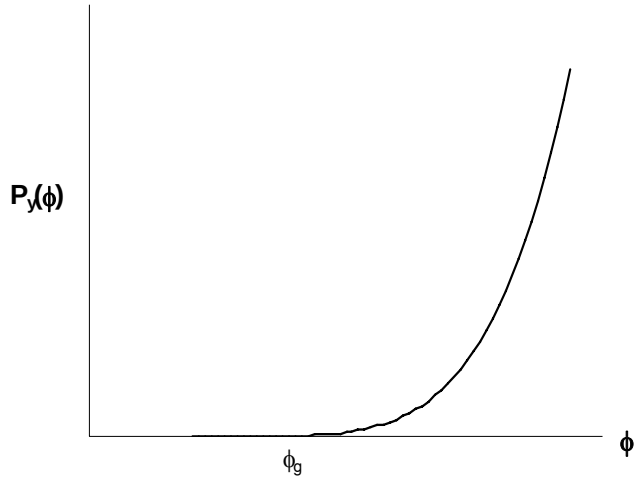

Figure 2-4 Compressive yield stress curve as a function of solid volume fraction

The gel point, ϕ_g, is intrinsically linked to $P_y(\phi)$. When the solid volume fraction is less than the gel point, the particles or aggregates are not inter-connected and therefore there is no mechanism for transmitting stress. In other words, the effective stress is zero, and the pressure is hydrostatic. Particle

collisions still give rise to a particle stress, which has been shown to be thermodynamically equivalent to the osmotic pressure, P_{os} [24]. However, the short-range nature of P_{os}, means that other than within the bed, the effect of P_{os} is negligible compared to the gravitational potential.

At solid volume fractions above the gel point, the effective stress steps to a finite value. The bed takes on the properties of a solid, including the ability to resist deformation elastically, characterised by a yield stress, P_y. At the top of the bed, the effective stress is zero by definition and the solid volume fraction is equal to the gel point. If the effective stress (P_e) is less than $P_y(\phi)$, energy is stored elastically within the particle network configuration. If P_e exceeds $P_y(\phi)$ the network consolidates irreversibly to a higher ϕ, fluid drains and additional bonds form so that the network is strong enough to support the load [57].

The salient features of $P_y(\phi)$ are demonstrated by Figure 2-4. For $\phi < \phi_g$, $P_y(\phi)$ is identically zero, while $\phi \geq \phi_g$, $P_y(\phi)$ increases monotonically with ϕ, and asymptotes to a close packed concentration ϕ_{cp}. The compressive yield stress data can be fitted by the following functional forms;

$$P_y(\phi) = k\left(\frac{\phi}{\phi_g} - 1\right)^n$$

$$P_y(\phi) = k\left(\frac{\phi^n}{\phi_{cp} - \phi}\right) \qquad (2.12)$$

$$P_y(\phi) = k\phi^n$$

where k and n are fitting constants. The kinetics of collapse is thought to obey the following rate equation;

$$\begin{aligned} \frac{D\phi}{Dt} &= 0 && P_e < P_y(\phi) \\ &= \kappa(\phi)\left[P_e - P_y(\phi)\right] && P_e \geq P_y(\phi) \end{aligned} \tag{2.13}$$

The parameter κ, is the dynamic compressibility, governing the rate failure occurs. If the kinetics of consolidation are assumed to be limited by the drainage rate, and not the rate of bond rupture and reformation, it can be shown that the value of κ is large [24]. Thus equation (2.13) can be restated as $P_e = P_y(\phi)$: in other words, failure is so rapid that the network stress never greatly exceeds the yield stress. In this model, the collapse is assumed irreversible. While some materials, i.e. clays, can swell slightly when the stress is removed, the bulk of experimental evidence supports irreversible consolidation, especially when the material is strongly flocculated.

Particulate suspensions or filter cakes consisting of large particles do not necessarily exhibit the compressional behaviour shown by Figure 2-4 since the particle interactions in this case are dominated by frictional forces. However, for a large number of mineral systems, where particles are typically fine and flocculated with high MW polymer, $P_y(\phi)$ does increase monotonically with solid volume fraction as shown by Figure 2-4. Each system studied in this thesis displays this behaviour; i.e. elastic when deformed at stresses less than a critical yield stress.

2.3.3 Continuous thickening

To simulate dewatering, mass and linear momentum balances for the solid and liquid phase, in combination with constitutive equations for $R(\phi)$ and $P_y(\phi)$ are solved over the height of the thickener. This approach has been described by numerous workers to predict dewatering in continuous flow thickeners [19, 40, 52, 80, 94]. The following is based on the analysis presented by Landman and co workers [92, 94].

The force balances on a volume element of fluid and particles are respectively;:

$$\phi R(\phi)(u-v)+(1-\phi)\nabla p_f+(1-\phi)\rho_f g=0 \tag{2.14}$$

$$\phi R(\phi)(u-v)+\phi\nabla p_s+\rho_s\phi g=0 \tag{2.15}$$

Dividing equations (2.14) and (2.15) by $(1-\phi)$ and ϕ respectively and subtracting the resulting equations, generates a force balance in terms of drag and effective stress;

$$-\frac{\phi}{1-\phi}R(\phi)(u-v)-\nabla P_e+\Delta\rho g\phi=0 \tag{2.16}$$

where $\Delta\rho=(\rho_s-\rho_f)$. The solid and fluid phase continuity can be expressed by equations (2.17) and (2.18) respectively;

$$\frac{\partial\phi}{\partial t}+\nabla\cdot(\phi u)=0 \tag{2.17}$$

$$\frac{\partial(1-\phi)}{\partial t}+\nabla\cdot\left[(1-\phi)v\right]=0 \tag{2.18}$$

Addition of equations (2.17) and (2.18) yields $\nabla \cdot \left[\phi u + (1-\phi) v \right] = 0$ which when integrated, yields an expression for the volume average velocity, $q(t)$;

$$q(t) = \phi u + (1-\phi) v \tag{2.19}$$

In batch settling, $q(t)$ is zero, while in continuous thickening $q(t)$ corresponds to the volumetric velocity of the solids settling in the thickener.

2.4 Characterisation and dewatering analysis

The practical application of dewatering theory is limited without means for determining the compressive rheology. The compressive rheology is material specific and therefore must be measured experimentally. Hence, the emergence of dewatering theory has spurned a concerted effort to develop techniques for measuring $P_y(\phi)$ and $R(\phi)$ in the laboratory [57, 58, 91, 95, 96, 154].

Characterising the rheology of a suspension can be instructive. Doing so can demonstrate the fundamental effect of chemical addition on dewatering and help identify optimum flocculation conditions. Aziz et al [7] characterised model alumina suspensions and industrial water treatment sludges using pressure filtration. Dewatering was quickest when the alumina suspension was at its iso-electric point, while water sludges dewatered quickest when dual dosed with alum and polyelectrolytes. Polyelectrolytes favourably alter the dewatering characteristics of alum treated sludges [77] however changes in compressibility were insensitive to the type and dosage of polyelectrolytes. Johnson et al [77] state this is due likely to the organics (humic and fulvic acids) bound to the surface of the Al(III) precipitates making the sludge resistant to chemical conditioning.

Perhaps the greatest challenge associated with characterising the suspension rheology is the large range over which the compressive yield stress and hindered settling function can vary. It is not uncommon for $R(\phi)$ to vary by three orders of magnitude for small increases in ϕ. At present, no single experiment can provide data across the entire range of solid volume fraction relevant to thickening. Instead, data obtained from several different experiments must be combined.

Generally, dewatering experiments can be classified according to the pressure. Low-pressure experiments including transient and equilibrium batch settling tests determine $R(\phi)$ and $P_y(\phi)$ at low solid volume fractions relevant to gravity thickening. Information at higher solid volume fraction is available from centrifugation and pressure filtration tests. Gravity permeation [96] is a useful technique for determining $R(\phi)$ at intermediate solid volume fractions. In this thesis batch settling and filtration were primarily employed. The theory and analysis of these tools are presented in the following section.

2.4.1 Transient Batch Settling

Transient batch settling tests are conceivably the simplest possible dewatering experiment. For years, batch settling tests have been used to design thickeners and assess flocculant performance. The advantage of batch settling tests is they are simple to operate, with no specialised equipment required. The main disadvantage is that the information obtained from these tests was in the past restricted to the initial solid volume fraction only. For ϕ_0 less than ϕ_g, the force balance can be rearranged and $R(\phi_0)$ solved directly;

$$R(\phi_0) = \frac{\Delta\rho g (1-\phi_0)^2}{u(\phi_0)} \tag{2.20}$$

For non-aggregated systems, determination of $R(\phi)$ is straightforward, as suspensions can be preparing at increasing ϕ_0 and $u(\phi_0)$ measured. However, for aggregated systems this approach does not work as it is not possible to produce the same flocs when the initial solid volume fraction is different. The alternative of flocculating at constant ϕ and then varying the concentration by adding or removing water is equally unfeasible, since consolidation of the flocs will inevitably occur. Therefore, the only remaining option is to measure the suspension rheology insitu.

2.4.1.1 Transient Settling Analysis

Transient settling tests contain important information regarding the dewatering dynamics of dilute suspensions, typically encountered in thickening. The information available ranges from the initial concentration up to some maximum concentration, expressed in the test. A challenge, as mentioned above, involved determining the interphase drag function or $R(\phi)$ directly from the settling curve. This problem was recently addressed by Lester [98] who described a method for estimating $R(\phi)$ by solving analytically the associated inverse problem, i.e. $h(t) \Rightarrow f(\phi)$ where $f(\phi)$ is the solid flux function $f(\phi) = \phi u = \frac{\phi(1-\phi)^2 \Delta\rho g}{R(\phi)}$. Analytical solutions of the solids flux function are only available for ϕ less than ϕ_g. For ϕ greater than ϕ_g, the solution must be obtained numerically.

For $\phi < \phi_g$, the conservation law (equation (2.16)) reduces to;

$$\frac{\partial \phi}{\partial t} + \frac{\partial}{\partial x} f(\phi) = 0 \tag{2.21}$$

To guarantee a unique solution, an entropy condition is enforced. This leads to several modes of settling including shocks, contact discontinuities and rarefaction waves. The amount of $R(\phi)$ information contained within $h(t)$ depends on the particular mode of settling. The maximum amount of information, i.e. $f(\phi)$; $\phi_0 < \phi < \phi_{\max}$ is obtained when settling occurs as a rarefaction wave (mode 3). The mode depends on ϕ_0 and the form of the individual flux curve. For further details, the reader is referred to Lester [97].

2.4.2 Equilibrium Batch Settling

Equilibrium batch settling provides a convenient way of measuring the compressive yield stress at comparatively low pressures relevant to thickening. An estimate of the gel point is also obtained. The technique involves a series of equilibrium batch settling tests, with either different ϕ_0 or h_0. This can be used to plot height data as a function of total solids in the cylinder. This approach has been described by several authors [56, 115, 149]. Green [56] assumed an average solid volume fraction in the bed when calculating $P_y(\phi)$, which is unlikely at low pressures. Tiller et al [149] estimate $P_y(\phi)$ based on knowledge of functional forms, while Lester [97] recently described an analytical method which improves upon the simplifications and limitations inherent with the alternative methods. This method was used to estimate the gel point and $P_y(\phi)$ from settling data throughout this thesis. Essentially the problem involves establishing a

relationship between equilibrium height, gel point and the compressive yield stress. For further detail the reader should refer to Lester [97].

2.4.3 Pressure Filtration

Pressure filtration has been increasingly employed to determine compressibility and permeability of concentrated suspension [7, 11, 57, 58, 95]. The technique involves loading a sample, initially at concentration ϕ_0, into a cylindrical cell, at an initial height h_0. A piston applies constant pressure and fluid is forced through a permeable membrane that is supported by a stainless steel sintered base. A cake builds up from the bottom of the cylinder with a solid concentration profile ranging from $\phi = \phi_\infty$, at the membrane, to $\phi = \phi_g$, at the top of the cake. This stage is known as cake formation. Assuming that the membrane resistance is zero and that pressure is applied instantaneously filtration theory predicts a quadratic relationship between filtration time and filtrate volume. Under these circumstances the transient filtration behaviour is exactly quadratic for $\phi_0 < \phi_g$, and approximately quadratic for $\phi_0 > \phi_g$ [93]. In certain systems (for example large, coarse particles), the traditional methods for the extraction of compressibility and especially hindered settling function information can not be applied [136]. However, for filtration of the fine flocculated systems studied in this thesis, this theory is adequate. Hence, plotting t vs. V^2 should yield a straight line. The inverse of the slope of this line, $\left(\frac{dt}{dV^2}\right)^{-1}$ is designated β^2 [92].

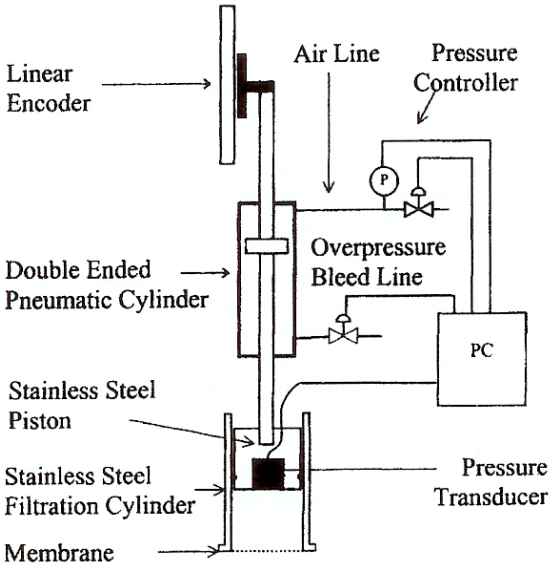

Figure 2-5 Stepped Pressure Filtration Apparatus taken from [154]

Eventually, the rising cake meets the piston marking the end of cake formation and the onset of compression. The transition happens at time t_c, and is detected by deviation from linearity in t vs. V^2, with V^2 instead decaying exponentially. Concentration gradients vanish so that the solid volume fraction is everywhere equal to ϕ_∞ the concentration corresponding to the applied pressure (ΔP). The equilibrium volume fraction ϕ_∞ is determined from $\phi_\infty = \frac{\phi_0 h_0}{h_\infty}$. Systematically increasing ΔP, yields the compressive yield stress as a function of solid volume fraction [56-58]. The hindered settling function may also be determined from linearized filtration theory;

$$R(\phi_\infty) = \frac{2}{\frac{d\beta^2}{d\Delta P}}\left(\frac{1}{\phi_0} - \frac{1}{\phi_\infty}\right)\left(1-\phi_\infty\right)^2 \tag{2.22}$$

A major limitation of filtration is the time scales involved. Reaching equilibrium can take several days or more; hence, evaluating P_y for a range of pressures would require several weeks. To circumvent these problems, de Kretser [39] and Usher [154] developed a stepped pressure filtration device. This technique reduces considerably the time required to measure the compressibility and permeability for a range of pressures. Using stepped filtration, $P_y(\phi)$ and $R(\phi)$ are determined in a matter of days, rather than weeks, a significant improvement on traditional centrifuge and single stage pressure tests. Rapid measurement is important because it increases the potential for "real-time" optimization of filtration and characterisation of materials which exhibit time dependent behaviour.

In certain cases stepped pressure filtration can result in a different measurement compared to single pressure filtration experiments; with the liquid pressure profiles differing in each case. This is especially true for systems that exhibit time dependency or are highly impermeable and compressible since these materials may not show linear t vs. V^2 behaviour. However, for the fine flocculated systems studied in this thesis, the differences between stepped and single pressure filtration have been found to be negligible [39].

2.5 Conclusions

In this chapter, the phenomenology of dewatering was outlined including descriptions of sedimentation and consolidation mechanics. A force balance model identified three important parameters; the compressive yield stress, hindered settling function and gel point. Because these parameters are material specific and cannot be easily predicted, they are usually determined experimentally. Experiments were described and the analytic tools available for

extracting $P_y(\phi)$ and $R(\phi)$ from settling height data were introduced. Using these tools, dewatering behaviour at different solid flux and bed heights can be simulated and flocculation performance assessed. This shall be addressed in the following chapters.

Chapter 3

Aggregation, suspension dewatering and its characterisation

3.1 Introduction

The aggregation of fine particles is widespread in colloidal suspension dewatering. Aggregation produces "flocs" which settle at nominally higher velocities compared to individual particles, a consequence of an increased ratio of mass in the floc to surface area. Thus, aggregation helps to overcome the characteristically slow settling rates and filtration times, which would otherwise inhibit continuous sedimentation and filtration processes [116]. Once settled, flocculated sediments are generally more permeable allowing thickeners and filters to operate at higher throughputs [116].

Countless studies of particle aggregation, both experimental and theoretical, are reported in the literature. Topics include; aggregation kinetics and evolution of floc size and structure [12, 134, 139], the relationship between polymer conformation and adsorption kinetics [169], and the role of chemistry and physical condition on flocculation [74, 81, 109]. These topics are, to a large extent, interrelated. For example, polymer adsorption depends on reagent type, particle size and solid concentration and influences aggregate size and structure [67, 120]. Likewise, aggregation rates depend on the frequency of inter-particle collisions, which are governed by hydrodynamic conditions and floc structure [85, 86], ultimately determining the maximum size, morphology and density of

the aggregate. Thus, while aggregation appears simple in concept, the reality is decidedly more complex.

Floc size, structure and density measurements provide a direct basis for assessing aggregation performance; however, because of their simplicity, indirect indicators such as settling rate and turbidity are common. While such parameters are important, they do not quantify dewatering, nor do they predict how a thickener will perform under different operating conditions. By only focussing on settling rate or floc size, overflow clarity and throughput may improve; but the dewaterability of the sediment and ultimate underflow solid concentration is not determined. To be comprehensive a flocculation assessment should incorporate both compressibility and permeability measurements across the range of volume fractions expressed in the thickener.

The aim of this chapter is to investigate the relationship between aggregation conditions and suspension rheology. Before presenting results, a brief background to aggregation is provided, including techniques for producing flocs in the laboratory.

3.2 Flocculation

Aggregation is a process in which two or more particles collide and attach to form loose, fragile structures known as "flocs". Aggregation generally comprises three stages; destabilisation, floc formation and floc degradation [68]. Particle destabilisation can occur in a number of ways. One method involves addition of electrolyte, effectively compressing the double layer and reducing the energy barrier. A suspension destabilised in this way is said to be coagulated.

The alternative to coagulation is to use high molecular weight polymer or polyelectrolyte to flocculate the particles. Flocculation has become increasingly common in dewatering; most thickeners feeds are now dosed with high molecular weight polymer, in addition to inorganic salts. Consequently, large improvements in stability, clarity and throughput have been reported [106, 107].

3.2.1 Mechanisms

There are two methods by which polymer molecules adsorb to the surface; hydrogen bonding, and electrostatic interaction. There is some dispute in the literature over which mechanism is more prevalent, however, it is generally accepted that both adsorption and desorption processes are involved. Interpreting flocculation is complicated because polymers are charged entities themselves, so electrostatic interaction is possible. In some cases, destabilization occurs because polymer has neutralized the surface charge of the particle.

3.2.1.1 Electrostatic patch effect

One possible mechanism for flocculation involves polyelectrolyte adsorbing to oppositely charged areas of the particle creating a localised "patch" of reversed charge [59]. The free surface retains the original charge. The charged patches then interact electrostatically with opposite charges on other particles as shown in Figure 3-1. Charge patch flocculation is most likely to occur when low molecular weight polymers with high charge density are used.

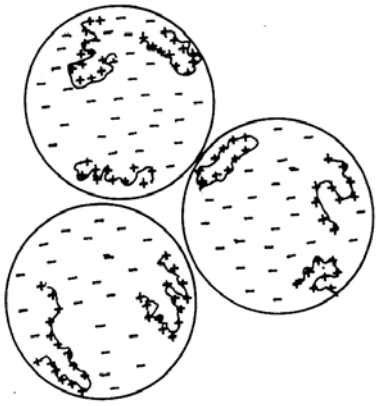

Figure 3-1 Charge patch mechanism adapted from Gregory [59]

3.2.1.2 Bridging mechanism

For high molecular weight polymers, it is likely that polymer adsorbs to multiple sites. In this case, the polymer acts as a bridge between particles. The theory of polymer bridging was originally postulated by Ruehwein and Ward [122] who observed aggregation of clays with polyelectrolytes. Further contributions were made by La Mer and Healy [63, 88, 122]. An important consequence of bridging flocculation is that the flocs are much larger and stronger than those formed by other mechanisms; for example, Tambo and Hozumi [141] estimated that clay flocs produced with a high MW non ionic polymer were 48 times stronger than when coagulated with alum.

To be effective, it is important that the polymer adsorbs to the particle in a conformation such that sufficient polymer molecules remain available to adsorb to other particles. If the polymer coverage is too high, additional bridging opportunities are reduced and the particle is described as sterically stabilised. The mechanism of polymer bridging is shown schematically in Figure 3-2.

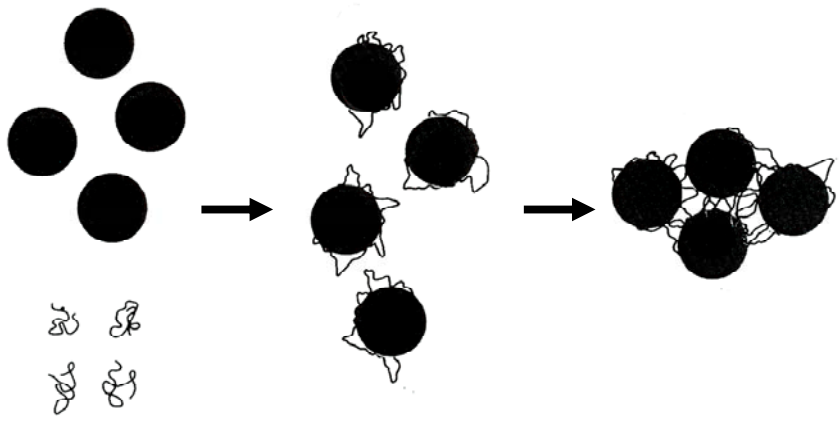

Figure 3-2 Polymer bridging mechanism [117]

3.2.2 Flocculant Synthesis

Flocculants are synthesised via chain polymerization. Unstable initiator molecules (e.g. 2,2'-azo-bis-isobutyrylnitrile, Cl_2 and benzoyl peroxide) undergo homolysis or photolysis generating radicals. These radicals then attack the monomer producing an activated monomeric species which can react with additional monomers to create a polymer [3]. The reaction is terminated either via coupling of two radicalized monomers, or disproportionation, the exchange of protons to form two terminated chains [3]. Figure 3-3 shows the polymerisation of acrylamide.

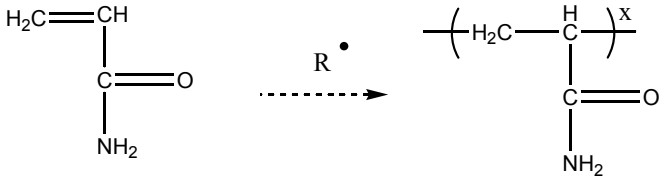

Figure 3-3 Polymerization of acrylamide

3.2.3 Factors influencing flocculation

3.2.3.1 Polymer type

Water soluble polyacrylamide and their ionic derivatives are common synthetic flocculants [106]. Synthetic polymers are preferred over natural flocculants as the ionic character, molecular weight and chemical structure can each be tailored to the requirements of individual applications. Within the mineral industry, conditions can vary from highly alkaline (Bayer process) to highly acidic (acid leaching) requiring polymers with different properties [105]. Use of synthetic flocculants is not limited to dewatering however, applications also exist in dust control, rheology modification, mineral beneficiation, and tailings disposal [35, 106]

Figure 3-4 shows examples of a few common flocculants with varying ionic character. Often, mineral flocculants are copolymers of acrylamide and sodium acrylate. Acrylamide is highly versatile as it reacts with a number of different monomers, in any ratio desired, to produce copolymers ranging between 100% anionic and 100% cationic character [106]. Because of the negatively charged carboxylate groups on the acrylate monomer, polyacrylate/acrylamide copolymers are anionic, the extent of which depends on the ratio of acrylate to acrylamide.

The role of each functional group is different. While in principle, both amide and carboxylate groups could adsorb to the particle, evidence suggests that it is the amide groups, which are primarily responsible for adsorption [35]. Comparison between acrylamide homopolymer and 25% acrylamide and 75% dimethylacylamide copolymer, showed lower flocculant activity in the methyl-substituted polymer than the acrylamide homopolymer. The carboxylate is thought to extend the polymer chain by electrostatic repulsion between negative

COO^- groups. Thus, activity of flocculants containing acrylate will depend on pH.

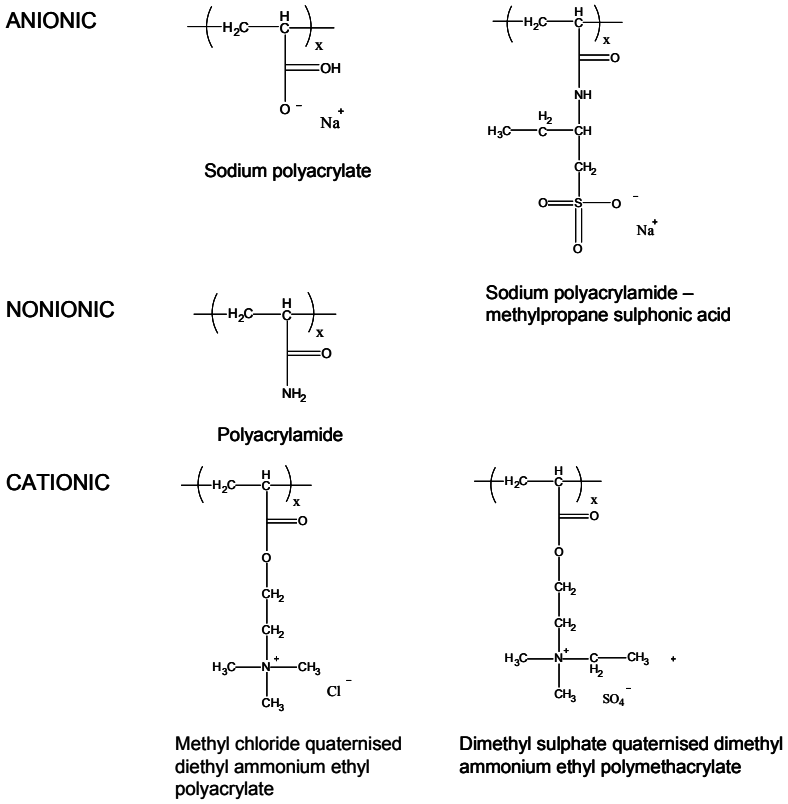

Figure 3-4 Examples of anionic, non-ionic and cation polymer flocculants

3.2.3.2 pH

Polymer conformation and therefore activity, strongly depends on solution pH. Solution pH affects both rheology and chemistry of the polymer chains [16, 61]. At low pH, carboxyl groups are fully protonated and the polymer can coil. When the pH is increased, the carboxyl groups begin to lose their protons so that electrostatic repulsion causes the polymer to uncoil, see Figure 3-5. The amount of uncoiling can be determined from intrinsic viscosity measurement. The

intrinsic viscosity $[\eta]$ is the limiting value of reduced viscosity at infinite dilution. A high $[\eta]$ indicates that a polymer is uncoiled [116].

$$[\eta] = \lim_{c \to 0} \left[\frac{1}{c} \left(\frac{\eta}{\eta_0} - 1 \right) \right] \tag{3.1}$$

The pK_a of acrylic acid is 4.25, therefore at pH 7 the ratio between the conjugate acid-base pair is 560:1. At pH 5 the ratio is 5.6:1, while at pH 3 the polymer is almost completely hydrated. Because of the loss of charge at low pH, the flocculant will coil and depending on the anionic character, may precipitate. This is obviously an undesirable outcome, and therefore, non-ionic polymers are more suitable for flocculation at low pH. Up to pH ~ 10, the performance of non-ionic flocculants is constant as there are no carboxylate groups. For pHs between 6 and 8, moderately anionic polymer should produce optimum results. At pH above 11, hydrolysis of amides compete with adsorption, so highly anionic flocculants are more suitable. Poor performance of anionic polymers at low pH can be improved by replacing carboxyl groups with a stronger acid i.e. sulfonic acid.

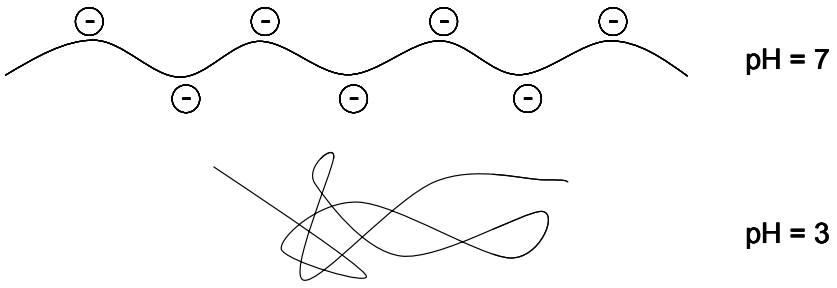

Figure 3-5 pH dependence of polymer conformation

3.2.3.3 Molecular Weight

The molecular weight (MW) of a polymer is important, particularly in bridging flocculation, since the longer the chain, the more bridges should result. A less desirable consequence of increasing the MW is that the solution becomes more viscous. In practice, an upper MW limit exists, because efficient dispersal of polymer becomes difficult in highly viscous solutions. A further consideration is that as the molecular weight increases the number of polymer molecules per unit volume decreases. It is possible that for high MW polymers, the number of chains is less than the number of particles, resulting in generally poor flocculation.

3.2.3.4 Solid concentration and particle size

The suspended solids volume fraction and particle size distribution effects flocculant dispersal. As the percentage of solids increases, uniform dispersal of flocculant becomes increasingly difficult and the flocculant demand on a mass per tonne basis increases as a consequence. Particle size changes show similar results – a small increase (< 10%) in fines fraction can double the flocculant consumption [105].

3.2.3.5 Flocculant dilution and dose

Flocculant dilution is an important consideration. Generally, the more dilute will the faster the settling rate and the lower the turbidity. This effect follows similar reasoning to the solids concentration; dilute solutions are less viscous and thus mix better. This reduces the tendency for poor distribution of polymer and local overdosing. Flocculant dose is equally important. A higher dosage, normally expressed as the mass of polymer per mass of dry solid, corresponds to a higher number of polymer molecules per volume of suspension. As a result, more particle bonds can form and the overall strength of the aggregate increases. As

shall be seen later, this result has important implications for suspension dewatering.

3.3 Laboratory methods of flocculation

There are several methods for producing flocculated material. These can be either batch or continuous and include simple plunger tests, stirred baffled reactors, pipe reactors and Couette shear reactors.

3.3.1 Batch Flocculation

3.3.1.1 Plunger Tests

The simplest method of flocculation is the plunger test. The plunger involves injecting a known volume of polymer into a measuring cylinder containing suspension and then moving a flat perforated disk (plunger) up and down a number of times. This forces the suspension through the narrow orifices, creating turbulent jets, which promote mixing. The main advantage of plunger tests is that they are simple to operate and require no specialised equipment, making them ideal for test work onsite. The drawbacks include poor mixing, resulting in low flocculation efficiency and local overdosing of polymer. Furthermore, shear rates are variable, operator dependent and difficult to quantify.

3.3.1.2 Baffle Reactor

Stirred baffled reactors are relatively common in flocculation studies, with a number of studies appearing in the literature [30, 49, 135]. The design of the stirred reactor is straightforward, and based on the standard tank configuration proposed by Holland [72, 86]. The reactor consisted of a flat-bottomed vessel,

with four equally spaced baffles reducing vortex formation, while an overhead motor and impeller provide agitation (see Figure 3-7). Several impeller types are available; including paddles, picket gate, flat radial blades, and axial blades, each producing slightly different hydrodynamic flow fields. The effect of different impeller type and hydrodynamic conditions on floc size and structure was recently investigated by Spicer [133].

The advantages of stirred baffle arrangement include its simplicity and the relatively small sample requirement. Flocculation tests can be performed by a single operator in the laboratory or on-site. The effect of physical conditions including temperature, pH and shear rate can be easily investigated. The disadvantages include the highly heterogeneous shear field which produces aggregates of varying sizes; and the inability to flocculate sufficient volumes required for continuous studies.

The hydrodynamics of turbulent mixing in stirred vessels is characterised by the following parameters [36];

- Reynolds number (Re);

$$Re = \frac{ND_i^2}{\nu} \tag{3.2}$$

where N is the impeller velocity, ν the kinematic viscosity and D_i is the impeller diameter.

- and a globally averaged velocity gradient (G) [26];

$$G = \left(\frac{P}{\mu V} \right)^{1/2} \tag{3.3}$$

where P is the power dissipation in the vessel, V is the stirred tank volume, and μ the dynamic viscosity. The power is related to a dimensionless power number, N_p, according to [36];

$$N_p = \frac{P}{\rho N^3 D^5} \tag{3.4}$$

while the dissipated power is directly related to the viscous dissipation rate ε;

$$\varepsilon = \frac{P}{\rho V} \tag{3.5}$$

For impeller Reynolds numbers above 10^3, N_p is approximately constant and is equal to 5 for the Rushton impeller [86]. Combining equations (3.3) and (3.5), the averaged velocity gradient is given by;

$$G = \left(\frac{\varepsilon}{\nu} \right)^{1/2} \tag{3.6}$$

Fluid flow in stirred tanks is highly heterogeneous so G is only an average. It does not account for localised velocity gradients, which will vary depending on the type of agitation [133]. The turbulent energy dissipation rate is obviously higher in the region near the impeller compared to the bulk. The frequency of floc exposure to this high shear is inversely related to a circulation time t_c [135];

$$t_c = \frac{V}{N_q N D_i^3} \tag{3.7}$$

where N_q is the dimensionless pumping capacity. For the Rushton impeller, $N_q = 0.9$. Radial flow impellers tend to possess higher circulation times than axial flow resulting from the different flow patterns. For most common impeller types the average shear rate varies linearly with impeller speed regardless of impeller size [113].

3.3.2 Continuous Flocculation

3.3.2.1 Linear Pipe Reactor

In this section continuous flocculation is discussed. Batch methods of flocculation in batch methods are generally inappropriate for the pilot scale experiments, because the amount of material required is prohibitively large. An alternative method for continuously flocculating large volumes of sample is the linear pipe reactor. The operation and set up of the pipe reactor has been described in detail elsewhere [139]. One advantage of pipe flocculation is that the hydrodynamic conditions are more representative of inside a thickener feed well. The reaction time or pipe residence time depends on the pipe length and flow rate while the shear rate also depends on the solids flow rate, in addition to pipe diameter and the properties of the suspension.

The main drawback of continuous flocculation is the large volume of material required. For example, to continuously flocculate a 0.05 w/w suspension, at a rate of 6 L min^{-1}, 3.3 kg of solids is consumed in 10 minutes, while 160 kg of solid is consumed over an 8 hour period. Furthermore, storage, sample

preparation and disposal requirements make this method of flocculation unsuitable for bench scale laboratory experiments.

3.4 Experimental

The research presented in this thesis was undertaken as part of a wider collaborative project investigating various aspects of thickener operation. In its fourth stage of funding, the project was supported by 27 sponsor companies including mining companies, flocculant suppliers and equipment manufacturers. The principal solid substrates used throughout this project are kaolin and calcite. To be consistent, and also to take advantage of the accumulated knowledge of flocculating these materials, calcite and kaolin are chosen in this thesis. In fact, there are few alternative particulate materials that are well characterised, have an average particle size less than 20 μm, are cheap, and readily available in tonne lots.

The experimental work presented in this thesis comprised laboratory, pilot scale and full scale studies undertaken at several sites. These included laboratory facilities at the University of Melbourne, pilot facilities at CSIRO Minerals sites in Clayton, Victoria and Perth, Western Australia and onsite work at Iluka Resources Yoganup mine near Capel, Western Australia. For logistical reasons it was not possible to conduct all experiments at the same site. Consequently, pipe reactors and water sources varied from site to site. Wherever possible, parameters such as average shear rates and floc formation times were matched. However, this was not always possible given the vast differences in volumetric flow rate between pilot and lab scales. In the laboratory, small scale flocculation experiments and dewatering characterisation including filtration were carried out. A tall pilot thickening column, described in Chapter 4 and Chapter 7 was located

at CSIRO Minerals, Clayton, Victoria. The Clayton site was chosen as the space, and equipment to prepare, store and dispose large quantities of suspension were already present. A facility for pilot scale pipe reactor studies with integrated online sizing was located at CSIRO Minerals in Perth, Western Australia.

3.4.1 Materials

3.4.1.1 Calcite

Calcium carbonate ($CaCO_3$) was the principal solid substrate used in this thesis. Calcite (Omyacarb 10) was chosen for its relatively pure form, (>98% according to information from the supplier), its narrow particle size distribution, and its availability in tonnage quantities at low cost. The solids are supplied in a ground powder form with a 12 μm nominal mean particle size and density ρ_s of 2700 kg m^{-3}. Calcite is sparingly soluble in water. At 25°C, the solubility product of calcite has been determined as $10^{-8.35}$ [83]. The crystal structure of calcite is shown in Figure 3-6

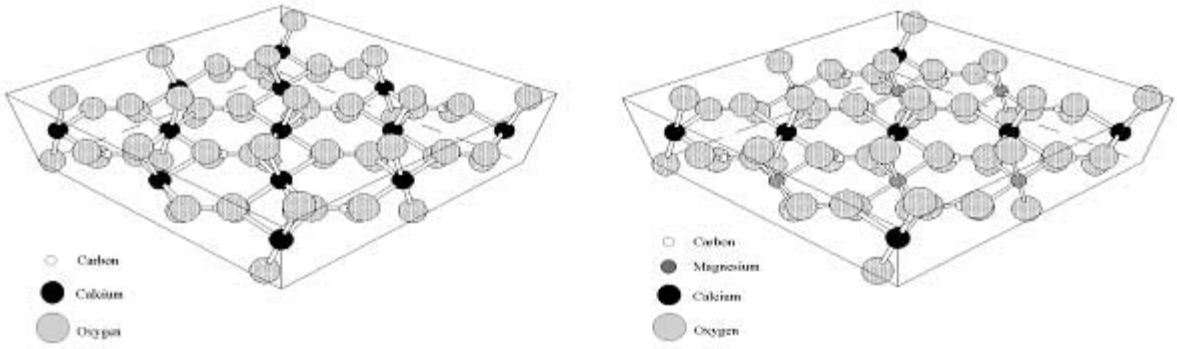

Figure 3-6 Crystal structure of calcite $CaCO_3$ (left) and dolomite $CaMg(CO_3)_2$ (right)

3.4.1.2 Kaolin

Kaolin was used in selected experiments as an alternative to calcite with significantly different dewatering properties. Because of the differences in particle size, shape and surface chemistry, kaolin requires a significantly higher flocculant dosage, shows a lower propensity to settle quickly (less permeable) and is easier to suspend in fluidisation experiments. The kaolin used in this study was acid-washed (LR) supplied by Ajax Chemicals. A manufacturer chemical assay indicated trace amounts of calcium (0.02 %), lead (0.002 %) and sulphate (0.05 %). Transmission electron microscopy shows that kaolin particles are hexagonal platelets with an average face diameter of approximately 0.5 μm and a mean edge thickness of approximately 0.05 μm. Further properties of kaolin are summarised in Table 3-1.

Table 3-1 Properties of Ajax kaolin particles. Data taken from Johnson [75]

Density (g cm^{-3})	BET specific surface area (m^2g^{-1})	Mean particle diameter (μm)
2.65	10.58	0.223

3.4.1.3 Water

Water is an important (and unavoidable) constituent of any dewatering experiment. Because the ionic strength of water can potentially influence particulate dewatering through surface chemistry effects, the type of water used in this thesis deserves some comment. Obviously, to avoid potential problems with ionic variability and the contribution of these ions to the surface chemistry, the best approach would be to use deionised water exclusively. However, large scale continuous flocculation and dewatering consumes large volumes of water

(~10 m^3 per day) such that at a pilot scale the use of deionised water was unfeasible.

To compromise, the best quality water available was used in each application. For lab scale experiments at the University of Melbourne this was milli-Q water; in pilot scale experiments at Clayton and Perth, local tap water was used; while full scale characterisation reported in Chapter 6 used process water sampled from the thickener. The fact that water varied between sites is unlikely to be a critical factor in the case of calcite and kaolin. The quality of water supplied to Perth and Melbourne is generally of high standard with a low ionic content. The composition of Melbourne tap water is shown in Table 3-2. Based on the solubility, it can be argued that the relative contribution of Ca^{2+} from the dissolution of calcite and on other surface contaminants will dominate the surface chemistry such that potential variation in the ionic strength of the tap water will have little effect.

Likewise, the contaminants present in the kaolin samples (see section 3.4.1.2) are sufficiently high to swamp any variation in the ionic strength of the water source. This is supported by conductivity measurements of clay suspensions, prepared with both with milli-Q and Melbourne tap water. The data in Table 3-3 shows that in each case the ionic strength is approximately 0.001 M Electrokinetic measurements of kaolin suspensions as a function of [$AlCl_3$] demonstrate that the zeta potential is relatively insensitive to small salt concentrations ([$AlCl_3$] < 10^{-2}) [76]. Given that the kaolin is equilibrated for several hours prior to flocculation, the small conductivity difference is unlikely to influence flocculation.

Table 3-2 Water Quality Analysis of Melbourne Water [162]

Property		Property	
pH (units)	7.0 - 7.8	Fluoride	0.85
Turbidity (NTU)	0.2 - 1.3	Iron	0.05
Specific Conductivity @ 20° C	60	Lead	<0.001
Total Solids	45	Magnesium	1.5
Total Alkalinity (as CaCO3)	14.5	Manganese	<0.01
Aluminium	0.050	Mercury	<0.0001
Arsenic	<0.005	Nickel	<0.002
Cadmium	<0.0005	Nitrate (as N)	0.20
Calcite	4.0	Potassium	0.5
Chloride	7.0	Selenium	<0.001
Chromium	<0.005	Sodium	4.5
Copper	<0.05	Sulphate	1.0
Cyanide	<0.01	Total Organic Carbon	2.0

All nominal chemical values are quoted in mg $L^{-}1$. Based on long term analysis between July 1995 and June 2000.

Table 3-3 Ionic Strength of kaolin suspension prepared in tap and milli-Q water

	Conductivity (mS m^{-1})
Melbourne tap water	10.11
Milli-Q water	0.4059
Kaolin suspension (tap)	12.36
Kaolin (milli-Q)	4.30

3.4.1.4 Flocculant

Two different polymers were used in this work. To flocculate kaolin, a non-ionic polyacrylamide (MAGNAFLOC® LT20 Ciba Specialty Chemicals) was used. To flocculate calcite, an anionic high molecular weight polyacrylate/polyacrylamide copolymer (AN934SH, SNF chemicals), was used. The properties of each polymer are shown in Table 3-4. These polymers were chosen because of their proven effectiveness in pipe flocculation of calcite and kaolin in other work [64, 65]. This provided useful background information regarding shear rates and kinetics of flocculation.

Table 3-4 Properties of flocculant used in this study

Commercial name	Flocculant type	Ionic character	MW	Chemical form	Supplier
Magna flocLT20	polyacrylamide	Non ionic	ca 10-15 x10^6 D	Powder	Ciba Specialty Chemicals
AN934SH	polyacrylate/polyacrylamide	30% anionic	>16 x 10^6 D	Powder	SNF

3.4.2 Laboratory flocculation in stirred baffle reactor

Flocculation occurred in a stirred baffled reactor shown in Figure 3-7 with dimensions shown in Table 3-5. An overhead stirrer (IKA Euro star SV PCZ) powered a six bladed Rushton impeller. The flocculant was injected into a cylindrical stainless steel port (i.d. = 4.37 mm), attached to one of the baffles [135]. The reactor vessel was 87 mm in diameter so that the total suspension volume after addition of flocculant was 514 ml. The flocculant port length, L_{FP} was 54.3 mm, and the immersed height, $L_{LIQ\,LEV}$ was 15.5 mm. The length of the injection port arm, L_{AL} was 24.2 mm.

In the case of kaolin, suspensions were prepared at solids concentration of 0.01 (w/w), while for calcite, 0.14 (w/w). Dry powder was added to a known volume of milli-Q water and mixed until homogeneous. The suspensions were sonicated for 10 minutes to break up any agglomerates and agitated on a shaking table for 24 hours. A 2 g L^{-1} stock solution of polymer was prepared by adding 1 mL of ethanol to 0.2 g of dry polymer, wetting the polymer crystals, and making the volume up to 100 mL by adding 99 mL of milli-Q water. To prevent UV degradation, aluminium foil covered the jar while rotating on an end over end stirrer overnight.

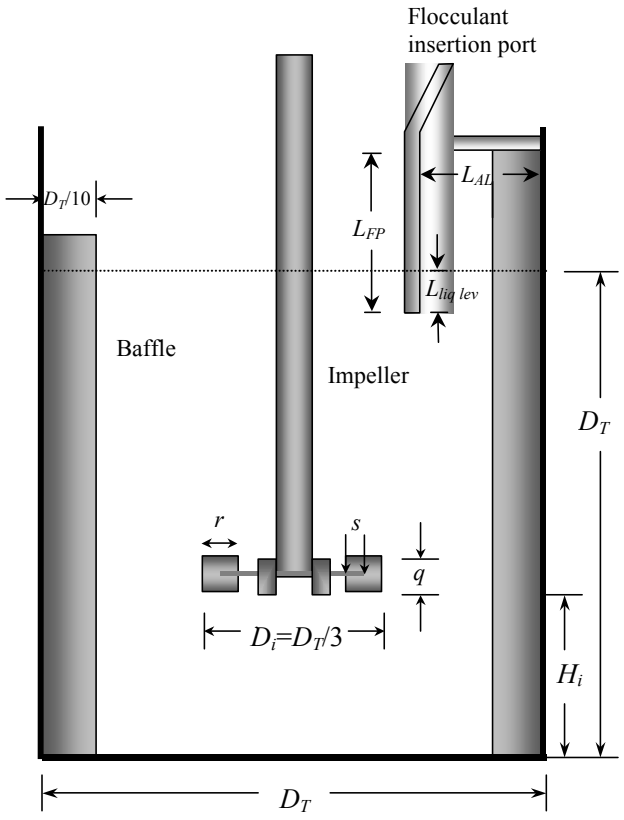

Figure 3-7 A schematic diagram showing the stirred baffle flocculation reactor configuration

Table 3-5 Stirred baffle reactor dimensions. Reproduced from Hulston [73]

Description	Symbol	Dimension (mm)
Tank diameter	D_T	87
Liquid height	$H_l = D_T$	87
Baffle width (4 baffles)	$W_b = D_T/10$	8.7
Impeller diameter	$D_i = D_T/3$	29
Impeller height from tank base	$H_i = D_i/3$	29
Impeller blade width	$q = D_i/5$	5.8
Impeller blade length	$r = D_i/4$	7.25
Length of blade mounted onto disk	$r_d = D_i/8$	3.625
Diameter of disk	$D_i - 2(r-r_d)$	21.75
Flocculant inlet tube diameter	T_d	4.37

A dilute working solution was prepared prior to flocculation. A 2 L beaker was half filled with milli-Q water, before transferring 100 mL of stock solution. Finally, 900 mL of milli-Q water was added to make 0.01 wt % solution. An electric motor and paddle impeller agitated the dilute solution for 30 minutes at 500 rpm. Excess dilute polymer was discarded at the completion of each run.

Suspensions were transferred to the flat-bottomed baffled vessel and were mixed for 10 minutes at 1000 rpm prior to flocculating. Then, a single dose of flocculant was injected. During flocculation the agitation speed varied between 400 to 700 rpm for kaolin, and 600 to 800 rpm for calcite. Higher agitation speeds were required for calcite since it settled faster. After flocculating for a specified time, (30, 40, 50 and 60 seconds for kaolin, and 30 seconds for calcite) the overhead stirrer was turned off and the height of the suspension-supernatant

interface was measured in situ. A video camera was used to record the interface height, for two hours, after which time the interface height did not decrease further.

3.5 Results and Discussion

3.5.1.1 Suspension rheology measurement for different flocculant dosage

Figure 3-8 and Figure 3-9 show height versus time for 0.01 w/w kaolin suspensions flocculated at 500 g tonne^{-1} in a stirred baffled reactor, as a function of rotation speed and mixing time. The shear rates corresponding to the rotation rates quoted in Figure 3-8 are shown in Table 3-6 and ranged between 240 and 690 s $^{-1}$. The impeller Reynolds number for this shear rate range varied from 5600 to 9800, so conditions were fully turbulent. There are two features of Figure 3-8 worth mentioning. First, the highest initial settling rate corresponded to the slowest rotation speed, and second, the equilibrium height decreased from $0.46\,h_0$ to $0.42\,h_0$ as the rotation rate increased from 400 to 700 rpm. This result suggests that aggregates forming at lower shear rates are either larger or denser (or both) than aggregates formed at higher shear rates. Although the size or density of flocs were not measured, visual observation showed that flocs forming at 60 g tonne $^{-1}$ were significantly larger than flocs forming at 20 g tonne $^{-1}$ dose.

Table 3-6 Hydrodynamic characteristic values for the stirred baffled reactor

N (rpm)	400	500	600	700	800
Re	5600	7000	8400	9800	11210
G (s^{-1})	243	340	447	563	687

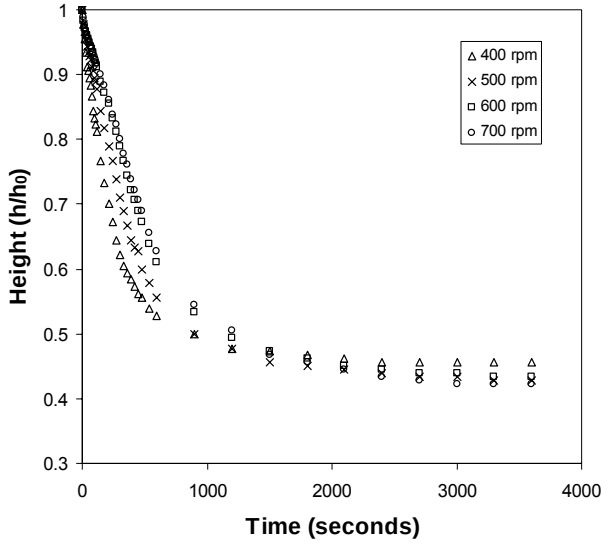

Figure 3-8 Height versus time for kaolin suspensions flocculated in a stirred baffled tank at 500 g tonne^{-1} and 60 seconds at different rotation speeds

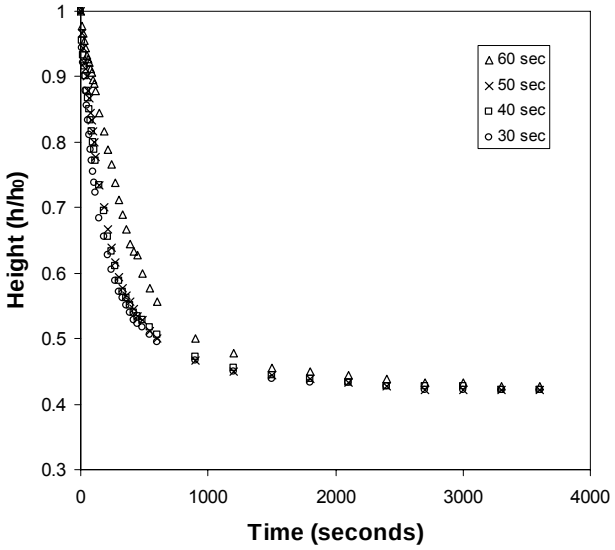

Figure 3-9 Height versus time for kaolin suspensions flocculated in a stirred tank with baffles at 500 g tonne $^{-1}$ and 500 rpm at different mixing times

Figure 3-9 shows the effect of mixing time on settling rate. At 500 rpm, settling rates and equilibrium heights did not vary when the mixing time was increased from 30, to 50 seconds. However, when the suspension was mixed for 60 seconds, the initial settling rate decreased, while the equilibrium height did not change. This suggests that when mixed at 500 rpm, flocculation was complete by 30 seconds and further mixing up to 50 seconds had no effect on the aggregate size or density. For times greater than 50 seconds, the settling rate decreased, implying that the aggregates had started to break apart.

Figure 3-10 and Figure 3-11 show $R(\phi)$ for the rotation speeds and mixing times discussed above. In Figure 3-10, the hindered settling function was a minimum when the agitation intensity was lowest (243 s^{-1}). This is true for solid volume fractions ranging from ϕ_0 to the gel point and supports the statement that larger floc sizes correspond to lower shear rates [18-20, 40, 80, 94, 99, 118]. An increase in shear during mixing from 243 to 340 s^{-1}, caused $R(\phi)$ to increase by a factor of ~ 1.5. Increasing the shear rate to 447 s^{-1} caused $R(\phi)$ to increase a further 1.5 times. However, exceeding 447 s^{-1} did not cause any further increase in $R(\phi)$. An important feature of Figure 3-10, also noticeable in the settling curves, is that the $R(\phi)$ curves crossover at approximately 0.017 v/v. This has important implications for dewatering. Flocs formed under low shear rates and short mixing times tended to dewater faster at low solid concentrations however, near the gel point, the trend is reversed. Thus, the concentration range specific to each application, determines whether low or high mixing shear is preferable. As expected, the effect of mixing time on $R(\phi)$ (Figure 3-11) follows the same trend as the settling curves in Figure 3-9. Increasing mixing time from 30 to 50 seconds had little effect on $R(\phi)$, while for 60 seconds, $R(\phi)$ increased significantly (~2 fold).

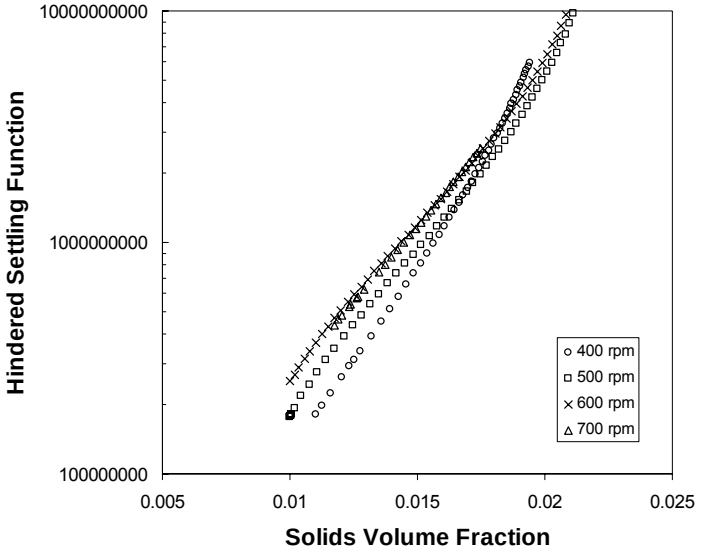

Figure 3-10 Hindered settling function of kaolin flocculated in a stirred baffled tank at 500 g tonne^{-1} and 60 seconds at different rotation speeds

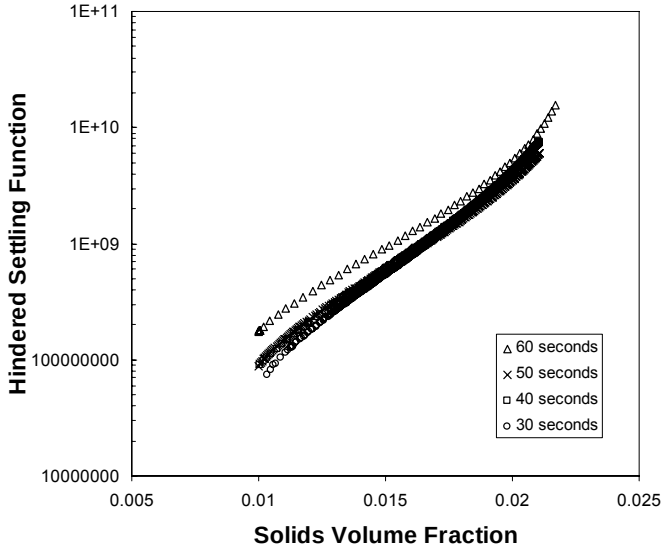

Figure 3-11 Hindered settling function of kaolin flocculated in a stirred tank with baffles at 500 g tonne $^{-1}$ and 500 rpm at different reaction times

The compressive yield stress was insensitive to changes in both agitation speed (Figure 3-12) and agitation time (not shown). Based on $R(\phi)$ data shown in Figure 3-10 and Figure 3-11, the optimum flocculation conditions for kaolin suspensions (0.01 w/w and 500 g tonne $^{-1}$ polymer) consisted of the minimum shear rate investigated (243 s^{-1} at 60 seconds mixing) and the shortest mixing time (30 seconds mixing at 340 s^{-1}). Under these conditions the aggregates reach a peak size; longer or more intense mixing tends to degrade the flocs.

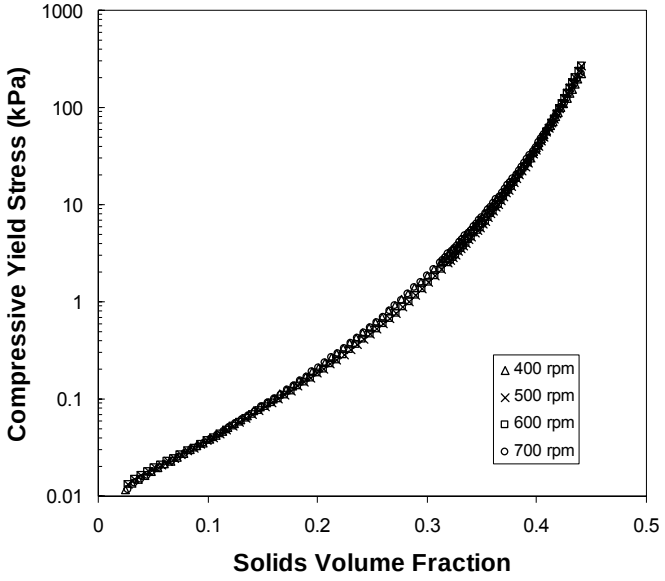

Figure 3-12 Compressive yield stress of kaolin flocculated in a baffled stirred tank at 500 g tonne $^{-1}$ and 60 seconds at different rotation speeds

As discussed in the theory (section 3.2), flocculation depends significantly on polymer dosage, so different optimum flocculation conditions could be expected if the polymer dosage were varied. Figure 3-13 and Figure 3-14 show $R(\phi)$ and $P_y(\phi)$ for calcite flocculated at 3 different dosages, 20, 40 and 60 g tonne^{-1}. Like

kaolin, a stirred baffled reactor was used. The rotation rate was 800 rpm (average shear rate of 688 s^{-1}) and the mixing time was 30 seconds.

Figure 3-13 shows that the flocculant dose has a significant effect on $R(\phi)$. Like kaolin, the effect on $R(\phi)$ depended on solids volume fraction. At $\phi = 0.063$, $R(\phi)$ decreased from 5.4 x 10^7 to 2.3 x 10^7 as the dosage increased from 20 to 60 g $tonne^{-1}$. This represents an increase of approximately 1.5 for each 20 g $tonne^{-1}$ increase, a similar increase in $R(\phi)$ to kaolin at different rotation rates. In other words, the inter-phase drag experienced by a floc (in a low solids concentration regime) decreased as the flocculant dosage increased. This is due to the larger aggregates structure forming at higher dosages. The increased density of polymer chains leads to more bonds and therefore, an overall stronger aggregate. The increased strength corresponds to larger sized aggregates for a given shear rate, and therefore settling rates increase. Figure 3-13 shows that as the solid volume fraction increases, the difference in $R(\phi)$ for the three dosage decreases until eventually the curves intersect. This occurred at $\phi \sim 0.13$ for the 40 and 60 g $tonne^{-1}$ curves and $\phi \sim 0.18$ for the 20 and 40 g $tonne^{-1}$ curves. This means that higher flocculant dosages, does not necessarily imply faster dewatering. This will depend on the solid volume fraction. Therefore, while increasing floc dose may be beneficial in sedimentation, in the thickener bed, it is possible that dewatering is adversely affected. This is rarely observed in practise because the trade off decrease in $R(\phi)$ is unacceptable.

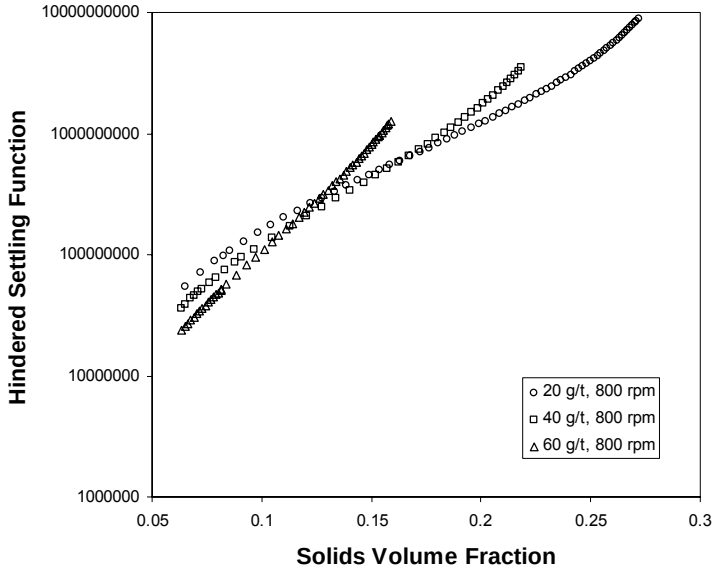

Figure 3-13 Hindered settling function of calcite flocculated in a baffled stirred tank at 20, 40 and 60 g tonne $^{-1}$ for 30 seconds and 800 rpm

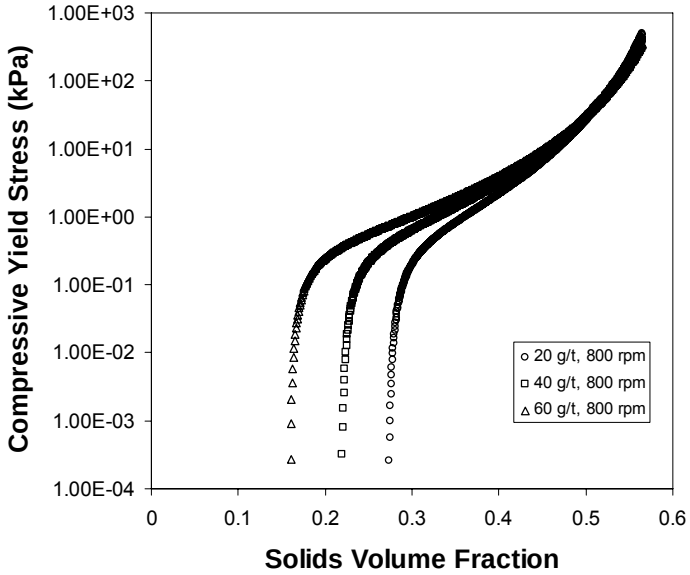

Figure 3-14 Compressive yield stress of calcite flocculated in a baffled stirred tank at 20, 40 and 60 g tonne $^{-1}$ for 30 seconds and 800 rpm

Figure 3-14 shows $P_y(\phi)$ for the three polymer dosages. For loads less than 100 Pa, the average final volume fraction was 0.17 (v/v) at 60 g tonne $^{-1}$. This increased to 0.22 (v/v) at 40 g tonne $^{-1}$ and 0.27 (v/v) at 20 g tonne $^{-1}$. Above 3 kPa, there was no appreciable difference between each dose.

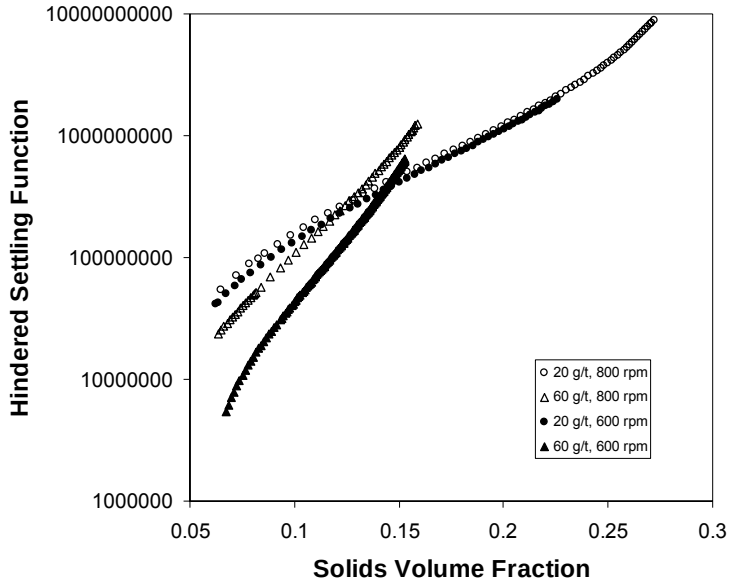

Figure 3-15 Hindered settling function of calcite flocculated in a baffled stirred tank for 30 seconds at 20 and 60 g tonne $^{-1}$ and agitation rates of 600 and 800 rpm

Next $R(\phi)$ and $P_y(\phi)$ were considered as functions of flocculant dose and shear rate. The $R(\phi)$ and $P_y(\phi)$ result for the three flocculant dosages did not differ significantly between 700 rpm and 800 rpm. Consequently, Figure 3-15 and Figure 3-16 will only compare the 600 and 800 rpm results. The result shows that for the 20 g tonne^{-1} dose, increasing the rotation rate from 600 to 800 rpm, had little effect on $R(\phi)$. However, for 60 g tonne $^{-1}$, $R(\phi)$ increased significantly when the rotation rate increased. This reflects the differing strengths

of the aggregates at each dose. At 20 g tonne $^{-1}$, the aggregates are relatively weak so that at a rotation rate of 600 rpm, it is likely that they have been sheared to a limiting size. At 60 g tonne $^{-1}$, the aggregates are more resilient, so the structural change occurred at higher rotation rates.

For a constant rotation rate of 600 rpm, when the dosage was increased from 20 g tonne $^{-1}$ to 60 g tonne $^{-1}$, the difference in $R(\phi)$ was ~ 7.5; almost 5 times higher than when the rotation rate was 800 rpm (Figure 3-15). Thus, the effect of flocculant dosage is significantly less at the higher shear rate.

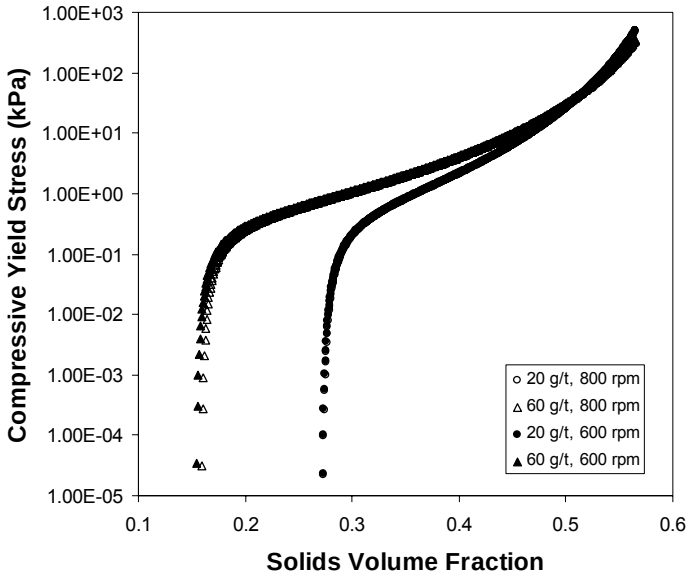

Figure 3-16 Compressive yield stress of calcite flocculated in a baffled stirred tank for 30 seconds at 20 and 60 g tonne $^{-1}$ and agitation rates of 600 and 800 rpm

Figure 3-16 shows $P_y(\phi)$ for the above cases. As expected, from Figure 3-14, $P_y(\phi)$ for the 60 g tonne $^{-1}$ dose, were higher than the respective 20 g tonne $^{-1}$

result. The gel point was lower for the 60 g tonne $^{-1}$ dose signifying that stronger flocs were formed. However, change in rotation rate had little effect on $P_y(\phi)$, at both 20 and 60 g tonne $^{-1}$ dosages. This is in agreement with the earlier results for kaolin, shown in Figure 3-12.

3.6 Conclusions

The effect of mixing time, mixing rate and flocculant dosage on dewatering of flocculated kaolin and calcite suspensions was observed. Increasing rotation rates from 400 to 700 rpm caused the initial settling rates and equilibrium heights to decrease. At a low solid volume fraction, the hindered settling function was a minimum when the mixing rate was lowest (243 s $^{-1}$). Increasing the shear rate from 243 to 340 s^{-1} caused $R(\phi)$ to increase by a factor of ~ 1.5. Increasing the shear rate to 447 s^{-1} caused $R(\phi)$ to increase a further 1.5 times. However, above 447 s $^{-1}$ $R(\phi)$ did not change. The hindered settling function curves as a function of shear rate crossed at approximately 0.017 v/v so that flocs formed under low shear rates and short mixing times dewatered faster at low solid concentrations, but at concentration near the gel point, the trend is reversed. The compressive yield stress was insensitive to change in agitation speed and agitation time but increased when the flocculant dosage increased.

Flocculant dose had a significant effect on $R(\phi)$ and depended on solids volume fraction. At $\phi = 0.063$, $R(\phi)$ decreased from 5.4 x 10^7 to 2.3 x 10^7 when the dosage increased from 20 to 60 g tonne $^{-1}$. As the solid volume fraction increased, the difference in $R(\phi)$ for the three dosages decreased until the curves eventually intersected. This occurred at $\phi \sim 0.13$ for the 40 and 60 g tonne $^{-1}$ curves and $\phi \sim 0.18$ for the 20 and 40 g tonne $^{-1}$ curves. Thus, higher flocculant

dosages do not necessarily imply faster dewatering. The effect of rotation rate on dewatering depended on dosage. At 20 g tonne^{-1}, no change in dewatering was observed, while for 60 g tonne $^{-1}$, dewatering was significantly affected.

Chapter 4

1−D Modelling and Pilot Validation in the Absence of Shear

4.1 Introduction

Over the past two decades, several models have been developed to predict dewatering in applications including; gravitational thickening, [27, 53, 150, 160] centrifugation, [53, 79, 92, 93, 95, 150] and pressure filtration [41]. Mathematical modelling is attractive as it provides the ability to understand, optimize, or control a system or process. Steady state models convey important information concerning thickener performance at different solid fluxes, helping identify stable operating regions. Because of increased processing speeds, a large array of variables can be considered in relatively short times. Furthermore, the cost of modelling is often lower than experimentation and risks associated with pilot and laboratory work minimised.

As mentioned in Chapter 1, over the past ten years, the 1−D steady state thickener model developed by Landman and White [153], has been applied to several industrial thickeners, with the results largely inconsistent [123]. The model typically under predicts thickener performance; the amount by which depends on the type of thickener, the material, the operating conditions, and whether the thickener is raked [94, 102, 127, 128, 148, 151].

The discrepancy between simulation and reality suggests that either the one-dimensional model framework is inadequate for describing large thickeners, or otherwise, the model inputs, i.e. the permeability and compressibility are not representative of the conditions inside of the thickener. The aim of this chapter is to validate the 1−D steady state thickener model through a series of pilot scale experiments. This study initially does not consider shear forces. Shear is introduced to the column in Chapter 7.

4.2 Previous pilot thickening studies

In contrast to the theoretical interest thickening has received [33], experimental studies of thickening at a pilot scale are rare in the literature. Examples include the work of Comings [42-44], Eklund [48], Fitch [124], Scott [152] and Turner [33]. Most are now half a century old and aimed to provide data against which to assess the accuracy of the design methods discussed in Appendix 2. Rarely, did the experimental results correlate with the design. Fifty years later, not a great deal has changed.

In addition to model validation, pilot thickening studies can serve a more fundamental purpose, by providing insight into full-scale thickener behaviour. The paper by Comings [33] was important in this respect, summarizing over two decades of continuous thickening research. In one experiment, Comings considered the effect of residence time on underflow solids, while keeping the bed height constant. The residence time $\left(t_{res}\right)$, was calculated from;

$$t_{res} = \frac{A}{V_f C_f} \int_0^{h_b} C(z)\,dz \tag{4.1}$$

where V_f is the volumetric feed flow rate and C_f is the mass of solid per unit volume of the feed. Thus, the residence time is directly proportional to the bed height and indirectly proportional to the volumetric flux. $\left(V_f / A \right)$.

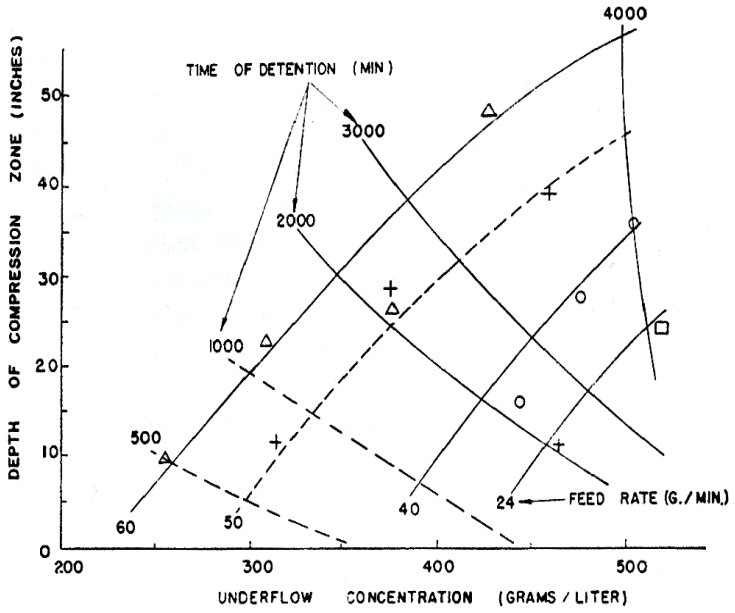

Figure 4-1 Bed height versus underflow concentration as function of residence time and feed rate. Reproduced from Comings [33]

In a different series of experiments, the residence time was kept constant by allowing the bed height, the feed and the underflow flow rates to vary [33]. The results are summarized by Figure 4-1. The positively sloping curves correspond to constant feed conditions while the negatively sloping curves correspond to constant residence time. For example, when the bed height was a constant 23 inches (0.58 m), an increase in the residence time from 1500 to 4800 minutes (25 to 80 hours) caused the underflow density to increase from 300 to 510 g L^{-1} (0.134 v/v to 0.202 v/v) [152]. Conversely, when the residence time was constant

(2000 minutes) an increase in the bed height from 10 to 27 inches caused the underflow concentration to decrease from 460 to 380 g L^{-1}. The shorter the residence time, the more pronounced the decrease (steeper slope). This result may appear counterintuitive because a higher bed corresponds to a larger compressive stress; hence, the additional weight should squeeze out more fluid in the same time. Clearly, factors other than compression must be involved. To maintain a constant residence time, at a higher bed height, the solid flux must increase from equation (4.1). The higher the solid flux, the larger the hydrodynamic drag opposing compression, so that permeability considerations must also be taken into account.

4.3 Variables in Continuous Thickening

It is generally possible to operate a pilot thickener in three modes;

- constant bed height
- constant solids flux
- constant residence time

In the first mode, the column is operated at a constant bed height and the solids flux varies by changes in both feed and underflow flow rates. The residence time differs necessarily for each flux. In the second mode, the column is operated at a constant solids flux while the bed height varies, in this case only the underflow flow rate changes. In the final mode, the column operates at a constant solids residence time, for which both bed height and solids flux must change.

4.3.1 Feed flux density

The feed flux density is the mass flow rate of solids (on a dry basis) per unit area with the units of tonne m^{-2} h^{-1}. The effect of increasing the feed flux density is to cause the thickener to shift from a settling to filter mode [94]. There is an upper limit for the feed flux density, which will depend on the solids settling velocity. Operating the thickener at the maximum feed rate is not advisable, since a small change in aggregate properties, i.e. as caused by a temporary reduction in flocculant activity, or dose, could lead to lower settling rates and solid overflow. Furthermore, low residence times limit the opportunity for compressive dewatering and consequently underflow densities do not greatly exceed the material gel point.

4.3.2 Compression Height

Compression can be important in low flux, deep-cone type thickeners, which produce highly compact, paste like material. The deep beds provide for high compressive stresses; while the typically low solid fluxes mean that residence times are relatively high.

To achieve a high underflow density, the compressibility of the material is important. The lower the compressive yield stress, the more compressible a suspension. However, the yield stress is only half the story since consolidation also involves escape of fluid. Therefore, dewatering is optimized when the sediment is both compressible and permeable. However, improvement in one usually comes at the expense of the other.

4.4 Thickener modelling

Figure 4-2 shows schematically a one-dimensional continuous gravity thickener. Feed is introduced continuously at a height z, volumetric flux Q_f and solid volume fraction ϕ_f. At heights less than z, solids fall freely in a hindered settling zone. Fluid, expelled by the settling solids, exits the thickener via an overflow stream, at a flux Q_0. For steady-state conditions, the solid and fluid fluxes are constant at all heights in the thickener.

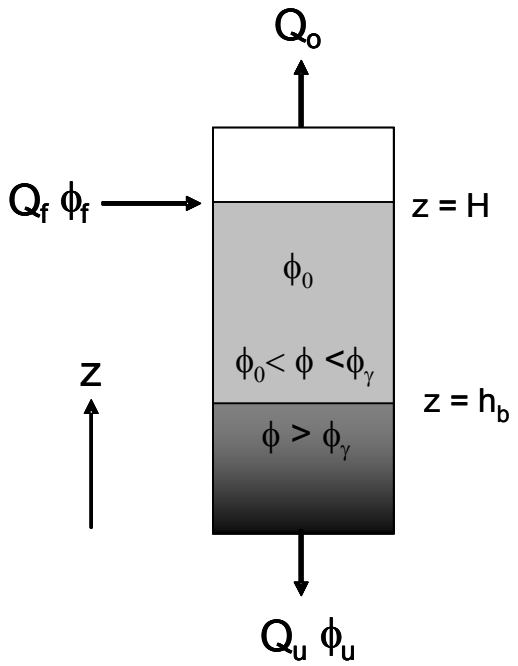

Figure 4-2 Ideal 1−D continuous flow thickener

If the feed flux is fixed, the only remaining variable is the underflow flux Q_u. The magnitude of Q_u is important as it dictates height of bed and the solid volume fraction in the underflow ϕ_u. The boundary between settling and

consolidation zones is denoted z_e. The solid volume fraction in the consolidation zone $(0 < z < z_e)$ increases non-linearly with increasing compression and thus depth.

4.4.1 Assumptions

There are two key assumptions inherent to the steady state thickener model [152]. The first is that dewatering can be described as a one-dimensional process, i.e. the only change in ϕ occurs in the vertical (z) direction. Thus, the solid volume fraction is constant over a horizontal plane. For this to be satisfied, the solid settling velocity also must be constant at a given vertical height. Consequently, the particle sizes and densities cannot vary; a condition termed zone settling. The permeability, which is a function of volume fraction, is also constant across a horizontal plane. In one dimension, macroscopic flow phenomena including channelling and re-circulation of solids and fluid cannot be described. According to Turner, these macroscopic flow effects are not significant when the vessel diameter is less than 0.3 m [153]. Since, the tall column used in this work is 0.285 m, channelling and re-circulation were not expected. However, in large-scale thickeners variation in velocity and solid concentrations could be significant. Thus, the one-dimensional assumption is a simplification allowing trends in behaviour to be understood, however, exact predictions may not necessarily be possible.

The other assumption is that shear forces are not significant in 1−D dewatering. Shear, by nature is a two dimensional property and therefore cannot be defined in a one-dimensional framework. While this assumption may be appropriate in the case of undisturbed sediment that is laterally large; the assumption of zero shear is invalid when there is significant lateral motion of solid and fluid due to raking.

Often thickeners are not straight walled, but instead, slope at a certain angle to discourage scaling and dead zone formation. In this case, the area A, is a function of z. The one dimensional model can accommodate variation in cross sectional area by way of a shape factor. This allows any geometry thickener to be modelled.

4.4.2 Inputs

The steady state model inputs include the following;

- constitutive relationships for the compressibility and permeability as functions of solid fraction
- the thickener diameter (if the area is not constant for all heights, the diameter as a function of height is required)
- the solid volume fraction of the feed $\left(\phi_f\right)$
- the density of the solid and fluid phases
- the bed height $\left(H_b\right)$

4.4.3 Outputs

The model predicts solid throughput as a function of underflow solids in two parts. The first part involves solving the governing dewatering equation under hindered settling, where $P_y\left(\phi\right)$ is universally zero. The second part considers the consolidation zone, where the equations must account for a solid stress gradient. In the following equations, the solid flux term is volumetric, with units $\left[\frac{\text{volume of solid}}{\text{time}\cdot\text{area}}\right]$. In this case, the area is the maximum cross sectional area of the thickener. However, all graphs appearing in this thesis adopt the units

$\left\lfloor \frac{\text{tonnes}}{\text{hr}\cdot\text{m}^2} \right\rfloor$ on the ordinate axis. This is done primarily to adhere to the minerals industry convention [32]. From a material balance, the solids flux is given by;

$$\frac{q}{\alpha\left(h_b\right)} = \frac{u\left(\phi\right)}{\left(\frac{1}{\phi} - \frac{1}{\phi_u}\right)} \tag{4.2}$$

This is similar to the form originally given by Coe and Clevenger [153] with an added shape factor. The shape factor (α) defined as $\alpha\left(z\right) = \left(\frac{d\left(z\right)}{d_{\max}}\right)^2$ accounts for the effect of varying thickener areas while the settling rate $u\left(\phi\right)$ was given previously as;

$$u\left(\phi\right) = \frac{\Delta\rho g\left(1-\phi\right)}{R\left(\phi\right)} \tag{4.3}$$

When the solids form a network, the change in volume fraction $\Delta\phi$, with height, z, is described by a function which relates $R\left(\phi\right)$ and the solid stress gradient $\frac{dP_y\left(\phi\right)}{d\phi}$ to the volume averaged solid velocity, $q\left(t\right)$.

$$\frac{d\phi\left(z\right)}{dz} = \frac{\frac{R\left(\phi\left(z\right)\right)}{\left(1-\phi\left(z\right)\right)^2}\frac{q}{\alpha\left(z\right)}\left(1-\frac{\phi\left(z\right)}{\phi_u}\right) - \Delta\rho g\phi\left(z\right)}{\frac{dP_y\left(\phi\left(z\right)\right)}{d\phi\left(z\right)}} \tag{4.4}$$

At steady state, $z = H_b$ and $\phi = \phi_g$ at the top of the bed, while $z = 0$ and $\phi = \phi_u$ at the base of the thickener. In general, an analytical solution of equation (4.4) for q does not exist. Instead, the solid flux is evaluated numerically using an iterative process. The algorithm involves an initial guess for q, and integrating equation (4.4) from $z = 0$ to $z = h_b$ subject to the boundary condition $\phi(0) = \phi_u$. The initial q is adjusted until the condition at the top of the bed, (i.e. $\phi(H_b) = \phi_g$) is satisfied. This is repeated for a range of underflow concentrations and bed heights, generating a series of curves which plot q versus ϕ_u as a function of bed height. A limiting solids flux is obtained by combining free settling and compression calculations, and choosing the minimum value [139].

Figure 4-3 shows the model output for flocculated calcite. The bed heights range between 0.1 and 10 metres. At solid fluxes above ~ 0.3 tonne m^{-2} h^{-1}, the model predicts that bed height will not influence the solid concentration in the underflow. The solids flux is sufficiently high that solids do not spend enough time in the thickener for compressive forces to act. In this case, the underflow concentration depends solely on the permeability. Consequently, thickeners operated in this solids flux regime are described as permeability limited. When the solid flux is less than ~ 0.3 tonne m^{-2} h^{-1}, the model predicts that the underflow concentration will increase. The longer residence times mean that compression becomes the limiting factor. Under this regime, if the compressive force is increased by increasing the bed height, the underflow solids concentration should also increase. The transition from permeability limited to compressibility limited is often sharp. In this region a small variation in solids flux can correspond to a large decrease in underflow solid density. To validate the model, fluxes corresponding to both compressibility and permeability must be considered.

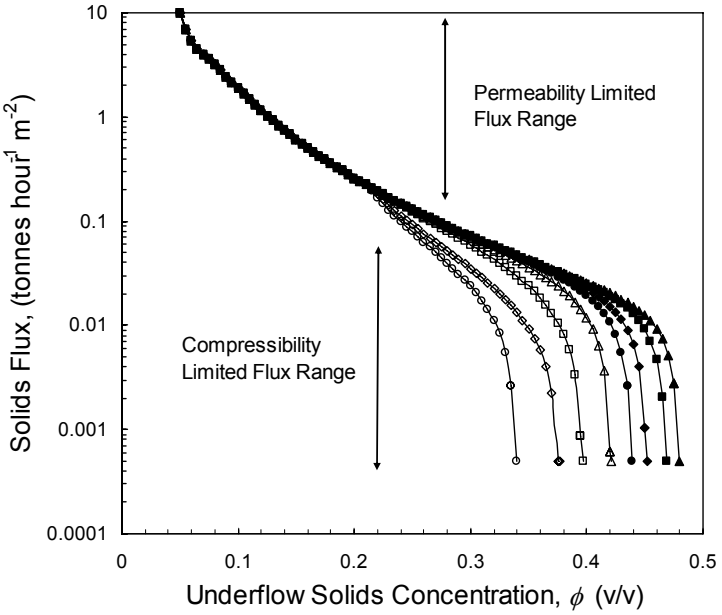

Figure 4-3 1−D thickener model output; solids flux dry tonnes solid versus underflow solids concentration. Data is for curves ranging from 0.1 to 10 metres. The fitting parameters appear in Appendix 1, Table A-2 and Table A-3

4.5 Experimental

4.5.1 Materials

The material used in this work consisted of calcite (Omyacarb 10) and a high molecular weight anionic polyacrylamide/polyacrylate copolymer (AN934SH SNF). These are the same as described in Chapter 3 (refer to section 3.4.1 for more detail).

4.5.2 Characterisation of calcite

4.5.2.1 Flocculation of calcite in a stirred baffled tank

Calcite suspensions were prepared at a solids concentration of 0.1 w/w by the addition of dry powder to a measured volume of tap water. The suspensions were sonicated for 10 minutes and agitated on a shaking table for 24 hours. The same stirred baffled reactor described in section 3.3.1.2 was used to flocculate. The optimum flocculation condition required a single polymer injection of 30 g tonne $^{-1}$ while mixing at 500 rpm. The suspension and flocculant were mixed for 10 seconds, before turning the stirrer off and measuring the settling rate. After settling had finished, (24 hours later) a sample was loaded into the filtration rig and the compressibility and permeability were measured.

4.5.2.2 Laboratory flocculation in linear pipe reactor

Calcite (Omyacarb 10) suspensions were prepared at a solids concentration of 0.05 w/w in 40 L batches by gradually adding 2.06 kg of calcite to 39 L of local tap water to produce a suspension of 0.05 w/w solids. The lower solids concentration was chosen to match previous flocculation pipe studies. Using an overhead stirrer, the suspension was mixed for 30 minutes prior to flocculation to allow thermal equilibrium. A 2 g L^{-1} stock solution of polymer was prepared following the same procedure outlined in section 3.4.2.

Flocculation occurred in a linear pipe reactor, described in section 3.3.2. A centrifugal pump delivered suspension at a volumetric flow rate of 6.3 L min^{-1} through a 12.5 mm ID pipe. Two pipe lengths were used, 1.8 m and 9.66 m, corresponding to residence times of 1.8 and 10.8 seconds respectively. A peristaltic pump (Masterflex LS) delivered flocculant at flow rates varying from 81 and 323 mL min $^{-1}$ depending on the dose. For each residence time four flocculant dosages were investigated (25, 50, 75 and 100 g tonne^{-1}).

Figure 4-4 shows the pipe reactor arrangement schematically. During start-up, where flow had not yet reached steady state, suspension was returned to the holding tank via a recycle loop, to conserve volume. The instrumentation was relatively basic, comprising a flow meter (F_I) on the slurry line. A more sophisticated control scheme was adopted in the work described in Chapter 7.

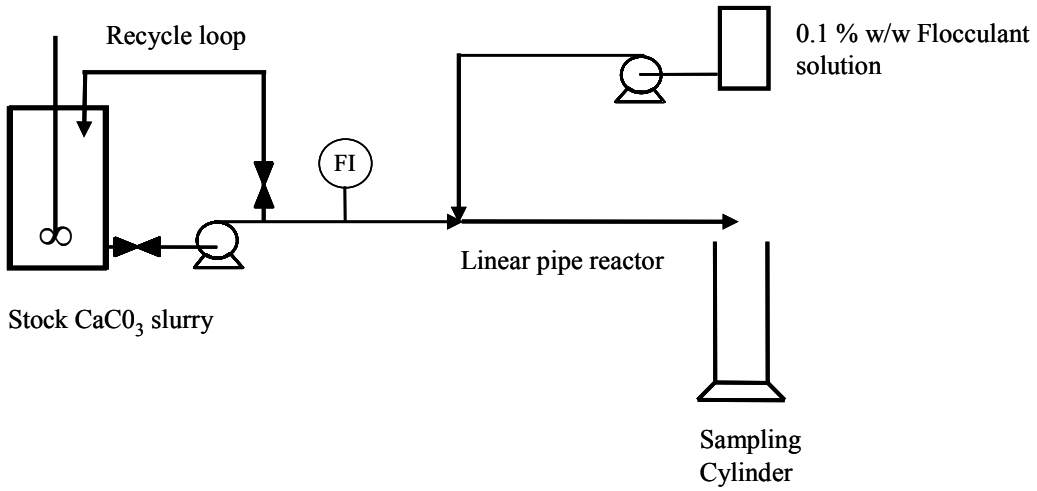

Figure 4-4 Laboratory pipe reactor arrangement used for dewatering characterisation

Before sampling, the pipe reactor was operated for approximately five minutes allowing the flocs to reach equilibrium. Five 1 L measuring cylinders were filled directly from the pipe outlet. The first cylinder was filled to a height (h_0) of 0.4 m and subsequent cylinders were filled to progressively lower heights (0.8 h_0, 0.6h_0, 0.4 h_0, and 0.2 h_0). The sediment-supernatant interface $h(t)$ was measured for two hours, and then after 24 hours, the final sediment height was measured. Combined with filtration data, $P_y(\phi)$ and $R(\phi)$ for each flocculation condition were determined according to the methods discussed in Chapter 2.

4.5.2.3 Yield stress

To avoid pumping and mixing problems, the yield stress was measured as a function of solids concentration using a vane rheometer. The results are shown in Figure 4-5. For solid volume fractions less than 0.4 (0.62 w/w), the measured yield stress was less than 10 Pa, so that the suspension flowed freely. Consequently, calcite suspensions were not prepared above 0.4 v/v.

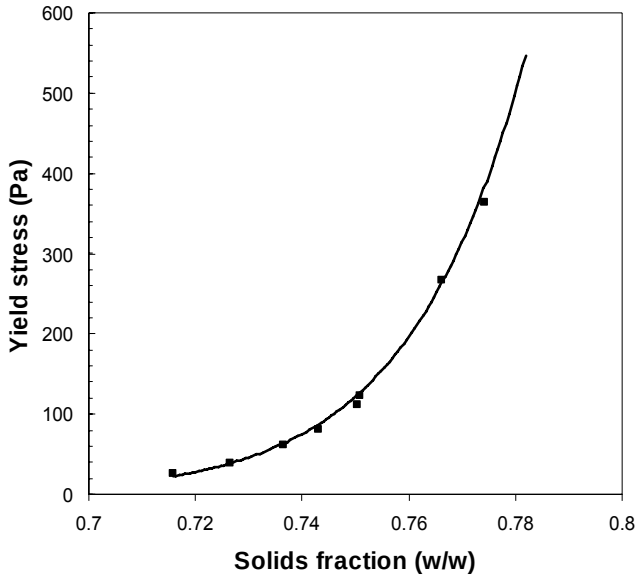

Figure 4-5 Yield stress for calcium carbonate measured using vane rheometer

4.5.3 Pilot thickener operation

A photograph of the tall column used in the following experiments is shown in Figure 4-6. Upon close inspection, the feed and clarified water interface can be observed. The interface between settling and consolidating material, which is defined by H_b can also be seen, (although less easily) just above the second ring.

Figure 4-7 shows schematically the tall column and ancillary equipment. The height of the column was 2.2 metres and the internal diameter was 0.285 metres. Additional column information is supplied by Table 4-1.

Figure 4-6 Tall pilot column used to validate thickener model

Table 4-1 Tall column dimensions

Height (m)	2.2
Truncated cone height (m)	0.205
Column diameter (m)	0.285
Cone angle (degrees)	60
Diameter of truncated cone at base (m)	0.05
Cone volume (L)	4.4

A centrally located feed pipe delivered feed to the column, while the overflow was collected by a peripheral launder. The launder was designed to accommodate flow rates up to 70 L min^{-1}. To minimise shear, the column was operated without any moving components including rakes, pickets or scrapers. A narrow diameter was chosen deliberately so the assumption of 1−D flow was valid. The column was operated continuously for periods ranging between four and six hours. Longer operational times were not possible because of site access restrictions and the lack of an adequate control system. It is possible that operating for relatively short times will not allow true steady conditions to develop in the column, although the results were reasonably stable. This is addressed in Chapter 7 where a more sophisticated control system is developed enabling operation for extended periods.

4.5.3.1 Solids flux of 0.3 tonne m^{-2} h^{-1}

A solids flux of 0.3 tonne m^{-2} h^{-1} was chosen for investigation because it corresponds to a region in which the thickener operation is permeability limited. This expectation is based upon initial modelling of calcite settling data. A large number of thickeners have been found to operate in this typical flux range for which the solids throughput has yield stresses of less than 10 Pa [15]. In the

minerals industry, the majority of thickening operations produce tailings within this rheological range.

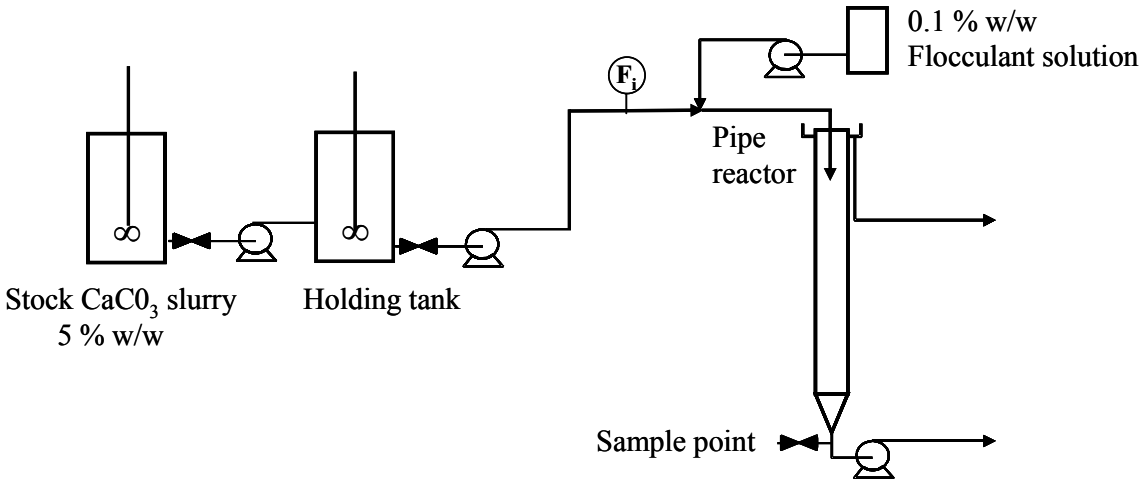

Figure 4-7 Pilot tall column flow circuit used to validate 1D model

Calcite suspensions were prepared at a concentration of 0.05 w/w in a 500 L holding tank using local tap water. Suspensions were transferred to a second tank, which was agitated constantly to keep the particles suspended. The second tank allowed additional batches to be prepared during operation without introducing concentration or dilution shocks which would disrupt steady state.

A flux of 0.3 tonne m^{-2} h^{-1} corresponds to a volumetric flow rate of 6.8 L min^{-1} for a 0.05 w/w concentration. The pump speed was periodically adjusted to maintain the flow rate at the required rate. The suspension was transferred from the tank to the column by a progressive cavity positive displacement pump. The slurry was flocculated using the pipe reactor described in section 4.5.2.2 and elsewhere [97]. The flocculant was dosed at 25 g $tonne^{-1}$, the minimum required to produce satisfactory flocculation. The feed point was located approximately 0.5 m beneath the overflow launder.

Shortly after filling, three distinct zones became distinguishable. The lower zone was defined by a marked interface between the hindered settling region, where individual flocs could be observed settling and an opaque bed that settled more slowly. The interface height, or bed height, increased to approximately 80% of the target height at which point the underflow pump was turned on. This was necessary to compensate for the slow dynamical response in the column. Assuming that all solids exit via the underflow and the underflow solid concentration is known, the required underflow rate can be calculated from an overall mass balance;

$$U = \frac{\phi_0 F}{\phi_u} \tag{4.5}$$

However, because the underflow concentration was variable and instantaneous measurement of the underflow solid concentration was not possible, constant adjustment of the underflow pump speed was necessary to keep the bed height constant. Over the course of the experiments, the bed did not vary by more than 10 %. Four bed heights were investigated; 1.0 m, 0.8 m, 0.6 m and 0.4 m. For each height the column was allowed to reach steady state before sampling. A common industry standard for estimating steady state is two bed turnovers. On this basis, steady state conditions could take anywhere between thirty minutes and two hours to develop depending on the bed height. Once this time had passed, underflow samples were collected at 30 minute intervals and the solids concentration determined by drying.

4.5.3.2 Solids flux of 0.03 tonne m^{-2} h^{-1}

The solids flux of 0.03 tonne m^{-2} h^{-1} represents thickener operations where the output solids from the underflow are above the gel point. In this case, the rheology of the underflow material will likely have a yield stress greater than

10 Pa, based on the data in Figure 4-5. Operation of the column to produce underflow with a measurable yield stress may pose difficulties in the absence of raking, since the movement of solids will no longer be homogeneous.

The procedure described in section 4.5.2.3 was repeated for a lower solids flux corresponding to 0.03 tonne m^{-2} h^{-1} so that dewatering was compressibility limited. Because the pipe velocity was one-tenth the velocity at 0.3 tonne m^{-2} h^{-1} the flow was insufficient to keep calcite suspended. To address this problem a smaller 6 mm ID pipe was used. The volumetric flow rate was 0.7 L min^{-1} so that the column solids flux now corresponded to 0.037 tonne m^{-2} h^{-1}. To keep the residence time approximately five seconds, the pipe reactor length was reduced to 2.3 m.

Despite efforts to maintain constant flocculation conditions, the aggregates forming at the lower flux were considerably larger and settled significantly faster than those at the higher flux. To compensate, the polymer dosage was reduced to 5.5 g tonne $^{-1}$, in which case the settling rate was approximately equivalent to the higher flux case. Three bed heights were investigated; 0.75 m 0.5 m and 0.3 m, at this flux. Once steady state was reached, the underflow was sampled at 30 minute intervals and the solids concentration determined by drying.

4.5.3.3 Varying flocculation conditions

The column was operated according to the procedure described in 4.5.2.3. Calcite suspensions were prepared at solids concentration of 0.05 w/w by metering 3.2 m^3 of water into a 4.5 m^3 storage tank, to which 150 kg of dry calcite was gradually added. The solids flux was 0.3 tonne m^{-2} h^{-1} so that the required flow rate was 6.8 L min^{-1}. Two different flocculant dosages were investigated; 25 and 75 g $tonne^{-1}$. The residence time in the pipe for each dose was 10 seconds. For The bed was maintained at one metre height. When steady state was

reached, the underflow was sampled every 10 minutes and the solids concentration determined by drying.

4.6 Results and Discussion

4.6.1 Error analysis

Before proceeding to the tall column results, this section will first address the issue of experimental error. The aim is to identify potential sources of error and quantify their effect on the dewaterability predictions. In this thesis the predominant cause of variability between results is due to flocculation. With flocculation, any one of several parameters can significantly affect the outcome. The potential of flocculation to affect the experimental results is therefore considered far greater than typical measurement errors. Consequently, great efforts were required to ensure that the methods of flocculating and sampling were controlled and as reproducible as possible. This was achieved by flocculating primarily in a linear pipe reactor, which delivered a known volume of suspension and polymer directly to the measurement vessel under reproducible shear conditions.

The reproducibility of flocculation is relatively easy to assess; batch settling tests provide this information directly. Indeed, the repetitive nature of the work appearing in Chapters 5 and 8 meant that experimental variability could be detected immediately. To illustrate the typical variability in flocculation, three calcite suspensions were flocculated on consecutive days using identical experimental conditions. The suspension interface was measured over time and $h(t)$ is shown in Figure 4-8. The three $h(t)$ curves evidently show reasonable agreement. The maximum deviation between curves did not exceed 0.5 mm, consistent with the figure quoted by Pashias [115]. Since, the data are discrete

points and in principal may be discontinuous, standard smoothing and filtering techniques are unsuitable. Consequently, fitting methods are used to provide continuous functions over both the linear and nonlinear regions of $h(t)$ [98]. This introduces another potential source of error, however, Table 4-2 shows this error was small. The error value represents the difference between experimental and curve fits over the initiation, linear and non linear sections of the curve. The more data points sampled the greater the confidence in the curve fit. Thus, to minimise this error it is important that the number of data points sampled is adequate, especially in the non-linear region of the curve [97]. Consequently, the number of discrete data points usually sampled in a batch settling test was 100 or more. In the three examples given above, the data sets are smaller, with between 35 and 60 points. The $h(t)$ data for each batch settling test is listed in Appendix 1, Table A-1.

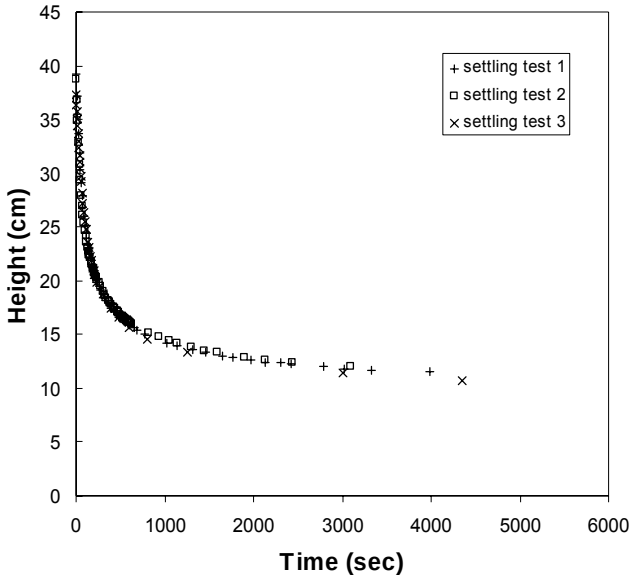

Figure 4-8 Triplicate measurement of $h(t)$ for calcite (0.07 v/v) flocculated at 40 g tonne^{-1}

Table 4-2 Input and output parameters for $h(t)$ analysis for (0.07 v/v) calcite dosed with 40 g tonne^{-1} polymer

	Settling Test 1	Settling Test 2	Settling Test 3
Number of data points	61	57	35
Initial height	0.392	0.388	0.374
Final height	0.101	0.102	0.107
Error in $h(t)$ curve fit	1.0E-5	1.3 E-5	1.85E-4

To examine the potential of $h(t)$ variance to affect $P_y(\phi)$ and $R(\phi)$ measurement, each of the $h(t)$ curves in Figure 4-8 were analysed using the $h(t) \Rightarrow f(\phi)$ transform.. Figure 4-9 shows $R(\phi)$ corresponding to the $h(t)$ curves of Figure 4-8. The average $R(\phi)$ is depicted by the solid line. Good agreement between individual $R(\phi)$ data was obtained for all ϕ. In Table 4-3, the calculated, average and standard deviation of $R(\phi)$ is shown for three ϕ values.

Table 4-3 Parameters and output from the $h(t)$ analysis for (0.07 v/v) calcite dosed with 40 g tonne^{-1} polymer

	$R(\phi)$			Average $R(\phi)$	Std Dev	Avg Std Dev
	Test 1	Test 2	Test 3			
$\phi = 0.07$	8.46E+06	7.98E+06	9.23E+06	8.56E+06	6.29E+05	2.21E+07
$\phi = 0.15$	3.00E+08	3.58E+08	3.23E+08	3.27E+08	2.91E+07	
$\phi = 0.20$	1.41E+09	1.42E+09	1.32E+09	1.38E+09	5.34E+07	

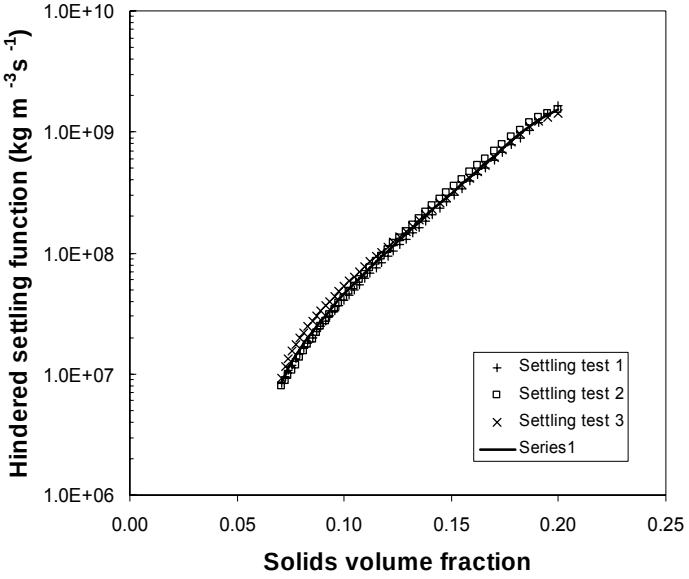

Figure 4-9 Hindered settling function from $h(t)$ in Figure 4-8

The treatment of $P_y(\phi)$ is less straightforward because both ϕ_g and $P_y(\phi)$ depend on the final height h_∞. Thus, to estimate the variability of $P_y(\phi)$ due to experimental $h(t)$ error, the average and standard deviation of h_∞ is determined. These are then used to calculate $P_y(\phi)$ and ϕ_g corresponding to upper and lower bounds of h_∞ (i.e. $h_\infty^+ = h_{\infty avg} + 2\,\text{s.d}$ and $h_\infty^- = h_{\infty av} - 2\,\text{s.d}$). The final height information is outlined in Table 4-4.

The results of $P_y(\phi)$ and ϕ_g do not correlate as closely as $R(\phi)$ (see Figure 4-10). For the three cases the gel point was estimated as 0.2311, 0.2145 and 0.2503 v/v (for $h_{\infty av}$, h_∞^+ and h_∞^- respectively). The average ϕ_g was 0.2319 v/v with a standard deviation of 0.0179 v/v, see Table 4-5. It shall be seen later that these limits are considerably smaller than changes observed when shear is applied

to the suspension (see Chapter 5). The $P_y(\phi)$ results were even more variable, especially at low solid volume fractions. At $\phi = 0.25$, the average value of $P_y(\phi)$ was 120 Pa, with a spread of approximately 100%. However, at $\phi = 0.35$, the average value of $P_y(\phi)$ was 1276 Pa with a spread of 200 Pa, (see Table 4-6). In real terms, these differences are small when compared to the stress changes observed in real thickeners, where the bed height can suddenly increase several metres, the total stress change is of the order kPa rather than Pa.

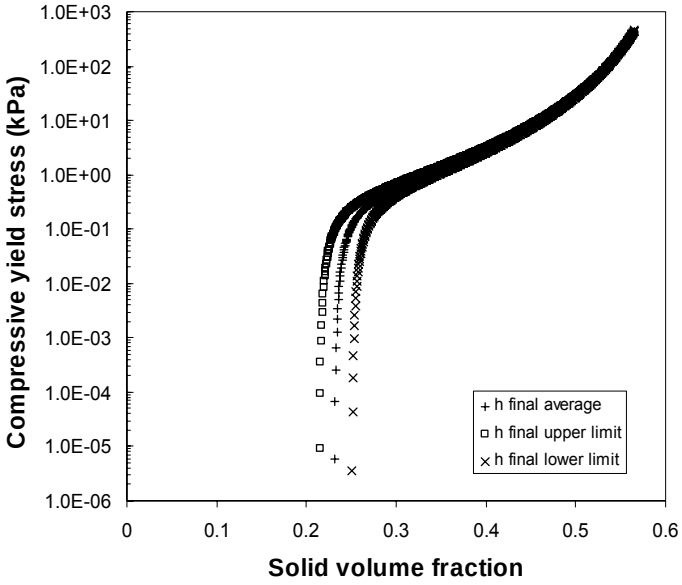

Figure 4-10 Compressive yield stress from $h(t)$ with three different final heights

Table 4-4 Final height h_∞ analysis

Final Height (m)			Average height (m)	Standard deviation (m)	Upper bound (m)	Lower bound (m)
Settling Test 1	Settling Test 2	Settling Test 3				
0.101	0.102	0.107	0.103	3.22E-2	0.1097	0.0970

Table 4-5 Gel point sensitivity to final height

Gel point (v/v)			Average Gel point (v/v)	Standard deviation
$h_\infty = h_{\infty\,avg}$	$h_\infty = h_\infty^+$	$h_\infty = h_\infty^-$		
0.2311	0.2145	0.2503	0.2319	0.0179

Table 4-6 Parameters and output from the $h(t)$ analysis for (0.07 v/v) calcite dosed with 40 g tonne^{-1} polymer

	Compressive yield stress (Pa)			Mean (Pa)	Std Dev (Pa)
(v/v)	$h_\infty = h_{\infty\,avg}$	$h_\infty = h_\infty^+$	$h_\infty = h_\infty^-$		
$\phi = 0.25$	112	244	≈ 0	119	122
$\phi = 0.3$	553	674	409	545	133
$\phi = 0.35$	1270	1437	1084	1264	176

To assess the potential error in thickener performance prediction, several combinations of the minimum and maximum curves for $P_y(\phi)$ and $R(\phi)$ were run through the steady state thickener model. The results in Figure 4-11 show excellent agreement and it will be seen shortly, that this variability is far lower

than expected based on changing flocculation conditions. In any case, the error is certainly within the range typical of a plant.

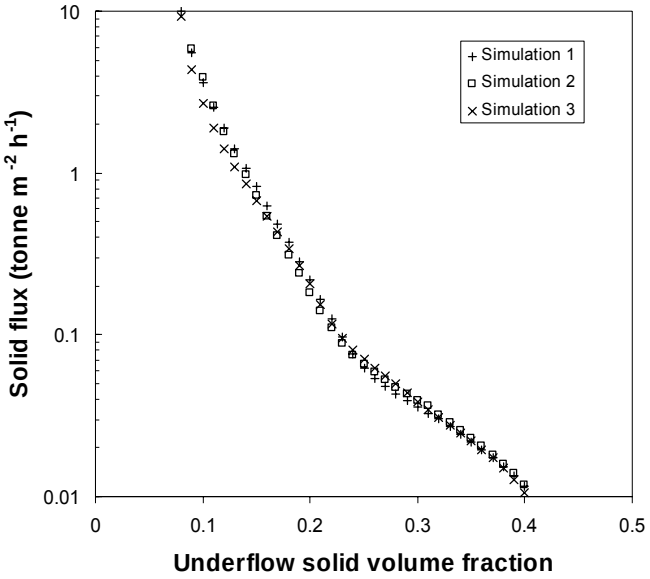

Figure 4-11 Steady state thickener modelling from $h(t)$ in Figure 4-8

The level of precision obviously decreases with increasing scale. Laboratory experiments are highly precise, pilot scale measurements less so, while full scale plant measurements are quite inaccurate and subject to sudden fluctuations in solids concentration, composition or throughput. The errors in plant are difficult to quantify and can be large. This obviously makes the task of predicting this behaviour from lab measurements difficult. Nevertheless, steps were taken to ensure, as far as possible, that the pilot scale work was as controlled and the results reproducible. The manual control used in Chapter 4 was not ideal and therefore a feed back control system was introduced in Chapter 7. Furthermore, density meters were installed on feed and underflow streams to give instantaneous indication of change within the column while the column was

operated for long periods (72 + hours) to help establish a steady state. The down side of long operation times is the number of possible experimental variables considered was reduced; (and repeating experiments was equally unfeasible). The cause of the error associated with pilot column and full scale experiments is explored further in the relevant chapters (Chapters 6 and 7).

Table 4-7 Predicted solid flux for a thickener with the tall column dimensions and bed height 1 metre

	Predicted solids flux (tonne m^{-2} h^{-1})			Mean (tonne m^{-2} h^{-1})	Std Dev (tonne m^{-2} h^{-1})
(v/v)	Test 1	Test 2	Test 3		
$\phi_u = 0.1$	3.643	3.898	2.711	3.417	0.625
$\phi_u = 0.2$	0.217	0.183	0.206	0.202	0.017
$\phi_u = 0.3$	0.036	0.039	0.038	0.037	0.002

4.6.2 Compressive rheology of calcite

Figure 4-12 and Figure 4-13 show the permeability and compressibility of the flocculated calcite feed sampled from the pipe. The data were fitted with following functions; the constants appear in Table A-2 and Table A-3 in Appendix 1;

$$R(\phi) = r_a\left(\phi^{r_b} + r_c\right) \tag{4.6}$$

$$P_y(\phi) = \left(1 - \frac{\phi_g}{\phi}\right)^{p_m} Exp\left(p_a\phi^{pn} + p_b\right) \tag{4.7}$$

The compressive yield stress and hindered settling function curves shown in Figure 4-12 and Figure 4-13 includes both pressure filtration and settling rate

data. Because the work preceded the analytic solution for $R(\phi)$ [82, 134, 135, 139] the settling data was only collected for ten minutes. Consequently, the analytical $h(t) \Rightarrow f(\phi)$ transform could not be applied leaving a noticeable gap in $R(\phi)$ for ϕ ranging between 0.2 – 0.4 v/v. However, more recent $R(\phi)$ data presented in Chapter 3 was obtained using the transform. Allowing for slightly different flocculant dosages (30 and 40 g tonne^{-1}) and initial volume fractions (0.04 and 0.06 v/v) in each case, $R(\phi)$ in Figure 4-12 and Figure 3-13 do not differ significantly.

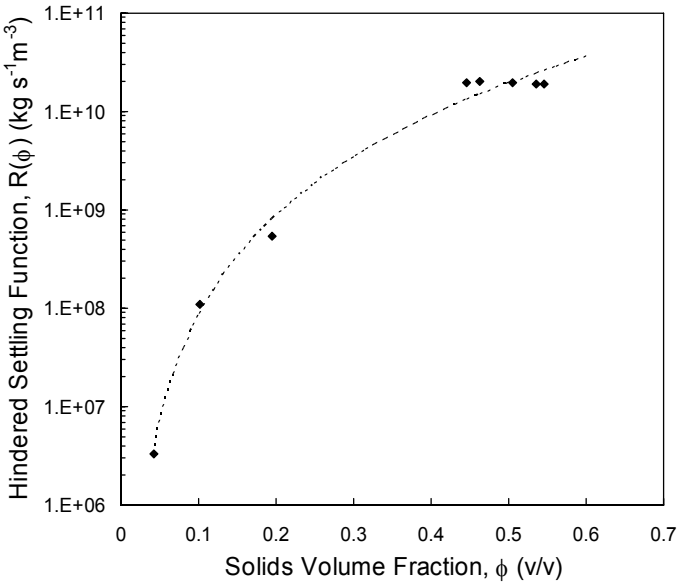

Figure 4-12 Hindered settling function for calcite flocculated in a 12.5 mm pipe reactor at 6.1 L min $^{-1}$.

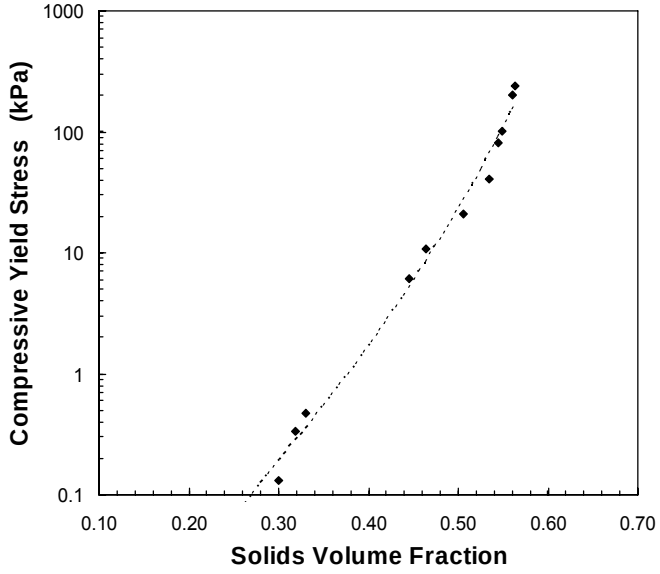

Figure 4-13 Compressive yield stress of calcite flocculated in a 12.5 mm pipe reactor at 6.1 L min^{-1}

4.6.3 1−D Modelling Predictions for Thickening Column

4.6.3.1 Pipe reactor feed to column

Figure 4-14 shows the 1−D model prediction based on permeability and compressibility of the flocculated pipe reactor feed to the column. The dewatering behaviour was significantly different to that predicted for flocs produced in the stirred baffled reactor. This demonstrates that flocculation conditions (in this case the differences between baffled stirred tank and pipe reactor hydrodynamics) can influence the aggregate size, density and strength. The difference in hydrodynamics for each flocculation method is shown in Table 4-8.

4.6.3.2 Different aggregation conditions

Flocculation conditions were chosen based on a population balance model, which predicted the evolution of floc size as a function of pipe residence time for different hydrodynamic conditions [64, 65]. The aim was to select two conditions, which produce significantly different aggregate structures. Based on the hydrodynamic conditions in the pipe, the model predicted a maximum aggregate size at t = 1.8 seconds. The first flocculation condition considered was therefore a 2 second residence time, marginally higher than 1.8 to ensure aggregates were no longer in a growth stage. The second flocculation condition was a residence time of 10 seconds, since this should produce smaller aggregates due to shear rupture, with different dewatering characteristics.

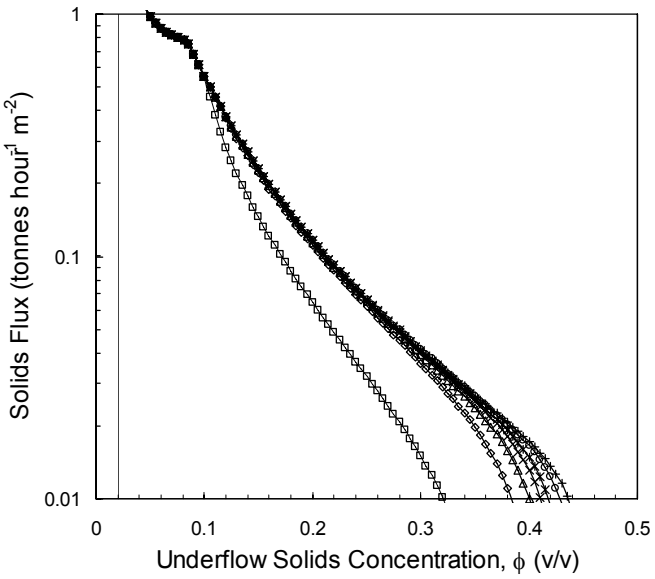

Figure 4-14 Flux curve predicted from characterisation of calcite flocculated in linear pipe reactor. Data represents the following bed heights □ 0.5 m; ◇ 1 m; △ 2 m; ○ 4 m; + 6 m; ∗ 8 m; x 10 m

Figure 4-15 shows the predicted solids flux as a function of underflow solid concentration for the different flocculation conditions and a 1 m bed. Comparing the results in Figure 4-15 with Figure 4-11, it is clear that the effect of flocculation conditions on the predicted thickener performance is far greater than the potential error caused by reproducibility and transformation of data. For a solids flux ranging between 0.003 and 3 tonne m^{-2} h^{-1}, the model predicts that the maximum underflow solid density is obtained when the dosage is highest (75 g $tonne^{-1}$) and residence time longest (10 sec). For the same flux, these conditions also produce the highest underflow solids concentration. Conversely, dewatering was slowest when the dosage was minimum (25 g $tonne^{-1}$) and pipe residence time shortest (2 sec). At solid fluxes less than 0.003 tonne m^{-2} h^{-1} the curves appear to asymptote to the same solids concentration. This is because $P_y(\phi)$ did not differ significantly at high ϕ (refer to Appendix 1 for $P_y(\phi)$ as a function of flocculant dose).

Table 4-8 Hydrodynamic characteristics of flocculation

	0.3 tonne m^{-2} h^{-1}	0.0375 tonne m^{-2} h^{-1}	Baffle reactor
Feed Flow rate (L min^{-1})	6.8	0.7	–
Pipe diameter (m)	0.0125	0.006	–
Reynolds number (–)	11295	2422	7008
Shear rate (s^{-1})	972	507	340
Residence time (s)	5.02	5.6	10

If equivalent dosages are compared, both 50 g $tonne^{-1}$ and 75 g $tonne^{-1}$ dosages resulted in higher underflow density when the residence time was longer. The 25 g $tonne^{-1}$ result showed opposite behaviour and may be anomalous. Based on Chapter 3 results, a longer residence time should adversely affect dewatering as

flocs are broken down. It is possible however, that the 2 second residence time was insufficient to allow flocs to grow to their maximum size.

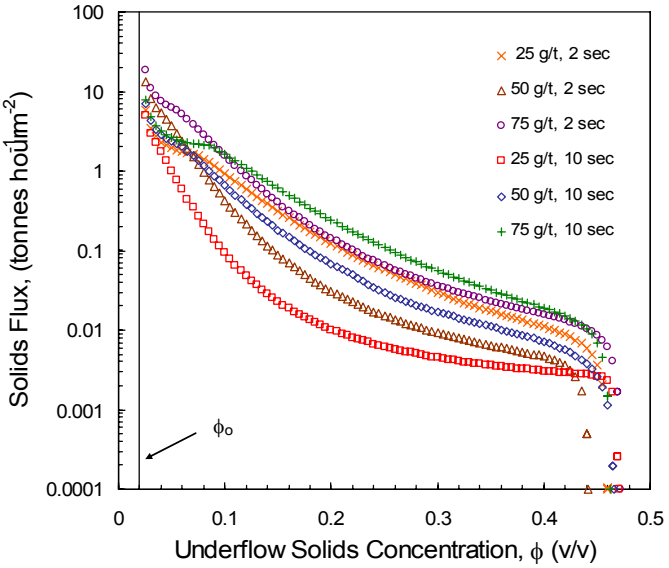

Figure 4-15 Predicted solids flux as a function of underflow solid concentration for six different flocculation conditions (three flocculant dosages and two residence times) and 1 m bed

4.6.4 Tall column validation results

4.6.4.1 Solids flux

In this section, the tall column results are compared with the 1−D model predictions. Under steady state operation, it was expected that the 1−D model would successfully predict the output solids from the column where the assumption of 1−D dewatering is satisfied, and where the model framework and material characterisation approach are sound and relevant to conditions within the column. Then, errors associated with the full-scale thickener simulations could be either due to the assumptions inherent in a 1−D model not applying, or

alternatively, the characterisation method not representing conditions inside the thickener.

The results from the tall column runs at a solids flux of 0.3 tonne m^{-2} h^{-1} are plotted in Figure 4-16. The underflow solids concentration was not constant so it is possible that steady state conditions had not fully developed. The variability is more significant for 1.0 and 0.8 metre bed heights, with the underflow solid concentration still decreasing after 6 hours. For a one-metre bed this corresponds to more than six bed turnovers, see Table 4-9.

Figure 4-17 shows the underflow solids concentration when the column was operated at a solids flux of 0.037 tonne m^{-2} h^{-1}. For this flux, the maximum bed that could be sustained was 0.75 m. Higher bed heights were not possible because for heights above 0.75 m, the consolidation rate was faster than the solid deposition rate.

Table 4-9 Residence time for the two solids flux and bed heights

Solids flux	Residence time (minutes)			
	0.4 m	0.6 m	0.8 m	1.0 m
0.3 tonne m^{-2} h^{-1}	17	32	48	57
0.03 tonne m^{-2} h^{-1}	397	698	1000	-

As with the 0.3 tonne m^{-2} h^{-1} results, the underflow solids concentration data showed significant non-uniformity. With the two bed turnover as a guide, a 0.03 tonne m^{-2} h^{-1} flux would require 33 hours to reach steady state. Operation for this length of time was not possible without additional instrumentation and control schemes. These are introduced in Chapter 7.

Despite efforts to maintain constant shear condition and residence times in the pipe, the aggregates forming at the lower flux were noticeably larger and settled significantly faster than the flocs formed at the higher flux. Referring to Table 4-8, this result is expected since the shear rate in the pipe was considerably less at the lower flux. A 5 mm pipe was required to give a shear rate comparable to the higher flux value; however, piping in this diameter was unavailable. Instead, to produce comparable aggregates sizes and settling rates, the polymer dosage was decreased to 5.5 g tonne^{-1}. Although settling rates were similar, the two cases were not expected to show identical $R(\phi)$ and $P_y(\phi)$ profiles.

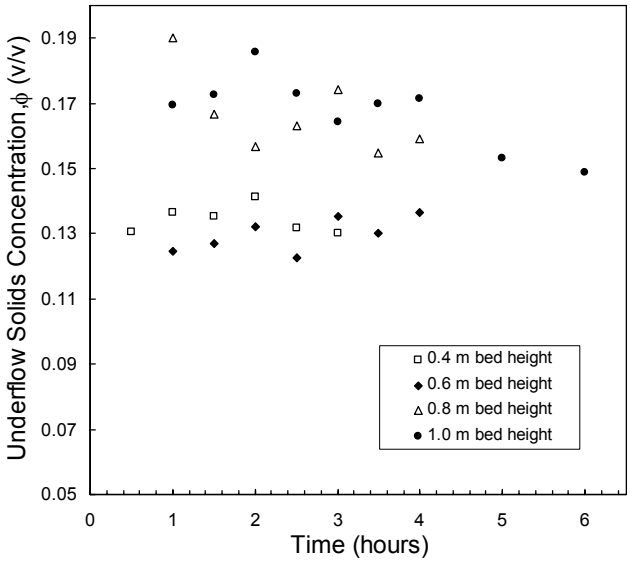

Figure 4-16 Underflow solid concentration as a function of time and bed height for flocculated calcium carbonate in the pilot scale tall column at a flow rate of 0.3 tonne m^{-2} h^{-1}

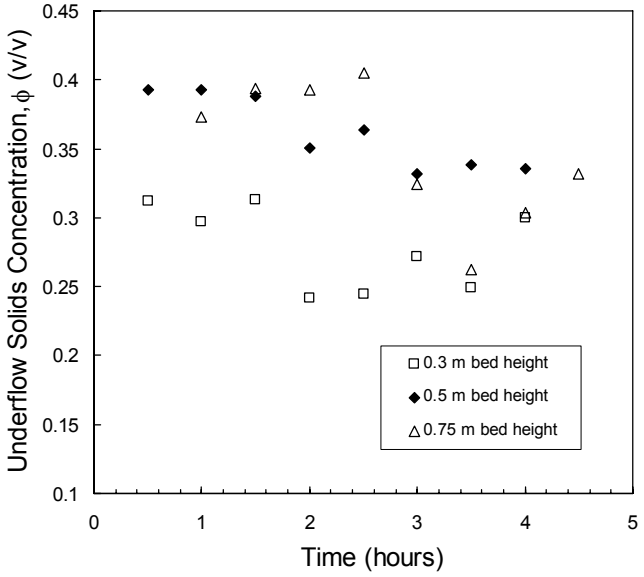

Figure 4-17 The solid concentration of underflow samples, by drying, as a function of run time and bed height for flocculated calcium carbonate in the pilot scale tall column at a flow rate of 0.0375 tonne m^{-2} h^{-1}

Figure 4-18 shows the underflow solids concentration when the column was operated at several bed heights and solids fluxes. The discrete data points in red correspond to ϕ_u at the completion of each run at the 0.3 tonne m^{-2} h^{-1} flux, while the blue points show the ϕ_u values corresponding to the 0.037 tonne m^{-2} h^{-1} flux. For both fluxes, the left most data point corresponds to the lowest bed height while data to the right represent progressively increasing bed heights, see Figure 4-16 and Figure 4-17. The errors are relatively small ranging from less than one percent for the smallest bed heights at each flux, (0.35 and 0.4 m), to a maximum of 20% for the higher flux and bed heights.

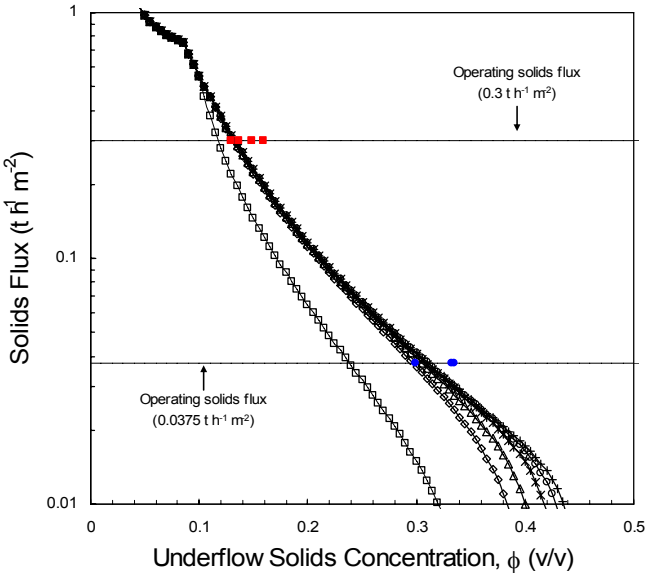

Figure 4-18 Solids flux of flocculated calcium carbonate slurry as a function of underflow solid concentration for: □ 0.1 m; ◇ 0.2 m; △ 0.4 m; x 0.6 m; ○ 0.8 m; and + 1.0 m bed heights. The 0.3 tonne m^{-2} h^{-1} column results are represented by the red squares; while the 0.03 tonne m^{-2} h^{-1} flux data by the blue circles

The effect of changing flocculation conditions on the column operation was considered. Figure 4-19 shows the underflow solids concentration measured over the course of the run when the suspension was flocculated with 75 g tonne $^{-1}$ and pipe residence time of 10 seconds. The bed height was maintained at 1 m for the duration of the experiment. The underflow density fluctuated between 0.20 and 0.24 v/v with an average of 0.21 v/v. The column was also operated at a lower flocculant dose of 25 g $tonne^{-1}$. The average underflow flow rate and solids concentration for each dose are shown in Table 4-10.

Table 4-10 Effect of flocculant dosage on underflow solids volume fraction

Dosage (g tonne^{-1})	Avg underflow rate (mL min^{-1})	Avg UF Solids Volume Fraction	Solids flow (tonne hr^{-1})	Solids flux (tonne m^{-2}hr^{-1})
25	826.6	0.14	0.017	0.26
75	511.8	0.22	0.017	0.26

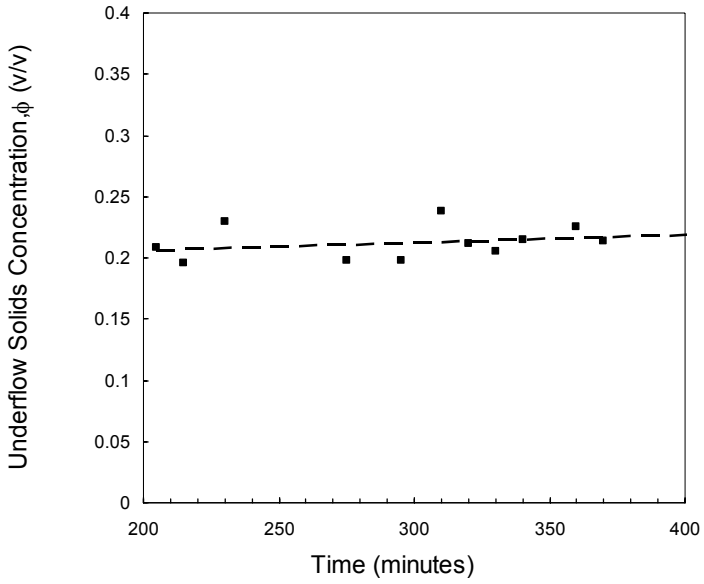

Figure 4-19 Underflow solids concentration as a function of time when pilot column operated with a constant 1 m bed and feed flocculated at 75 g tonne $^{-1}$ in a 10 m pipe reactor.

Figure 4-20 compares the measured underflow density with the model predicted underflow density for two different flocculant dosages. When flocculated at 75 g tonne $^{-1}$, the measured underflow density (0.21 (v/v)) was within 1 % of the model predicted value (at a solids flux of 0.3 tonne m^{-2} h^{-1}). When the flocculant was decreased from 75 to 25 g tonne $^{-1}$ the UF solids volume fraction decreased

to 0.139 (v/v). This could be expected from $R(\phi)$ alone, since the column was operating under permeability limited conditions. Reducing the polymer dosage caused the sedimentation rates to slow, and accordingly the solids flux is expected to decrease. Figure 4-20 shows that while the model correctly predicts the direction of the shift in underflow concentration, the predicted underflow (0.075 v/v) was considerably lower than the result from the column (0.139 v/v).

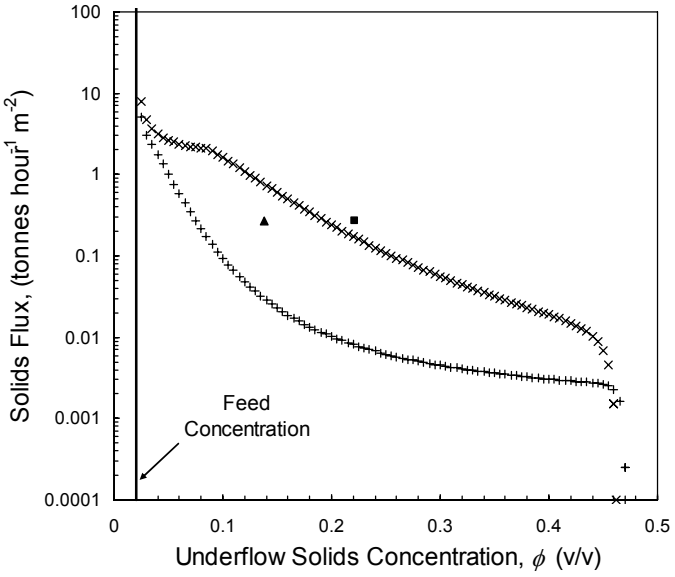

Figure 4-20 Predicted underflow solid concentration versus solids feed flux; × 75 g tonne^{-1} flocculant and 10 m pipe; + 25 g tonne^{-1} flocculant and 10 m pipe; ■ underflow solids from pilot column (75 g tonne^{-1} flocculant, 10 m pipe) ▲ underflow solids from pilot column (25 g tonne^{-1} flocculant, 10 m pipe)

The explanation is not clear at this stage, although data presented in later chapters intimate that a major factor could be the sensitivity of flocs to shear at low solid concentrations. These results indicate that deviations are more likely for weaker flocs and longer residence times in the column. In terms of model

assumptions, in particular the appropriateness of the material characterisation to the conditions in the column, the shorter residence times (low bed heights) and higher flocculant dosages are most likely to satisfy this assumption. In fact, these cases were closest to the predicted model outcomes.

4.7 Conclusions

Initial dewaterability characterisation and simulation established a set of operating conditions for the pilot thickening column. The 1−D model was validated by operating the column under pseudo steady state conditions for two different solid fluxes, 0.3 and 0.03 tonne m^{-2} h^{-1} fluxes, bed heights ranging from 0.3 to 1.0 metre, and two different flocculant dosages. The agreement between model prediction and column outputs was reasonable, with predictions differing from experimental values by between 1 and 20 %. This is considered a good result considering the lack of control over operating conditions, (slurry feed rate, flocculant dosing etc). It must be remembered when assessing the performance of the model, that substantially larger discrepancies between model prediction and thickener output have been observed, see Figure 1-3.

Therefore, under idealised and approximately one-dimensional flow, the model was considered validated. The remainder of this thesis is devoted to studying conditions for which the current model assumptions are not expected to be valid, i.e. when shear is taken into account. The following chapter begins by introducing a method for characterising suspension dewatering subject to a shear field.

Chapter 5

Effect of Shear on Compressive Rheology

5.1 Introduction

A large amount of information concerning the inter-relationship between shear, flocculant type and concentration and the subsequent formation of aggregates has been established [139]. Inside the feed well, shear affects flocculation kinetics by influencing both the frequency of particle collisions and distribution of flocculant [81, 134, 135]. In comparison, relatively little is known about the dewatering properties of a suspension once flocs have formed under given shear conditions. Understanding the relationship between shear, aggregate structure and dewatering is clearly important; since not only the size and settling rate of aggregates is important but how the aggregates dewater when shear and compressive forces are applied. This knowledge is necessary to predict or optimise thickener behaviour where compression or raking effects are important.

Previous studies have demonstrated that gentle agitation greatly improves dewatering [77]. The energy input by shear allows the particles or flocs to consolidate to higher solid volume fractions in shorter times [146]. Likewise, Channel [28, 29] showed that when shear was applied during filtration, the dewaterability of the cake improved considerably. However, the effect of shear on dewatering is not beneficial in every case, and is likely to depend on the magnitude of the shear rate. For instance, Novak and Bandak [33, 125, 157] demonstrated that when high shear was applied, the suspension dewatering

performance actually deteriorated. While such studies clearly demonstrate the importance of shear to dewatering phenomena, they do not quantify the effect of shear on dewatering, nor do they provide any indication of the shear rates typically involved.

The aim of this chapter is to quantitatively assess the role shear plays in the dewatering of flocculated suspensions. This can be achieved by measuring the dewatering parameters $P_y(\phi)$ and $R(\phi)$ for a range of shear rates. From Chapter 2, both of these parameters are non-linear functions of solids concentrations and depend on the type of solids, flocculant type and concentration, aggregate formation conditions and post formation shear conditions. Therefore, quantifying the relationship between shear, aggregate structure and dewaterability is clearly not a straight-forward process as there is a wide range of variables to consider. Suspension dewatering under shear is studied in Couette geometry. Consequently, the shear rate is directly proportional to the rotation rate (through azimuthal velocity gradients). A compressive force; either due to gravity or mechanical loading can be applied simultaneously. Mechanical compression could be useful to investigate shear in processes involving high amounts of compression (such as deep cone thickeners or filters). In this work however, only gravitational compression is considered.

5.2 A mechanism for dewatering with raking

In order for solid particles to rearrange into a more closely packed space, the particle network must at some point fail. Failure can occur due to either changes in the total stress or the hydrostatic (pore) pressure of the fluid. Such changes might arise as a result of a sudden change in the thickener bed height or the movement of a rake. In fact, it is the combination of total stress and pore

pressure that governs the compressive and shear strength of a flocculated network. According to Terzaghi's principle, any measurable effect caused by a change in stress state, including compression and shear deformation, must involve a change in effective stress [146]. The effective stress is directly proportional to a critical or yield stress, defined as the shear stress developed along a slip surface when shearing at a constant volume. Hence, a reduction in effective stress, due for instance to a sudden increase in pore pressure, effectively reduces the strength of the material in shear.

A networked suspension can fail by at least two mechanisms. The first mechanism involves a change in the network stress, which could arise from mechanical raking or shear stresses at the wall or conical base surface. If this stress exceeds the critical shear strength, which in turn is related to the bridging forces holding the polymer and particles together, the bonds will break. The particle is then released and free to occupy a vacant positions with a lower gravitational potential, so that a denser structure results. The second mechanism involves compression of material by the rake blade. This results in an instantaneous increase in pore pressure in front of the blade. The increased pore pressure causes a corresponding decrease in effective stress ($\Delta\sigma$) according to equation (2.7), and consequently the maximum shear strength is reduced by $\Delta\tau$ causing possible failure.

Because the fluid and particles are incompressible, consolidation to a higher solids volume fraction must involve displacement of entrained water. The low pressure region behind the blade could provide a potential escape route for this water. Thus, a third possible mechanism can be proposed; the formation of channels. Observed improvement in dewatering due to raking has been attributed to channel formation and the increased permeability these channels cause [70, 112, 157]. Because the channel provides a more direct escape path for

the liberated water, the hydrodynamic drag experienced by the particles is lower and so $R(\phi)$ decreases accordingly. In a full sized raked thickener, any of the above mechanisms could contribute. To determine which mechanism dominates requires an experimental technique capable of isolating one or more mechanism. Stirred settling experiments are popular for mimicking the effect of raking on dewatering [84]. However, because all of the above mentioned mechanisms potentially compete, little mechanistic information is obtained. In contrast, Couette flow has no appreciable pressure gradients; therefore the effect of shear can be isolated.

5.3 Theory of concentric cylinders

5.3.1 Rheology characterisation

To characterize the steady state rheology of non-Newtonian fluids, the ideal geometry is two parallel planes. The shear stress (calculated as the ratio of tangential force to planar area) is uniform throughout the sample and the shear rate is calculated simply by the ratio of velocity to planar distance. However, the usefulness of these devices is limited in practise by leakage and end effects. An alternative to parallel plates is to use two concentric cylinders, since the flow patterns are similar to parallel plates [110]. A schematic of a concentric cylinder rheometer is shown in Figure 5-1. Concentric cylinder rheometers are popular since they are relatively inexpensive, simple to operate and require small volumes of sample. However, exact determination of the shear rate is difficult unless a fluid model is known or assumed *a priori* [129]. The accuracy of the shear analysis depends on the ratio of the cylinder radii and the nature of the non-Newtonian fluid in question [108].

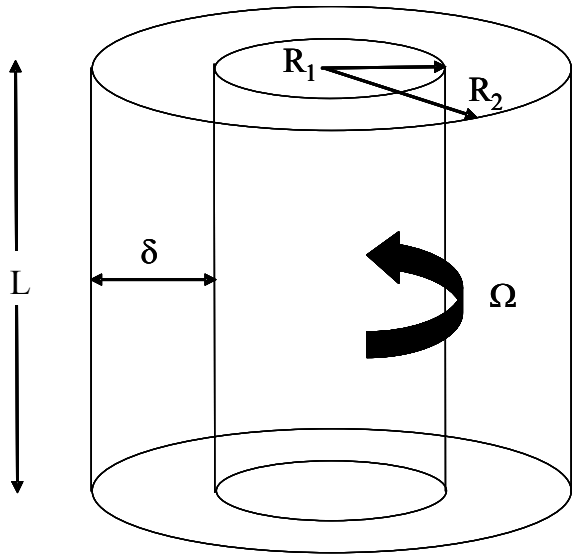

Figure 5-1 Schematic of a Couette device

In Couette geometry, under steady shear conditions and in the absence of wall slip, the fluid flows at an angular velocity v_θ, where $0 \le v_\theta \le \Omega$ (see Figure 5-2). The θ component of the equations of motion, in cylindrical coordinates is written;

$$\frac{1}{r^2}\frac{\partial}{\partial r}\left(r^2\tau_{r\theta}\right) = 0 \tag{5.1}$$

which, upon integration yields;

$$\tau_{r\theta} = \frac{c}{r^2} \tag{5.2}$$

where the constant c can be determined from the known stress boundary condition. The torque on the outer cylinder is the product of shear stress,

surface area and lever arm, giving $T = \tau_w \cdot 2\pi R_1 L \cdot R_1$. Then $c = \frac{T}{2\pi L}$ and the stress is determined via;

$$\tau_{r\theta} = \frac{T}{2\pi L r^2} \tag{5.3}$$

For purely tangential flow the shear rate can be written;

$$\dot{\gamma} = r\frac{d\omega}{dr} = r\frac{d}{dr}\left(\frac{v_\theta}{r}\right) \tag{5.4}$$

5.3.2 Shear rates in a concentric cylinder device

At low volume fractions $\left(\phi < \phi_g\right)$ a particulate suspension exhibits the same rheological behaviour as the carrier fluid, which is usually Newtonian. Then the relationship between stress and strain is linear, i.e. $\tau_{yx} = \mu\dot{\gamma}$ and the shear rate can be determined analytically. However, suspensions with an average solid volume fraction greater than ϕ_g tend to display more complex rheology.

For non-Newtonian suspensions, the shear rate is a non-linear function of shear stress and depends on the material, flocculant type and flocculation conditions. The relationship between stress and strain for generalised Newtonian fluids is written as;

$$\boldsymbol{\tau} = -\eta\boldsymbol{\Delta} \tag{5.5}$$

where the scalar quantity η is the non-Newtonian viscosity. The viscosity η can be expressed as an assumed function of $\boldsymbol{\Delta}:\boldsymbol{\Delta}$, where $\boldsymbol{\Delta}:\boldsymbol{\Delta}$ is the second invariant of the rate of deformation tensor.

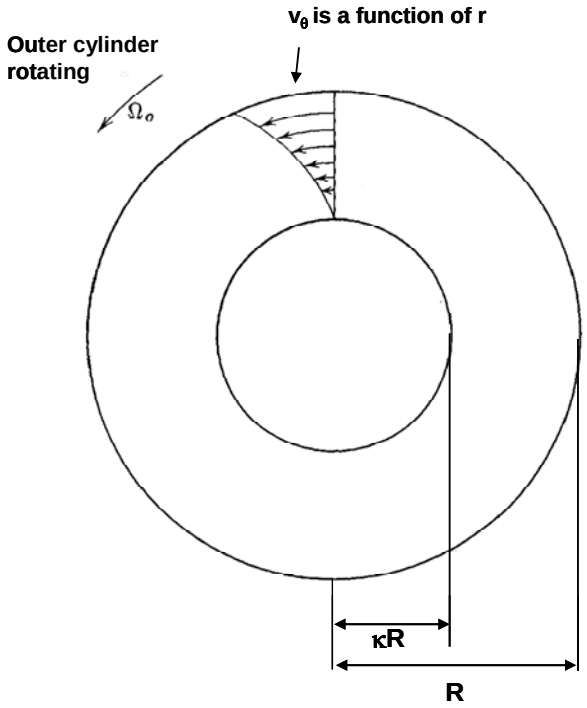

Figure 5-2 Velocity profile in a fluid contained within two concentric cylinders, the outer rotating at Ω_0

Empirical models describing the shear stress, shear rate dependence include; the two-parameter power law, Bingham, and Cason and the three-parameter Herschel-Bulkley models. The rheological behaviour of concentrated 0.2 w/w calcite suspensions was measured by Mosquet [110] as a function of polymeric dispersant concentration. Increasing polymer concentration caused both the yield stress and plastic viscosity to decrease due to particle stabilisation effects. At a concentration of 0.83 mmol L^{-1} the fluid flow was approximately Newtonian. The model parameters are shown in Table 5-1.

Table 5-1 Parameters of the Herschel-Bulkley fluid model for a 0.2 w/w calcite suspension

	τ_y	m	n
No polymer	10.5	3.94	0.381
0.83 mmol/L	0.03	0.0023	0.9823

In multidimensional form, the Herschel Bulkley model is expressed as;

$$\boldsymbol{\tau} = -\left\{ \frac{\tau_y}{\sqrt{\tfrac{1}{2}(\boldsymbol{\Delta}:\boldsymbol{\Delta})}} + m\left|\sqrt{\tfrac{1}{2}(\boldsymbol{\Delta}:\boldsymbol{\Delta})}\right|^{n-1} \right\}\boldsymbol{\Delta} \qquad \text{for} \frac{1}{2}(\boldsymbol{\tau}:\boldsymbol{\tau}) > \tau_y{}^2$$

$$\boldsymbol{\Delta} = 0 \qquad \text{for} \frac{1}{2}(\boldsymbol{\tau}:\boldsymbol{\tau}) \le \tau_y{}^2 \tag{5.6}$$

where τ_y is the yield stress, m and n are model parameters (often referred to as consistency and flow index respectively), $\boldsymbol{\tau}$ is the stress tensor and $\boldsymbol{\Delta}$ is the stretching tensor. The scalar products $\boldsymbol{\Delta}:\boldsymbol{\Delta}$ and $\boldsymbol{\tau}:\boldsymbol{\tau}$ are the second invariants of the second order tensors $\boldsymbol{\Delta}$ and $\boldsymbol{\tau}$. The appropriate expression in equation (5.6) depends on the value of $\tfrac{1}{2}(\boldsymbol{\tau}:\boldsymbol{\tau}) = \tfrac{1}{2}\sum_i\sum_j \tau_{ij}{}^2$. Since $\tau_{r\theta}$ is the only non-zero component of $\boldsymbol{\tau}$ in Couette flow;

$$\tfrac{1}{2}(\boldsymbol{\tau}:\boldsymbol{\tau}) = \tau_{r\theta}{}^2 \tag{5.7}$$

Thus, when $\left|\tau_{r\theta}{}^2\right|$ is less than the τ_y the stretching tensor is identically zero (zero strain, i.e. the fluid does not flow).

For fluid in tangential annular flow the second invariant of $\boldsymbol{\Delta}$ is;

$$\tfrac{1}{2}(\boldsymbol{\Delta}:\boldsymbol{\Delta}) = \left[r\frac{d}{dr}\left(\frac{v_\theta}{r}\right)\right]^2 \tag{5.8}$$

If equation (5.8) is substituted into equation (5.6) the following relation between stress and velocity field results;

$$\tau_{r\theta} = \tau_y + m\left(r\frac{d}{dr}\left(\frac{v_\theta}{r}\right)\right)^n \tag{5.9}$$

To determine the shear rate it is necessary to evaluate the tangential velocity, v_θ. Substituting equation (5.9) into (5.2) and rearranging yields;

$$d\left(\frac{v_\theta}{r}\right) = \left(\frac{\frac{c}{r^2}-\tau_y}{m}\right)^{1/n}\frac{dr}{r} \tag{5.10}$$

Integrating over the indefinite limit $R_1 \rightarrow r$

$$\int_{\frac{v_\theta(R_1)}{r}}^{v_\theta(r)} d\left(\frac{v_\theta}{r}\right) = \left(\frac{1}{m}\right)^{1/n}\int_{R_1}^{r}\left(\frac{c}{s^2}-\tau_y\right)^{1/n}\frac{ds}{s} \tag{5.11}$$

$$v_\theta(r) = v_\theta(R_1) + \left(\frac{r}{m^{1/n}}\right)\int_{R_1}^{r}\left(\frac{c}{s^2}-\tau_y\right)^{1/n}\frac{ds}{s} \tag{5.12}$$

Equation (5.12) gives v_θ as a function of r. Determining the shear rate now becomes an exercise of solving c. In fully sheared flow the non slip boundary conditions at the outer cylinder yield $r = R_2$ and $v = v(R_2) = 0$. Hence;

$$v_\theta(R_2) = v_\theta(R_1) + \left(\frac{R_2}{m^{1/n}}\right)\int_{R_1}^{R_2}\left(\frac{c}{s^2} - \tau_y\right)^{1/n}\frac{ds}{s} \tag{5.13}$$

If the function $f(c)$ is defined;

$$f(c) = v_\theta(R_2) - v_\theta(R_1) + \left(\frac{R_2}{m^{1/n}}\right)\int_{R_1}^{R_2}\left(\frac{c}{s^2} - \tau_y\right)^{1/n}\frac{ds}{s} \tag{5.14}$$

The value of c can be found using an iterative root solving technique such as Newton-Raphson method.

$$c_{n+1} = c_n - \frac{f(c_n)}{f'(c)} \tag{5.15}$$

Once the constant c is determined, the shear stress can be calculated at all radii using equation (5.2), while the shear rate is calculated using equation (5.9).

5.3.3 Yield stresses, gap sizes and flow instabilities

If the material possesses a yield stress, the problem of determining shear rates in Couette flow is compounded. The yield stress is a function of solids volume fraction (ϕ), and for volume fractions above the gel point, the yield stress increases exponentially with ϕ. Because the shear stress decays with increasing distance from the rotating surface, it is possible that the stress falls below the yield stress at some point, in which case fluid beyond this point in the annulus will not be sheared. The conventional methods for determining shear rates outlined in section 5.3.2, no longer apply since the reduced gap width is not taken into account [13].

To ensure that material within the annulus is completely sheared, the size of the gap can be reduced or the rotational rate Ω increased. A small gap is preferable since yield surfaces and other non uniformities are exacerbated with large gaps because the stress decays exponentially with distance. However, because aggregates can grow to sizes of millimetres, the gap size cannot be too small. To ensure a continuum within the gap, the width should be at least ten times greater than the average size of the aggregates [163]. An upper limit also applies to the rotation rate. To ensure that the flow between cylinders is laminar and purely tangential, and that no flow instabilities develop, the angular velocity cannot exceed a critical value. The onset of flow instabilities was first predicted by Taylor who visualised flows between rotating cylinders to confirm his predictions. The instabilities appear as pairs of counter rotating toroidal vortices stacked upon each other.

5.4 Experimental

Transient batch settling tests were performed in a double walled Couette apparatus. Three polymer dosages and six different shear rates were investigated. In each test, the suspension-supernatant interface $h(t)$ was measured until equilibrium was reached. In a separate series of experiments, the Couette device was replaced by two alternate rake configurations to mimic raking (see Figure 5-4).

5.4.1 Equipment

The double walled Couette shear device comprised three concentric cylinders, shown schematically in Figure 5-3. The inner and outer cylinders were kept stationary while the middle (shaded) cylinder was rotated at a constant velocity.

The cylinders were constructed from polyacrylate tube of nominal thickness 3 mm. The dimensions of the cell were $R_1 = 0.035$ m, $R_2 = 0.048$ m, $R_3 = 0.051$ m and $R_4 = 0.060$ m so the resulting gap widths were $\delta_i = R_2 - R_1 = 0.013\,\text{m}$ and $\delta_o = R_4 - R_3 = 0.009\,\text{m}$. The radius ratios were $\eta_i = R_1 / R_2 = 0.73$ for the inner and $\eta_o = R_3 / R_4 = 0.69$ for the outer. The height of the cylinders was 0.5 m so that the aspect ratio Γ was 38.46 and 55.56 for the inner and outer gaps respectively. The cylinders were held in place by a stainless steel end cap. Rotation of the middle cylinder was driven by a variable speed overhead motor (IKA Eurostar SV PCZ) with a gearbox ratio of 1:50.

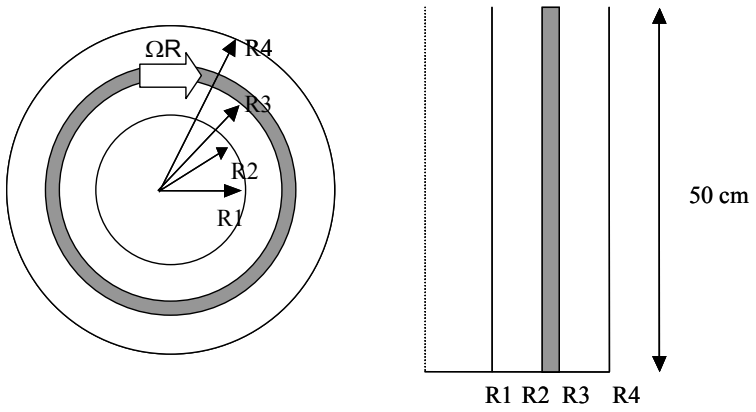

Figure 5-3 Schematic of the Couette shear cell used in sheared batch settling experiments

Additionally, two simple raking devices (see Figure 5-4) were used in place of the Couette, to simulate raking in a thickener, where normal stresses could be important. The horizontal rake consisted of a vertical central shaft attached to which were approximately 20 horizontal prongs (5mm diameter and 50 mm length). The vertical rake consisted of four vertical prongs, (5 mm diameter and

300 mm length) welded to a horizontal arm. The space between prongs in both cases was 12 mm.

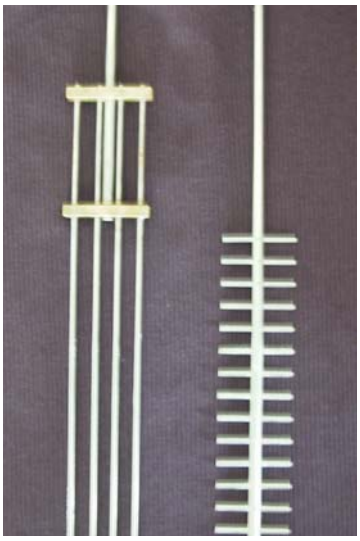

Figure 5-4 Photograph of the vertical (left) and horizontal (right) "rake" configurations used in the sheared batch settling experiments

5.4.2 Procedure

Concentrated calcite suspensions were prepared at a solids concentration of 0.4 w/w using tap water. The suspensions were mixed by an overhead stirrer for approximately 60 minutes to ensure homogeneity. Flocculation occurred continuously in a linear pipe reactor (12.5 mm ID and 1.8 m in length) with a single addition of flocculant. Just prior to entering the pipe reactor the concentrated 0.4 w/w suspension was diluted by metering tap water to produce a 0.1 w/w suspension. Each of the flocculant, dilution water and concentrated slurry flows were regulated using PID control. The flocculant flow rate was adjusted to give the specified flocculant dose. A density meter was installed on the slurry line after the water addition point to monitor the feed density over the duration of experiments. When flows had stabilised the vessel was filled from

the pipe reactor, the motor was turned on at the specified rotation speed and the height of the suspension-supernatant interface was measured. The change in interface height with time was recorded using a Sony TRV50 digital video camera for a period of two hours. A halogen lamp provided backlight to increase the contrast. Three flocculant dosages 20, 40 and 60 g tonne^{-1} and 6 different rotation rates 0, 2, 3, 4, 6, and 8 rpm were investigated in the Couette device. For the raked experiments, the procedure was similar, with the pipe reactor feed being fed instead to a 1 L measuring cylinder filling to a height of approximately 0.4 m. For the raking work, only one dosage 40 g tonne^{-1} and 6 rotations speeds (0, 1, 3, 5, 7, 9 rpm) were investigated.

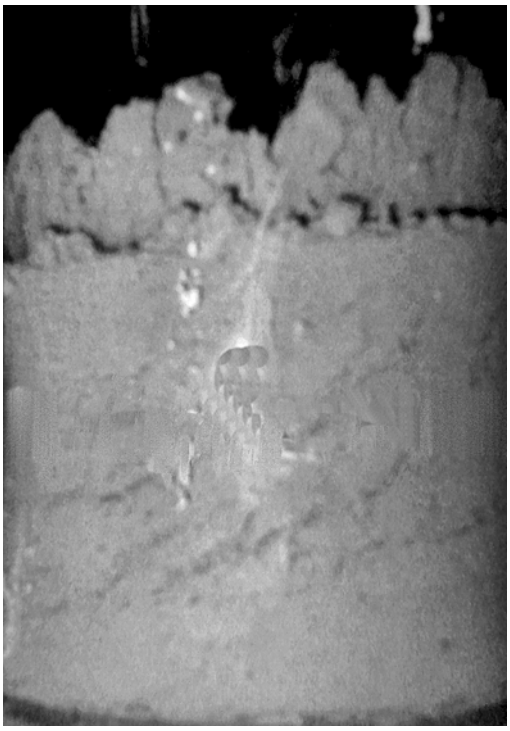

Figure 5-5 Photograph of Couette cell after two hours operation. Two final interface heights can be easily distinguished. Note that in the central un-sheared region was not filled

5.4.3 Shear rate distribution

An important objective was to ensure that the chosen geometry and rotation speeds provided shear rates relevant to thickening. In a raked thickener bed, shear rates vary significantly depending on the position in the bed. However, as a guide shear rates typically range between 1 and 20 s^{-1}. Because the suspension is settling, the concentration and therefore rheology (n, m and τ_y) is not constant, instead depending on both time and position (r, θ, z) so that exact determination of the shear rate at any time is difficult. To simplify matters, two limiting cases were considered. Initially, the suspension is dilute and thus behaves as a Newtonian fluid. The shear rate can be calculated analytically [14] and is shown in Figure 5-6 as a function of radial distance. After several minutes of settling, sediment forms with a characteristic shear yield stress. The yield stress depends on the solids concentration, which in turn increases with normal stress [114]. In batch settling, because the normal stresses are typically only a few Pascals, it is unlikely that the yield stress (τ_y) will exceed more than around 20 Pa. Assuming τ_y of 20 Pa, and average volume fraction of 0.08 (v/v), the shear rate distribution was calculated using a Herschel-Bulkley model with $n = 0.69$ and $m = 5$. The data is presented in Figure 5-7. To achieve shear rates in the range 1-20 s^{-1} in the Couette geometry specified in section 5.4.1, rotation rates ranging between 1 and 20 rpm were required.

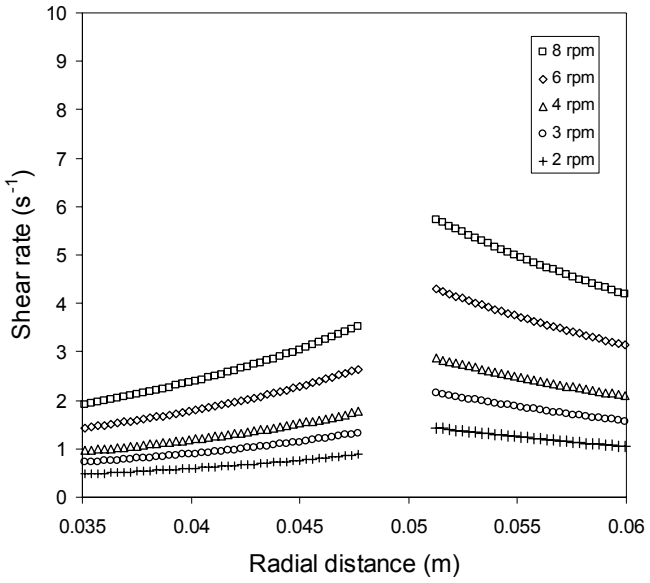

Figure 5-6 Shear rate as a function of radial distance in Couette shear cell for a Newtonian fluid

The shear rate profiles for the Newtonian fluid were more uniform and the maximum shear rate was lower than the corresponding non-Newtonian fluid profiles. For Newtonian fluids, the calculated shear rates varied by less than 1 s^{-1}, at any given rotation rate, while variation for a non-Newtonian fluid is somewhat higher, ranging between 2.5 to 8 s^{-1} across the gap. Compared to the typical shear rate variation in a raked thickener, these differences are relatively minor. While both average and maximum shear rates across the gap can be determined, the maximum shear rate is quoted throughout this thesis, since the maximum shear rate dictates whether a certain sized floc of is likely to break when stressed.

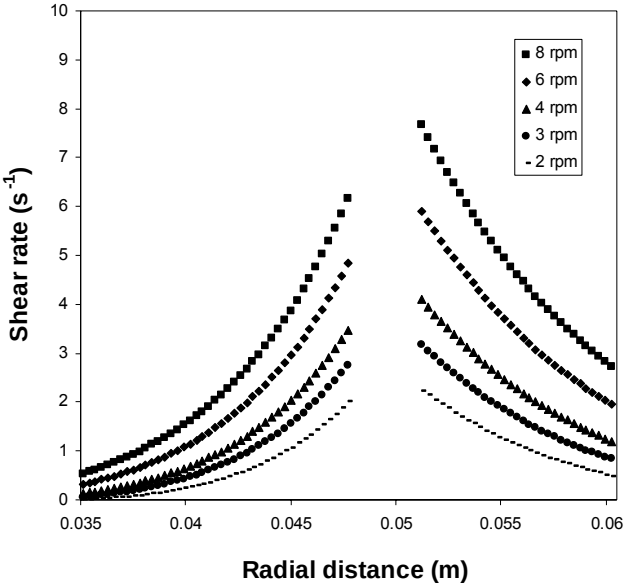

Figure 5-7 Shear rate as a function of radial distance in Couette shear cell for a Herschel-Bulkley fluid

5.5 Results and Discussion

5.5.1 Initial raked experiments

Figure 5-8 shows the hindered settling function of kaolin flocculated at two dosages, 250 and 1000 g tonne $^{-1}$ as a function of rotation rate. As a result of increasing the dose from 250 to 1000 g tonne^{-1}, the hindered settling function at the initial solids concentration, $R(\phi_0)$ decreased between 4 and 9 times. The greatest change in $R(\phi_0)$ occurred at intermediate rotation rates (between 3 and 7 rpm). In this speed range, $R(\phi_0)$ was almost independent of rake speed. When the highest rotation rate was employed (9 rpm), the change in $R(\phi_0)$ was smaller (4-5 fold decrease). This response is similar to when the suspension was un-raked. This suggests that both the speed of the rake and flocculant dosage

must be considered together when studying dewatering of flocculated systems. Only the initial settling rates were measured in this work – the analytical solution for $R(\phi)$ up to ϕ_g was not developed at the time − so quantitative dewatering information was available for the initial solid concentration only.

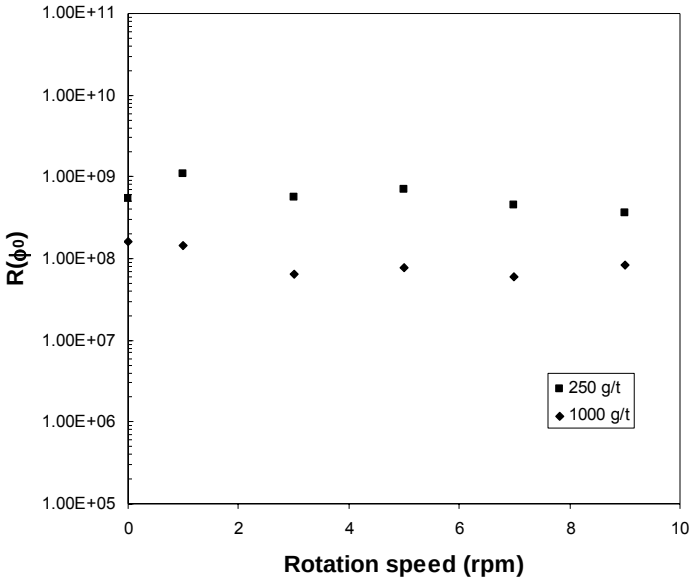

Figure 5-8 Hindered settling function of kaolin at ϕ_0=0.01 (v/v) as a function of the rake rotation rate for two different flocculant dosages

Figure 5-9 shows the average volume concentration after raking continuously for 2 hours. The average solid concentration was calculated from the final bed height, from $\phi_f = \phi_0 h_0 / h_f$. By increasing the rake speed, the equilibrium height decreased, such that the average final solids in the bed increased. This trend was generally observed, although slight differences between the two flocculant dosages were observed. For the lower dose, the average solids concentration peaked at approximately 0.06 v/v when the rake speed was 5 rpm. Increasing the

speed beyond 5 rpm, actually caused the average solids concentration in the bed to decrease. However, when a higher polymer dose was applied, while the average solids concentration still peaked at 5 rpm, further increase in rake speed did not change the solids concentration. This outcome is in contrast to the usually observed result for un-raked suspensions. For rotation speeds less than 5 rpm, there was little difference in average solid concentration between the two polymer dosages.

5.5.2 Transient settling in Couette shear cell

Figure 5-10 shows the suspension and supernatant interface $h(t)$ as a function of time for a series of batch-settling tests in the Couette. In each test the initial height (0.40 ± 0.004 m) and concentration (0.105 ± 0.05 w/w) were the same allowing direct comparison between the $h(t)$ curves measured for different dosage and shear rates. Three bands are evident corresponding to the different flocculant dosages from left to right; 20, 40 and 60 g tonne $^{-1}$. The solid data points correspond to $h(t)$ in the central un-sheared region. In the absence of shear, the equilibrium height, h_∞ was noticeably higher than when shear was applied.

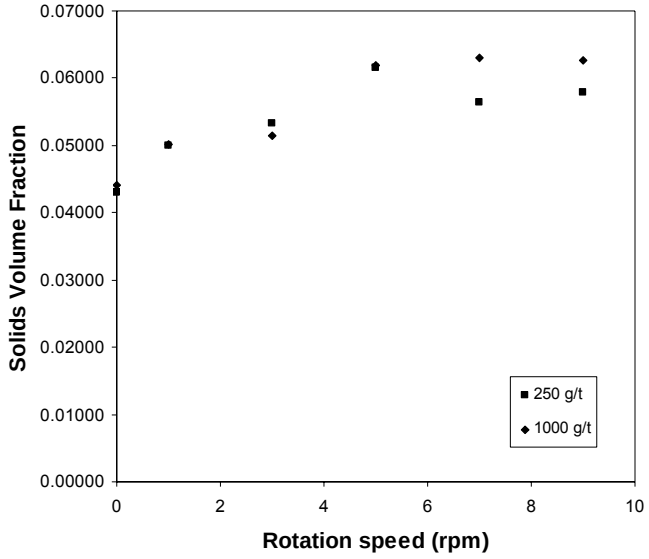

Figure 5-9 Average solid volume fraction after 120 minutes of settling for kaolin flocculated at two dosages and stirred at various speeds

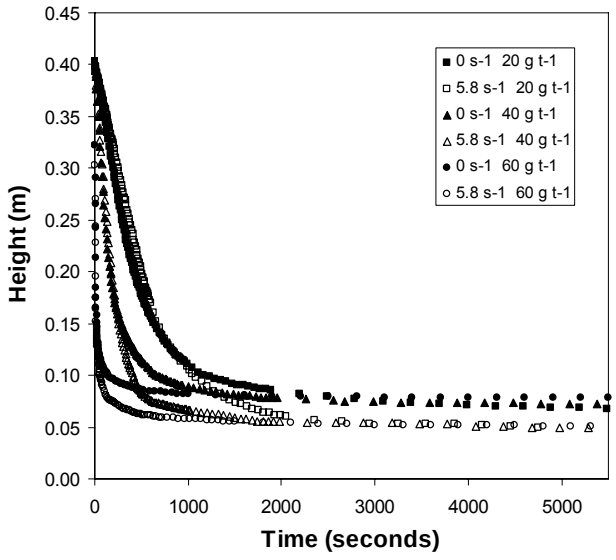

Figure 5-10 Batch settling curves in the Couette shear cell for calcium carbonate flocculated with 20 g tonne^{-1} ■,40 g tonne^{-1} ▲ and 60 g tonne^{-1} ● added flocculant under zero shear and optimum shear rate (5.8 s^{-1})

When sheared the shape of $h(t)$ changes significantly compared to the un-sheared $h(t)$. The initial linear region slope is identical in both cases; however, when sheared, the linear region of $h(t)$ increases to longer time. When the sheared $h(t)$ curves eventually become non-linear, they follow the behaviour non-sheared $h(t)$ behaviour so that the equilibrium height is lower. Interestingly, the deviation between sheared and un-sheared $h(t)$ curves occurred at a solid volume fraction well below the gel point. This suggests that shear is affecting hindered settling prior to the formation of a stress-bearing network. It is not clear whether this is due to changes in the hydrodynamic forces experienced by individual particles, or whether hindered settling is somehow affected by the change in gel point and the different compressive behaviour that ensues. Under shear, the final height was the same irrespective of flocculant dose. However, un-sheared, a difference was observed. The final heights from highest to lowest corresponded to dosages of 60, 40 and 20 g tonne^{-1}. This suggests that the network resistance to compression increases in proportion with the amount of polymer added.

Figure 5-11 and Figure 5-12 show the effect of shear on dewatering for two different polymer dosages. The former shows $h(t)$ data for 40 g tonne^{-1} while the latter shows the same data for 60 g tonne^{-1}. In the 40 g tonne^{-1} case, the sheared curves overlap, while in the 60 g tonne^{-1} case, the $h(t)$ curves fan probably on account of the higher network strength. Figure 5-12 shows that the linear to non linear transition occurs at progressively longer times with increasing shear rate so that the equilibrium bed height decreased. The exception to this trend is the $h(t)$ curve corresponding to the highest shear rate (7.7 s^{-1}). This demonstrates that shear improves dewatering up to a point. However, too much shear can have an adverse effect.

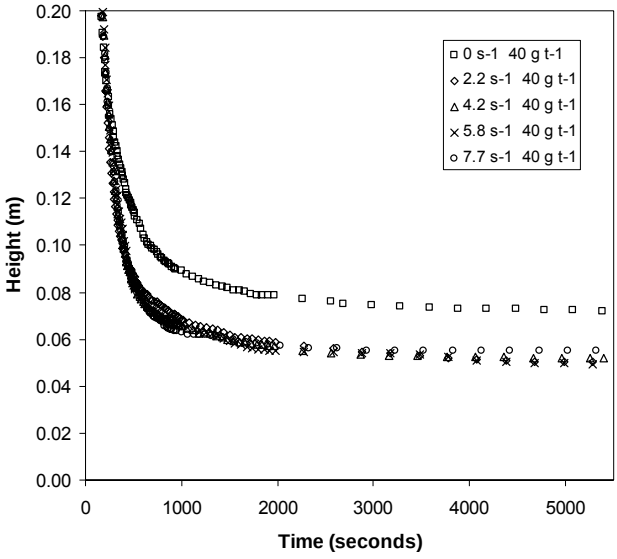

Figure 5-11 Batch settling curves in Couette shear cell for calcium carbonate flocculated with 40 g tonne^{-1} added flocculant in 1.8 m length pipe reactor

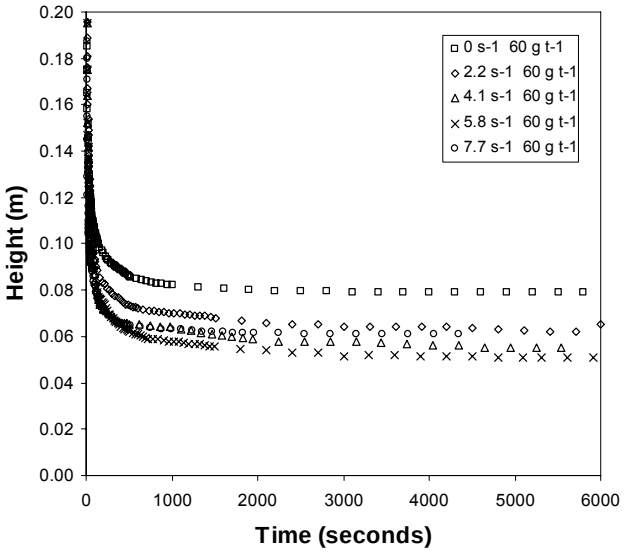

Figure 5-12 Batch settling curves in Couette shear cell for calcium carbonate flocculated with 60 g tonne^{-1} added flocculant in 1.8 m length pipe reactor

5.5.3 Horizontal Rake

The above results for the Couette shear cell demonstrate that pure shear (i.e. no rakes) improved dewatering up to a critical shear rate. Now it remains to be established how the shear in the Couette compares to a rake where both shear and pressure gradient act in unison. Did raking produce significantly different results to shear in the Couette shear cell, and if so, which performed better? To compare the two mechanisms, flocculated calcite suspensions were prepared exactly as before. The suspensions were then raked and $h(t)$ measured. Figure 5-13 shows $h(t)$ curves for different rake speeds. It is evident that the trends observed in the Couette, apply equally when raked. The final height was significantly lower in all cases when compared to the un-raked result. The final bed height was a minimum when the rotation rate was 8.4 rpm. Thus, this rotation rate was designated the "optimum" rotation rate for the rake..

Figure 5-14 compares the optimum raked result with the optimum result obtained using the Couette device. This shows that there is a difference between raking and pure shear. While the final bed heights are the same for both methods, the final height is reached much faster in the Couette. While this does not prove conclusively that dewatering occurs by shear-assisted failure exclusively, it does demonstrate the importance of shear in suspension dewatering.

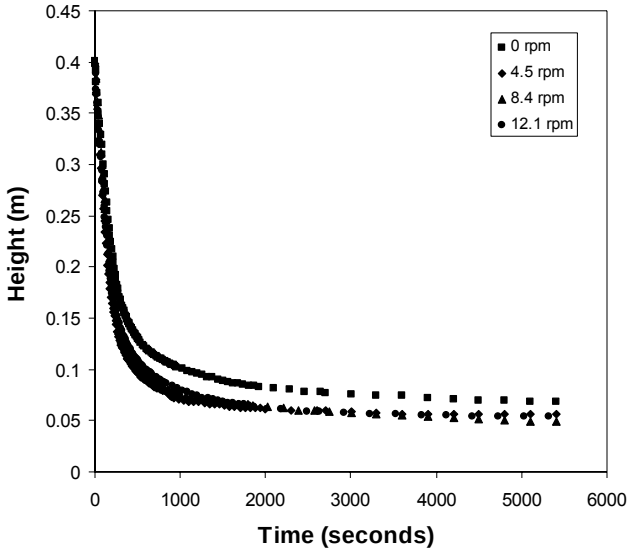

Figure 5-13 Horizontal raked batch settling curves for calcium carbonate flocculated with 40 g tonne $^{-1}$ added flocculant in 1.8 m length pipe reactor

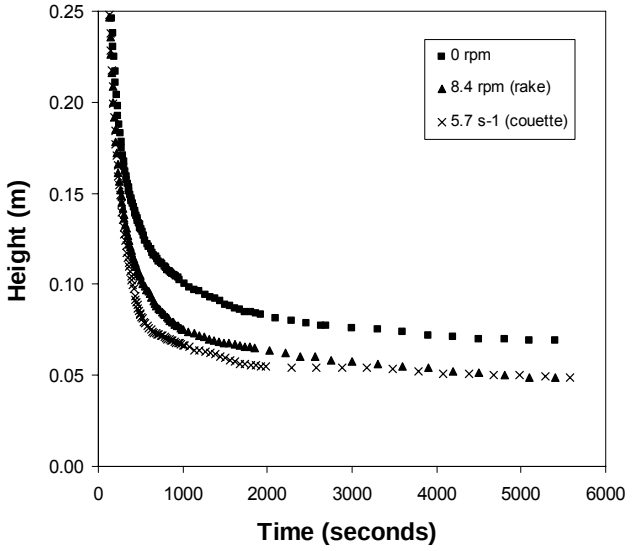

Figure 5-14 Optimal raked and Couette shear cell batch settling curves for calcium carbonate flocculated with 40 g tonne^{-1} added flocculant in 1.8 m length pipe reactor

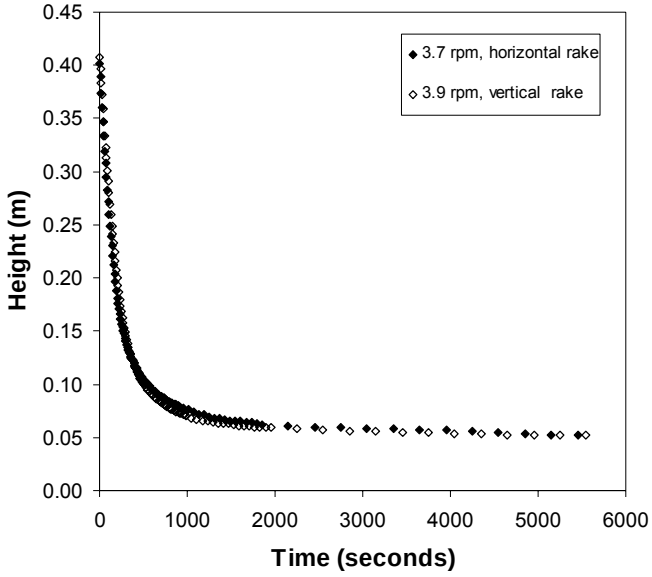

Figure 5-15 Horizontally and vertically raked batch settling curves for calcite flocculated with 40 g tonne^{-1} added flocculant in 1.8 m length pipe reactor.

5.5.4 Vertical Rake

A vertical rake configuration was chosen to promote channel formation, which has not been observed so far in the Couette settling tests studied so far. In the earlier kaolin work reported in section 5.5.1, channels were observed forming when a vertical rake was used; however, no channels formed when the horizontal rake was used. The kaolin suspension dewatered faster when a vertical rake was used, presumably because of channel formation. However, with calcite no channels were observed with either rake configuration. As such, there was virtually no difference between $h(t)$ for the two blade configurations (see Figure 5-15). It is difficult to make generalised statements regarding channel formation based on the limited data available other than to say that channelling does not appear to be an important factor with flocculated calcite. Further work involving

a wider range of materials and flocculant types is required to better understand the role of channelling.

5.5.5 Dewatering Analysis

5.5.5.1 Couette shear cell

The batch settling data of sections 5.5.2, 5.5.3 and 5.5.4 was analysed and $P_y(\phi)$ and $R(\phi)$ data extracted as outlined in Chapter 2. This data is shown in Figure 5-16 through to Figure 5-27. Each $P_y(\phi)$ and $R(\phi)$ curve comprises data obtained from both batch settling and filtration experiments. The filtration data was used primarily to fix the high end of $P_y(\phi)$ and $R(\phi)$. Measurement of $P_y(\phi)$ and $R(\phi)$ for freshly flocculated material and material that had been sheared in the Couette showed that the filtration results were not sensitive to the shear history of calcite. Consequently, the same filtration data is used throughout.

Figure 5-16 and Figure 5-17 show $P_y(\phi)$ and $R(\phi)$ for calcite suspension flocculated at 60 g tonne^{-1} and sheared at six different shear rates. Without shear, the material gel point was approximately 0.22 (v/v). However, when shear was applied, the $P_y(\phi)$ curves shifted to the right (for $P_y(\phi)$ less than 1 kPa). As a result, the gel point increased to between 0.3 and 0.38 (v/v) depending on the shear rate. This result implies that the network strength was affected by shear. The higher the shear rate, the more compressible the sediment became (up until a critical shear rate). If the critical shear rate is exceeded, the improved compressibility decreases. In the 60 g tonne^{-1} case, the maximum compressibility occurred at a shear rate of approximately 6.1 s^{-1}.

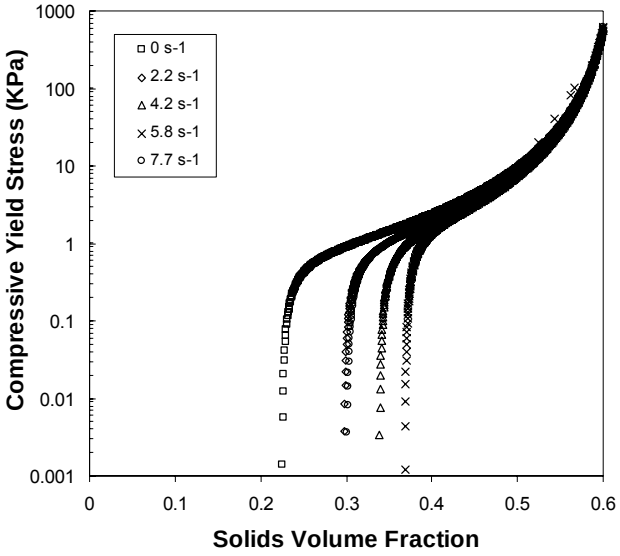

Figure 5-16. Compressive yield stress as a function of volume fraction for calcite flocculated with 60 g tonne^{-1} added flocculant and sheared in the Couette shear cell

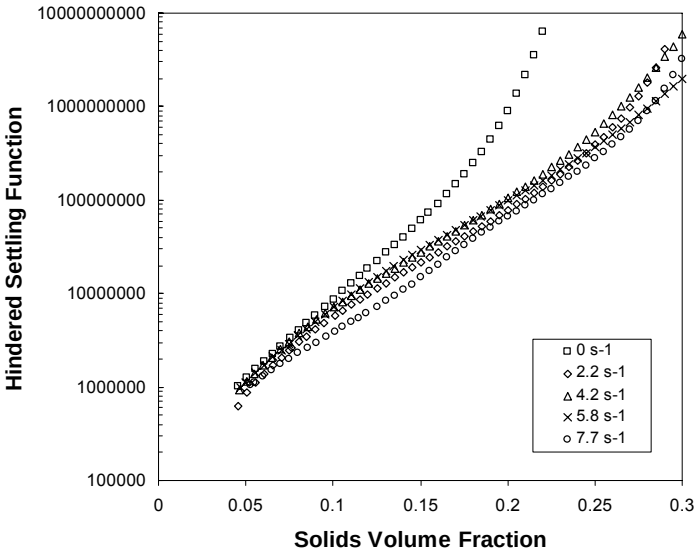

Figure 5-17 Hindered settling function as a function of solids volume fraction for calcite flocculated with 60 g tonne^{-1} added flocculant and sheared in Couette shear cell.

Figure 5-17 shows the effect of shear on $R(\phi)$. In the absence of shear, the $R(\phi)$ of calcite was significantly higher than $R(\phi)$ measured with shear. For example, when ϕ = 0.16, $R(\phi)$ is 1 x 10^8 un-sheared. When shear was applied, the same value of $R(\phi)$ corresponded to ϕ = 0.2 v/v; an improvement of 25%. Also, $R(\phi)$ diverge at a solid volume fraction significantly less than the gel point. For 60 g tonne^{-1}, the $R(\phi)$ curves diverge at $\phi \approx 0.08$, well below the gel point (0.22 v/v).

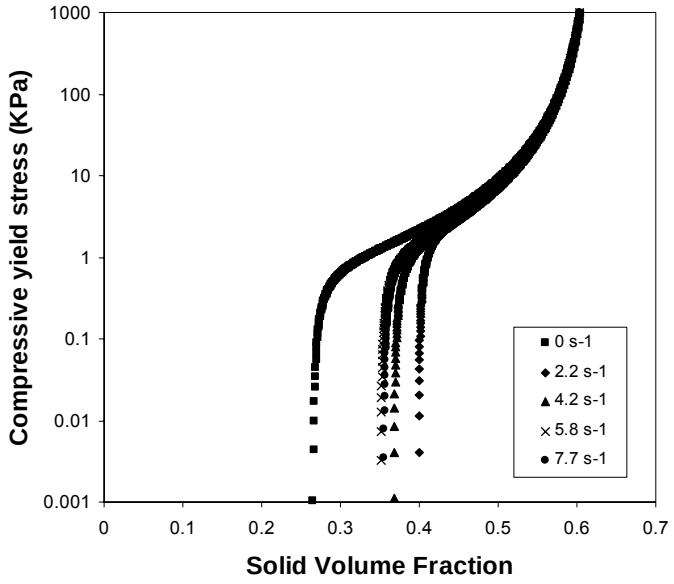

Figure 5-18 Compressive yield stress as a function of solids volume fraction for calcite flocculated with 20 g tonne^{-1} added flocculant and sheared in Couette shear cell

Figure 5-18 and Figure 5-19 show $P_y(\phi)$ and $R(\phi)$ for calcite flocculated at 20 g tonne^{-1} and sheared at the same shear rates as before. At this lower flocculant dose the sediment was most compressible when a shear rate of 2.3 s $^{-1}$

was applied. Increases above 2.3 s^{-1} caused the sediment to become less compressible and approach the un-sheared result. Therefore, the sediment again showed a maximum in compressibility with shear, although this maximum corresponded to a significantly lower shear rate. This is because a higher flocculant dose can sustain higher shear rates. Therefore, to fully characterise the effect of shear on dewatering, both flocculant dose and shear rate must be considered together. Figure 5-19 shows that like the higher flocculant dose, $R(\phi)$ improved significantly with shear, although no clear trend was evident with respect to shear rate.

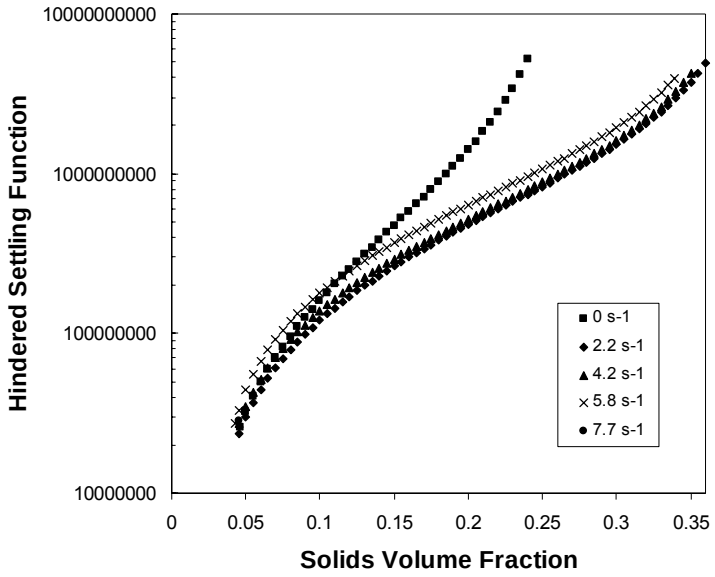

Figure 5-19 Hindered settling function as a function of solids volume fraction for calcite flocculated with 20 g $tonne^{-1}$ added flocculant and sheared in Couette shear cell.

Figure 5-20 and Figure 5-21 compare $P_y(\phi)$ and $R(\phi)$ for three flocculant dosages and two different shear rates, 0 and 6.1 s^{-1}. The un-sheared $P_y(\phi)$ data

lie to the left in Figure 5-20, while the sheared data lie to the right. The un-sheared gel point increased progressively with flocculant dose from 0.23 v/v at 60 g tonne^{-1} to 0.27 at 20 g tonne^{-1}. This could be predicted based on network strength considerations. However, when sheared the 20 g tonne^{-1} case became the least compressible, followed by the 60 g tonne^{-1} and 40 g tonne^{-1} cases. The greatest change in $P_y(\phi)$ as a result of shear occurred at the highest dose. At 60 g tonne^{-1}, the change in gel point due to shear $(\Delta\phi_g)$ was 63 % of the un-sheared value. At the lower dosages, $\Delta\phi_g$ was 49 and 32 percent for 40 and 20 g tonne^{-1} dosages respectively.

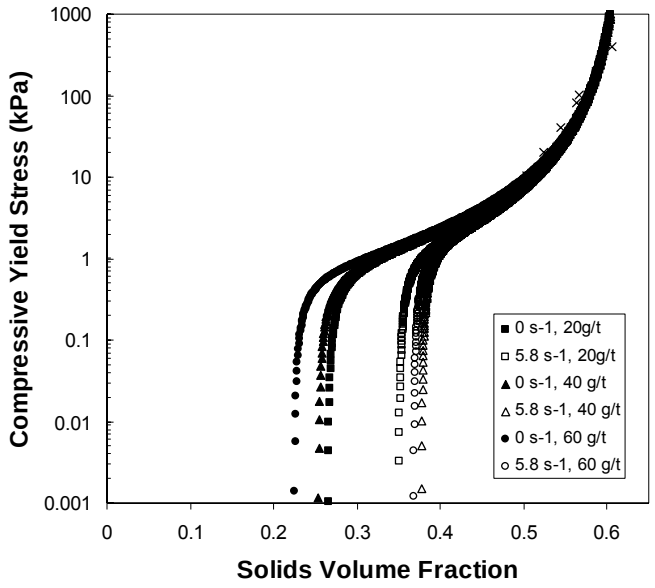

Figure 5-20 Compressive yield stress as a function of solids volume fraction for calcite flocculated with 20 g tonne^{-1} ■, 40 g tonne^{-1} ▲,60 g tonne^{-1} ● added flocculant at zero shear (solid) and maximum shear (hollow).

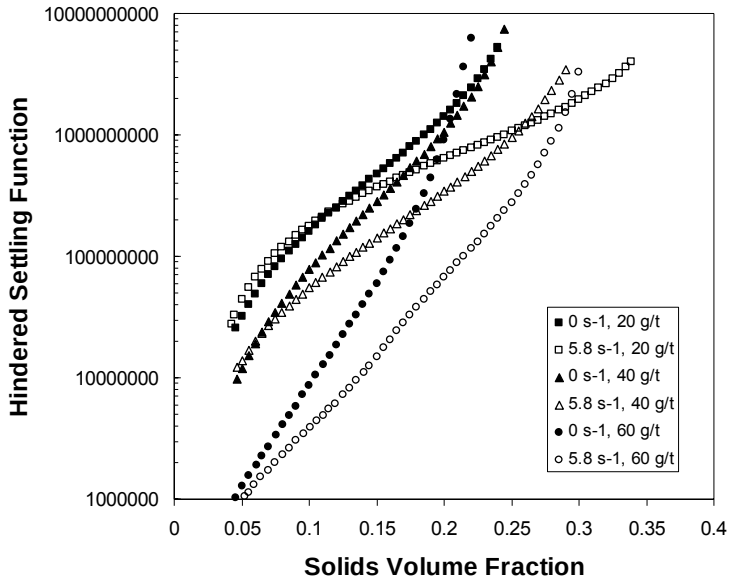

Figure 5-21 Hindered settling function as a function of solids volume fraction for calcite flocculated with 20 g tonne^{-1} ■, 40 g tonne^{-1} ▲,60 g tonne^{-1} ● added flocculant and maximum shear in Couette shear cell.

Figure 5-21 shows the effect of flocculant dosage and shear on $R(\phi)$. As expected, $R(\phi)$ decreased as the flocculant dose increased. In the absence of shear, this observation applied for volume fractions up to approximately 0.2 v/v. At a solid volume fraction marginally less than the gel point the $R(\phi)$ curves cross over. This implies that while increasing flocculant dosages increase the sedimentation dynamics below the gel point, the opposite is true when the solids are in compression. With shear, the same phenomenon was observed, however $R(\phi)$ cross over at a higher solids concentration, between 0.26 and 0.3 (v/v) depending on flocculant dosage. Thus, overdosing of flocculant is not as problematic, when the system is sheared. Figure 5-21 also demonstrates that the

greatest improvement in $R(\phi)$ arising from flocculant overdosing occurs at low solid volume fractions.

5.5.5.2 Horizontal Rake

The horizontal rake showed similar dewatering trends as the Couette shear device. Figure 5-22 shows $P_y(\phi)$ for calcite suspensions raked with a horizontal rake at different speeds. To the left of Figure 5-22 lays the curve corresponding to no raking. As the rotation rate increased, the curves shifted progressively to the right. Figure 5-23 shows that $R(\phi)$ displayed similar behaviour to the Couette shear device. The zero shear $R(\phi)$ curve lies clearly above a band of raked $R(\phi)$ curves; however, no clear trend is evident $R(\phi)$ between the various rotation rates.

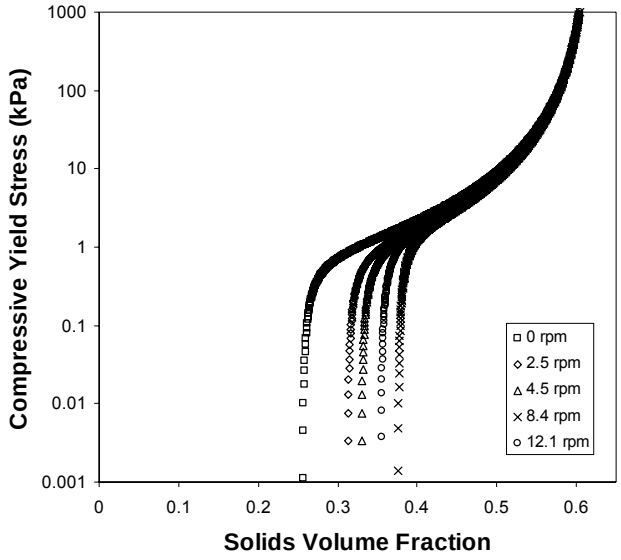

Figure 5-22 Compressive yield stress as a function of solids volume fraction for calcite flocculated with 40 g tonne^{-1} added flocculant and raked with a horizontal blade at 2.5, 4.5, 8.4 and 12.1 rpm

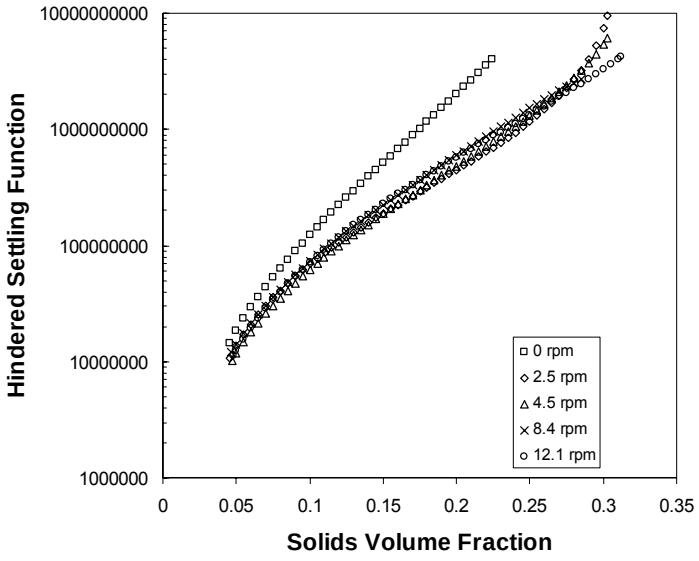

Figure 5-23 Hindered settling function as a function of solids volume fraction for calcite flocculated with 40 g tonne^{-1} added flocculant and raked with a horizontal blade at 2.5, 4.5, 8.4 and 12.1 rpm

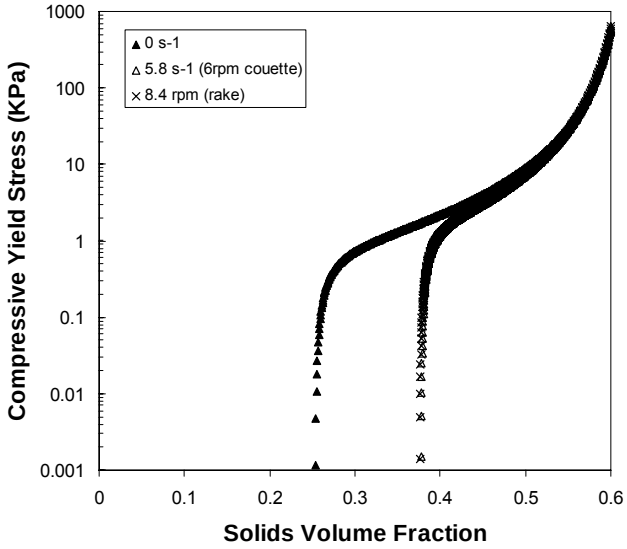

Figure 5-24 Compressive yield stress as a function of solids volume fraction for calcite flocculated with 40 g tonne^{-1} added flocculant and optimum shear rate in Couette cell ▲ and horizontal rake ×

Figure 5-24 and Figure 5-25 compare $P_y(\phi)$ and $R(\phi)$ between Couette shear and raked settling tests. These results represent the maximum dewatering possible in each device at a dose of 40 g tonne^{-1}. Figure 5-24 shows that the $P_y(\phi)$ in each case is almost identical. This suggests that the method by which one "disrupts" flocculated calcite has little bearing on $P_y(\phi)$. While no real difference in $P_y(\phi)$ was observed between the rake and Couette, $R(\phi)$ did show a difference (see Figure 5-25). For all $\phi < \phi_g$ the $R(\phi)$ measured using the Couette device was lower than the corresponding $R(\phi)$ in the rake. This was despite the fact that the gel point change was identical in each case. One explanation for this result is that the Couette constantly shears the entire suspension, while the rake only shears material in the immediate vicinity of the blade.

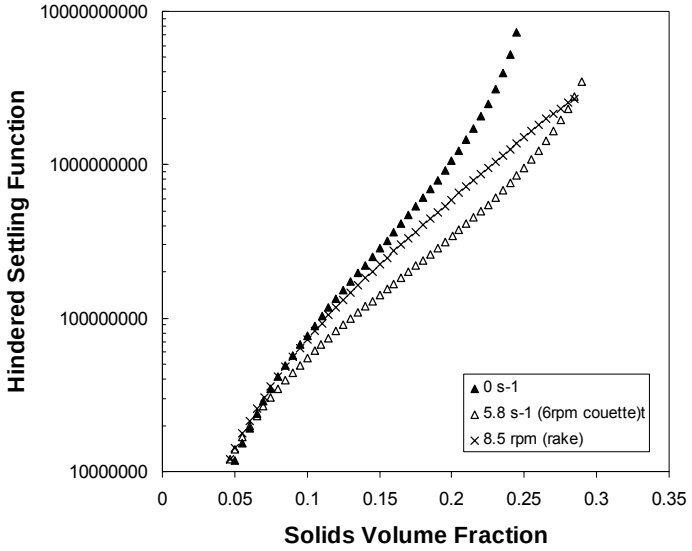

Figure 5-25 Hindered settling function as a function of solids volume fraction for calcite flocculated with 40 g tonne^{-1} added flocculant and maximum shear in Couette ▲ and horizontal rake ×

5.5.5.3 Vertical Rake

Figure 5-26 and Figure 5-27 compare $P_y(\phi)$ and $R(\phi)$ for two different raking configurations; horizontal and vertical. No channels were observed to form with either rake and the h,t curves were identical for both rakes. Therefore it is not surprising that $P_y(\phi)$ and $R(\phi)$ are the same.

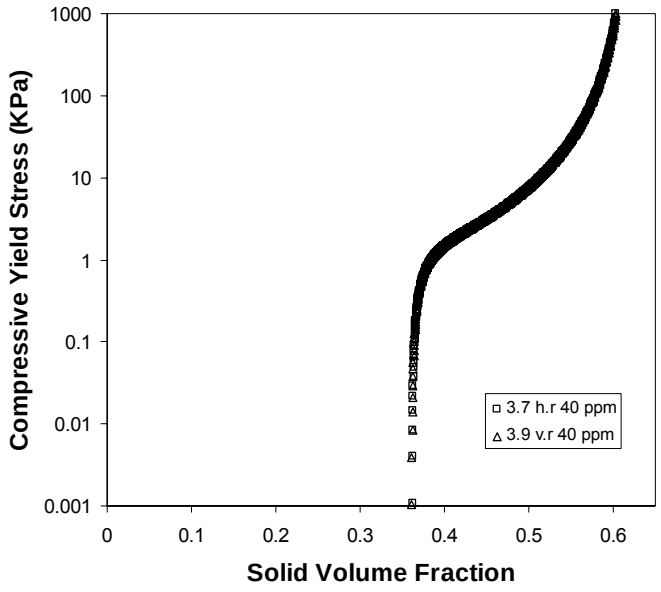

Figure 5-26 Compressive yield stress as a function of solids volume fraction for calcite flocculated with 40 g tonne^{-1} added flocculant and raked with horizontal □ and vertical Δ blades

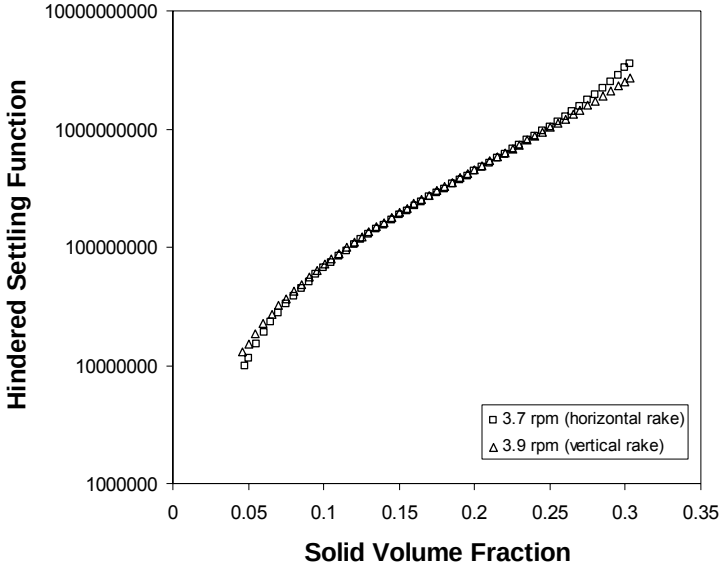

Figure 5-27 Hindered settling function as a function of solids volume fraction for calcite flocculated with 40 g tonne^{-1} added flocculant and raked with horizontal □ and vertical △ blades

5.5.6 One-dimensional Thickener Model Results

Modelling of gravity thickeners using one-dimensional models can lead to significant differences between the prediction and thickener output, as discussed in Chapter 4. If the thickener were remodelled with the shear modified compressive yield stress and hindered settling function used as inputs instead, a new predicted flux curve is obtained. Comparison of this flux curve to the previously un-sheared result allows the effect of shear on thickening to be quantified.

Figure 5-28 shows the model prediction for the calcite sheared in the Couette shear cell at three different dosages. The predictions were made based on $P_y(\phi)$ and $R(\phi)$ for the zero and optimum shear rate. The results show that the

predicted solids flux required to produce a given underflow concentration increased when shear is taken into account. The enhancement is greatest at the 60 g tonne^{-1} dose; approximately 10 times the un-sheared prediction when $\phi_u \approx$ 0.3 v/v. The increase in prediction is slightly less for the other dosages; between 6-8 times, for $\phi_u \approx 0.3$ v.v.

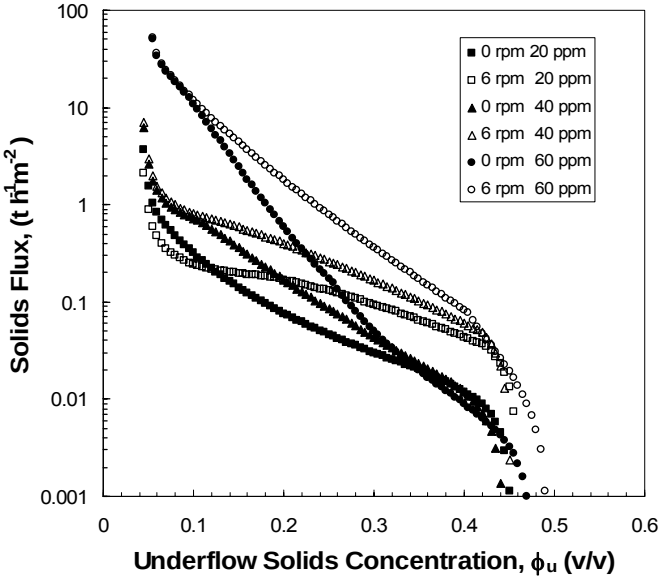

Figure 5-28 Predicted solids flux as a function of underflow solid concentration for 3 different flocculation conditions and two different shear conditions (Couette) for a 1 m bed of calcite.

In the absence of shear, the model predicts that the 60 g tonne^{-1} dose should allow the highest solids flux for a specified underflow concentration. The difference between solid fluxes for varying flocculant dosages is greatest at low underflow solid fractions. Above an underflow concentration of 0.3 (v/v) the difference is negligible. When shear is taken into account, the highest flocculant dosage still gives the best dewatering result. This is true for underflow solids

concentrations up to 0.45 (v/v), considerably higher than 0.3 (v/v) in the absence of shear. The benefit of shear to solids flux is highest at dense underflow solids concentrations (>0.3 v/v). This is true for all flocculant dosages. When the solid volume fraction is less than 0.15 (v/v), there is little difference between the sheared and un-sheared throughput predictions.

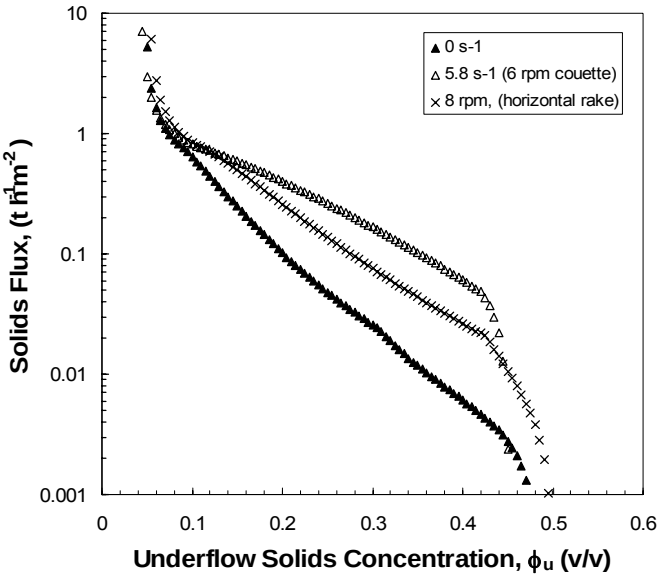

Figure 5-29 Predicted solids flux as a function of underflow solid concentration for 40 g tonne^{-1} flocculation dose, 1 m bed of calcite. Sheared in Couette ▲ and horizontal rake ×

Figure 5-29 shows the one-dimensional thickening model output for suspensions that were either sheared in the Couette or raked. For a given solids flux, the predicted underflow solids density increases due to shear. The amount by which the underflow density increases because of shear depends on the solids flux. At high fluxes (>1 tonne m^{-2} h^{-1}) shear has little effect since the residence times are too low. At low fluxes (<0.01 tonne m^{-2}h^{-1}) compression due to the weight of the bed is the dominant factor and the effect of shearing or raking is insignificant.

Thus, the maximum benefit from raking the sediment is expected when the thickener operates at intermediate fluxes between 0.01~1.0 tonne $m^{-2}h^{-1}$.

5.6 Conclusions

A Couette geometry was used to quantify the effect of post formation shear on the dewatering by measuring $P_y(\phi)$ and $R(\phi)$ for a range of shear rates. The role of flocculants in changing the dewatering properties of aggregated particulate suspensions has been examined. A critical shear rate transition has been observed between beneficial and detrimental effects in dewatering of added shear in manipulation of the flocculated aggregate structure. The degree of improvement depended on both shear rate and flocculant dose.

The mechanism of network failure under shear and compression was considered by comparing the Couette results to dewatering in a series of raked batch settling tests with different rake configurations. The results showed that dewatering was faster when sheared in the Couette device compared to simple raking, demonstrating the importance of shear to dewatering. These findings also raised issues concerning how and where the shear is applied. The compressive yield stress $P_y(\phi)$ in the presence of shear decreased, while the gel point of the material increased, suggesting a more densely arranged network structure forms. The hindered settling function $R(\phi)$ was similarly affected; the un-sheared suspensions exhibiting a higher $R(\phi)$ than the sheared ones. For solid volume fractions of less than 0.1 (v/v), the difference in $R(\phi)$ between the sheared and un-sheared was negligible. One dimensional thickener modelling showed the maximum improvement that could be expected from a rake. In the case of

flocculated calcite, a maximum raking factor of 10 was obtained for a shear of 5.8 s^{-1} in the Couette cell for $\phi_u \approx 0.3$.

Chapter 6

Shear characterisation of an industrial thickener feed

6.1 Introduction

In the previous chapter the compressive rheology of flocculated calcite was characterised under steady shear conditions. This helped quantify the role of shear in enhancing suspension dewatering and identify a critical shear rate, above which, this enhancement due to shear diminished. The material dewatering properties $P_y(\phi)$ and $R(\phi)$ determined can be used to model dewatering performance for a range of operating conditions. Simulated dewatering in the pilot column (section 5.5.6) indicated that the predicted solid flux required to yield a given underflow concentration, increased by a factor between 5 and 10 times, when a critical shear rate was applied in the laboratory.

The aim of this chapter is to compare the steady state thickener model prediction with thickened underflow sampled from an operational thickener. To demonstrate the material property characterisation and modeling process at full scale, a mineral sands site in southern Western Australia was chosen for investigation. The clay rich tailings from the extraction process were fed to a conventional thickener. The material properties $P_y(\phi)$ and $R(\phi)$ are determined as a function of shear rate and these parameters are used to simulate dewatering in the thickener. Differences between the model prediction and operational reality

are examined and elements of thickener operation which are presently poorly understood are identified

6.2 Experimental

6.2.1 Sampling

Several 5 L samples were collected from different locations of the feed-well at a depth approximately one metre below the surface. For each sample, cylinder setting tests were performed and the settling rates measured. Next, two 40 L samples, (prior to flocculation in the feed well), were collected for subsequent laboratory shear tests. Finally, a 20 L sample of underflow material was collected. A small sub sample of each of the feed, feed-well and underflow samples was dried overnight to determine the solid concentration. The results of all solid concentration measurements are shown in Table 6-1. The data shows that that the solid concentration varied significantly as a function of feed well position, and most likely time, so that the solids distribution in the feed well was highly non uniform. It is likely that dilution by the up flowing water in the feed well contributes to this non uniformity. Consequently, determining an average settling rate was difficult since the settling rate depends on solids concentration and flocculant dose, which both varied. The feed solids concentration prior to the feed well was more constant, varying between 0.0318 and 0.0380 (w/w) depending on sample. Likewise, the underflow concentration was constant and approximately 0.17 v/v.

6.2.2 Flocculation

To mimic the flocculation process occurring in the thickener feed well, a 1 litre measuring cylinder was filled with the un-flocculated feed and flocculant was

injected using a syringe. The flocculant was a high molecular weight, non ionic polymer. The volume and concentration of polymer were calculated to provide an equivalent gram per tonne dosage as applied operationally. A dose of 600 g tonne^{-1} was used. The measuring cylinder was capped, and inverted several times to flocculate. The number of inversions was varied until the settling rate equalled the average settling rate of the samples collected from the feed-well. The inversion method was repeated a number of times until reproducible flocculation was achieved.

Table 6-1 Solid Fraction Results (w/w)

	Sample 1	Sample 2	Sample 3
Feed solids concentration (prior to feed-well)	0.0318	0.0380	---
Feed concentration in feed-well	0.0362	0.0317	0.0255
Underflow Solid concentration	0.167	0.172	---
Dissolved solids in overflow	<0.001	<0.001	<0.001

6.2.3 Couette Modification

The effect of shear/raking on the settling behaviour of the flocculated sample was measured using the controlled shear Couette device. In this work a slightly smaller Couette was used in comparison to the device described in Chapter 5. The new dimensions, shown in Table 6-2, were chosen to reduce the volume of the device, and therefore the volume of sample required. The sheared experiments follow the same procedure described in section 5.4.2. The height of the suspension-supernatant interface was measured for two hours. In total, nine different shear rates were investigated, (see Table 6-3 for details). Batch settling

tests in each of the Couette devices resulted in the same $h(t)$ as measured in 1 L measuring cylinder, in the absence of shear. Therefore, it is unlikely that wall effects in the smaller geometry will influence the results. The $h(t)$ data was analysed according to section 2.4.1, and $P_y(\phi)$ and $R(\phi)$ were determined as functions of shear rate. The Newtonian shear rate distribution is shown in Figure 6-1. By assuming τ_y of 20 Pa, and average solid volume fraction of 0.08 (v/v), the non Newtonian shear rate distribution was determined as previously described in Chapter 5. The Herschel-Bulkley model parameters used were $n = 0.5$ and $m = 0.927$. The resulting shear rate distribution is presented in Figure 6-2.

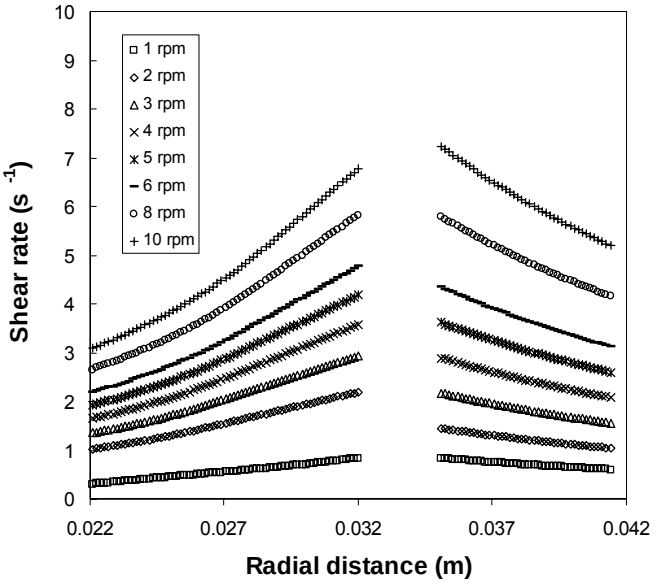

Figure 6-1 Shear rate distribution in outer gap and inner gap for a Newtonian fluid

Table 6-2 Couette shear cell dimensions

Radius (mm)		δ (mm)	R_i / R_o	Annular area (m^2)
R_1	22	7	0.7586	1.69×10^{-2}
R_2	29			
R_3	35	6.5	0.8433	1.56×10^{-2}
R_4	41.5			

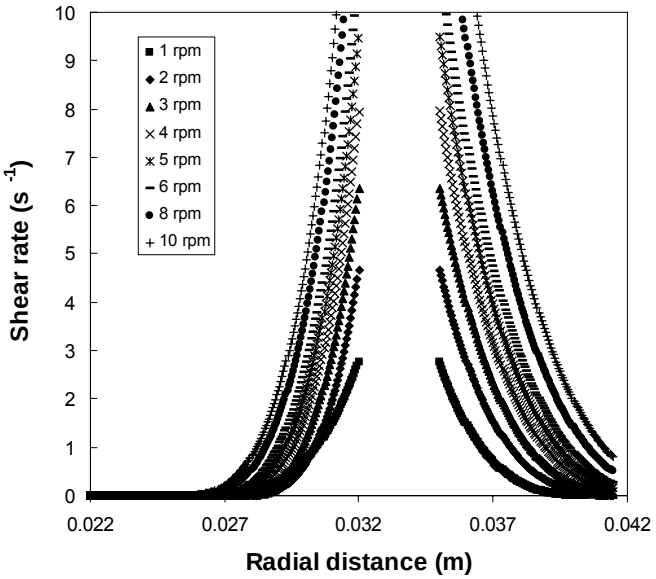

Figure 6-2 Shear rate distribution in outer gap and inner gap for a Herschel-Bulkley fluid (n = 0.5, m = 0.927, τ_y = 20 Pa)

6.3 Results and Discussion

Figure 6-3 shows the results of batch sedimentation tests performed on the flocculated feed and the effect of shear on the short (free settling) and longer (1-2 hours) sedimentation process. The settling rate of the flocs in Figure 6-3 (1.88 ±

0.3 m h $^{-1}$), was close to the average settling rate in the feed-well, although as already noted, there was a wide variation observed in the operational feedwell. The results of the settling tests show fairly conclusively the effect of shear rate on dewatering. Like calcite in Chapter 5, the final bed height progressively decreased as the shear rate increased. A minimum bed height of 5.2 cm was reached when a shear rate of 13.78 s $^{-1}$ was applied, almost three times lower than the final height when no shear was applied (13.2 cm). However, further increasing the shear rate from 13.78 to 16.51 s $^{-1}$ caused the final height to rise from 5.2 to 6.2 cm. At this shear rate the settling rate is noticabely slower suggesting that at a shear rate of 16.51 s $^{-1}$ other factors including the onset of flow instability and possible floc breakup are interfering with settling. Although the optimum shear rate of 13.78 s $^{-1}$ was more than twice the optimum shear rate determined for calcite in Chapter 5, the value is still a low value relative to shear rates tpically associated with floc formation (often >100 s^{-1}).

Table 6-3 Rotation rates and shear rates in Couette shear device

Rotation Rate	Maximum shear rate (s^{-1})	Average shear rate (s^{-1})
1 rpm	2.75	0.58
2 rpm	4.66	1.17
3 rpm	6.36	1.77
4 rpm	7.96	2.36
5 rpm	9.48	2.96
6 rpm	10.85	3.56
8 rpm	13.78	4.75
10 rpm	16.51	5.95

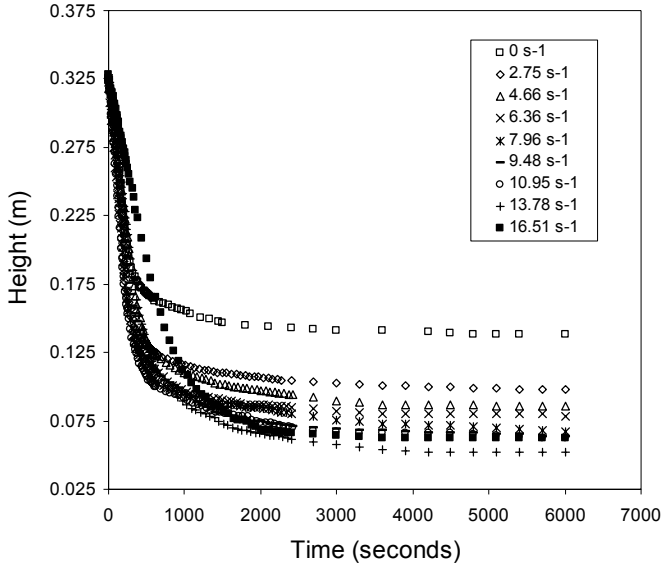

Figure 6-3 Batch settling curves in the Couette shear cell for thickener feed flocculated with 600 g tonne^{-1} flocculant as a function of shear rate

6.3.1 Flocculant optimization

Figure 6-4 shows the final equilibrium height as a function of shear rate. The solid concentration in the bed is clearly a maximum at a shear rate of ~ 14 s^{-1}. This result can be applied in two possible ways. The first is to adjust the shear rate inside the thickener so that it corresponds to the optimum shear rate identified in the experiment. In theory, the shear rate could be adjusted in several ways including varying the rotational speed of the rake, or modifying the type, height, or pitch of the rake blade. However, this approach is not always practical, especially for operational thickeners. The high torque motors driving the rake are usually quite limited in their speed and torque range. Modifying the rake design is equally unfeasible, without a back up thickener, since stopping production to empty the thickener and install a new rake is a costly and time consuming exercise. The second possible application could be to change the optimum or

critical shear rate so that is corresponds to the shear rate in the thickener. This could be achieved by tailoring the chemistry or physical properties of the polymer. This requires some research and design on the part of the flocculant suppliers although this information is already known to some extent.

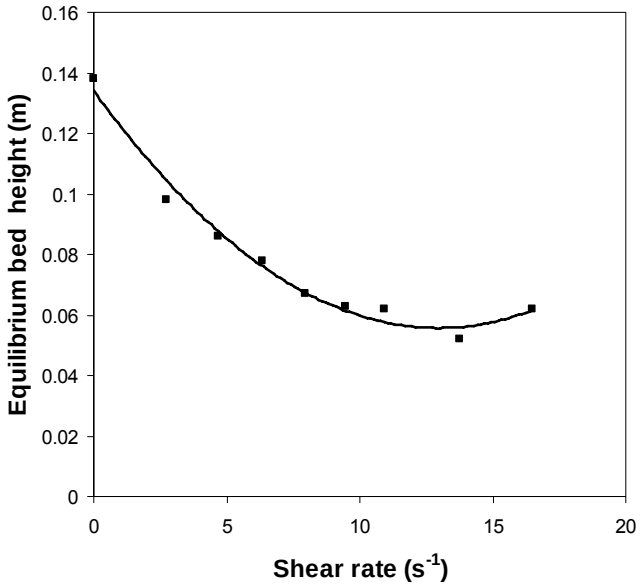

Figure 6-4 Equilibrium bed height as a function of shear rate in Couette shear cell

Figure 6-5 and Figure 6-6 show $R(\phi)$ and $P_y(\phi)$ respectively as a function of shear rate. Like calcite, the shear rate has a significant effect on both $P_y(\phi)$ and $R(\phi)$. The gel point for the un-sheared sample was approximately 0.026 (v/v) (or 0.066 w/w). When shear was applied, the gel point shifted to progressively higher concentrations until at the optimum shear rate the gel point was 0.08 (v/v), nearly four times higher than if no shear was applied. The increased gel point signifies that the aggregates have compacted under shear, such that network formation is initiated at a higher concentration. Increasing the shear rate

beyond the optimum caused the gel point to decrease. This is likely to be either an artefact of the flow structures interfering with the sedimentation and consolidation process or break up of flocs. It has been established in shear rheology that an inverse relationship exists between yield stress and particle size [171] so that floc break-up is expected to result in a decrease in the gel point. Figure 6-7 replots the data of Figure 6-5 as a function of shear rate. For ϕ less than 0.03, $R(\phi)$ was independent of shear rate, up to the critical shear rate of 14 s^{-1}, while for ϕ above 0.03, increasing the shear rate to approximately 14 s^{-1} caused $R(\phi)$ to decrease. Above 14 s^{-1}, $R(\phi)$ began to increase for all volume fractions. Thus, the critical shear rate not only indicates the extent of dewatering, it also determines the rate at which dewatering occurs.

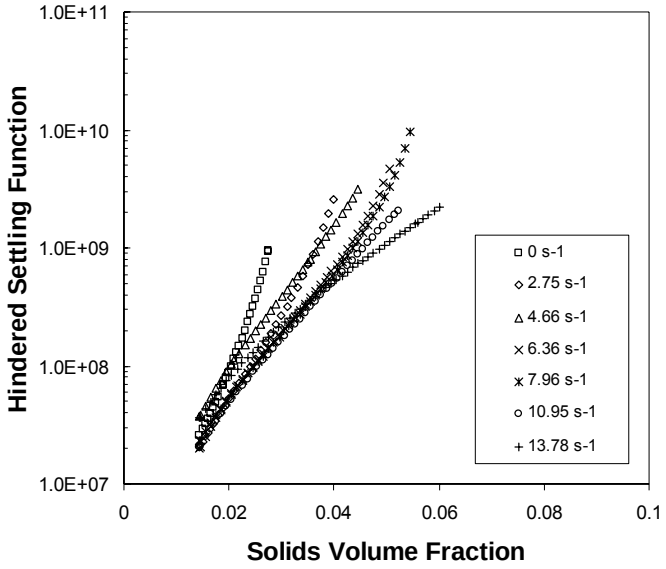

Figure 6-5 Hindered settling function for thickener feed flocculated with 600 g $tonne^{-1}$ flocculant at various shear rates

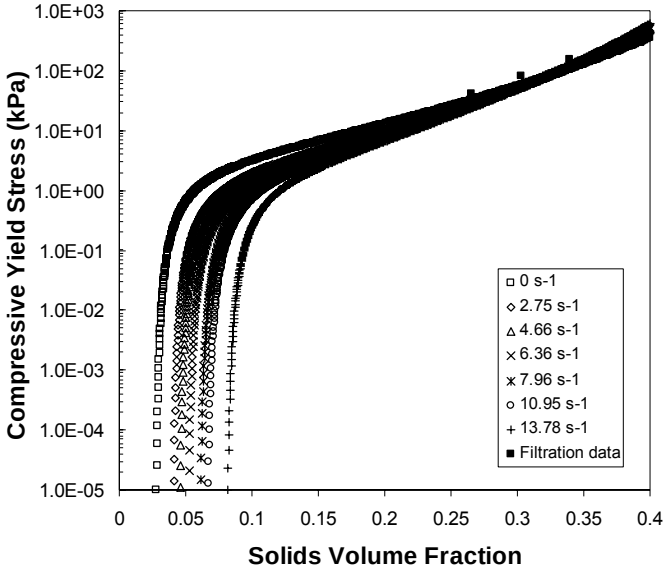

Figure 6-6 Compressive yield stress for thickener feed flocculated with 600 g tonne^{-1} flocculant at various shear rates

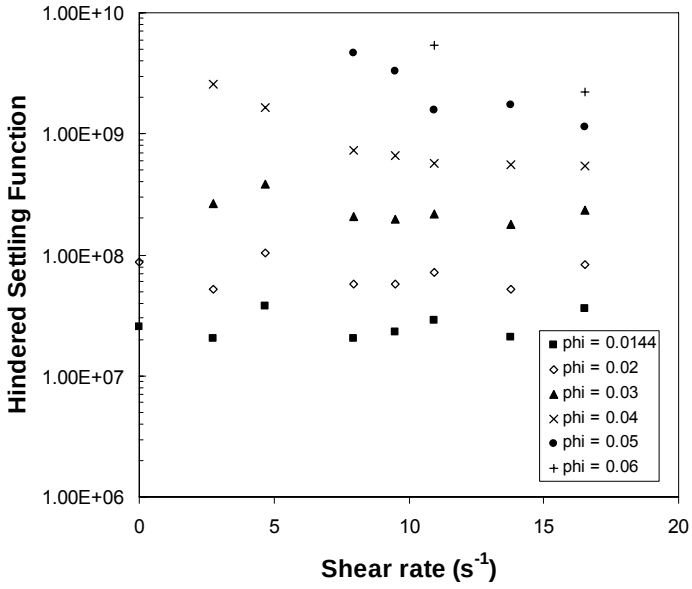

Figure 6-7 Hindered settling function versus $\dot{\gamma}$ for different volume fractions

Figure 6-8 shows the predicted flux from the pseudo 1−D model as a function of underflow solids concentration using the data of Figure 6-5 and Figure 6-6 as model inputs. Based on an average value of the solids throughput and the thickener cross sectional area (see Table 6-4), the operating point for the thickener was calculated. Given that the thickener had a volumetric feed throughput of 2250 $m^3\ hr^{-1}$, a diameter of 13.5 m, height of 6 m and flocculant dose rate of 600 g $tonne^{-1}$, equating the volumetric flow rate to the feed solids concentration gives a solids throughput of between 71 and 85 tonne hr^{-1} or an average solids throughput of 0.2 tonne $hr^{-1}\ m^{-2}$. The data is shown in Figure 6-8. Examining the model output for the data characterised in the absence of shear, the predicted flux of 0.0015 tonne $h^{-1}\ m^{-2}$ was more than 100 times lower than the actual operating flux of 0.2 tonne $h^{-1}\ m^{-2}$. However, when shear was applied to the settling suspension in the Couette device, the predicted flux increased by a factor of 10 at the measured underflow solids concentration.

Thus, the error was reduced to a factor of ten. This result may still appear a poor correlation. However, this result reflects the current state of the art and is consistent with other results reported by workers from the same research group [155]. Data collected over a several year period from numerous operating sites reveals that the model under-estimates the actual throughput anywhere from 1 (good correlation) to 100 times. (see Figure 1-3).

Table 6-4 Physical properties of the thickener

Thickener volumetric throughput ($m^3\ h^{-1}$)	2250
Thickener diameter (m)	13.5
Height (m)	6
Flocculant dosage	600 g $tonne^{-1}$

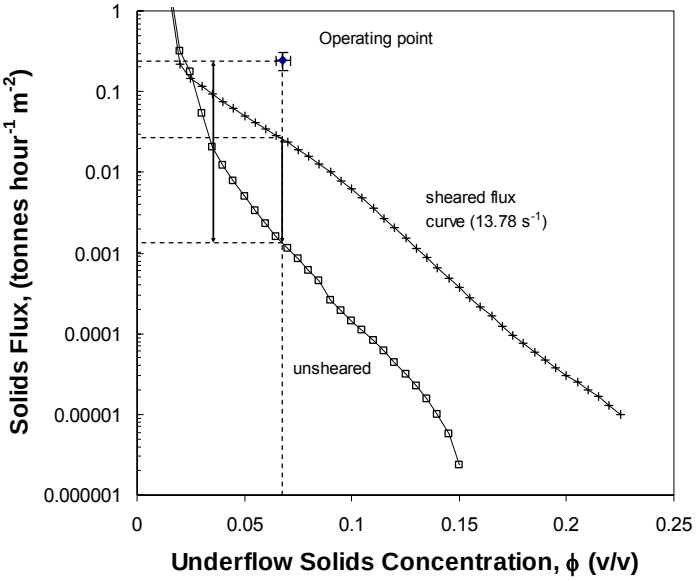

Figure 6-8 Solids flux versus underflow solid prediction showing the thickener operating point

The fact that the mode correlates well for selected cases suggests that it is unlikely that the model is the root cause of the discrepancy, but rather the inputs to the model. The data of Figure 6-8 shows that when taking shear effects in the thickener into account, the model approaches the operational point; however, a more rigorous examination of the deficiencies of the model is still required. A simple comparison between the clay system examined herein and calcite (in Chapter 5) suggests that the effect is greater for clay than for calcite (refer to Figure 6-9) so that the effect of shear on dewatering is not universal This might be expected since effects such as over-flocculation are known to result in more robust flocs.

Several explanations can be given to account for the observed difference between the 1−D model prediction and the thickener operating point. As pointed out in Chapter 4, it is possible that the 1−D model is simply incapable of predicting the

bulk flow phenomena typical of large-scale thickening device. However, multidimensional analysis has revealed that a maximum solids flux exists and approaches the 1−D prediction [97]. Therefore, by accounting for multidimensional behaviour including recirculatory flow and stress anisotropy, the error between the model prediction and plant data can only increase relative to the 1−D case.

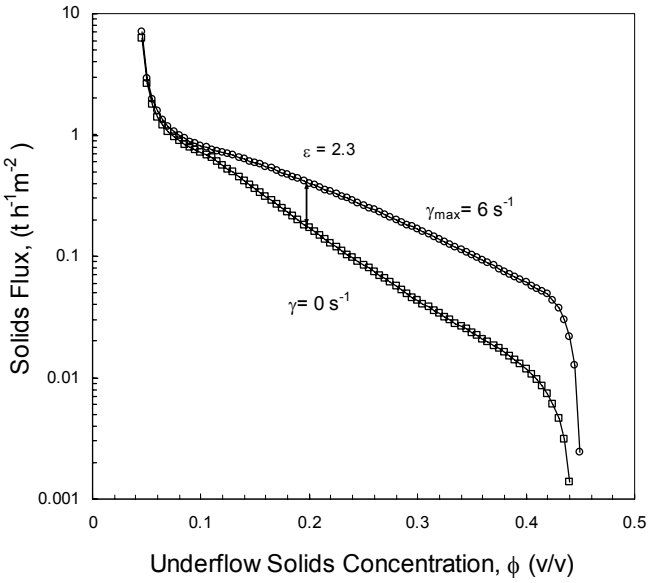

Figure 6-9 Change in model predicted flux for calcite in tall column sheared at 0 and 6 s^{-1}

A major limitation to interpreting the effect of shear in full-scale thickening is the inability to properly define shear rate. The range of shear rates explored in the laboratory was selected based on those typically encountered in conventional raked thickeners. However, because no CFD modelling of this particular thickener had been undertaken, it is possible that shear inside the thickener was significantly higher in certain zones than the shear applied in laboratory. The

shear rate depends on the angular velocity of the rake, and thus increases proportionally with radial distance. Material near the wall will be subjected to much higher shear rates compared to material near the centre of the thickener. Because of the disparity in shear rate, dewatering may be improved in one area and impaired in another. To further complicate matters, material does not consolidate in a fixed lateral position; instead, material at the bottom of the thickener is transported radially inward through raking (on average). Thus, to solve this problem, the shear rate distribution must be known, as well as the spatial variation of particles as a function of time. Shear anisotropy is less of a problem in the tall column, introduced in Chapter 4. Because the shear can be accurately defined and also varied if necessary, continuous dewatering in the pilot scale column is considered as an alternative. This will form the basis for the experiments appearing in Chapter 7.

Another issue is that as the solids settle and consolidate, the shear yield stress in the sediment could exceed the shear stress in the gap and consequently part of the sediment will not experience shear. The outcome may be a lower equilibrium solids volume fraction than would have been attained otherwise, affecting both gel point and compressive yield stress measurement. A possible solution is to ramp the shear rate. Although the results indicate that shear rates above 12-14 s^{-1} adversely affect sedimentation, once the sedimentation zone disappears, this may no longer apply, because the bed can sustain higher shear. Therefore, during settling a shear rate of 12-14 s^{-1} might be applied, and during consolidation the shear rate could be increased further and improvement monitored. Densification studies in other types of flocculated systems have reported success using this approach [103].

The shear strength and subsequent deformation properties of sediments are governed by the magnitude of effective stress, and also by the past shear stress

history [38]. Failure requires that either the normal or shear stress exceeds a critical value. Shear enhancement therefore represents a complicated relationship between shear and normal stress. Thus, it is possible that the response in dewatering due to shear depends on the magnitude of the normal stress in addition to the shear stress. In the laboratory, shear was applied under effective normal stresses of no more than a few Pascals. In contrast, vertical stresses in thickeners can exceed 1 kPa. In effective stress terms, 300 Pa is typical for laboratory settling, while in a thickener stresses 5 kPa or above are typical. Even if the shear rate in the laboratory was identical to the thickener, the shear is necessarily applied under a much lower relative normal stresses, and thus, different dewatering behaviour could result.

Despite the array of proposed explanations accounting for the observed difference between the 1−D model and the thickener underflow solids concentration, the maximum predicted operational point is still significantly less than reality. Careful analysis of the experimental arrangement suggests that the characterisation method for measuring the hindered settling function and compressive yield stress may not be representative of continuous dewatering in thickener devices, even with the application of shear.

When considering the time evolution of the shear modified hindered settling and compressive yield stress data, it is clear that using batch sedimentation methodology is not appropriate. If the h vs. t data contained in Figure 6-3 is transposed to h vs. ϕ, the time of shear for solids at concentrations less than the gel point is very short, of order seconds. The time evolution of shear at the equivalent concentration in a thickener at steady state is likely to be of order tens of minutes to hours. This idea forms the basis for the experimental studies reported in Chapter 8.

It is interesting to question whether the thickener operating point could have been determined empirically by simply assuming that the escape of water was not limited by the suspension permeability. If that were the case, the maximum solids would be instead dictated by the operational torque capability of the rake, which in this example restricted the underflow solids concentration to a shear yield stress less than 10 Pa. This value represents a solids concentration only marginally greater than the maximum predicted gel point. Without shear, the gel point was found to equal 0.066 w/w, but when an optimum shear rate was applied, the gel point increased to 0.187 w/w. Interestingly, the observed underflow solids was 0.169 ± 0.003 w/w indicating that while the Couette shear device may have failed to quantify the rate effects associated with shear dewatering, the compressional and floc densification effects were adequately captured.

6.4 Conclusions

The operation of a full scale thickener has been simulated using a one dimensional thickener model. A large discrepancy between the model output and the operational point of the thickener was observed. The difference was partially accounted for through the incorporation of the effect of shear into the consolidation and settling behavior of the flocculated feed to the thickener. This result suggests that shear is important; by accounting for shear effects the observed difference between the model prediction and plant data was halved.

The work indicates that further experimental development is required, particularly in relation to understanding the time evolution of the effect of shear on flocculated suspension dewatering. The development of these methodologies is seen as critical to providing improvements in the performance of thickening devices. These areas are explored in the Chapter 7 and Chapter 8.

Chapter 7

Operation of a continuos pilot thickening column with shear

7.1 Introduction

The aim of this work is to gain a better understanding of the effect of shear and compression on thickening. The pilot scale tall column (introduced in Chapter 4) was used to continuously dewater flocculated calcite under controlled flocculation conditions. Material is sheared at a known rate by rotating a series of concentric cylinders so that the column essentially behaves like a large scale Couette device. The Couette geometry was chosen over a more traditional rake for the same reasons as in Chapter 5; i.e. shear is more easily quantified in Couette flow. The shear rate can be easily modified by varying the cylinder rotation rate. Thus, dewatering at several different shear rates can be compared with the 1−D model predictions for the same corresponding shear rates. The ability to quantify and control the shear in the column represents a significant advantage over full scale studies. The plant data presented in the previous chapter could not be compared to the model since the shear rate in the thickener was unknown.

Some of the key questions this chapter aims to address include;

- What is the effect of varying shear rate on the underflow solids concentration at a constant feed flux and bed height?

- Does the effect of shear depend on bed height?
- Can the one-dimensional model predict dewatering when the system is sheared?

7.2 Shear in a compressing bed

Most of the continuous thickening studies described in Chapter 4 utilised a raking device. Raking has been found to significantly improve dewaterability in thickening [33, 46, 77]. Johnson et al [77], examined the relationship between dewatering, shear and polymer dose by operating a 6.0-metre thickening column. By slowly raking alum sludges at a speed of 1 rpm, a significant increase in underflow concentration was observed. After ten hours operation, the underflow concentration increased from 3.5 to 10%, while after 60 hours, the concentration increased further to 17%.

Comings reported similar results when calcite was slowly raked [33]. The concentration profile (Figure 7-1) shows that in the region of the rake, the concentration rose rapidly from 270 $g\,L^{-1}$ to any where between 340 and 500 $g\,L^{-1}$ depending on the residence time. The increase was higher for longer residence times, with the bed height constant.

This present study differs from those mentioned above in two important ways;

- the effect of varying shear rate on column dewatering is considered
- the effect of bed height at different shear rates is considered

It is emphasised that the column is operated at a solids flux where dewatering is expected to be permeability limited. Consequently, the underflow solid volume fraction is not expected to change if the bed height is increased.

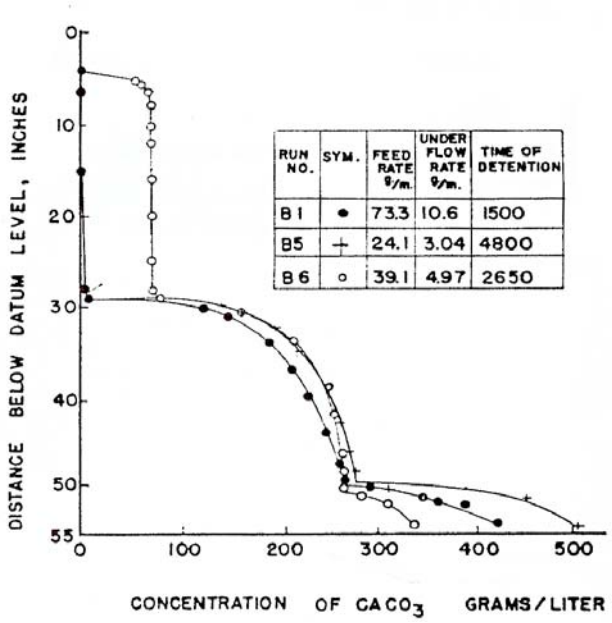

Figure 7-1 Continuous thickening results for calcium carbonate at a constant compression zone height 0.9 m; feed concentration = 0.017 v/v. reproduced from [33]

7.3 Experimental

The tall column was operated at a solid flux of 0.3 tonne m^{-2} h^{-1} so that dewatering is expected to be limited by the permeability. Three bed heights were investigated; one, two and four metres. The column was operated continuously until steady state was attained. Then, steady shear was introduced by rotating the concentric cylinders at a fixed speed. For the one-metre bed, three rotation rates were considered; 1, 10 and 20 rpm. For the higher bed heights only zero and 10 rpm were considered. The shear rates in the column corresponding to the above rotation rates are approximated in Table 7-1. The nominal shear rate is estimated using;

$$\dot{\gamma} \approx \frac{v_{R_0} - v_{R_i}}{R_0 - R_i} \tag{7.1}$$

7.3.1 Materials

The material and flocculant were the same as described in Chapter 4. Flocculant solutions were prepared at 5 g L^{-1}, according to the procedure outlined in section 3.4. Fresh working solutions (0.2 g L^{-1}) of polymer were prepared every 24 hours and excess solution discarded.

7.3.2 Column modifications

The tall column, described in Chapter 4 was modified to allow continuous, operation for extended periods under shear. Longer operating times were deemed necessary to allow steady state to be established. The modifications included;

- extending the column height from 2 to 5 metres, to enable the investigation of higher beds than in Chapter 4
- designing and installing a series of concentric cylinders to provide shear. The cylinders were 100 cm in height and positioned at a distance 40 cm above the cone apex
- installing a scraper blade in the cone section to prevent material accumulating on the surface and prevent the possible formation of rat holes

Figure 7-2 shows the column from above and includes the cylinder dimensions, while Figure 7-3 shows the front elevation. The outer cylinder was rotated by attaching it to a stainless steel shaft which was driven by an overhead-geared

motor, see Figure 7-4. The motor output corresponded to rotation rates ranging between 0 and 20 rpm. To produce Couette flow, the inner cylinder had to be kept stationary. This was achieved by attaching the inner cylinder to a stainless steel outer sheath, which fitted over the shaft. The vertical position of the cylinders could be adjusted by loosening two grub screws, which attached the cylinders to the shaft/sheath, see Figure 7-4. Therefore, any region could be sheared.

The scraper was driven by a high torque motor gearbox mounted underneath the cone. The maximum scraper speed was approximately one rpm. Because of the scraper, the underflow take off point was no longer centrally located, instead being shifted to one side of the cone. Furthermore, the scraper unavoidably sheared the material. Because it is difficult to de-convolute the effect of the scraper and the cylinders, the scraper was not used in the following experiments.

Table 7-1 Dimensions of concentric cylinders and nominal shear rate in tall column;

Radius (mm)		R_i/R_o	Rotation rate (rpm)	Shear rate (s^{-1})	Rotation rate (rpm)	Shear rate (s^{-1})	Rotation rate (rpm)	Shear rate (s^{-1})
R_1	9.5	0.4318	1	0.08	10	0.79	20	1.59
R_2	22							
R_3	25	0.4201	1	0.08	10	0.76	20	1.51
R_4	59.5							
R_5	62.5	0.4355	1	0.08	10	0.81	20	1.61
R_6	143.5							

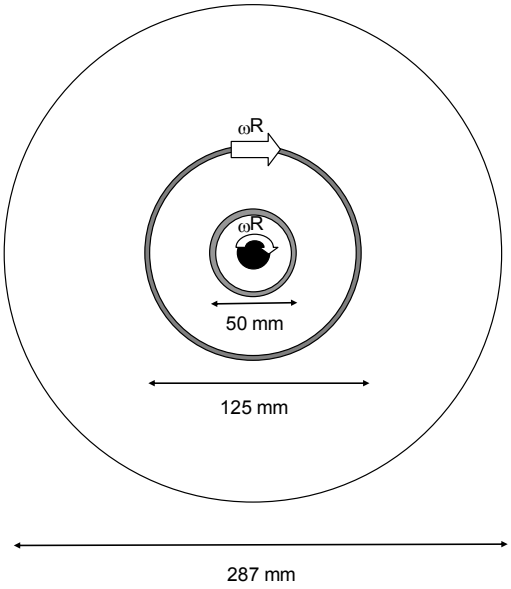

Figure 7-2 Cross-section of tall column with Couette type shear device

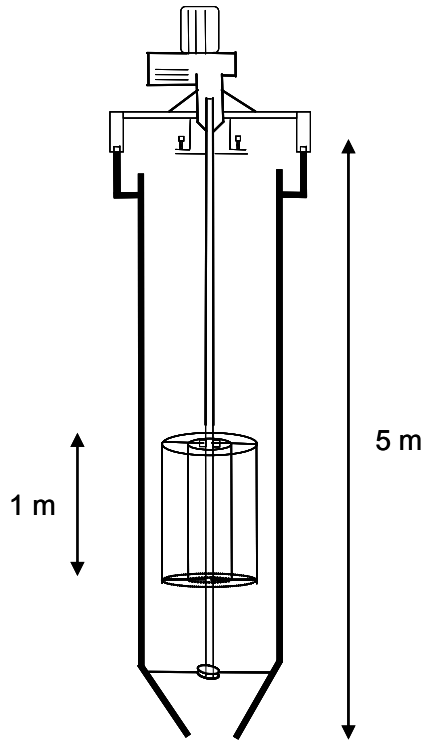

Figure 7-3 Tall pilot column with internal concentric cylinder shear device

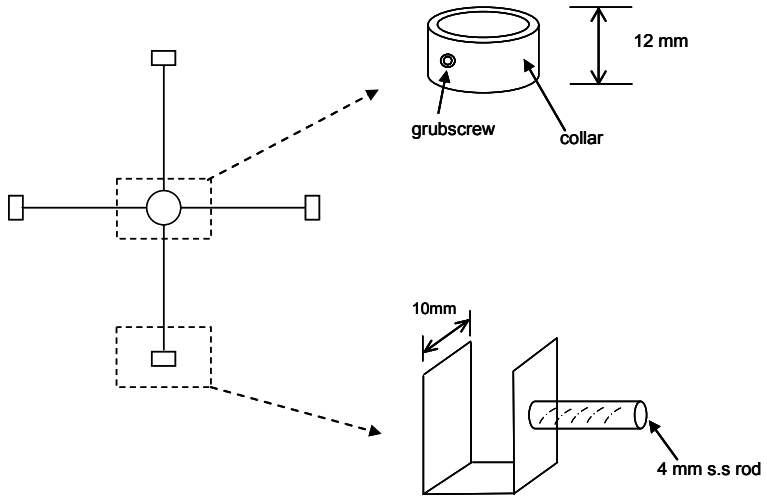

Figure 7-4 Shear device internals

7.3.3 Experimental method

Feed suspension was sampled from the pipe outlet and $h(t)$ measured in the Couette device for three shear rates: 0, 4.1 and 10.8 s^{-1}. The procedure was the same as outlined in section 5.4.2, while the Couette device was described previously in section 6.2.3. The shear rates include the optimum shear rate determined from earlier batch settling studies, while an intermediate shear rate was also considered.

The tall column and ancillary equipment is shown schematically in Figure 7-5. Concentrated calcite suspension was prepared at 40 % w/w using local tap water. An approximate volume of 3.5 m^3 of suspension was prepared by adding 1845 kg of calcite to 2.77 m^3 of water. An overhead stirrer mixed the suspension for twenty-four hours prior to use. When the tank level dropped below fifty percent,

calcite and water were added in the same ratio to restore the tank level back to full capacity.

The concentrated slurry was blended with tap water to produce a 10% w/w suspension. The desired solids flux of 0.3 tonne m^{-2} h^{-1} corresponded to a volumetric flow of 3.0 L min^{-1}. The feed was flocculated in a linear pipe reactor similar to Chapter 4, with a diameter of 12.5 mm and length of 1.8 metres. The flocculant was dosed at 40 g $tonne^{-1}$ corresponding to a polymer flow rate of 64.8 mL min^{-1} Each of the flocculant, dilution water and slurry flows were regulated using PID feedback control, as shown in Figure 7-6.

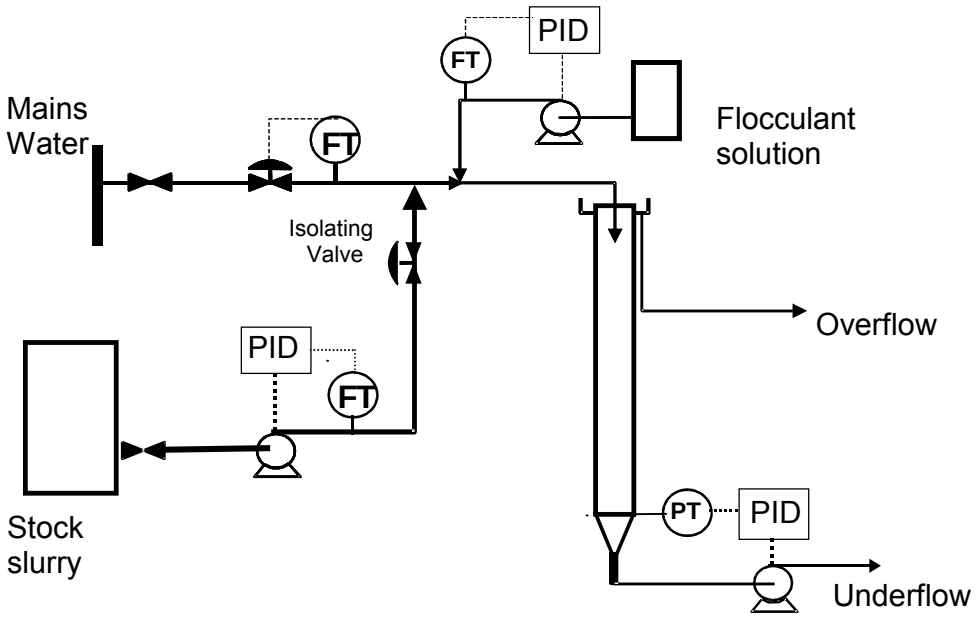

Figure 7-5 Upgraded flow circuit incorporating feed back control and online density measurements. Fc and Pc are flow and pressure controllers respectively

The flocculated calcite was fed to the column approximately 0.5 metres from the top. After operating for several minutes, three zones became apparent; a

clarification zone, a hindered settling zone and bed zone. The bed gradually increased in height as solids accumulated. Consistent with Chapter 4, the bed is defined as the interface between settling zone and consolidation zones (see Figure 4-2). The bed height can be easily detected by eye as a well defined interface between free (hindered) settling flocs and bed which consolidated as a whole.

The pressure was measured via a pressure transducer mounted on the conical base. When the bed reached the desired height, the pressure was recorded, with this value to be used as the set point for the pressure control loop. The control involved a feedback signal from the transducer to a variable frequency motor drive with onboard PID control. The pressure was constantly monitored and any deviation was corrected by manipulating the underflow pump speed.

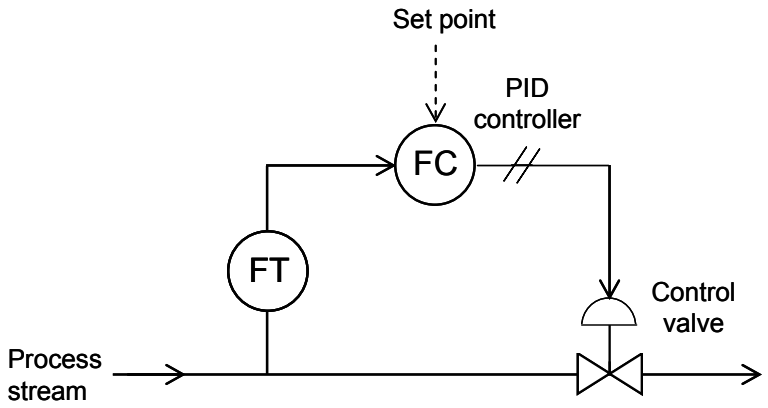

Figure 7-6 Flow control system

Online density meters recorded the mass flow of solid entering and exiting the column. Flow rates, densities, temperatures and pressure were logged so that the cause of any perturbation or disturbance could be traced. A digital video camera was used to monitor the bed height.

In the one-metre experiment, the bed was relatively constant at 1.0 ± 0.2 metres. After approximately 19 hours, steady-state was assumed and samples were collected (~20 mL) from several heights in the bed, at a vertical spacing of 20 cm. For each sample, the solid concentration was determined by drying overnight. After sampling was complete, the concentric cylinders were rotated at a speed of 1 rpm. The column was operated until steady state was re-established. The bed sampling was repeated and then the rotation rate was increased further to 10 rpm. In total, three rotation rates were investigated for the one-metre bed, while for the higher beds, only two rotation rates were considered.

7.4 Results and Discussion

7.4.1 Pilot column runs

Figure 7-7 shows the change in flow-rates when the column was operated at a solids flux of 0.3 tonne m^{-2} h^{-1} and one metre bed. Both flocculant and slurry flow rates were effectively constant for the duration of the run, implying that the control scheme was successful. The water flow rate did drift slightly; this was probably due to slight variations in the mains water pressure. The change was gradual and represented less than 4% of the total flow.

Because the underflow pump was manipulated to control the bed height, the underflow flow rate varied for the duration of the run. The flow tended to oscillate because of the integral component of the PID control. Complete damping of the oscillation was difficult because of the high gain, necessary to compensate for the slow dynamics. In the first 20 hours, the average underflow rate increased from 700 mL min^{-1} to approximately 1400 mL min^{-1}. This reflects that the underflow solid density was decreasing as the system adjusted from transient to steady state. To maintain a constant solid mass, the underflow pump

had to withdraw a greater volumetric rate compensating for the lower underflow density.

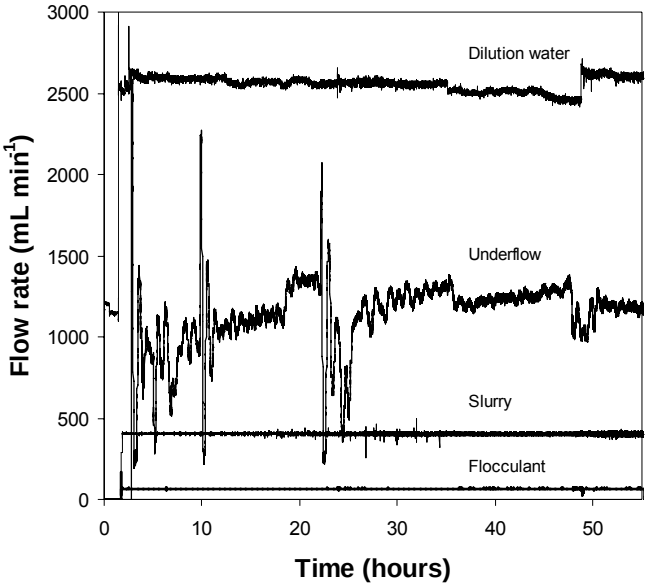

Figure 7-7 Variation of flow rates of controlled variables for 0.3 tonne m^{-2} h^{-1} run at 1m bed

Figure 7-8 shows the variation in pressure when the column was operated at one, two and four metre bed heights. As expected, an increased bed height corresponded to an increase in column pressure. For a one metre bed height, the pressure was 52.8 kPa; for two metres, 54.6 kPa; while for four metres, the pressure was 58 kPa. Like flow rates, the PID control of column pressure was effective. This was important in order to maintain a constant bed height.

Figure 7-9 shows the feed and underflow (UF) densities for two bed heights; one and four metres. The results for a two-metre showed identical trends and have been omitted for the sake of clarity. For each run, the feed density was constant and equal to 1080 kg m^{-3}. Upon filling the column to one metre, the UF density

was initially 1265 kg m^{-3}. Upon filling to four metres, the UF density was 1390 kg m^{-3}. The higher underflow density is due partly to the higher compressive load and partly to the longer residence time. The residence times and bed volumes for each height are shown in Table 7-2.

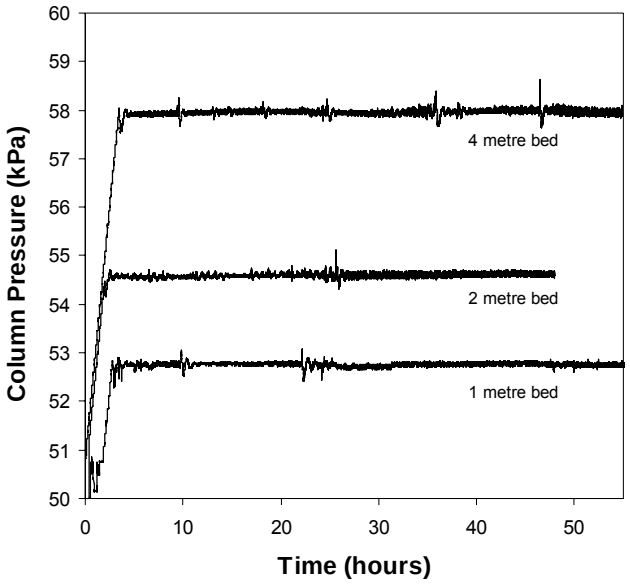

Figure 7-8 Variation in column pressure for 1, 2 and 4 m high beds

Table 7-2 Volume and residence time for different bed heights

Bed Height (m)	0.5	1	2	4
Volume of Bed (L)	23.5	55.8	120.5	249.9
Residence time (mins)	20	50	155	420

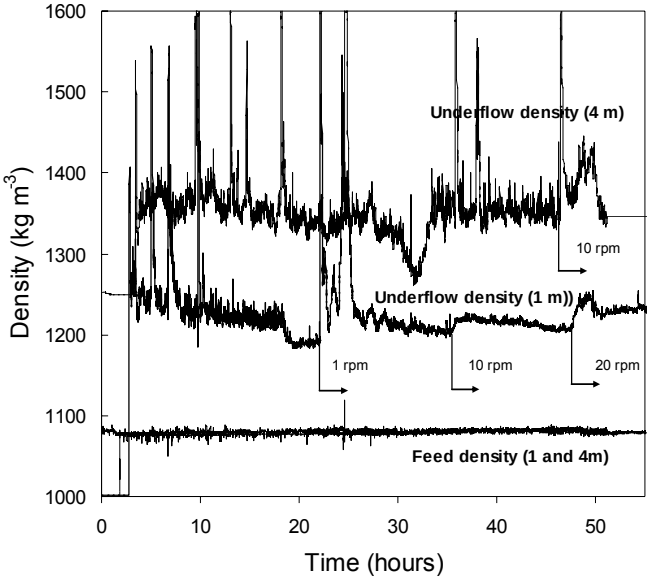

Figure 7-9 Variation in feed and underflow density for 1 m and 4 m bed runs

The underflow density tended to be more unsteady than the other measured variables; as Figure 7-9 shows, a number of concentration spikes are present. These spikes were a feature of all the tall column runs and occurred more frequently in the early stages of the run (< 20 hours) and were also more prevalent at higher bed heights. One explanation for the spikes is that solids are caking (adhering to the cone section) where they consolidate for relatively longer periods. Intermittently, this material becomes dislodged causing the observed spikes. Caking is more likely to occur for solids with appreciable yield stress, which increases with solids concentration, which in turn increases with bed height. Scraping the cone was not an option because of the additional shear this would introduce. Even though the concentration spikes are undesirable, it should be pointed out that when steady state was declared, the underflow solids concentration varied by less than 3% for the 4 m run (and even less for the 1 m

bed). This variability is significantly less than expected typically in even the most well behaved thickeners.

For the one metre bed, it took approximately 19 hours to reach a steady underflow (UF) density of 1190 kg m^{-3} (0.12 v/v). When shear was introduced by rotating the cylinders at a rate of 1 rpm, the UF density became unsteady. Eventually the oscillations stabilised at 1205 kg m^{-3} or 0.13 v/v. Increasing the rotation rate to 10 rpm, caused the UF density to increase to 1215 kg m^{-3} (0.135 v/v), while further increasing the rotation rate to 20 rpm caused the UF density to increase to 1230 kg m^{-3} or 0.145 (v/v).

For a four metre bed, steady state took considerably longer, approximately 31 hours, to develop. Upon filling, the UF density was 1390 kg m^{-3}. Then for the next 12 hours the UF density continually decreased before suddenly rising to 1350 kg m^{-3} where it remained constant for ten hours. This result was unexpected. Based on the model, the column was permeability limited, in which case the UF density should have continued to decrease until reaching the same UF density as in the one metre run. Reasons for this outcome will be discussed later.

When shear was introduced by rotating the cylinders at 10 rpm, the UF density rose to 1430 kg m^{-3} where it remained for approximately 10 hours before suddenly falling to 1330 kg m^{-3}, a value slightly less than the UF density without shear. The reason for the sudden decrease in UF density is not known for certain, although one possible explanation is that the gap had become partially clogged so that material bypassed the shearing zone. Clogging is considered more likely for the 4 m run, since the average solid concentration, developed during the transient fill stage, was greater at the higher bed height.

7.4.2 Shear Characterisation in the Laboratory

Figure 7-10 and Figure 7-11 show $P_y(\phi)$ and $R(\phi)$ of calcite determined from batch settling tests in the Couette at shear rates of 0 s^{-1} and 10.8 s^{-1}. Because $P_y(\phi)$ and $R(\phi)$ show the same trends discussed previously in Chapter 5 and Chapter 6, these results will not be commented upon here.

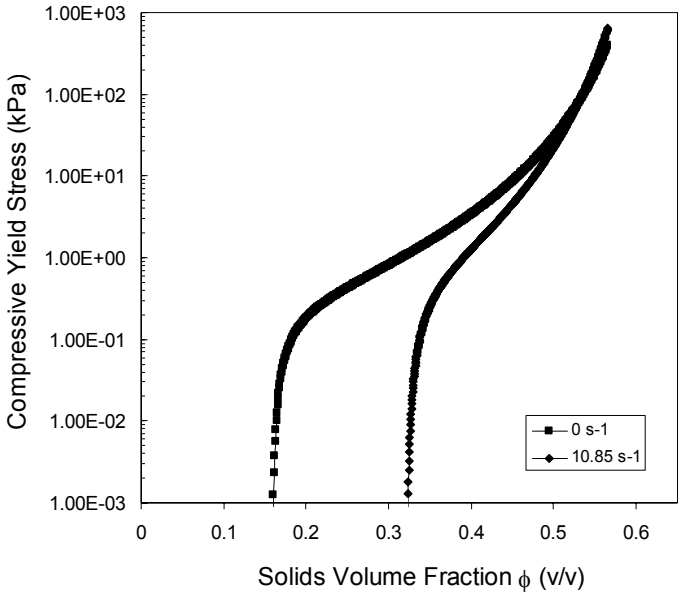

Figure 7-10 Compressive yield stress for tall column feed flocculated at 40 g $tonne^{-1}$ under influence of zero shear and 10.85 s^{-1}

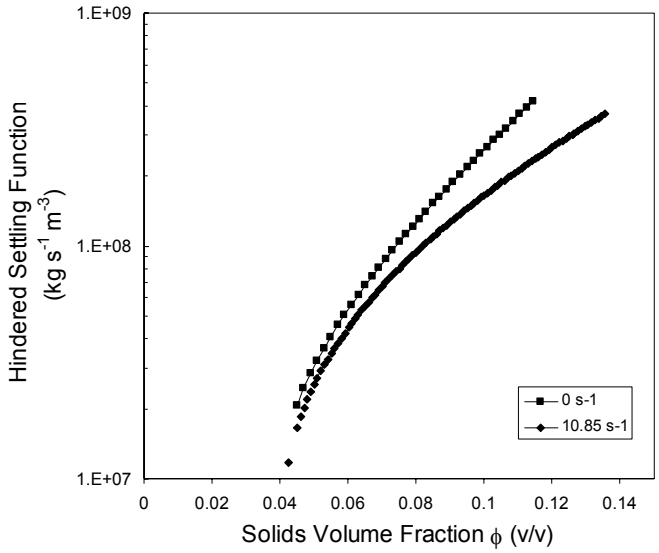

Figure 7-11 Hindered settling function for tall column feed flocculated at 40 g tonne^{-1} under influence of zero shear and 10.85 s^{-1}

7.4.3 1−D Modelling

7.4.3.1 Zero Shear

The compressive yield stress and hindered settling functions corresponding to no shear (Figure 7-10 and Figure 7-11) were input into the 1−D model which resulted in the solid flux curves in Figure 7-12. Because, the column was operated at 0.3 tonne m^{-2} h^{-1}, dewatering should depend solely on the permeability. Consequently, dewatering should be the same regardless of bed height.

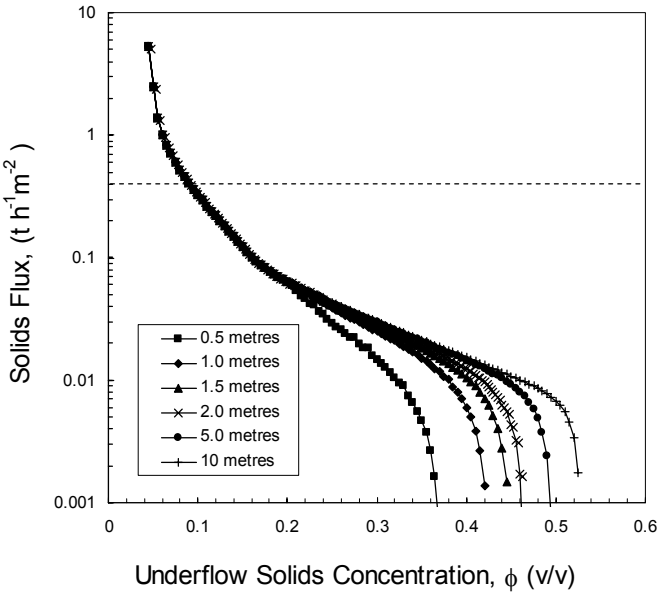

Figure 7-12 Thickener solid flux versus underflow for different bed heights (predicted from an un-sheared batch settling test characterisation) The dashed line shows the operating flux of 0.3 tonne m^{-2} h^{-1}

7.4.3.2 Optimum shear

When $P_y(\phi)$ and $R(\phi)$ corresponding to 10.8 s^{-1} (Figure 7-10 and Figure 7-11) were input into the 1−D model, the solids flux curve in Figure 7-13 was obtained. The predicted solid flux in the absence of shear has been shown for reference. The diamonds correspond to the sheared prediction; while the squares represent the un-sheared prediction. Both relate to a 1 metre bed. The effect of shear is to shift the predicted solids flux curves to higher underflow solid concentrations. For the flux in the column, the UF volume fraction is predicted to increase from 0.105 to 0.12 (v/v).

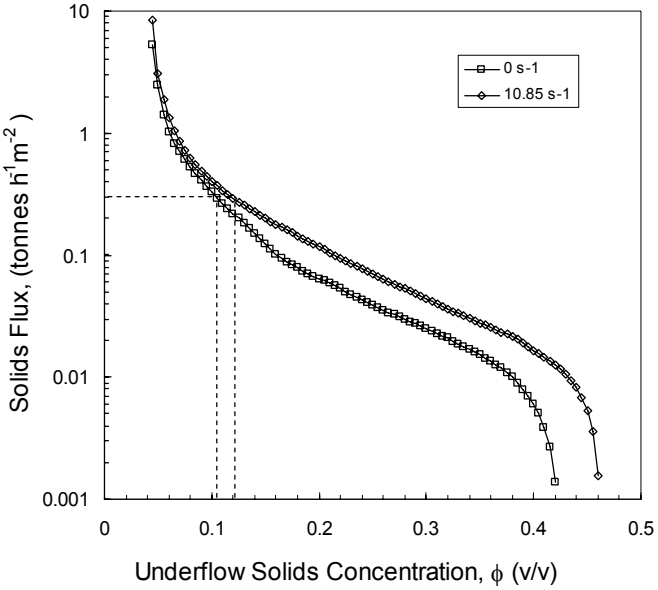

Figure 7-13 Predicted effect of shear on thickener solid flux versus underflow curves under influence of; □ zero shear and ◇ 10.85 s^{-1} for a 1 m bed height

The predicted solids flux curve for calcite, both when sheared at 10.8 s^{-1} and zero shear are reproduced in Figure 7-14. This time predictions for two bed heights are shown; 1 and 4 metres. This is done to reemphasise that for the solids flux in question, dewatering of flocculated calcite is independent of bed height. For comparison, Figure 7-14 shows the column data on the predicted solids flux plot. Clearly, the UF concentration did depend on bed height.

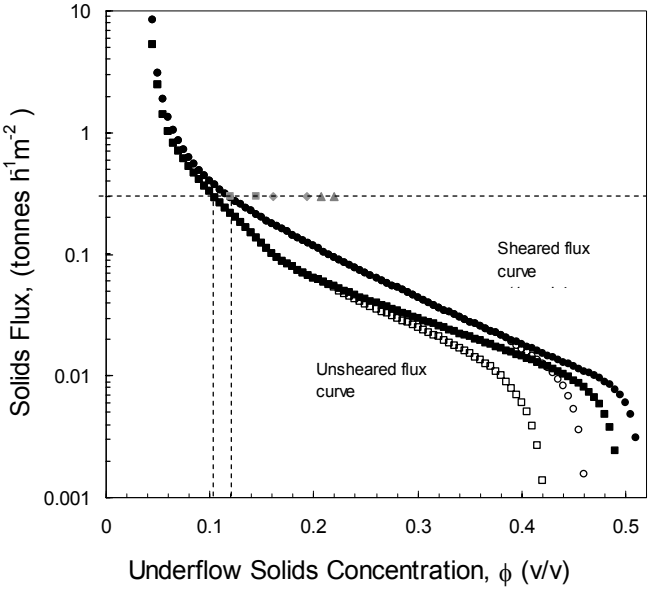

Figure 7-14 Predicted solids flux for; □ zero shear and 1 m bed; ■ 10.85 s^{-1} and 1 m bed; ○ zero shear and 4 m bed; ● 10.85 s^{-1} and 4 m bed. Also shown, experimental data for ■ 1, ◆ 2 and ● 4 m bed heights

Figure 7-15, plots the experimental UF data shown in Figure 7-14 against rotation speed for a 1 metre bed, while Figure 7-16 plots the UF solids concentration against bed height for 0 and 10 rpm. In Figure 7-15, the UF concentration increases monotonically with rotation rate, and asymptotes to a value of 0.16 v/v. Thus, it appears likely that shear rates above 1.6 s^{-1} will not cause further increase in ϕ_u . Figure 7-16 shows that the relationship between UF solids concentration and bed height is also non linear. For reference the model predictions for both zero and 10.85 s^{-1} shear rates are shown (as straight dashed lines). The figure clearly shows that when both bed height and rotation rate increase, the column output exceeds the 1−D prediction by increasing amounts. Thus, discrepancies between full scale modelling and plant data must involve both shear and bed height effects. The underflow solids concentration

for one metre of bed without shear was reasonably close to the model prediction. Similarly, the model and experimental results for the one-metre bed agree when the material was sheared. At higher beds the effect of shear was different. The increase in density due to shear was greatest at the smallest bed height. As the bed height increased, $\Delta\phi_u$ decreased, and at four metres, the two curves cross. Whether this result is true is questionable. It could be that at a 4 metre bed height, the solid concentration in the bed was sufficiently high that shearing had no additional effect. This assumes an upper ϕ limit exists with respect to shear, which is likely to depend on the material, flocculation conditions, and shear history. However, given that the UF density initially increased when sheared the explanation of clogging appears more likely.

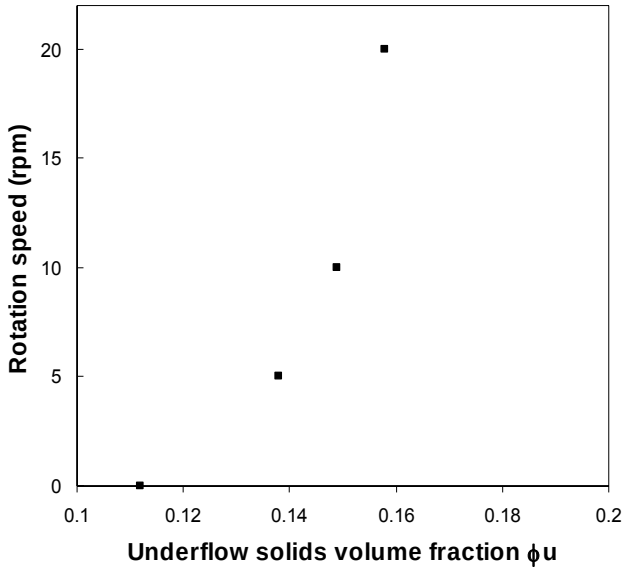

Figure 7-15 Rotation speed versus underflow solid volume fraction for a one metre bed height

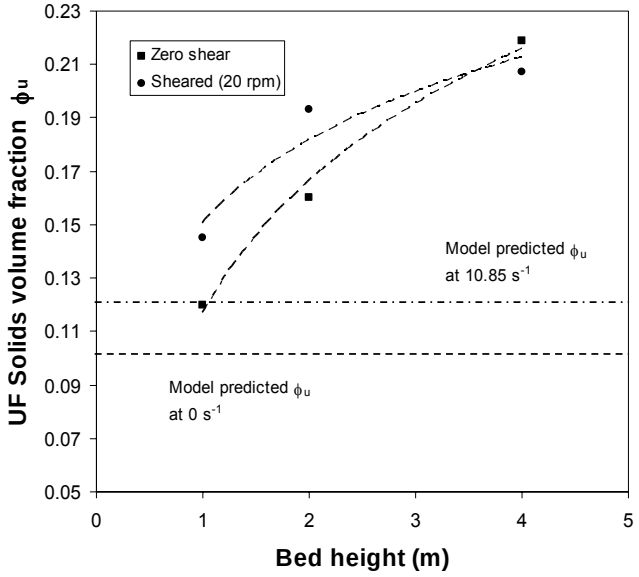

Figure 7-16 Steady state underflow solid concentration as a function of bed height for two different shear rates

Figure 7-17 shows the solid volume fraction profile in the two metre bed under steady state shear. The result shows that the underflow density increased continuously in the bed indicating that densification occurred. The rate of change of solids with increasing depth was greatest in the region of shear. At 0.4 metres, the bed concentration was almost 0.3 (v/v), significantly higher than the measured underflow concentration (0.193 v/v. This could suggest short-circuiting. Figure 7-17 also shows that for z > 0.8 m, the solids concentration was lower than ϕ_g. This is interesting since the interface was at two metres height. Consequently, 60 % of what was perceived the bed was in fact un-networked. Remember that the gel point is by definition the solid concentration at the top of the bed. The region (0.8<z<2.0) could correspond to transitional or fan region for which $\phi_0 < \phi < \phi_g$ while the observed interface is a shock corresponding to ϕ_0.

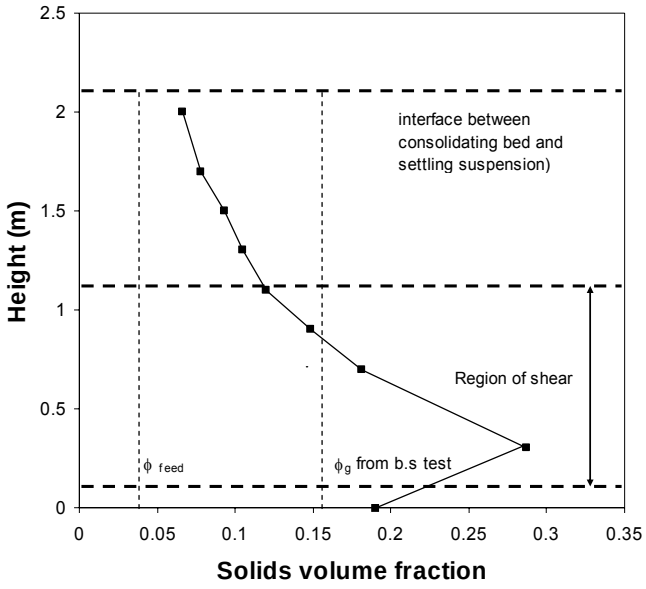

Figure 7-17 Solid volume fraction profile of a two metre bed under steady state shear

The effect of increasing bed height on underflow density remains to be explained. Normally, the role of bed height in dewatering is considered in terms of compressive force exerted by the bed; by increasing the bed height, the total "compressive squeeze" naturally increases. Compression is most effective at low solid fluxes where residence times are sufficiently long for aggregates to consolidate. However, in this case the throughput was too high to allow consolidation to occur. The average volume fraction also depends on the permeability, or the hydrodynamic drag experienced by the bed which is assumed to be constant for a given ϕ.

In Chapter 5 it was shown that if a settling suspension is subjected to shear, the permeability significantly increased. The change in $R(\phi)$ depended on the solid concentration at which the shear was applied. Because $R(\phi)$ showed sensitivity at solid volume fractions less than the gel point, individual aggregates must be affected. In the Couette, because of settling, the aggregates experienced shear, at low solid volume fractions ($\phi_0 \leq \phi < \phi_g$) for only a short duration (seconds to minutes) before the gel point was exceeded. It is possible that in the Couette experiments, because of the brief exposure time, the aggregates did not reach an equilibrium state in shear. In the tall column, aggregates settle at a concentration $\phi_0 \leq \phi < \phi_g$ for far longer periods, and thus shear, whether applied externally (i.e. from mechanical raking) or internally (fluid stresses and collisions between aggregates) occur over significantly longer time scales. The potential for this prolonged, low-level shear to enhance dewatering by changing the structure of the individual flocs could be an important factor explaining the modelling discrepancies. This concept will be explored in Chapter 8.

7.4.4 Further work

Clearly there is a great deal of scope to extend the experiments reported in this chapter and possibly confirm or contradict these findings. In the column the following work could be performed;

- Shear the material at different heights. This could help identify the optimum region to shear. Would a different underflow concentration have resulted had the material been sheared higher in the column?
- Operate at a solids flux where dewatering is compressibility limited. This would establish a relationship between shear and bed height, when compressive forces are expected to be important and probe whether a

four metre bed behaves differently to a one metre bed, under the same applied shear?

However, before undertaking this work, it was decided to first investigate the possibility of time dependent restructuring of aggregates, alluded to above.

7.5 Conclusions

In this work, the effect of shear on continuous thickening was investigated at different bed heights in the column. The effect of shear depended on bed height of the bed, a result not predicted by the 1−D model. At low bed heights, when the shear rate was increased from 0 to 1.6 s^{-1}, (by increasing the rotation rate from 0 – 20 rpm), the underflow solid volume fraction increased from 0.11 to 0.16 v/v. The predicted underflow density of 0.1 and 0.12 v/v were slightly less than these experimental results. Interestingly, increasing the bed height caused the underflow concentration to increase to 0.17 v/v for 2 metre, and 0.23 v/v for 4 metres. Shearing the sediment at these two heights had a different effect to the one metre result. For two-metres, the underflow concentration increased to 0.21 v/v, however, at four metres shear did not cause improvement, dewatering was in fact slightly worse. This is possibly due to clogging between the cylinders. The dependence on bed height is difficult to explain through reasoning of compression because of the high flux. However, the shear sensitivity of flocs, especially at low flocculant dosages, could introduce a time dependence factor to the problem, which is not considered in a steady state model. Time and bed height are directly related in this case since the solids flux was constant.

Chapter 8

Aggregate densification in a fluidized bed

8.1 Introduction

In the previous chapter, the underflow solids concentration showed an unexpected dependence on bed height which was not predicted by the model. The dependence of underflow density on bed height, to the best available knowledge, is unreported in the literature. Importantly, the model assumes that $P_y(\phi)$ and $R(\phi)$ do not change as a function of time for a specified ϕ. This implies the aggregate structure (size and density) does not change over time scales applicable to thickening. However, the constant buffeting of aggregates by fluid and other aggregates as they settle may mean this assumption is not always satisfied; and if this were the case, the current dewatering characterisation methodologies would be deficient.

Changes in floc structure depend on several factors; including shear rate, solid residence time, and local solid volume fraction. The residence time determines the maximum time in which an aggregate may break or restructure. For a four-metre high bed in the tall column considered in Chapter 7, the aggregates spent over five hours in the column. For a large proportion of that time, the average solid volume fraction was less than ϕ_g ruling out compression as the cause for the increased underflow solid concentration.

The aim of this chapter is to consider the possibility of time dependent restructuring of aggregates, by measuring $P_y(\phi)$ and $R(\phi)$ as a function of time. Batch settling tests in the Couette device are not suitable for investigating possible time dependency in continuous thickening because of the differences inherent between batch and continuous dewatering processes. In the Couette shear batch experiments, suspensions were sheared for two hours. However, the total time aggregates are sheared at ϕ less than ϕ_g was short; approximately 100 seconds for the 60 g tonne $^{-1}$ case. To maintain an un-networked suspension for times comparable to thickening requires that the gravitational force be offset. This can be achieved by fluidization. By varying the time of fluidization and subsequently measuring the settling rate, $P_y(\phi)$ and $R(\phi)$ are determined as a function of time. A change in the dewatering parameters $P_y(\phi)$ and $R(\phi)$ implies that the aggregates are restructuring over time.

8.2 Floc size, structure and density

8.2.1 Theory of aggregate structure

To interpret and explain changes in $P_y(\phi)$ and $R(\phi)$ that may arise during the low level agitation in the fluidized bed, a basic understanding of aggregate structure is required. Floc structure, including size, morphology and mass density is important, since these dictate the permeability and compressibility.

Generally, aggregates are considered fractal objects [100]. The fractal nature of flocs can be expressed by a power law relationship between the particle mass (M) and a characteristic linear length (L);

$$M \propto L^{d_f} \tag{8.1}$$

where d_f is the mass fractal dimension. If M is plotted against L on logarithmic coordinates, a straight line should result, and d_f is found from the slope [60]. The fractal dimension is a scaling measure indicating how the floc density varies with size. In three-dimensional Euclidean space, a solid body will have a fractal dimension of 3. For flocs, d_f is typically a non-integer number and can range between 1 and 3. A fractal dimension less than one is possible by breaking the floc into linear segments so the floc now represents a collection of points with zero dimension. A defining property of fractal objects is self-similarity, or infinite nesting of structures independent of the scale of observation [25, 60].

Equation (8.1) can be written more specifically;

$$N = k\left(\frac{d}{d_0}\right)^{d_f} \tag{8.2}$$

where N is the number of particles, d is the size of the aggregate, d_0 the size of the primary particles and k is a proportionality constant. In real systems equation (8.2) is constrained by a lower and upper size limit, which for aggregates are the primary particle and aggregate size respectively [100].

A feature of aggregate growth is the formation of large open structures for which the effective density decreases as the size increases. Tambo *et al* [145] and Lagvankar [89] observed this behaviour in water treatment flocs. The effective aggregate density is given by its buoyant density,

$$\rho_{eff} = \rho_{floc} - \rho_f \tag{8.3}$$

while the average solid volume fraction of the aggregate is;

$$\phi_{floc} = \frac{\rho_{floc} - \rho_f}{\rho_s - \rho_f} \tag{8.4}$$

The density of a floc can be calculated by;

$$\rho_{floc} = \frac{m_{particles} + m_{entrained\ fluid}}{V_{floc}} \tag{8.5}$$

$$\rho_{floc} = \frac{\rho_s N\left(\frac{\pi {d_0}^3}{6}\right) + \rho_f\left(\left(\frac{\pi d^3}{6}\right) - N\frac{\pi {d_0}^3}{6}\right)}{\frac{\pi d^3}{6}} \tag{8.6}$$

Thus, substitution of (8.2) into the mass balance above gives the following expression for effective density;

$$\rho_{eff} = k\left(\frac{d}{d_0}\right)^{d_f - 3} \tag{8.7}$$

On a log–log plot of floc density versus size, the density should decrease linearly with size. The fractal dimension is calculated from the slope (see Figure 8-1).

In principle, aggregate growth can occur via two pathways; addition of individual particles or addition of clusters to a growing floc. Early studies, including Vold [158] and more recently Meakin [101], simulated aggregation assuming single particle growth. The aggregates formed in this manner were relatively dense with fractal dimensions of the order 2.5.

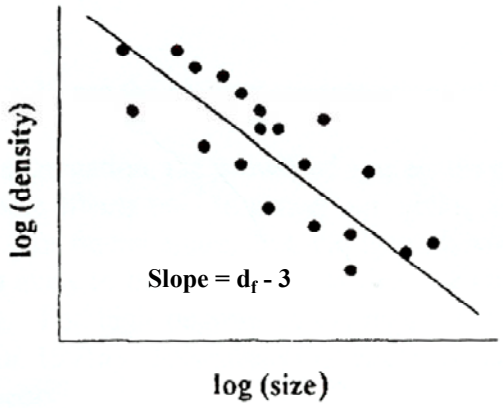

Figure 8-1 Density versus size on logarithmic coordinates [60]

However, single particle growth models are not relevant to most practical systems as aggregation occurs more commonly by cluster addition [60]. Simulations and experiments show that flocs formed by cluster addition are more open and extended with a fractal dimension of ~1.8 [78]. This is because single particles can penetrate the floc structure further before they encounter and attach to another particle or cluster [60].

The fractal dimensions quoted above are for cases where electrostatic repulsion between particles does not occur. Then, every collision between particles results in attachment and the growth is limited by how quickly particles can be transported to the floc. This is known as diffusion limited aggregation (DLA). However, when repulsive forces are important, the probability of two particles or clusters bonding is reduced. In this case aggregation is limited by the rate particles can attach. This is known as reaction limited aggregation (RLA). Fractal dimensions for RLA are much higher than DLA for arguments similar to particle addition. For RLA, cluster-cluster addition results in fractal dimensions of

around 2.1, significantly higher than the DLA case of 1.8. The structures of aggregates produced by both RLA and DLA are shown in Figure 8-2.

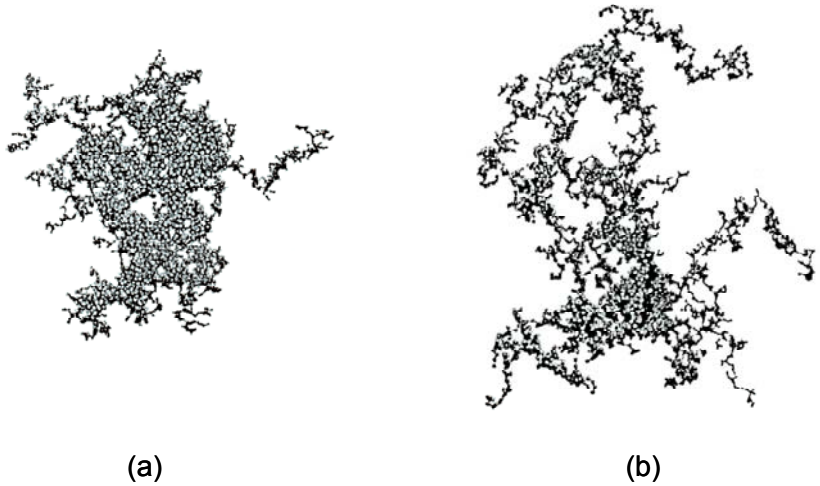

Figure 8-2 Model predicted floc structure for; (a) RLA (b) DLA taken from Bushell [25]

8.2.2 The strength of aggregates

The strength of an aggregate is a major factor determining structure and the propensity for break up under shear. A number of workers have considered aggregate strength both theoretically and experimentally [1, 8, 54, 55, 103, 132, 166]. Knowledge of aggregate strength allows maximum aggregate sizes and breakage due to shear to be predicted. These studies also provide valuable information regarding the breakage mechanism [55].

To model floc breakage, the cohesive force between particles, F_c must be quantified. Tambo and Hozumi [141] proposed a simple model which assumes that F_c is the product of a strength constant and the area of the plane across which failure occurs, i.e. $F_C \propto \sigma A_f$.

Adler and Mills [1] modelled floc breakage by assuming flocs as uniformly porous spheres. In this case, the local hydrodynamics are governed externally by Stokes equation (8.8), while inside the aggregate, the Brinkman equation (8.9) is employed [131].

$$\nabla p = \mu \nabla^2 \mathbf{u} \tag{8.8}$$

$$\nabla p = \mu \nabla^2 \mathbf{u} - \left(\frac{\mu}{k}\right)\left(\mathbf{u} - \mathbf{u_s}\right) \tag{8.9}$$

In these equations, p is the pressure, μ is the solution viscosity and k is the permeability. The Brinkman equation is valid for large and porous aggregates, in which case the length scale of the change in velocity gradient is larger than the primary particle size [131]. Only fluid stresses are considered; the contribution due to particle collision is neglected. By assuming an appropriate failure criterion, a critical shear stress can be found. Adler et al [1] use Mises yield criterion;

$$\sigma_D : \sigma_D \leq S^2 \tag{8.10}$$

where $\sigma_D : \sigma_D$ represent the deviatoric components of the solid stress tensor and S is the characteristic strength of the aggregate. Failure is due exclusively to shear stresses and therefore the isotropic components of the stress tensor are neglected.

Because aggregates are fractal, the assumption of uniform porosity is generally invalid. This partly explains the discrepancies between experimental results and theory [131]. Sonntag and Russel [132] extended the model of Adler et al [1] by considering breakage of flocs where the solid volume fraction varies as a function of radial position. Thus, by combining the concept of fractal geometry with

appropriate solid and fluid momentum balances, they determined the following yield criterion;

$$\frac{\mu\dot{\gamma}_{\min}}{S} = fn(d) \tag{8.11}$$

where $\dot{\gamma}_{\min}$ is the critical shear rate required to break an aggregate of size d. For $\frac{\mu\dot{\gamma}_{\min}}{S} < 1$, the aggregate is not expected to break.

Experiments by Glasgow and Hsu [54], and Glasgow and Liu [55] quantified aggregate strength by blasting flocs with high intensity jets and observing the disintegration process. The effect of the physicochemical environment on breakage was investigated by varying pH [54]. For both coagulated and polymer flocs, the limiting size $d_{\lim}$ and breakage force F_C were correlated by;

$$F_C \propto {d_{\lim}}^m \tag{8.12}$$

The propensity for aggregates to internally restructure is related to the aggregate strength. Restructuring generally forms a denser aggregate and can involve several different mechanisms. The main two are aggregate breakage and subsequent reformation; and rotation, folding and twisting of clusters into denser arrangements without bonds breaking [78]. To restructure by bond breakage, the energy of inter-particle forces must be overcome and thus shear rates between $10^2 - 10^3$ are necessary. Because there is no bond breakage in the second method, the shear rate required is usually far lower.

Jullien and Meakin [78] simulated three dimensional cluster-cluster aggregate restructuring and reported an increase in d_f from ~1.9 to ~2.1. Population

balance models have also been applied, providing further evidence for restructuring, while explaining the aggregation kinetics [126, 147].

Aubert and Cannel [4] observed aggregate restructuring experimentally by investigating the aggregation of silica under different conditions. For RLA, the flocs had a fractal dimension of 2.1. With appropriate pH and silica concentrations, DLA was induced and the fractal dimension reduced to 1.75. However, over time the lower density flocs (d_f = 1.75) restructured to form aggregates with fractal dimension 2.08, the same as for RLA. The time scale of restructuring varied between minutes and hours. After 10 minutes, d_f was 1.77; this increased to 2.1 after 30 minutes; while no change was observed after 60 minutes.

8.2.3 Floc densification

The density of two equivalent sized flocs depends on the primary particle size; larger particles form denser aggregates assuming flocculation conditions are the same [31]. Clark and Flora [31] reason that when a floc breaks into smaller clusters, with a similar density to the primary particle, upon reformation a denser floc should result. Clark and Flora aggregated latex particles at constant shear rate (G = 35 s^{-1}) for 30 minutes, then subjected flocs to high shear rates (between 150 and 1800 s^{-1}) for 1 minute to induce breakage. The flocs were then allowed to reform (at G = 35 s^{-1}) for 30 minutes. Regrowth was observed when the high shear was removed and the aggregate density was higher than initially. The final floc size and density increased with reformation time although the increase was not monotonic. Peaks in density (and troughs in floc size) occurred at two different shear rates ~ 350 and 900 s^{-1}. Clark *et al* [31] attribute the oscillatory behaviour to the existence of multiple levels within the floc;

increasing G successively degrades these organisational levels. The amount of restructuring was greatest, for lower shear rates. Above ~ 900 s^{-1}, d_f did not change.

To achieve dense aggregates Tambo, Wang and co workers [142-144, 161] describe a pilot scale fluidized bed separator. The fluidized environment assists dewatering by improving the flocs morphology and settling characteristics. The suspended solids, BOD and phosphorous removal also improved [161]. By fluidizing dense, almost spherical aggregates formed, with a density up to ten times higher than conventional flocs [144]. The dense aggregates, or pellets, formed via two pathways: addition of single particles to the parent floc, and mechanical syneresis [145]. Formation of these aggregates occurred over 4 to 5 hours during which time the flocs were constantly agitated. The solid concentration increased as a result from ~0.25 to ~7 w/w %.

The same authors reported experiments in a 10 cm column [144]. Charge neutral kaolinite was continually fed into the bottom and a non-anionic polymer was added. As the aggregate size increased, the feed rate was increased to compensate for the faster settling rates. A rake was used (shear rate of 30 s^{-1}) to ensure uniform aggregate growth. Flocculant and salt dosages were important, as effective fluidization occurred over a relatively narrow range. Polymer dosing was crucial since overdosing led to large clumps, which were difficult to fluidize.

The density of alum-coagulated kaolin (random flocs) was compared with the density of flocs that had been rotated in a barrel for varying times. The two flocculation conditions produced different types of flocs, which Yusa [170] expressed in terms of a floc bulkiness (see Figure 8-3). The bulkiness is the ratio of the floc volume to the volume of solids contained in the floc i.e. $b = \frac{1}{\phi_{floc}}$.

The lower slopes of the pelleted flocs imply a higher fractal dimension; a zero slope would correspond to a d_f of 3. Interestingly, an increase in rotation time caused the density to increase, (albeit slightly); while the slope remained constant. In this case, the higher density must be due to smaller sizes resulting from floc break-up rather than aggregate restructuring.

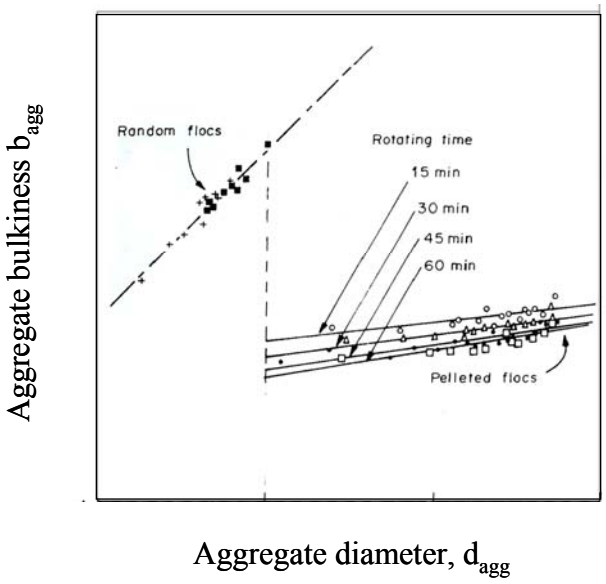

Figure 8-3 Aggregate bulkiness $\left(\frac{1}{\phi_{floc}}\right)$ as a function of diameter [170]

8.2.4 Experimental techniques for determining floc structure

Several methods are available for determining size and density of aggregates. These include light scattering and sedimentation.

8.2.4.1 Light scattering

A common technique for measuring aggregate structure is small angle static light scattering [4, 66, 159, 165]. When a light beam strikes a suspension of particles,

part of the incident light is scattered. For fractal aggregates of monodisperse particles, the scattered intensity follows a power law relationship;

$$I(Q) \propto Q^{-d_f} \tag{8.13}$$

The scattering wave vector Q is a function of scattering angle;

$$Q = \frac{4\pi\eta_0}{\lambda_0} \sin\left(\frac{\theta}{2}\right) \tag{8.14}$$

where η_0 is the refractive index of the dispersing medium, λ_0 is the wavelength and θ is the scattering angle of the incident light. Thus, plots of I(Q) as a function of Q yield a fractal dimension. One advantage of light scattering is the ability to characterise aggregate structure online, as rapid determination of d_f is possible. However, no direct visual information of floc structure is obtained and size determination is restricted to the scattering wavelength vector range of the instrument i.e. $\frac{1}{r} < Q < \frac{1}{r_0}$. Fractal dimensions are often overestimated by light scattering techniques, due to a change in dependence of Q near the edges of the aggregate.

8.2.4.2 Sedimentation

Direct observation of settling flocs can convey information about their size, shape, and effective density. Tambo and Watanabe [145] were among the first to characterise floc density using sedimentation rates. Several others including Farrow and Warren [47] and Klimpel and Hogg [82] have adopted similar approaches.

The determination of density or fractal dimension from sedimentation rates is complicated by several issues. From Chapter 2, the hydrodynamic force on a single particle was given by;

$$F_D = \frac{1}{2}\rho_f u_\infty^2 C_D A \tag{8.15}$$

For spheres settling in Stokes regime, where the particle Reynolds number is less than 0.2, the hydrodynamic drag coefficient is given by $C_D = \frac{24}{\mathrm{Re}_p}$. Therefore, the density can be determined directly from Stokes equation. The applicability of Stokes is subject to several assumptions including;

- Particles are smooth spheres so there is zero slip between particle and fluid
- Inter-particle forces are neglected
- Wall effects are negligible
- The flocs are impermeable, i.e. no fluid flows through the structure
- Particles are small such that inertial forces are neglected

However, most flocs are not spherical. Random flocculation produces flocs which range from highly irregular to almost spherical. To estimate settling behaviour using Stokes, it is necessary to approximate the floc shape as a sphere. The hydrodynamic drag function depends on particle shape so that C_D must be modified by an empirical factor. For a sphericity of 0.8, a value commonly assumed for flocs, C_D is given by $45/\mathrm{Re}_p$, twice the drag experienced by a sphere of the same size [145].

Because of the irregular shape, defining an equivalent diameter for use in Stokes equation is not straightforward. The approach adopted in this chapter is to approximate the aggregates as ellipsoids. Then, by defining major and minor axes an equivalent Stokes diameter can be determined; the diameter of a sphere with an equivalent resistance as the ellipsoid. The main problem with this approach is that it is often based on 2-D analysis, since 3-D images are difficult to obtain practically. When a floc is viewed along an axis of symmetry, an aspect ratio of 1 could indicate either a true sphere or a spheroid (prolate or oblate).

The effect of hydrodynamic interactions is an important consideration. These interactions are difficult to account for theoretically and consequently, as far as possible, interactions are reduced by sample dilution. For separation distances 20 times greater than the particle radius the resulting error in C_D is less than 5% [73]. The role of floc permeability is another area of uncertainty. If appreciable flow of fluid through the structure occurs, the drag on the floc is reduced. The effect of the reduced drag becomes increasingly important as the floc porosity increases, i.e. $\left(\left(1-\phi_{floc}\right)\to 1\right)$. Thus, a porous floc will settle faster relative to an impermeable object of the same size and density. To account for flow, the drag needs to be modified. For highly porous flocs with $d_f < 2$, the Brinkman equation can be used, while for $d_f > 2$, Darcy's law is more appropriate. However, because the pressure gradients are small, in most cases fluid flow can be ignored safely.

Published studies concerning floc structure differ to the work in this chapter in several ways. First, shear rates are large, typically exceeding 1000 s^{-1}. These shear rates may represent flow conditions within a feed well; however, these are likely to be far higher than those encountered when flocs settle outside of the feed well. Another important difference is that the solid volume fractions

considered are often low; for example Sonntag used ϕ = 0.0074, in an effort to reduce the contribution of particle stresses [131]. These studies are interesting fundamentally; however, it is the study of higher concentration suspensions, where particle collisions cannot be ignored, that is of more relevance practically.

8.3 Fluidization theory

The role of fluidization is to increase interphase contact, helping improve heat and mass transfer rates. Fluidization is therefore employed in a range of separation processes including; adsorption, distillation and flotation. Fluidization involves flowing fluid counter current to the direction of a force, which in most cases is gravity. Fluidization is governed by the same mechanics as sedimentation, described in Chapter 2. The flow of fluid gives rise to a hydrodynamic force that partially supports the weight of the particles. The hydrodynamic force is a function of fluid velocity. The linear fluid velocity, (also called superficial) is equal to $\frac{q}{A}$. Therefore, by increasing the volumetric flow rate eventually a point will be reached where the solid weight is supported entirely by the fluid. The force balance can be written as,

$$\Delta P = h\phi\Delta\rho g \tag{8.16}$$

where ΔP is the pressure drop and h is the height of the fluidized bed.

Figure 8-4 shows the relationship between pressure drop and superficial velocity. The linear region corresponds to flow through a packed bed where ΔP can be predicted using Carman Kozeny or Ergun equations. In this velocity range, the bed is stationary and solid volume fraction constant. The fluid velocity corresponding to the maximum pressure drop is the minimum or incipient

fluidization velocity u_{mf}. By definition, the volume fraction at incipient fluidization is the material gel point.

8.3.1 Pressure drop in packed beds

The frictional force, and therefore pressure drop ΔP is related linearly to the superficial velocity u_c according to Darcy's law,

$$u_c = K\frac{-\Delta P}{h} \tag{8.17}$$

The hydraulic conductivity coefficient K is given by;

$$K = \frac{1}{\frac{\mu}{k(\phi)} + \frac{\alpha(\phi)\mu}{h}} \tag{8.18}$$

where μ the fluid viscosity, $\alpha(\phi)$ the specific volume cake resistance, and $k(\phi)$ is the Darcian permeability, related to $R(\phi)$ by [57];

$$k(\phi) = \frac{\mu}{R(\phi)}\frac{(1-\phi)}{\phi} \tag{8.19}$$

For laminar flow conditions, the Carman-Kozeny equation reasonably predicts fluid pressure drop. This equation was derived by assuming that the tortuous flow through the channels of the bed is equivalent to the flow through a series of tubes of diameter D_e and height H_e. Pressure drop in this case is given by the Hagen Poiseuille, equation (8.20).

$$\frac{-\Delta P}{He} = \frac{32\mu u_e}{D_e^2} \tag{8.20}$$

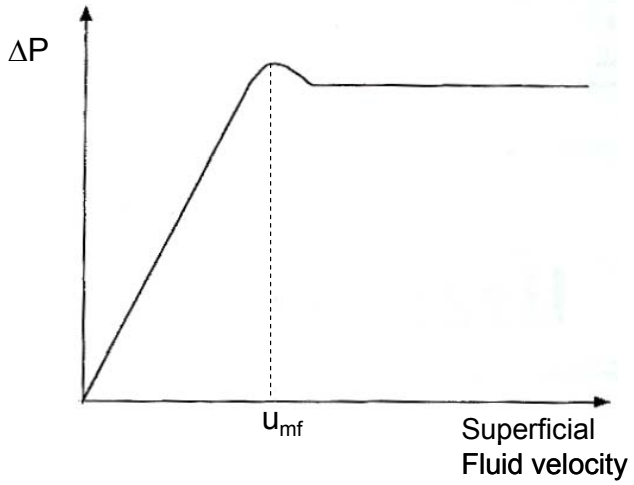

Figure 8-4 Pressure drop in fluid as a function of superficial fluid velocity

The tube height H_e is proportional to the bed height, where $D_e \equiv \frac{(1-\phi)A}{S_B A}$ the ratio of flow area to wetted perimeter, and S_B is the particle surface area per unit volume of bed. Therefore, the superficial velocity is found using;

$$u_c = -0.0055\frac{(1-\phi)^3 \Delta P d_p^2}{\phi^2 \mu h} \tag{8.21}$$

8.3.2 Regions of fluidization

Figure 8-5 (a) shows several possible regions of fluidization. These regions depend on the superficial velocity and fluid phase (gas or liquid). At low fluid velocities, fluidization is the same irrespective of type. As the velocity

approaches u_{mf}, the behaviour of liquids and gases begins to deviate. For liquids, bed expansion occurs slowly and relatively uniformly, a process called particulate fluidization. Gases, on the other hand, display what is called aggregative fluidization in which a dense emulsion phase and a lean bubble phase form. Gas added in excess of the incipient fluidization velocity passes through the bed as bubbles. Therefore, aggregative fluidization is unsuitable for the purpose of the current study and a particulate fluidization is used instead.

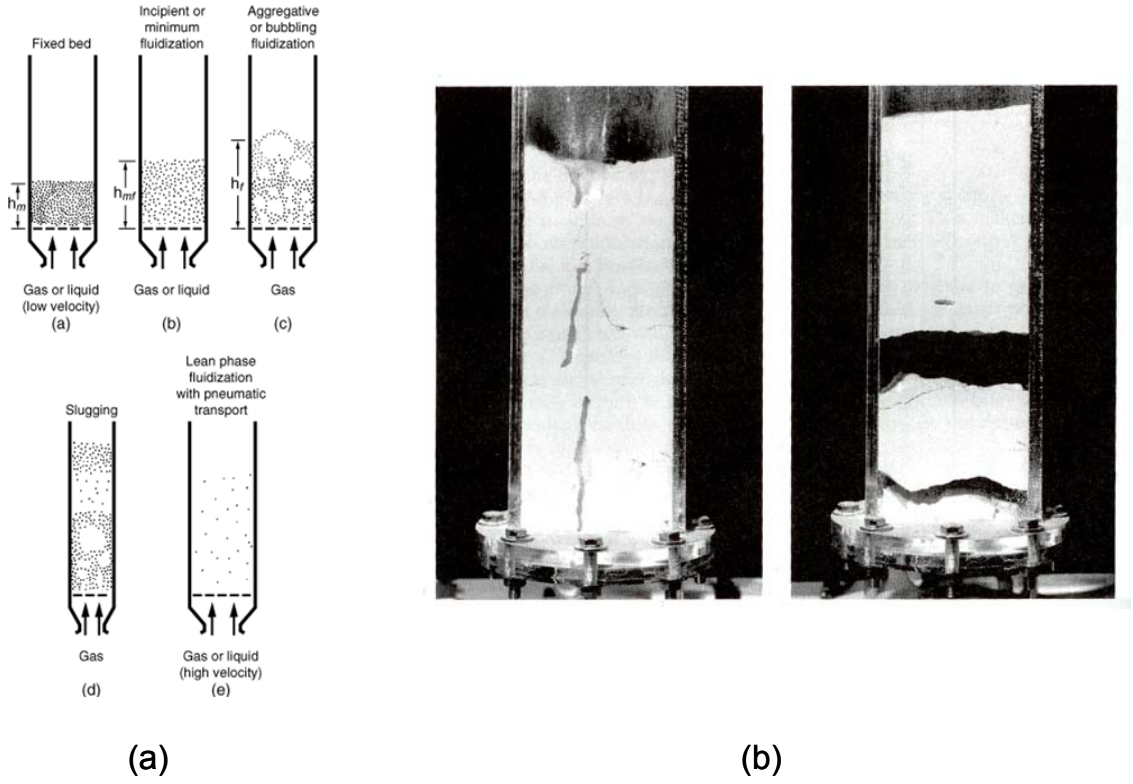

Figure 8-5 (a) Regions of fluidization (b) Channel formation in fluidized bed [121]

To describe the fluidization of powders, a classification system is used which identifies different groups based on their expansion and bubbling properties

[121]. Highly cohesive materials including cement and flour are difficult to fluidize as shown by Figure 8-5 (b). This figure shows; on the left, jets and volcanoes erupting at the surface; while on the right, a bed rising as a discrete plug [121]. These problems are unlikely in the present work, since relatively dilute suspensions are used with ϕ less than ϕ_g at all times; i.e. the fluid does not possess a yield stress.

8.3.3 Minimum fluid velocity

The superficial velocity is determined by substituting Ergun's equation into the general force balance, yielding the following equation;

$$Ar = 150\frac{\phi}{(1-\phi)^3}\mathrm{Re}_{mf} + 1.75\frac{1}{\phi^3}\mathrm{Re}_{mf}^2 \tag{8.22}$$

where $Ar = \dfrac{\rho_f \Delta\rho g d_p^3}{\mu^2}$ and $\mathrm{Re}_{mf} = \dfrac{u_{mf} d_p \rho_f}{\mu}$. To calculate the minimum fluidization velocity, therefore requires knowledge of the gel point. Because the solid volume fraction is less than the gel point, Darcy's law no longer applies. However, if the solid concentration is uniform, the fluidization velocity can be found from $R(\phi_0)$ since;

$$R(\phi_0) = \frac{\Delta\rho g(1-\phi_0)}{u-v} \tag{8.23}$$

At the point of fluidization, u_s is zero, and the fluidization velocity is given by;

$$u_{mf} = -\frac{\Delta\rho g(1-\phi_0)}{R(\phi_0)} \tag{8.24}$$

The above equation was used to calculate the required fluid velocity for each of the fluidization experiments presented in this chapter.

8.4 Experimental

8.4.1 Materials

The material used in these experiments was the same as in Chapter 4 (Omyacarb 10) and AN934 SH flocculant). Polymer solutions were prepared at a concentration of 2 g L^{-1}, according to the procedure outlined in section 3.4. The concentrate was diluted to 0.2 g L^{-1}, one hour prior to use.

8.4.2 Methods

The time dependence of dewatering was investigated by fluidizing flocculated calcite suspensions and measuring the resultant properties of the aggregates; including its dewaterability (settling rate, equilibrium solid concentration) and its structure (size and density). The method comprised three key components namely, flocculation, fluidization and sedimentation. The experimental arrangement, shown schematically in Figure 8-6, is essentially the same setup described in Chapter 5, with a fluidization column instead of the Couette shear device.

Flocculation was achieved either in a pipe reactor or stirred baffle reactor. Once flocculated, the suspension was transferred directly to the column. Immediately after transferring the flocs, water was pumped into the bottom of the column to keep the flocs suspended. The flow rate was calculated using equation(8.24). The flow was maintained constant for the designated period while the height of the suspension and supernatant interface was recorded. After the designated

time had elapsed, the water flow was stopped and the interface measured as the suspension settled. Additionally, in selected experiments, a focussed beam reflectance measurement (FBRM) probe was used to measure changes in the aggregate chord length during fluidization. Finally, for the two flocculation methods, a small volume was sampled from the column before and after fluidization and the density determined by from sedimentation rates of isolated flocs. Because this analysis is time consuming, only a limited number of cases could be considered.

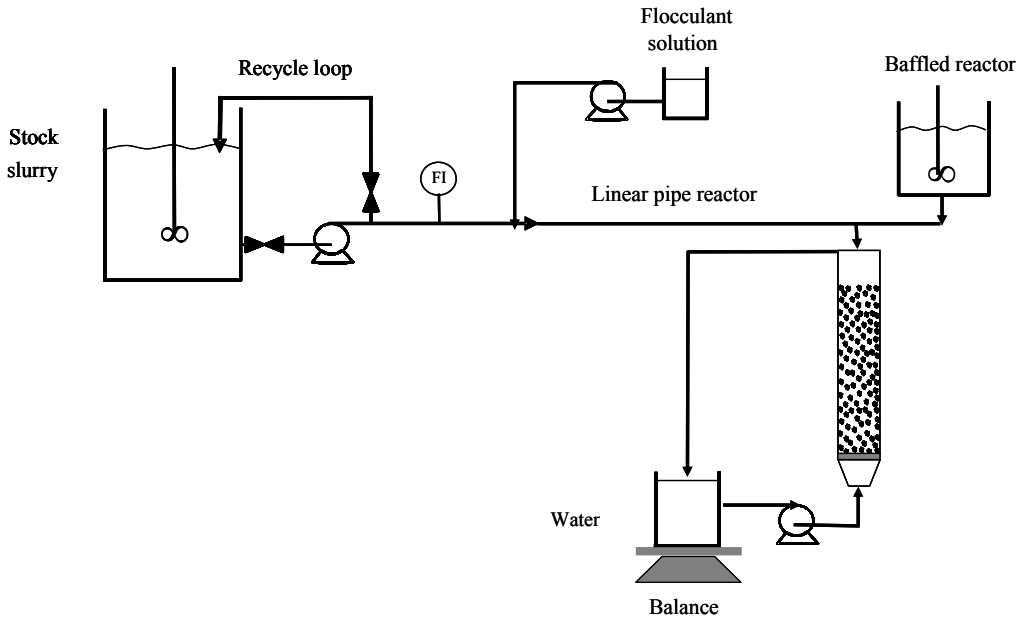

Figure 8-6 Schematic of experimental fluidization of calcite flocculated either in pipe or baffle reactor

Figure 8-7 shows a photograph of the fluidization column. The column was made from acrylic with the dimensions; 460 mm in height, 30 mm in length and 21 mm in width, while the inlet had an internal diameter of 10 mm. The total volume was 276 mL. The inlet fed into a tapered reservoir 16 mm in height (see Figure 8-6) which was designed to minimize entry effects due to a sudden

expansion. A sintered disk, 3 mm thick, with 10 μm pores was fitted over the reservoir to distribute the water evenly across the column. This was sealed to ensure water did not preferentially flow up a face or edge. At a height of 210 mm, a 24.8 mm port was installed to allow the insertion of the FBRM probe. The probe was supported by a 50 mm bracket (see Figure 8-8) and sealed using three o-rings. The cell was mounted on a horizontal platform (see Figure 8-7). The platform was supported by three legs, which could be adjusted to ensure the column was level. This was important, because a small inclination from the vertical promoted preferential flow so that fluidization was inefficient.

Figure 8-7 Photograph of the fluidization column

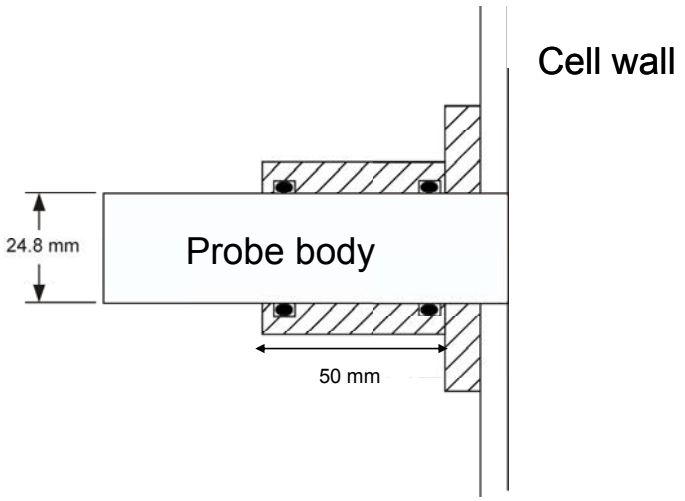

Figure 8-8 Schematic of the FBRM probe support

Omyacarb 10 suspensions were prepared at a solids concentration of 0.15 (w/w). This concentration corresponded to the solid concentration in the tall column bed and is significantly higher than the initial solid concentration flocculated in previous chapters. To demonstrate that flocculation at this concentration is possible, settling rates and turbidity levels were measured for initial solid concentrations ranging between 0.1 and 0.2 w/w. At ϕ_0 = 0.15 w/w, flocculation was still efficient. Above 0.17 w/w, the turbidity levels began to increase..

Initially, a linear pipe reactor was used to flocculate calcite at 40 g tonne $^{-1}$. The pipe was 1.8 metres in length, and 0.008 m in diameter. This diameter was chosen over a smaller 0.006 m ID pipe to reduce shear and promote the formation of larger, more open flocs, since these are more likely to restructure. The pipe reactor was operated continuously for approximately five minutes to allow steady state to develop. The column was then filled with flocculated material from the pipe outlet. In the first instance, the solid supernatant interface was measured as a function of time in the absence of water flow. The hindered

settling function and compressive yield stress for the flocculated calcite was measured as described in section 2.4. This was necessary to determine the required water flow rate. From the value of $R(\phi)$ at the solids concentration of interest (0.15 w/w) and the available flow area, the flow rate required to suspend the flocs was determined. Prior to filling the column, the inlet pipe was primed establishing a pressure gradient in the pipe. This was done to prevent flocs from clogging the pores of the sintered disk.

In the initial series of experiments, the column was fluidized continuously for the following times; 0, 1, 2, 4, 8 and 24 hours. The column was filled to an initial height of approximately 35 centimetres. The flow rate required to suspend the flocs was 32 mL min^{-1}. The interface was measured at regular time intervals, between sixty seconds initially and thirty minutes after a few hours had passed. When the suspension had been fluidized for the specified time, the water flow was stopped and the interface settling height was recorded more frequently. The interface height was recorded for 24 hours to determine a final height; however, this showed that the final height was achieved after approximately two hours. The water flow rate was logged continuously for the duration of the experiment. The flow rate was controlled via a PID controller, identical to the one in the previous chapter.

In a second series of experiments, calcite was flocculated in a linear pipe reactor under the same flocculation conditions as initially. Instead of fluidizing at 30 mL min^{-1}, flow rates less than the critical flow rate were investigated; 15, 20 and 25 mL min^{-1}. Again, the interface was recorded for the duration of fluidization, which lasted twenty-four hours.

A further series of experiments were undertaken at CSIRO Minerals, Waterford, Perth. The purpose of these experiments was to measure the aggregate size as a

function of fluidization time using a FBRM probe. Results for three flocculant dosages were obtained, corresponding to 20, 40 and 60 g tonne $^{-1}$.

A final series of experiments was undertaken at The University of Melbourne. In these experiments, both a stirred reactor and pipe reactor were used to flocculate calcite. In the baffle reactor, three different flocculation times were investigated; 5, 10 and 30 seconds. A dose of 20 g tonne $^{-1}$ and rotation speed of 700 rpm was used (except for 5 seconds, where the rotation rate was 600 rpm). After flocculation, material was transferred to the fluidization column. To transfer the flocculated suspension, the stirred reactor was located directly above the column so the suspension could be gravity fed. This method intended to reduce shear to the flocs during transfer. Once transferred, the flocs were fluidized for the following times; 0, 0.5, 1, 1.5, and 2 hours. After each fluidization experiment, settling heights were recorded until equilibrium was reached. A balance recorded the water mass overflowing from the column. This technique was designed to check that the water flow rate remained constant. For all experiments reported, there was no significant change in the water flow rate. The above procedure was repeated using a pipe reactor. The pipe diameter was 12.5 mm ID and 2 metres in length. The solids concentration was 0.15 w/w and volumetric flow rate 4.3 L/min. The flocculant was dosed at 40 g tonne $^{-1}$. Flocs were fluidized for a maximum of 2 hours before the settling curves were measured.

8.4.2.1 Focussed beam reflectance measurement

FBRM measurements were made using a M500 field unit (Lasentec, Redmond, Washington, USA). The probe consisted of a 12 mm diameter window encased by a 25 mm diameter stainless steel body. The focal point was close to the probe window. Thus, only aggregates near the wall, at a fixed vertical height were measured. The probe was positioned at right angles to the column, with the

window flush against the wall. Measurements were recorded at a 5 second interval for the duration of fluidization.

8.4.2.2 Floc density measurement

Changes in floc size and density were analysed using the settling test technique. The procedure was outlined in detail by Hulston [73]. The important aspects and some modifications are outlined below.

Four samples were analysed. Two samples were flocculated in the pipe reactor, the other two in a stirred baffle reactor. For each flocculation method, a sample was collected immediately after flocculation. A second sample was collected after fluidizing for 2 hours. The flocs were sampled using a wide bore pipette. The large bore diameter was significantly larger than the largest floc reducing shear during sampling. Flocs were immediately diluted by placing them in a water dish. During transfer, flocs tended to settle within the sampling tube leading to possible densification or aggregation. To reduce this likelihood, each sample was collected and diluted as quickly as possible.

The floc density was measured by introducing a sub sample of flocs into a rectangular settling column. The settling column is shown in Figure 8-9. The column was rectangular with dimensions 470 x 20 x 30 mm. The cell was made from perspex. The column was filled with deionised water; the same fluid used to prepare the suspension. To ensure flocs fell within the focal plane, a 5 mm diameter inlet tube was used to guide the flocs. The tube was located 200 mm above the level of the camera lens so entry effects could be ignored and terminal velocity reached. Using a 4 mm diameter pipette, flocs were transferred from the sample reservoir to the inlet tube.

A digital CCD camera recorded the size and settling rates of the flocs. Settling was recorded in a second dimension using an analogue camera positioned orthogonal to the first camera. Using this approach, the assumption of ellipsoidal aggregate shape could be verified. Flocs which were radically non uniform in shape in either direction were rejected. The cameras were calibrated using a small reticle, accurate to one tenth of a millimetre. An LED light provided backlighting, increasing the contrast and assisting the image analysis. The additional light enabled a faster shutter speed, reducing the possibility of motion blur, especially for the faster settling flocs. To maximise the depth of field, the aperture was set to a minimum, creating further need for a LED light source. Once all flocs had settled pass the camera a further aliquot was introduced. This was repeated until a statistically sufficient number of flocs was analysed, as a guide in 6 hours, 200 to 300 flocs were measured. At the completion of each run, the solution temperature was measured allowing the density and viscosity to be calculated.

Images were captured at a frame rate of 40 frames per second; this frame rate was required because of the relatively quick settling rates. The resulting image sequence ("movie") was saved as "avi" files using Adobe® Premiere and converted to "tiff sequences". Individual frames were exported sequentially as "tiff" files and analysed using the "Scion Image for Windows" image analysis software. A visual basic macro automated the analysis of individual frames, by recording in a series of text files the Cartesian coordinates, the cross sectional area, lengths of the major and minor axes, and the particle angle. The text files were imported into Excel and calculations were performed to determine the floc size, settling rate and density based on the theory and assumptions outlined in section 8.2.4.2. For further information on the macro and image analysis, the reader is referred to Hulston [73].

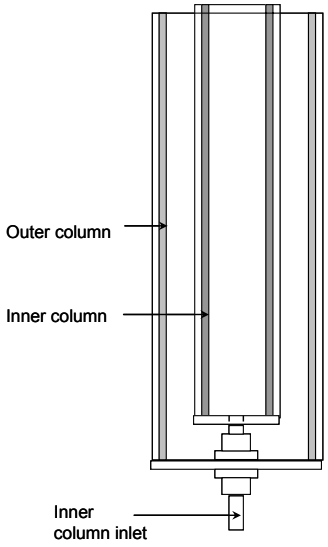

Figure 8-9 Settling column used to measure floc density

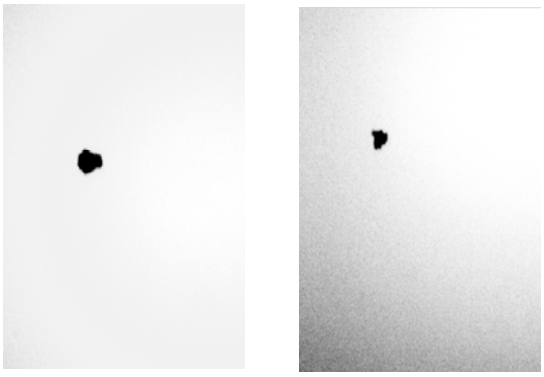

Figure 8-10 Frames from video footage of flocs settling in FDA column

8.5 Results and Discussion

Figure 8-11 shows the variation of the interface height with fluidisation time for a flocculated suspension formed in a pipe reactor at a flocculant dose of

40 g tonne $^{-1}$. In total six curves are shown; corresponding to five different fluidization times, ranging between 1 and 24 hours. Each data set represents a separate experiment. The un-fluidized curve (0 hours) is included for comparison. The height has been normalised against initial height h_0. This caused the height versus time for each fluidization experiment to collapse onto a master curve. Normalisation was necessary, because although an effort was made to fill the column to the same h_0, some variation occurred. Calculations, based on predetermined $R(\phi)$, showed that for calcite at $\phi = 0.07$, u_{mf} was equivalent to a volumetric flow rate of 32 mL min $^{-1}$. This calculated volumetric flow rate was found to overestimate the real flow rate as solids overflowed. Instead, a volumetric flow rate of 30 mL min $^{-1}$ was used in each experiment shown in Figure 8-11.

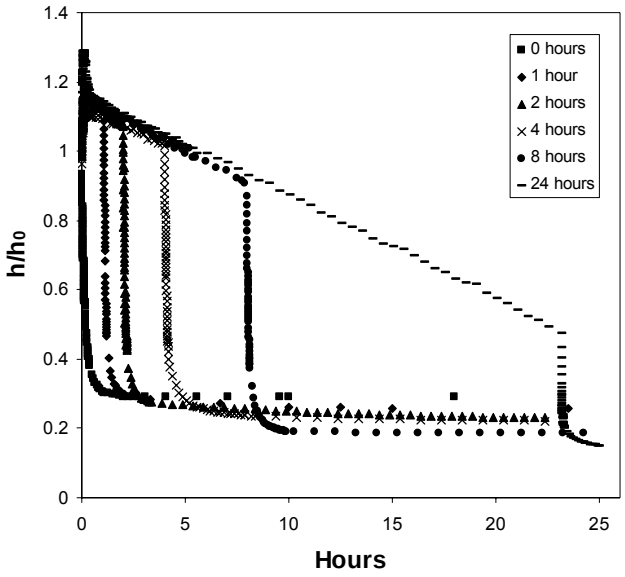

Figure 8-11 Normalised height as a function of time at the critical fluidization velocity

In the first fifteen minutes, the interface rose steeply. Originally, this was interpreted to mean that the fluidization velocity exceeded the minimum fluidization velocity (u_{mf}). However, the same initial increase was observed for flow rates as low as 15 mL min $^{-1}$. This result could be due to an induction period similar to settling, in which aggregates reorientate towards the direction of flow. After the induction period, t_{ind} the interface height stabilised and decreased linearly with increasing fluidization time. The interface height was measured for a maximum of 24 hours. Longer times were not possible because the interface became increasingly cloudy after approximately 16 hours and was therefore difficult to discern.

The negative slope of the interface for times greater than t_{ind} in Figure 8-11 was an important result. Because ϕ was less than ϕ_g, there was no mechanism for compression. Assuming a constant water flow rate and uniform aggregates, the only explanation for the decreasing interface height is that the settling velocity of the aggregates increased. In other words, the permeability of the suspension was changing over time. In this way, a dynamic equilibrium was established in which the suspension height decrease corresponded to an increase in permeability.

Increased suspension permeability, at ϕ less than ϕ_g, must involve change in aggregate structure. Neglecting flow through the aggregates, a higher permeability equates to a lower overall hydrodynamic resistance. Consequently, the relative solid velocity must increase. An increased settling velocity could occur in two ways; either by increasing the aggregate size or increasing the aggregate density. As shown later, the aggregate size does not increase. Therefore, the aggregate density must be increasing.

Densification could involve either breakage or reformation of flocs, or restructuring, in which the polymer branches fold, rotate or bend into a more compact conformation. The results shown in Figure 8-11 do not distinguish between the above two mechanisms; however, because shear rates are assumed small, the second pathway is considered likely. Either way, the time scale of restructuring during hindered settling must be significantly longer than previously assumed and of the order of hours.

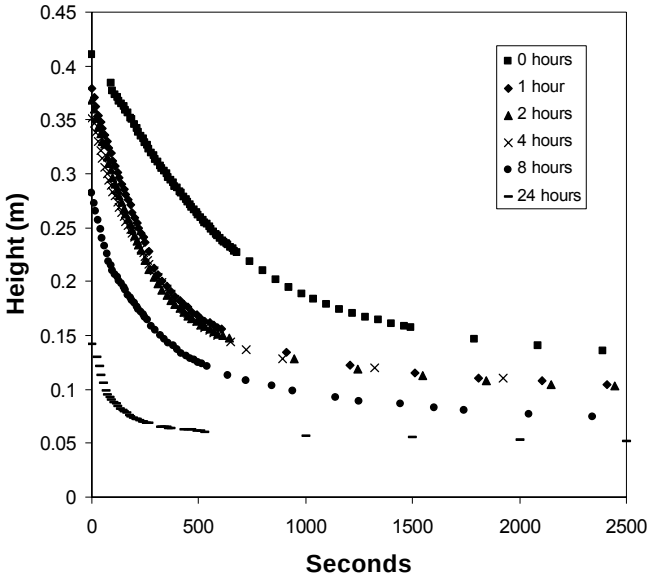

Figure 8-12 Sedimentation curves as a function of fluidization time

It now becomes necessary to relate structural changes over time to the parameters $P_y(\phi)$ and $R(\phi)$. This involved turning the water flow off, measuring the settling interface height, and using the techniques described in Chapter 2 to determine $P_y(\phi)$ and $R(\phi)$. Figure 8-12 shows the results of the sedimentation tests. Height is plotted versus an adjusted time, with $t_{adj} = t - t_f$,

and the initial volume fraction found from $\phi_{0t} = \frac{h_0}{h_{0t}}\phi_0$. Two observations can be made. First, as the fluidization time was increased, the initial settling rate increased. Second, the final equilibrium height of the sediment decreased monotonically with increasing fluidization time.

The final height was used to estimate the gel point after fluidization. Figure 8-13 shows that the gel point increases non-linearly as the fluidization time increased. For calcite, the gel point increased from ~0.21 to 0.35 (v/v), an increase of 70% in eight hours. Previously, the gel point was regarded as a measure of the strength of a flocculated network; the higher the gel point, the weaker (or more compressible) the suspension. However, in this context, the gel point also provides an indication of the solid density, since the gel point is proportional to the solid volume fraction of the aggregate. Thus, a high gel point signifies a structure, which has restructured to become denser, with an increased number of bonds, and therefore mechanical strength.

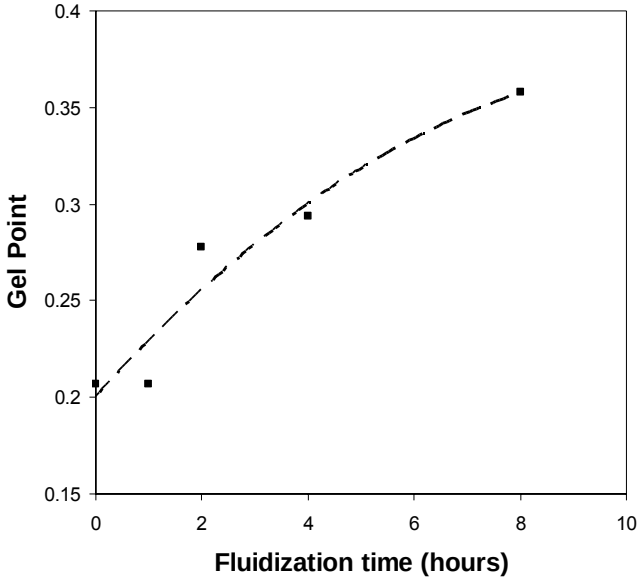

Figure 8-13 Variation in gel point with time of fluidization

Changes in $R(\phi)$ as a function of fluidization time were equally significant (Figure 8-14). The result for $R(\phi)$ as a function of time differs from the shear dependency of Chapter 5 in two ways. Unlike, Chapter 5 where change in $R(\phi)$ was only observed at moderate volume fractions, in this case $R(\phi)$ decreased over the entire range of ϕ for which the analytical solution for $R(\phi)$ was valid. Furthermore, for a given ϕ, the change in $R(\phi)$ with fluidization time was constant, over the range of ϕ expressed in the settling test (see Figure 8-15). This suggests that aggregates reach structural equilibrium at lower solid volume fractions. This is an important point, since $R(\phi)$ in this volume fraction range ($0.04 < \phi < 0.07$) is where many thickeners operate. This was not the case in the Couette shear device, because the time scale for dewatering was too short at low solid volume fraction.

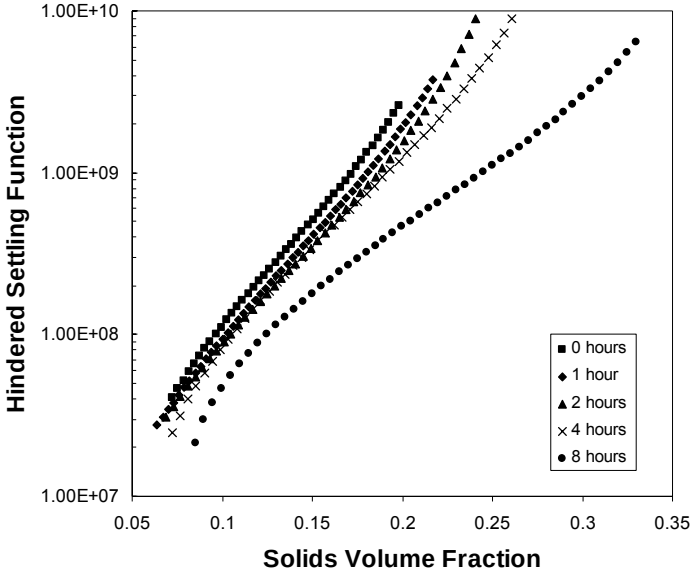

Figure 8-14 Hindered settling function as a function of volume fraction at different fluidization times

Figure 8-15 shows $R(\phi)$ as a function of time for four different volume fractions. The relationship is linear, with a constant slope for each ϕ except ϕ = 0.02, where the slope is slightly higher. Thus, the data can be fitted with a simple exponential relation;

$$R(\phi,t) = k\exp^{-mt_f}$$

where k and m are constants. In practice, there must be an upper limit for changes in $R(\phi)$ because there is a finite extent by which a floc can restructure. Therefore, these curves must flatten eventually, or possibly increase with time if floc break up occurs. Data from Aziz [6] shows that above a critical shear rate, the effect of shear is detrimental, i.e. $R(\phi)$ increases. Evidently, behaviour of

$R(\phi)$ is complex and depends on three interrelated parameters; solid volume fraction, time and shear rate.

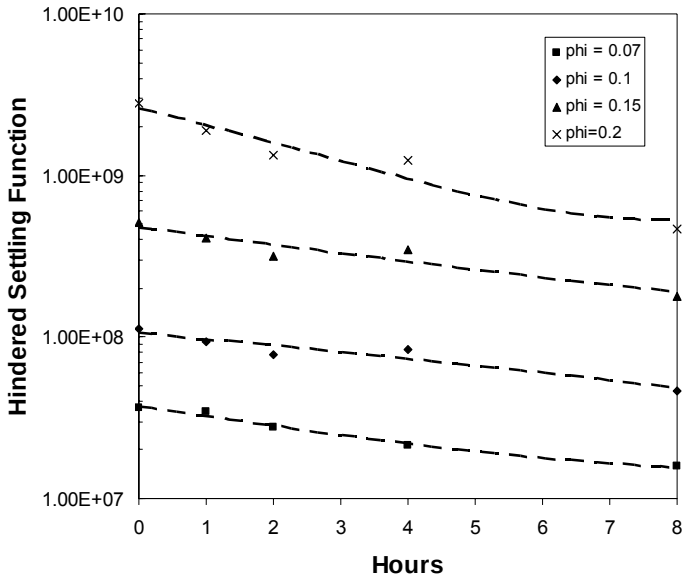

Figure 8-15 Hindered settling data as a function of fluidization time for four different volume fractions

Figure 8-16 shows the height versus fluidization time for five different flow rates, each with superficial fluid velocity $u_c < u_{mf}$. Flow rates ranged between 15.5 and 30 mL min $^{-1}$. As mentioned earlier, the flow rate of 30 mL min $^{-1}$ was probably excessive and 25 mL min $^{-1}$ appears closer to the true u_{mf}. This figure demonstrates several important points. When u_c is less than u_{mf}, the interface drops rapidly (at time $t < t_{ind}$) until drag and buoyancy forces balance. The significantly different dynamics between $u_c = u_{mf}$ and $u_c < u_{mf}$ suggests that the observed decrease in interface height during fluidization ($t > t_{ind}$) cannot be explained by insufficient velocity.

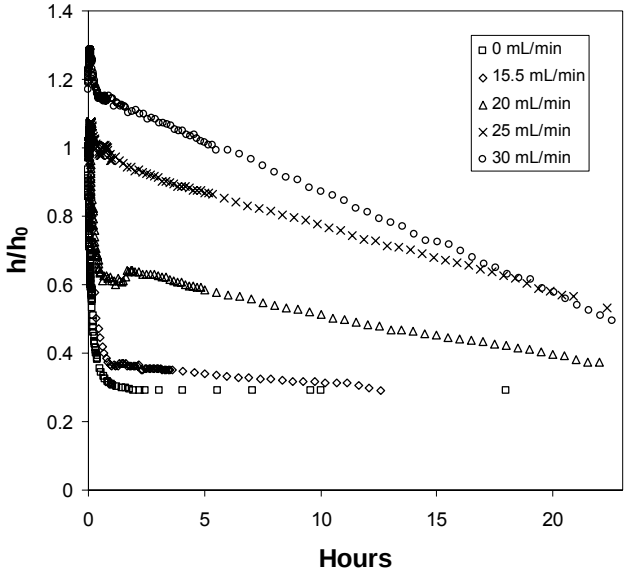

Figure 8-16 Normalised height as a function of time for different water flow rates less than the critical fluidization rate

An interesting feature of these curves is that the slope of the interface height versus time curve increased monotonically with increasing fluid velocity for $t > t_{ind}$. This implies that restructuring was more rapid at higher fluid velocities. This seems reasonable and may be explained in two ways. The increased velocity equates to a higher fluid stress and the magnitude of this stress is related to aggregate breakage (surface erosion or fragmentation) and restructuring. The other explanation is that the average solid volume fraction differed significantly in each case, since the suspension settled to lower heights, and thus higher average volume fraction. The higher volume fraction corresponds to increased strength because the number of inter-particle attractions is higher. The decrease in slope with increasing fluid velocity could be examined further by applying shear simultaneous to fluidization. Keeping the water flow rate constant isolates the effect of shear.

In a separate series of experiments, calcite was flocculated at three different polymer dosages, 20, 40 and 60 g tonne $^{-1}$. Figure 8-17 shows the normalised height as a function of fluidization time. Note that because the aggregates settled faster at higher dosages, the flow rates were different for each case (17 mL min $^{-1}$, 30 mL min $^{-1}$ and 62 mL min $^{-1}$ respectively). Furthermore, because the interface height was not measured post fluidization, $P_y(\phi)$ and $R(\phi)$ could not be determined.

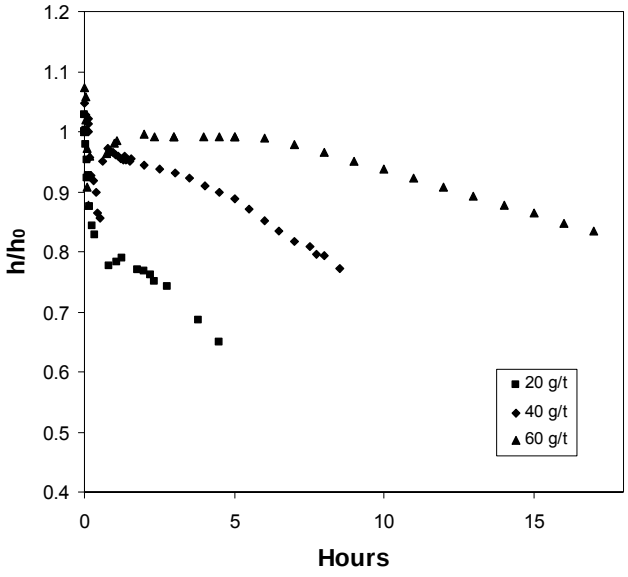

Figure 8-17 Normalised height versus time of fluidization for three flocculant dosages; ■ 20 g tonne $^{-1}$ and 17 mL min $^{-1}$; ◆ 40 g tonne $^{-1}$ and 30 mL min $^{-1}$; ▲60 g tonne $^{-1}$ and 62 mL min $^{-1}$

At 60 g tonne $^{-1}$, the slope is almost zero for the first 7 hours implying strong aggregates able to resist breakage or deformation. When the dosage decreased, the slope of the interface height versus fluidization time curve became increasingly steep, implying more rapid restructuring. The results for the

different flocculant dosages, while not comprehensive (since $P_y(\phi)$ and $R(\phi)$ were not determined), demonstrate that the settling behaviour of flocs in fluidized environments depend on the flocculant dosage, a parameter routinely varied during thickener operation. This result encourages further experimental studies of flocculant dosage effects, a subject for further work outside the scope of this thesis.

The extent of restructuring was expected to depend on the initial state of the aggregates. In the following experiments, the aim was to identify flocculation conditions, which produced an initial floc structure most susceptible to restructuring. A baffle reactor was used to flocculate calcite for a range of shear rates, times and flocculant dosages. Based on the work discussed in Chapter 3, three conditions were selected for fluidization, corresponding to 5, 10 and 30 seconds mixing time, a polymer dose of 20 g tonne $^{-1}$ and a mixing speed of 700 rpm. The polymer dose of 20 g tonne $^{-1}$ was chosen for the baffle reactor flocculation to provide a weak aggregate, which was expected to restructure more readily than flocs produced in the pipe reactor at 40 g tonne $^{-1}$.

Figure 8-18 to Figure 8-20 show fluidization results for calcite flocculated at 5,10 and 30 seconds respectively. In each case, four different fluidization curves are shown along with the base settling case. There was very little difference between the 10 and 30 second results. However, the 5 second result showed a lack of agreement between the four fluidization experiments. The reason for this is not clear, but may be attributed to broader size distributions at the shorter mixing time. Microstructural variation between experiments affects fluidization behaviour in the bed, as the fluid path will be different each time. To obtain reproducible results, inhomogeneities or channelling phenomena must be minimised as far as possible, although it must be accepted that flocculated material is not an ideal candidate for fluidization.

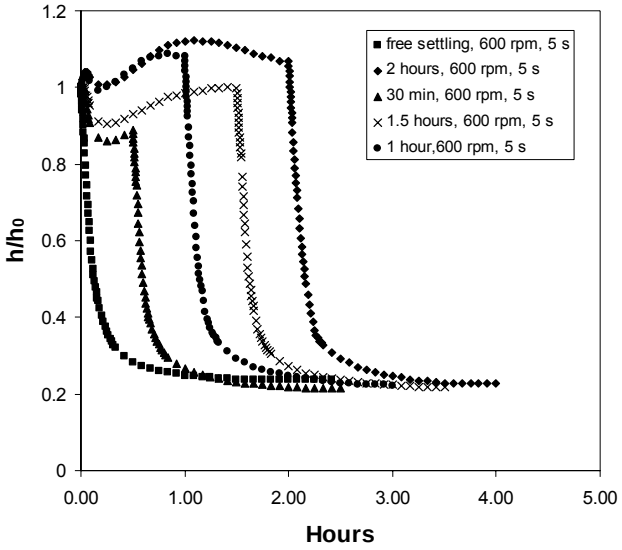

Figure 8-18 Normalised height as a function of time at the critical fluidization velocity for flocs produced in baffle reactor and sheared for 5 seconds and 600 rpm

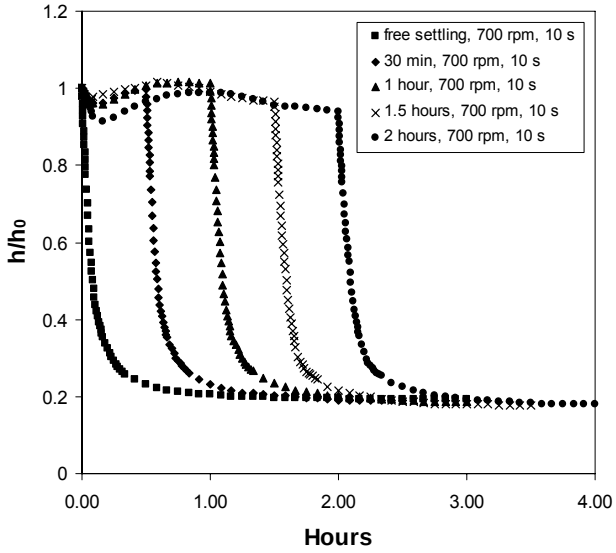

Figure 8-19 Normalised height as a function of time at the critical fluidization velocity for flocs produced in baffle reactor and sheared for 10 seconds and 700 rpm

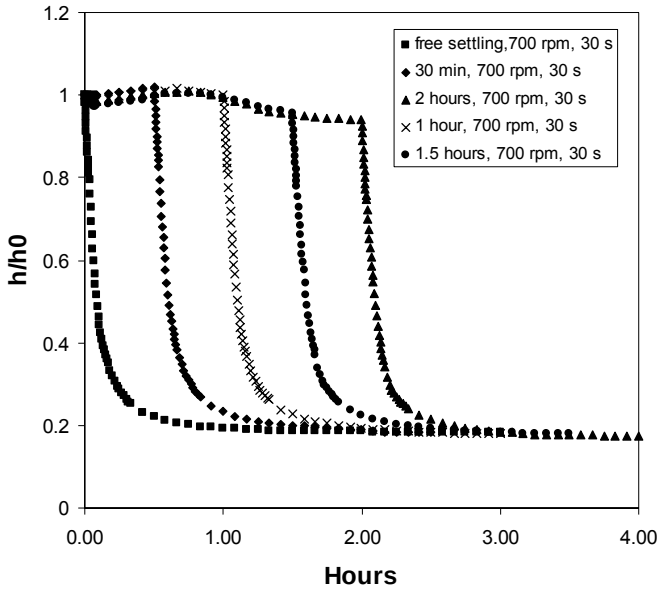

Figure 8-20 Normalised height as a function of fluidization time for flocs produced in baffle reactor and sheared for 30 seconds and 700 rpm

Because of the irreproducibility, the 5 second result will not be considered further. For the other two results, the height increased over the first hour. This result was different to the pipe reactor where the suspension height initially rose and fell within the first ten minutes. In the second hour, the height decreased in line with the pipe reactor results. However, the slope was lower (0.042) compared to the pipe (0.054). Therefore, restructuring of baffle reactor flocs occurred more slowly than the pipe flocs. Another important difference was evident in the sedimentation curves. Neither the rate nor the equilibrium height changed significantly as fluidization time increased.

The fluidization was only measured for two hours as longer times caused the interface to become cloudy and difficult to distinguish. This could be due to erosion of particle or fragments from the surface. Alternatively, it could be that

the capture efficiency during flocculation was lower. Because of the low capture efficiency, not all particles are incorporated into the floc. However, the particles can still become entrained within the floc structure. Over time, the entrained particles escape. An important factor determining the maximum fluidization time is the polymer dosage. In contrast, the interface height for flocs formed in the pipe reactor remained sharp for sixteen hours, where the dosage was 40 g tonne $^{-1}$.

Figure 8-21 and Figure 8-22 show $R(\phi)$ as a function of fluidization time for flocs forming at 10 and 30 second mixing times. These results show that aggregates formed in the baffle reactor, changed less over time than in the case of the pipe reactor flocs. For volume fractions up to $\phi \sim 0.15$, $R(\phi)$ did not change with time, while for $\phi > 0.15$, $R(\phi)$ decreased with increasing fluidization time. The gel point for these suspensions ranged from 0.26 to 0.3 v/v

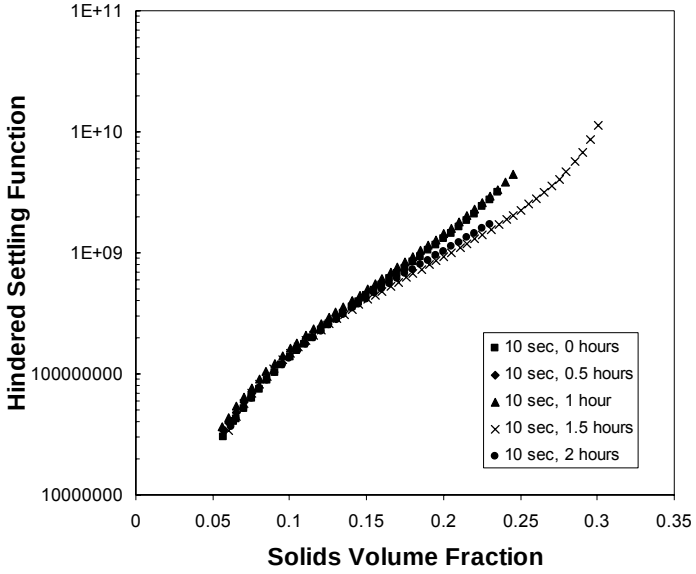

Figure 8-21 Hindered settling function for flocs produced in baffle reactor at 10 seconds as a function of fluidization time

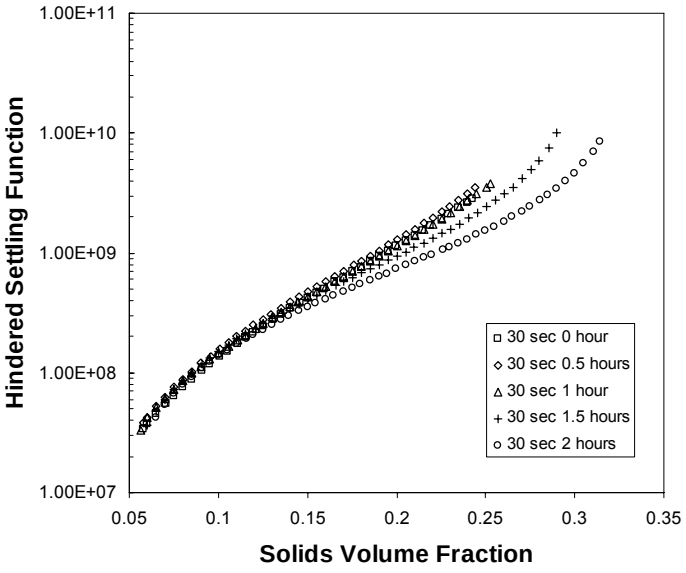

Figure 8-22 Hindered settling function for flocs produced in baffle reactor at 30 seconds as a function of fluidization time

Figure 8-23 compares $R(\phi)$ at zero and two hours fluidization for the two mixing times. For ϕ less than 0.13, the curves lie almost on top of each other, implying that for low volume fractions, fluidization does not reduce the hydrodynamic drag on baffle reactor flocs. Above ϕ ~ 0.13 v/v, the suspension flocculated at 30 seconds mixing had a significantly lower $R(\phi)$ after two hours fluidization, than for zero fluidization time. The same trend was observed for suspension flocculated for 10 seconds, but the change in $R(\phi)$ was lower. Therefore, based on the data collected, aggregates formed at longer mixing times appear more predisposed to structural rearrangement.

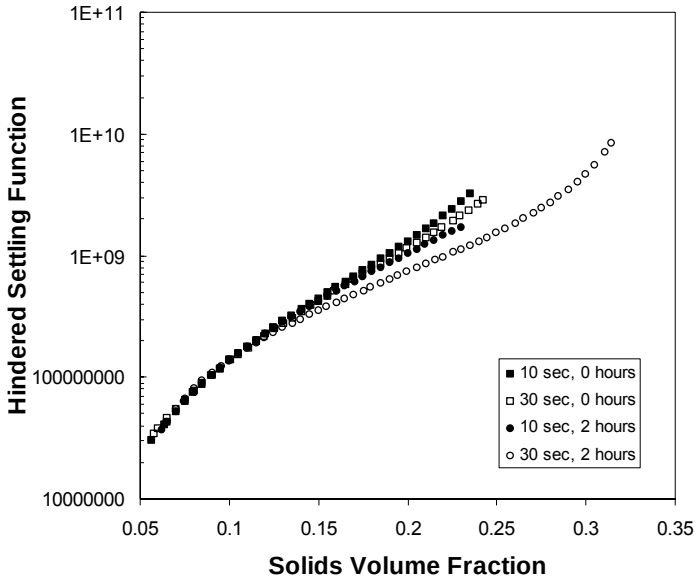

Figure 8-23 Hindered settling function for flocs produced in baffle reactor with 10 and 30 seconds mixing and zero and 2 hours fluidization

Figure 8-24 and Figure 8-25 show the compressive yield stress for suspension flocculated for 10 and 30 seconds in a stirred baffle reactor. In both cases, as

fluidization time increased, $P_y(\phi)$ shifted to higher ϕ. This behaviour is similar to the shear effect in the Couette, although less pronounced. The interpretation is also different. Previously, the increased gel point signified a weaker network, since lower compressive force was required to consolidate the aggregates. The increased gel point in Figure 8-24 is interpreted to mean denser or smaller aggregate were formed as a result of fluidization, which once formed will not deform readily. Figure 8-26 compares the compressive yield stress for zero and two hour fluidization for the two mixing times. The compressive yield stress was higher for the shorter mixing time.

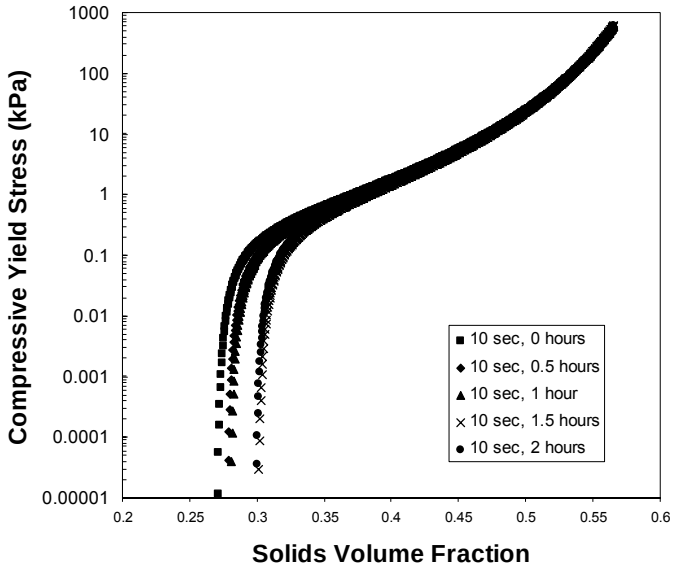

Figure 8-24 Compressive yield stress for flocs produced in baffle reactor at 10 seconds as a function of fluidization time

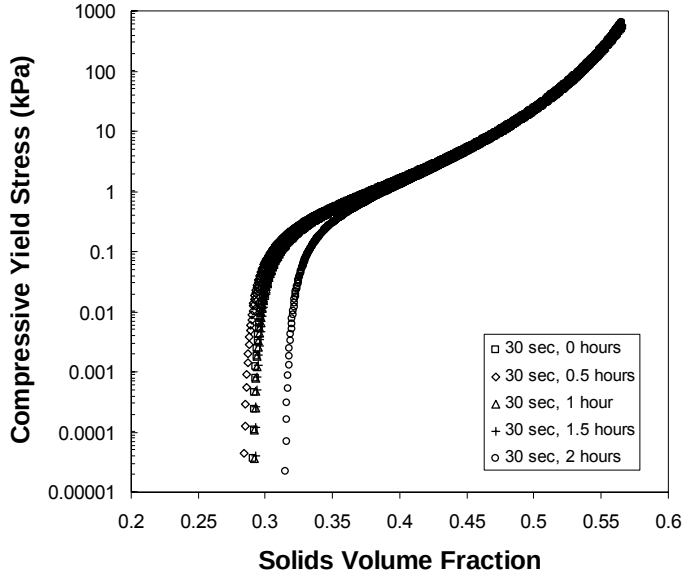

Figure 8-25 Compressive yield stress for flocs produced in baffle reactor at 30 seconds as a function of fluidization time

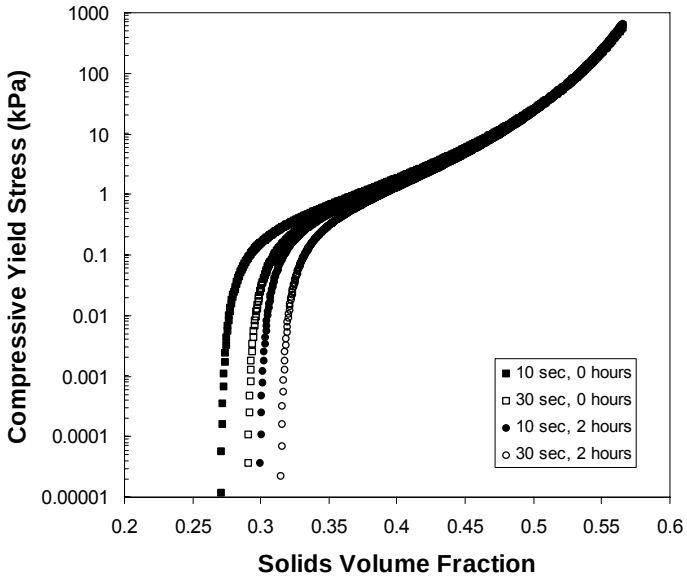

Figure 8-26 Hindered settling function for flocs produced in baffle reactor with 10 and 30 seconds mixing and zero and 2 hours fluidization

Figure 8-27 and Figure 8-28 show FBRM results obtained during fluidization of aggregates formed in a stirred baffle reactor, and pipe reactor, respectively. In both cases, the mean square weighted chord length, (related to aggregate size), decreased linearly with fluidization time. The decrease could mean that flocs are breaking up into smaller aggregates. If this were to happen without densification, settling rates would decrease. This is not supported by the interface height data. The other possibility is that the aggregates are breaking and immediately rearranging to form aggregates with a higher density.

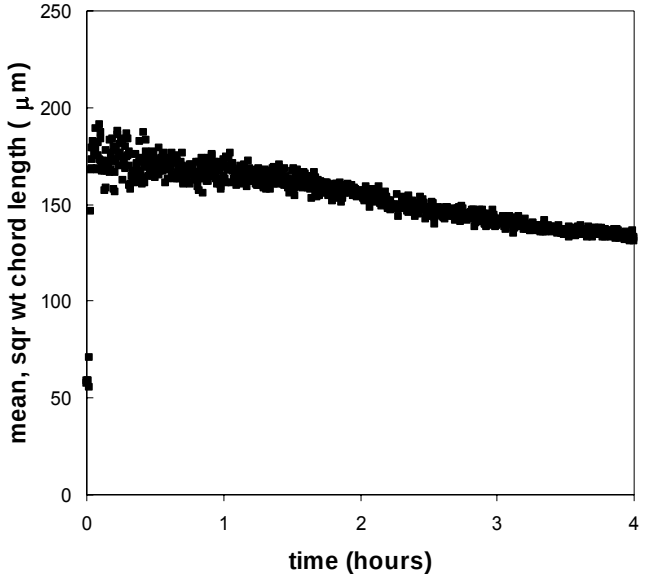

Figure 8-27 Mean square weighted chord length versus fluidization time for 20 g tonne $^{-1}$ flocculated in baffle reactor (30 seconds 700 rpm)

The FBRM results show that aggregates size formed in the baffle reactor (170 μm) were smaller than in the pipe (240μm). This is due to the higher average shear in the baffle reactor. If the smaller baffle aggregates are denser (relative to the larger pipe flocs), the potential to restructure during fluidization

will be lower, as will the time dependence observed in $R(\phi)$. It should be made clear that the height of the FBRM probe was fixed, therefore changes in chord length relate to a fixed position in the column.

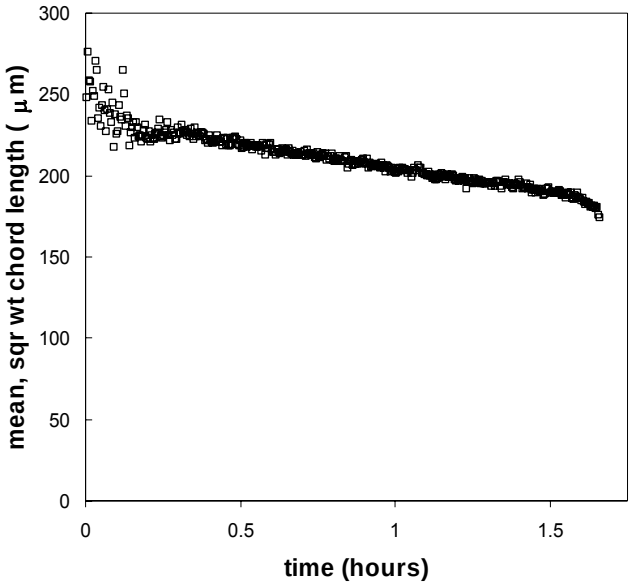

Figure 8-28 Mean square weighted chord length versus fluidization time for 40 g tonne $^{-1}$ flocculated in pipe reactor

Figure 8-29 and Figure 8-30 plot the density of aggregates versus equivalent Stokes diameter for flocs flocculated in a stirred baffle and pipe reactor respectively. Two data sets are shown in each figure, corresponding to zero and two hours of fluidization. For flocs produced in the baffle reactor, the flocs appear to be less dense and larger after two hours of fluidization (Figure 8-29). In the pipe reactor (Figure 8-30), the effect of fluidizing the aggregates was less pronounced, with no apparent change in density, and possibly a decrease in aggregate size.

These observations were supported by the calculated weighted mass averages shown in Table 8-1. For the baffle reactor flocs, the weighted mass average density decreased from 1803 to 1449 kg m $^{-3}$ due to fluidization, while the fractal dimension decreased from 2.23 to 1.69. The weighted mass average size increased from 126 to 147 μm and the settling velocity decreased from 24.6 to 17.6 m h^{-1}.

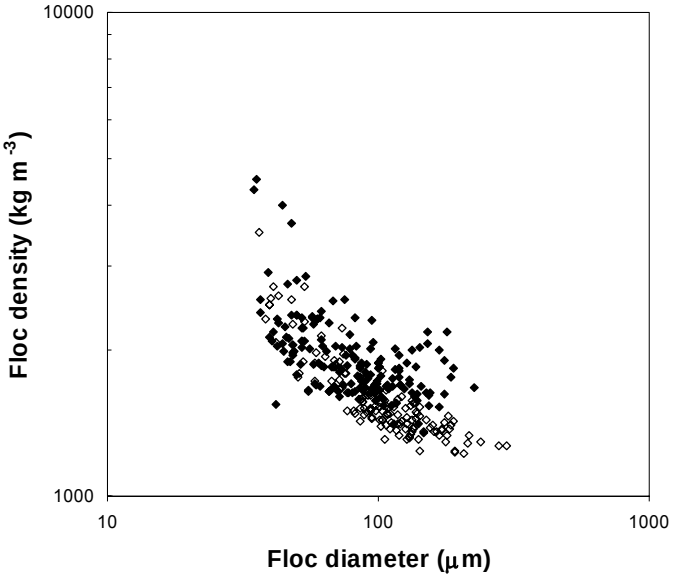

Figure 8-29 Baffle reactor ◆ sample at t=0 hr ◇ sample at t=2 hr

For the pipe reactor, fluidization for 2 hours resulted in the mass average size decreasing from 242.5 to 153.4 μm, the fractal dimension decreasing from 2.50 to 2.25 and settling rate decreasing from 37.6 to 17.3 m h^{-1}, while the weighted mass average density remained constant. This indicates that pipe reactor flocs were larger and less dense than those formed in the baffle reactor. This could be explained purely by the higher flocculant dosage in the pipe reactor, although hydrodynamics is likely to also be a factor.

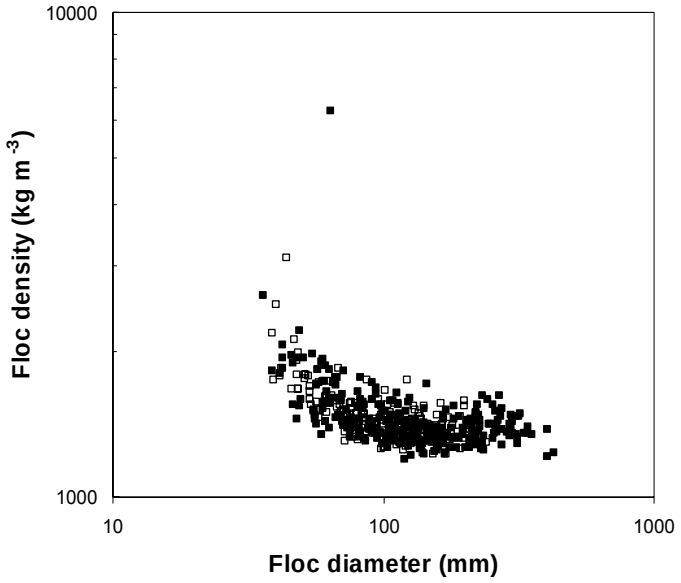

Figure 8-30 Pipe reactor ■ sample at t=0 □ sample at t=2 hr

From the fluidization and FBRM data where the settling rate increases and the particle size decreases, it is expected that the floc density would increase to account for the settling rate increase. This was not the case for the FDA data and this result remains largely unexplained. The calculations were based upon a number of assumptions, including primarily;

- Stokes settling
- Particle shape

To calculate the density of the aggregates, it was assumed that each aggregate settled according to Stokes law. For each aggregate, a particle Reynolds number Re_p was calculated and it was found that not every aggregate satisfied the above assumption. However, in most cases the calculated Re_p did not greatly exceed 0.2; of the aggregates that did, 60 % were less than 0.5. Across all the particles counted, the maximum Re_p was 9. To calculate an equivalent Stokes diameter,

the aggregates were approximated as prolate ellipsoids. Based on qualitative analysis of the images, this was considered a reasonable assumption. Obviously, flocs are highly irregular objects, and any assumed shape will not apply to every floc. This fact could partly account for the conflicting density results.

To determine the error associated with the assumed Stokes settling, the density was calculated using an empirical expression for the drag coefficient in the intermediate region [37]. This was done for the Re_p =9 particle, to indicate the worst case scenario. In this case, the calculated density was 12 % higher than had Stokes settling been assumed. It is clear on this basis that while assuming Stokes settling may affect the result quantitatively, the observed trends will remain the same. Another factor which may have contributed to the conflicting FDA result is the method of sampling. Sampling inevitably introduces an unquantifiable amount of shear to the flocs, causing breakage, collapse or consolidation forming different flocs. Assuming samples were collected in the same way, the data trends should be unaffected even if the absolute values change. This assumption may not be valid since sampling will be more detrimental to larger flocs.

For the two samples subjected to no fluidization, the sampling method was the same, samples being colleted immediately before settling occurred. For the two samples fluidized for two hours, the sampling was different. The flocs were sampled directly from the column at approximately 10 cm from the base both times. If aggregates in the column were of uniform size, the sampling height would not matter. However, the results show a clear distribution of floc size and density. In the fluidization column, it is reasonable to expect that over time the aggregates will segregate; so that the larger, denser aggregates accumulate near the bottom. Therefore, samples collected at a height 10 cm from the base represent aggregates that were overall less dense and smaller than were samples collected closer to the bottom. Another possibility is that the sample size was not large

enough to provide a statistically representative indication of the floc properties. On average, approximately 240 flocs were analysed in each experiment. Larger sample sizes were not obtained because of the lengthy time required to measure and analyse the data.

Density, size and velocities are quoted in Table 8-1 as mass weighted averages. The mass weighting was used to account for the fact that a large proportion of mass may be contained within a small number of the aggregates. Calculating number averages could skew the data towards smaller particles, which contain a small fraction of the total mass and therefore is unrepresentative of the behaviour of bulk suspension, in which the larger particles exert a greater influence. However, number averages were also calculated, and similar trends were observed, so the weighting method does not influence the trends observed in the FDA analysis.

Table 8-1 Mass weighted averages from Floc Density Analysis

	Pipe reactor (40 g tonne $^{-1}$)		Baffle reactor (20 g tonne $^{-1}$)	
Fluidization time (hours)	0	2	0	2
Weighted velocity (m h^{-1})	37.6	17.3	24.6	17.6
Weighted Average Diameter (μm)	243	153	126	148
Weighted Average Density (kg m^{-3})	1371	1381	1803	1449
Fractal dimension	2.50	2.25	2.23	1.69

8.5.1 Further work

This scope for further work using fluidization is broad. Possibilities for future research include investigating the following parameters;

- flocculant dose
- flocculant type
- fluid shear rate
- water flow rate

At lower fluid velocities the suspension had already settled, therefore sedimentation curves post fluidization were not measured and $R(\phi)$ could not be determined for $u_c < u_{mf}$. It may be possible to determine $R(\phi)$ directly from the initial curve where $u_c < u_{mf}$. This would require modification to the algorithm used to calculate $R(\phi)$ by incorporating the contribution of fluid velocity to the force balance

8.6 Conclusions

The fluidization of aggregates in a column with a continuous up flow of water was investigated. The result showed significant improvement in suspension dewatering due to the hydraulic agitation and improved with increasing time. The suspension interface decreased at a constant rate during fluidization. Because the solid volume fraction was less than the gel point, and the water flow rate was constant, the decreasing interface height must be due to an increase in hindered settling rate of the aggregates.

Fluidization times ranging between 30 minutes and 24 hours were considered and resulted in a continual improvement in dewatering as time increased. By fluidizing and subsequently settling, $P_y(\phi)$ and $R(\phi)$ were determined as functions of time. The data was fitted with a simple exponential relation; $R(\phi,t) = k\exp^{-mt_f}$ As a result of fluidisation for 8 hours, $R(\phi)$ decreased from

3 x 10^{9} to 5 x 10^{8}, at a volume fraction of 0.2. The compressive yield stress and gel point also increased non linearly with fluidization time. For calcite, the gel point increased from ~0.21 to 0.35 v/v, an increase of 70% in eight hours.

Comparison with the shear dependency in the Couette showed that the $R(\phi)$ behaviour with increasing time is different, decreasing for all ϕ from ϕ_0 to ϕ_g. This suggests that the aggregates were reaching equilibrium in the fluidisation cell, because the time available for restructuring was longer.

When the water flow rate was less than the minimum, the slope of the interface decreased. This implies that restructuring is more rapid at higher fluid velocities and higher fluid stresses. Different polymer dosages were studied and the slope of the curve showed similar behaviour. At 60 g tonne $^{-1}$, the slope was close to zero for the first 7 hours implying that the aggregates were not restructuring. When the dosage was decreased to 40 and again to 20 g tonne $^{-1}$, the slope became increasingly steep implying restructuring of aggregates was more pronounced.

A baffle reactor was used to flocculate calcite for 5, 10 and 30 seconds mixing time at a mixing speed of 700 rpm. A polymer dose of 20 g tonne $^{-1}$ was chosen to provide a weak aggregate, which may restructure readily. However, these attempts to produce an initial floc structure more susceptible to restructuring were largely unsuccessful. However, this did show that aggregates formed at longer mixing times in the stirred baffle reactor were more predisposed to structural rearrangement, than shorter mixing times.

FBRM results show that the mean square weighted chord length, (related to aggregate size), decreased linearly with fluidization time. The decrease could

mean that flocs are breaking up into smaller aggregates and immediately rearranging to form aggregates with a higher density.

Aggregate density versus diameter was measured before and after fluidization. Flocs produced in the baffle reactor, appeared to be less dense and larger after fluidization for two hours (Figure 8-29). For the baffle reactor flocs, the weighted mass average density decreased from 1803 to 1449 $kg\,m^{-3}$ due to fluidization, while the weighted mass average size increased from 126 to 147 μm

In the pipe reactor (Figure 8-30), the effect of fluidizing the aggregates was less pronounced, with no apparent change in density, and decrease in the mass average size from 242.5 to 153.4 μm. This indicates that pipe reactor flocs were larger and less dense than those formed in the baffle reactor. This could be explained purely by the higher flocculant dosage in the pipe reactor, although hydrodynamics is likely to also be a factor.

Chapter 9

Conclusions

In this thesis, the effect of shear on dewatering was investigated at laboratory, pilot and plant scales. Techniques for improving the characterisation of suspension dewatering were developed and these were applied to simulate the effect on thickening. The results show promise as the new techniques predict significant improvement in dewatering by including the effect of shear in the laboratory, so that dewatering is measured under conditions more representative of full scale thickening. This partly bridged the gap between previous simulation efforts, which tended to grossly under predict full-scale plant data. The results of Chapter 8 are important in this regard, since the model does not take into account floc densification and subsequent changes in $P_y(\phi)$ and $R(\phi)$.

9.1.1 1−D Model Validation in the absence of shear

To validate the model, a tall pilot column dewatered a flocculated calcite feed. To approximate one-dimensional flow with minimum shear, experiments were conducted in a tall narrow column with no moving parts. The dewatering of calcite was characterised and the column simulated to determine operating criteria. The permeability limited flux regime was found to correspond to solids fluxes 0.3 tonne m^{-2} h^{-1} and above.

The 1−D model was validated by operating the column under pseudo steady state conditions for two different solid fluxes, 0.3 and 0.03 tonne m^{-2} h^{-1} and bed

heights ranging between 0.3 and 1.0 metre. Furthermore, different flocculation conditions were considered. The results showed that the underflow density increased marginally with increasing height, although at the time, the variance was assumed to be within experimental error. In hindsight, this trend is consistent with Chapter 7 and demonstrates a possible residence time effect. However, given the lack of control over operating conditions, (slurry feed rate, flocculant dosing) and uncertainty regarding steady state, the agreement was considered reasonable, with model predictions for underflow solids differing by between 1 and 20 % of the experimental result.

9.1.2 Shear characterisation technique

The effect of shear on dewatering was investigated using a Couette shear device. Flocculated calcite was sheared at several shear rates ranging between 0.8 and 8 s^{-1} for several flocculant dosages, the results showing a significant change in dewaterability. The change depended also on the flocculant dose. These experiments showed that shear caused dewaterability to improve up to a certain critical shear rate, beyond which dewaterability was adversely affected. The relationship between critical shear rate and flocculation conditions was investigated using different flocculant dosages. The shear modified $P_y(\phi,\dot{\gamma})$ and $R(\phi,\dot{\gamma})$ can be input to the 1−D model, therefore incorporating shear indirectly. As a result, for the optimum shear of 5.8 s^{-1} the model predicted solid flux increased by an order of magnitude, when ϕ_u was ~ 0.3.

The Couette geometry was chosen to provide uniform and quantifiable shear. Furthermore, mechanistic information was sought, since in Couette flow, no normal stresses act in the direction of rotation, unlike with a rake. The overall results showed that dewatering was faster in the Couette device than for a simple

rake, indicating the importance of pure shear in dewatering, compared to pressure gradients caused by the rake. Comparison between results for the optimum determined raked and Couette shear, showed that the better dewaterability in the Couette, was due to difference in $R(\phi)$, as the compressive yield stresses were almost identical. Issues including the region and volume of material sheared may be important in this comparison.

9.1.3 Plant and pilot studies involving shear

The above Couette test was applied to characterise dewaterability of a feed to a full sized plant thickener. An optimum shear rate $\dot{\gamma}_{opt}$ was determined by identifying the minimum $R(\phi,\dot{\gamma})$. This along with $P_y(\phi,\dot{\gamma}_{opt})$ was input into the model and the maximum solids flux expected at this optimum shear was predicted. In this way the predicted solids flux curve could be compared to plant data. When characterised in the absence of shear, the model predicted a flux of 0.0015 tonne m^{-2} h^{-1}, which was over 100 times lower than the actual operating flux of 0.2 tonne m^{-2} h^{-1}. However, when an optimum shear was applied to the settling suspension, the predicted flux increased by a factor of 10 at the underflow solids concentration. Thus, the error was reduced to a factor of ten, but the prediction was still an order of magnitude too low.

Thus, the results of this chapter suggested that the 1−D model with its current inputs ($P_y(\phi)$ and $R(\phi)$ corresponding to $\dot{\gamma}_{opt}$), is inadequate for predicting dewatering in large scale devices such as thickeners. Still, the results show that shear was important, since by applying shear in the Couette and simulating the thickener, the error was half that of the un-sheared simulation.

To try to understand this result, the pilot work was revisited because greater control over experimental conditions was possible. To introduce shear to the tall column, rotating concentric cylinders were installed and the effect of bed height on underflow density was determined as a function of shear. The effect of shear depended on bed height. At low bed heights, increasing the shear from 0 to 1.6 s^{-1}, by increasing the rotation rate from 0 – 20 rpm, caused the underflow solid volume fraction to increase from ~0.11 to 0.16 v/v. The predicted underflow density by the model was 0.1 and 0.12 v/v, slightly lower than the experimental results. Increasing the bed height resulted in higher underflow concentrations 0.17 v/v (2 m) and 0.23 v/v (4 m). Shearing the two-metre bed was effective, increasing the underflow concentration to 0.21 v/v, however, shearing at four metres did not produce a change at steady state, possibly due to clogging.

The effect of shear on underflow density was secondary to bed height. For example, at one metre bed, the increase in ϕ_u due to shear was 0.11 to 0.16 v/v. Conversely, increasing bed height from one to two metres caused ϕ_u to increase from 0.11 to 0.17 v/v, while increasing from one to four metres, ϕ_u increased from 0.11 to 0.23 v/v

9.1.4 Fluidized bed

The tall column work showed an increase in underflow density with increasing bed height that was not expected from the model prediction. The bed height dependence could be explained if dewatering were not constant, but improved over time, since at four metres bed height, the residence time was eight times longer than at one metre. Improved dewatering is linked to possible time dependent restructuring of aggregates, which would cause associated change in

$R(\phi)$. Suspensions were fluidized for varying times corresponding to the times experienced by the flocs settling in the column at the different bed heights. Longer and shorter times were also considered. This allowed $P_y(\phi)$ and $R(\phi)$ to be determined, demonstrating a dependence of hindered settling function and compressive yield stress on time.

The fluidization of aggregates resulted in a significant improvement in suspension dewatering. Over time, the interface decreased at a constant rate during fluidization. Fluidization times ranging between 30 minutes and 24 hours were considered and resulted in a continual improvement in dewatering as time increased. By fluidizing and subsequently settling, $P_y(\phi)$ and $R(\phi)$ were determined as functions of time. The data was fitted with a simple exponential relation; $R(\phi,t) = k\exp^{-mt_f}$ As a result of fluidisation for 8 hours, $R(\phi)$ decreased from 3 x 10^{9} to 5 x 10^{8}, at a volume fraction of 0.2. The compressive yield stress and gel point also increased non linearly with fluidization time. In eight hours, the gel point increased from ~0.21 to ~0.35 v/v, an increase of 70%

Water flow rates less than the minimum caused the slope of the interface to decrease implying that restructuring was more rapid at higher fluid velocities and therefore stresses. A similar result was found for different polymer dosages. At 60 g tonne $^{-1}$, a slope of approximately zero resulted, while decreasing the dose to 40 and again to 20 g tonne^{-1}, caused the slope to become increasingly steep.

FBRM results show that the mean square weighted chord length, (related to aggregate size), decreased linearly with fluidization time. The decrease could mean that flocs are breaking up into smaller aggregates and immediately rearranging to form aggregates with a higher density. Aggregate density versus diameter was measured before and after fluidization. Flocs produced in the

baffle reactor, appeared to be less dense and larger after fluidization for two hours (Figure 8-29). For the baffle reactor flocs, the weighted mass average density decreased from 1803 to 1449 $kg\,m^{-3}$ due to fluidization, while the weighted mass average size increased from 126 to 147 μm.

9.1.5 Further work

The results reported in this thesis identify three major areas which could be investigated further;

- Continuous dewatering studies in the tall column could be extended by considering the effect of shearing at different heights in the column. The fluidization results in Chapter 8 suggest that shear densification occurs at solid volume fractions below the gel point. It would be interesting to observe the result of shearing; just above the bed surface, just below the bed surface and just above the base of the column. Such work could identify an optimum vertical height for raking in a thickener. The column could also be operated at lower solids fluxes so that dewatering is limited by the compressibility of the bed. In this case the bed height would be important and the result of shear could be different than observed in permeability limited operation, investigated in this thesis.
- Shear characterisation in the Couette could be extended to investigate material with significantly different settling rates. Such studies could establish a relationship between the time material experiences shear at a given solid volume fraction. The result may support the concept of long time fluidization in order to measure shear dewatering behaviour at equilibrium. Differential settling rates could be achieved by varying the type of solid, polymer molecular weight or initial solid concentration for example. Another experiment could consider shear in the Couette during

different stages of dewatering. Then the results of Chapter 5 (in which case shear was applied for the entire duration) could be compared to experiments in which shear is applied only during hindered settling, or only during consolidation. Such a study could shed light on proportionally how much of the improvement to dewatering is due to shearing the suspension above the gel point (i.e. a networked bed) and how much shear is affecting individual flocs, like in fluidization. Likewise, a Couette cell could be designed in which only the bottom 10 centimetres rotates. The result could be applied to shear in the tall column at different heights.

- The technique of fluidizing flocculated suspensions for extended time has been developed only recently and significant development is still possible and required. The results of Chapter 8 suggest that this method has significant potential to improve the existing characterisation methods; primarily because dewatering measurements are obtained under conditions more closely representative of hydrodynamic conditions inside a thickener. The next step in developing the technique would be introducing shear to the suspension during fluidization. This might be achieved by up-flowing water through a suspension of flocs in a Couette geometry, or alternatively by mechanical agitation or vibration. It is thought that the improvement in dewatering observed due to shear or fluidization alone could be even more significant. For example, a change in $R(\phi)$ due to 8 hours of fluidization may occur in less time when shear is applied. Other avenues of ongoing research include; varying the flocculant dosage, polymer type and water flow rate. The latter could be applied to determine $R(\phi)$ directly from a change in interface height during fluidization.

Appendix 1

Table A-1 Height versus time data from three replicate batch settling tests

Settling Test 1		Settling Test 2		Settling Test 3	
$h(t)$	(t)	$h(t)$	(t)	$h(t)$	(t)
39.2	0	38.8	0	37.35	0
37.2	10	36.8	10	36.35	5
35.5	20	34.9	20	35.7	10
33.75	30	32.9	30	35	15
31.85	40	30.85	40	34.4	20
30.3	50	29.35	50	33.7	25
29.1	60	27.95	60	33	30
27.9	70	26.95	70	32.35	35
26.85	80	26.1	80	31.7	40
25.95	90	25.4	90	31.05	45
25.2	100	24.7	100	30.4	50
24.4	110	24.2	110	29.75	55
23.9	120	23.6	120	29.2	60
23.4	130	23.15	130	28.1	70
23	140	22.8	140	27.25	80
22.5	150	22.4	150	26.3	90
22.1	160	22.1	160	25.5	100
21.85	170	21.8	170	24.8	110
21.5	180	21.5	180	23.6	130
21.2	190	21.2	190	23.1	140
20.9	200	21	200	22.7	150
20.55	210	20.75	210	22.25	160
20.3	220	20.5	220	21.9	170

20.05	230	20.3	230	21.15	190
19.8	240	20.1	240	20.95	200
19.5	260	19.8	260	20.6	210
19.1	280	19.45	280	19.9	240
18.75	300	19	300	18.75	300
18.45	320	18.7	320	17.5	390
18.15	340	18.45	340	16.55	480
17.9	360	18.2	360	15.6	600
17.65	380	18	380	14.6	810
17.45	400	17.75	400	13.3	1260
17.25	420	17.55	420	11.4	3000
17.05	440	17.4	440	10.7	4350
16.8	460	17.2	460		
16.6	480	17.05	480		
16.5	500	16.9	500		
16.4	520	16.75	520		
16.3	540	16.6	540		
16.15	560	16.45	560		
16	580	16.35	580		
15.9	600	16.2	600		
15.6	660	16.1	620		
15.4	687	16	632		
15	777	15.15	812		
14.2	1027	14.8	932		
13.95	1137	14.45	1052		
13.6	1317	14.2	1142		
13.3	1467	13.85	1292		
12.95	1647	13.5	1442		
12.9	1767	13.35	1592		
12.6	1977	12.85	1892		
12.4	2127	12.6	2132		
12.35	2307	12.4	2432		
12.25	2427	12	3092		

12	2787	10.2	9000
11.85	3027		
11.7	3327		
11.6	3987		
10.1	12000		

Table A-2 Fitting Parameters, $R(\phi)$ Baffle reactor

r_a	r_b	r_c
2.01E+11	3.38	-1194000

Table A-3 Fitting Paramters, $P_y(\phi)$ Baffle reactor

ϕ_g	p_a	p_b	p_m	p_n
0.182	28.86	6.80	0.065	2.26

Table A-4 Fitted Parameters, $R(\phi)$ Pipe Reactor

r_a	r_b	r_c
1.91E+11	3.13	3591000

Table A-5 Fitting Paramters, $P_y(\phi)$ Pipe Reactor

ϕ_g	p_a	p_b	p_m	p_n
0.080	46.71	7.03	0.02	2.85

Table A-6 Fitting Parameters, $R(\phi)$ for the different flocculant dosages in the tall column validation of Chapter 4

Flocculation condition	r_g	r_a	r_b	r_m	r_n
25 g tonne^{-1}, 2m	0.2	3.17	0.156	0	2.76
50 g tonne^{-1}, 2m	0.2	3.17	0.0853	0	4.46
75 g tonne^{-1}, 2m	0.2	3.14	0.126	0	3.48
25 g tonne^{-1}, 10m	0.2	3.17	0.0408	0	5.90
50 g tonne^{-1}, 10m	0.2	3.16	0.118	0.0036	3.45
75 g tonne^{-1}, 10m	0.2	3.18	0.192	0	2.38

Table A-7 Fitting Paramters, $P_y(\phi)$ for the different flocculant dosages in the tall column validation of Chapter 4

Flocculation condition	ϕ_g	p_a	p_b	p_m	p_n
25 g tonne^{-1}, 2m	0.234	75.10	5.35	10.00	4.00
50 g tonne^{-1}, 2m	0.168	59.68	11.08	0.0026	3.43
75 g tonne^{-1}, 2m	0.167	85.44	12.06	0.0025	4.67
25 g tonne^{-1}, 10m	0.143	35.78	1.45	10.00	2.10
50 g tonne^{-1}, 10m	0.182	29.69	5.65	10.10	3.00
75 g tonne^{-1}, 10m	0.182	48.90	3.63	10.16	2.92

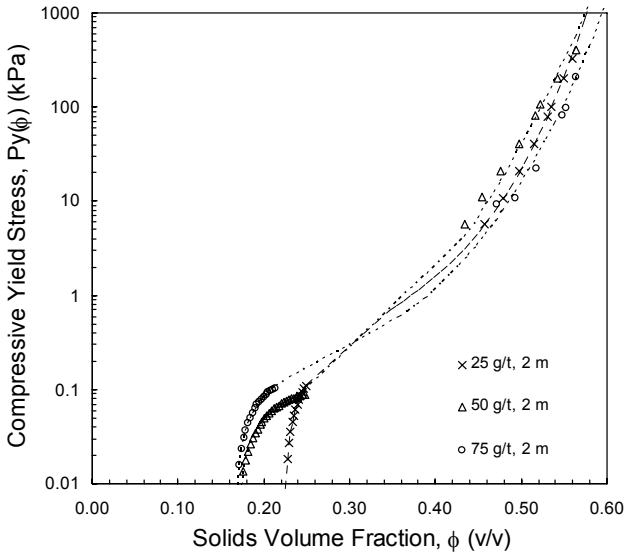

Figure A-1 Compressive yield stress as a function of solids volume fraction for calcite, flocculated with 25, 50 and 75 g tonne^{-1} of added flocculant in a 2 metre pipe reactor

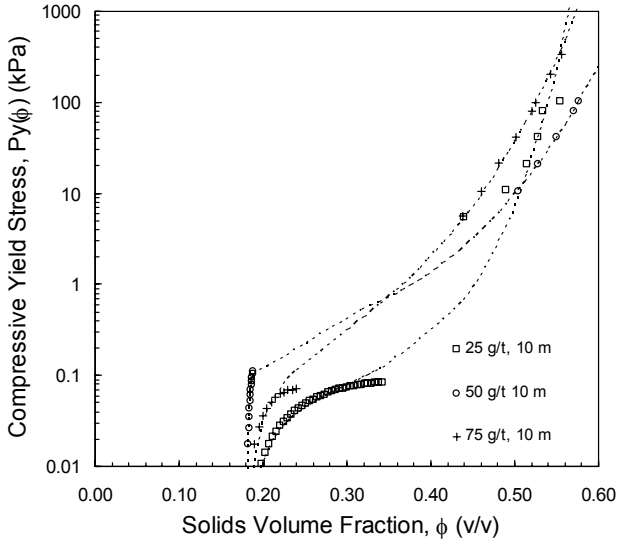

Figure A-2 Compressive yield stress as a function of solids volume fraction for calcite, flocculated with 25, 50 and 75 g tonne^{-1} of added flocculant in a 10 metre pipe

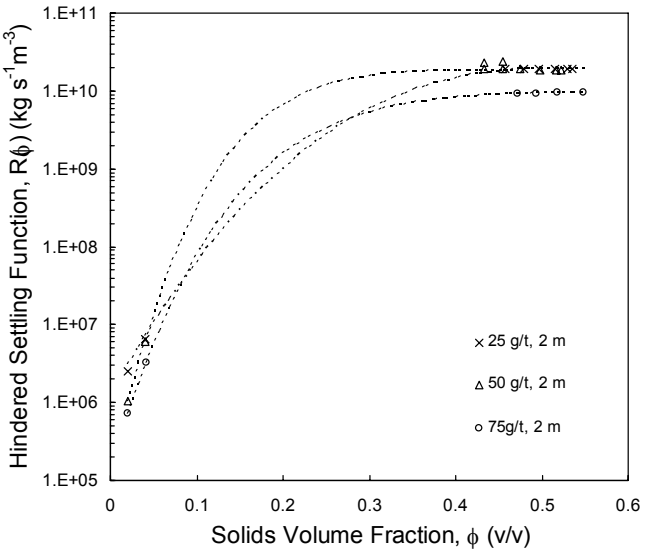

Figure A-3 Hindered settling function as a function of solids volume fraction for calcite flocculated with 25, 50 and 75 g tonne^{-1} of added flocculant in a 2 metre pipe reactor.

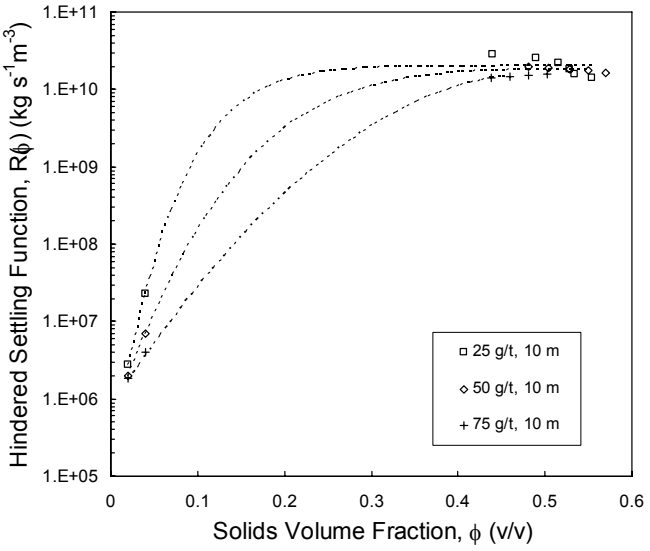

Figure A-4 Hindered settling function as a function of solids volume fraction for calcite flocculated with 25, 50 and 75 g tonne^{-1} of added flocculant in a 10 metre pipe reactor

Appendix 2

Classical dewatering theory and thickener design methodologies

Early research into thickening can be traced back to Dorr Oliver's invention of the continuous flow thickener in 1905. In the years following, various workers considered the effect of slurry temperature, bed height, thickener area, and electrolyte concentration on the performance in continuous thickeners [32, 50, 51, 104, 119]. Hazen [62] observed that the volume of solids removed from a thickener was proportional to its cross sectional area, and inversely proportional to the solids flux; while Mishler [104] noted that sedimentation rates did not depend on depth for dilute slurries; but increased with depth when slurries were concentrated. Although, sedimentation and consolidation were not recognised, the importance of concentration on dewatering quickly became clear.

Coe and Clevenger and macroscopic thickener design

In addition to practical studies, thickening also received theoretical interest. As it became increasingly popular, a design methodology for new thickeners became a pressing requirement. To this end, the efforts of Coe and Clevenger [34] are frequently cited. Coe and Clevenger contributed to early thickening knowledge in two ways. First, Coe and Clevenger observed that initial settling rates in batch settling decreased monotonically with solids concentration. Second, Coe and Clevenger identified zones in continuous thickening; now referred to as

clarification, hindered settling, and consolidation. Because the same zones are present in batch settling, Coe and Clevenger proposed a design method requiring only data available from batch tests. Essentially, the method was an area calculation based on the solid handling capacity of the settling zone. By applying macroscopic solid balances across the boundary of the thickener;

$$FD_f = UD_u + O \tag{A.1}$$

$$F = U \tag{A.2}$$

F and U are the mass flow rate of solids in the feed and underflow respectively while O represents the mass flow rate of fluid in the overflow. D, in the original notation of Coe and Clevenger, is the ratio of solid and fluid mass and the subscripts f and u refer to feed and underflow streams while ϕ is the solid volume fraction;

$$D = \frac{\rho_f (1-\phi)}{\rho_s \phi} \tag{A.3}$$

Because the mass flow rate of fluid O, is equal to $\rho_f Q_0$, where Q_0 is the volumetric flow rate, equation (A.1) can be rearranged to express the volumetric flow rate as;

$$Q_O = \frac{F(D_f - D_u)}{\rho_f} \tag{A.4}$$

The fluid flux in continuous thickening is by definition $\left(\frac{Q_0}{A}\right)$. Continuous thickening and batch settling can be related by equating the flux in the thickener

to the rate at which clarified water forms in a batch settling experiment, given by u_s. In terms of ϕ, the required area to handle a specified solids throughput A/F, is given by

$$\frac{A}{F} = G = \frac{1}{\rho_s u_s(\phi)}\left(\frac{1}{\phi} - \frac{1}{\phi_u}\right) \tag{A.5}$$

To avoid overloading, solids need to subside through the range of concentrations $\left(\phi_f \le \phi < \phi_u\right)$ at a rate at least as quick as the solid mass flow rate entering the thickener, per unit area. Therefore, the thickener area must be able to accommodate a concentration layer corresponding to the minimum handling capacity, i.e. $\min\left(\frac{F}{A}\right)$, or equivalently;

$$\begin{aligned} G &= \max\left(\frac{A}{F}\right) \\ &= \max_{\phi}\left[\frac{1}{\rho_s u_s(\phi)}\left(\frac{1}{\phi} - \frac{1}{\phi_u}\right)\right] \end{aligned} \tag{A.6}$$

The solid handling capacity is undoubtedly an important design consideration - if a thickener cannot accommodate the minimum or limiting flux, solids will accumulate and eventually overflow. However, thickener design cannot be reduced to a simple area calculation. This approach does not account for the effects of bed height and compression, where settling rates no longer depend only on solid concentration. Furthermore, this approach does not account for the effect of shear due to raking, or the variation in settling rates due to differing flocculation efficiencies. Therefore, a rigorous design needs to be holistic, considering the type of thickener, rake design, selection of flocculant and feed

well type. These have been independently modelled using computational fluid dynamics [45, 137, 164], however, to obtain a complete picture of thickening these models need to be incorporated within an overall multidimensional model.

Kynch theory and kinematical thickener design

Kynch [97] viewed sedimentation as a series of solid concentration fronts propagating through a suspension, similar to sound waves through air. Based on zone settling arguments, Kynch showed that sedimentation could be described by the following conservation law [140];

$$\frac{\partial \phi}{\partial t} + \frac{\partial f_{bk}(\phi)}{\partial z} = 0 \tag{A.7}$$

The solid flux $f_{bk}(\phi)$ is the product of solid velocity and volume fraction, $f_{bk}(\phi) = u_s \phi$. In principle, $f_{bk}(\phi)$ can be determined from a single batch settling experiment across the range of volume fractions expressed in the test [69]. This represents a substantial improvement on the approach of Coe and Clevenger, which requires multiple tests. A typical plot of solids flux versus ϕ is shown in Figure A-5. The solids flux can be seen to satisfy; $f_{bk}(0) = f_{bk}(\phi_\infty) = 0$ and $f_{bk}(\phi) < 0$ for $\phi_0 \le \phi < \phi_\infty$

Equation (A.7) can be written as;

$$\frac{\partial \phi}{\partial t} + f'_{bk}(\phi)\frac{\partial \phi}{\partial z} = 0 \tag{A.8}$$

where $f'_{bk}(\phi) = \dfrac{\partial f_{bk}}{\partial \phi}$.

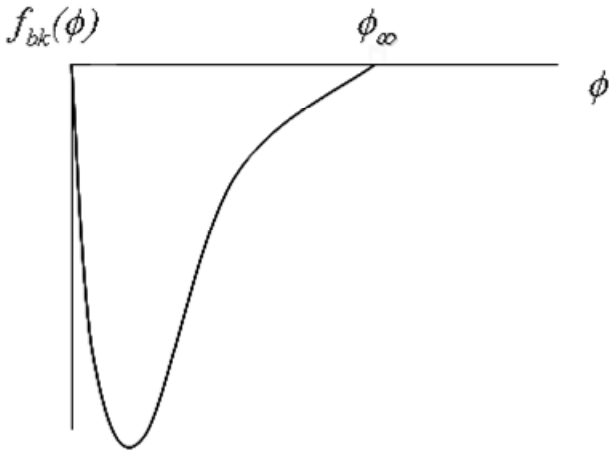

Figure A-5 Kynch flux density plot

Thus, the problem of sedimentation reduces solving $\phi(z,t)$ subject to the conditions;

$$\phi(z,0) = \phi_0$$

$$\phi(0,t) = \phi_\infty \tag{A.9}$$

$$\phi(H,t) = 0 \quad t > 0$$

A solution to equation (A.8) is obtained using the method of characteristics. Along a characteristic, ϕ is constant $\Rightarrow \frac{\partial \phi}{\partial z} dz + \frac{\partial \phi}{\partial t} dt = 0$ and the propagation velocity, $f'_{bk}(\phi)$ is equal to $\frac{dz}{dt}$. Since ϕ and $f'_{bk}(\phi)$ are both constant; the characteristics form straight lines;

$$z = z_0 - f'_{bk} t \tag{A.10}$$

If a suspension, initially at concentration ϕ_0 behaves ideally, the solid settling velocity u_s is given by the gradient of $h(t)$ at (h_k, t_k) while $\phi_k(z,t)$ is calculated from equation (A.11).

$$\phi_k = \frac{\phi_0 H_0}{Z} \tag{A.11}$$

$$u_s(\phi_k) = \left.\frac{dh}{dt}\right|_{z=h_k} = \frac{Z}{T} \tag{A.12}$$

where H_0 is the initial height and Z is the height corresponding to concentration ϕ_k.

If Kynch theory applies over the entire solids volume fraction range $(\phi_0 \le \phi < \phi_u)$, the thickener area can be found by;

$$G = \frac{1}{\rho_s \phi_0 H_0} = \max_{\phi_k}\left(\frac{T(Z - Z_u)}{Z}\right) \tag{A.13}$$

Using geometric arguments Talmage and Fitch [167, 168] showed that the settling velocity is expressed equivalently;

$$u_s(\phi_k) = \frac{Z}{T} = \frac{Z - Z_u}{t_k} \tag{A.14}$$

where, t_k is the time the original mass of solid $(\phi_0 h_0 A)$ takes to settle past a concentration layer ϕ_k. Rearranging the above equation, the thickener area equation (A.13) can be written;

$$G = \frac{1}{\rho_s \phi_0 H_0} = \max_{\phi_k}\left(t_k\right) \tag{A.15}$$

The maximum value of t_k, occurs when $z_k = Z_u$, since a tangent to $h(t)$ at any other value of ϕ intersects the horizontal underflow line at a lower abscissa value. Graphically, the construction involves determining Z_u from $Z_u = \frac{\phi_0 H_0}{\phi_u}$, and t_u is the intersection between the horizontal underflow line and $h(t)$. The required thickener area to handle the solid throughput is calculated from equation (A.15), with $\max\left(t_k\right) = t_u$.

An alternative design method proposed by Yoshioka [168] assumed knowledge of the solids flux density function. The solid flux density for continuous thickening is expressed by;

$$f_k(\phi) = q\phi + f_{bk}(\phi) \tag{A.16}$$

Under steady state conditions, the flux does not vary so $f_k(\phi) = f_f = f_u$. At the discharge point, the volume-averaged velocity is q_D so equation (A.16) is rewritten;

$$f_{bk}(\phi) = f_F - q_u\phi \tag{A.17}$$

Equation (A.17) is a thickener operating line. When superimposed onto a batch flux density plot, a straight-line passes through $(0, \phi_u)$ with a slope, q_u. If q_u and ϕ_u are known, the solids feed flux f_F can be determined from the intercept

between the operating line and ordinate axis. The required thickener area is calculated using $G = \frac{1}{\rho_s f_f}$.

Bibliography

[1] P. M. Adler and P. M. Mills. Motion and rupture of a porous sphere in a linear flow field. *Journal of Rheology*, 23(1): 25, 1979.

[2] O. E. Albertson and D. W. Okey. Evaluating scraper designs. *Water Environment and Technology*: 52-58, 1992.

[3] P. W. Atkins. *Physical chemistry*. Oxford University Press, Oxford, 1994.

[4] C. Aubert and D. S. Cannell. Restructuring of colloidal silica aggregates. *Physical Review Letters*, 56(7): 738-741, 1986.

[5] Auzerais F.M, Jackson R and Russel W.B. The resolution of shocks and the effects of compressible sediments in transient settling. *Journal of Fluid Mechanics*, 195: 437-462, 1988.

[6] A. A. A. Aziz. *Characterisation of Shear on the Dewaterability of Colloidal Suspensions*. PhD Thesis, Department of Chemical and Biomolecular Engineering, The University of Melbourne, 2004.

[7] A. A. A. Aziz, R. G. de Kretser, D. R. Dixon and P. J. Scales. The characterization of slurry dewatering. *Water Science and Technology*, 41(8): 9-16, 2000.

[8] D. H. Bache. Floc rupture and turbulence: a framework for analysis. *Chemical Engineering Science*, 59(12): 2521-2534, 2004.

[9] Batchelor G.K. Sedimentation in a dilute dispersion of spheres. *Journal of Fluid Mechanics*, 52(2): 245-268, 1972.

[10] D. Bemer and S. Calle. Evolution of the efficiency and pressure drop of a filter media with loading. *Aerosol Science and Technology*, 33(5): 427-439, 2000.

[11] L. Bergstroem, C. H. Schilling and I. A. Aksay. Compressive yield stresses of flocculated particle suspensions. In *Theor. Appl. Rheol., Proc. Int. Congr. Rheol., 11th,* 579-581, 1992.

[12] M. Berka and J. A. Rice. Relation between aggregation kinetics and the structure of kaolinite aggregates. *Langmuir*, 21(4): 1223-1229, 2005.

[13] R. B. Bird, W. E. Stewart and E. N. Lightfoot. *Transport Phenomena.* Wiley, 1960.

[14] D. V. Boger. *personal communication*, 2003.

[15] D. V. Boger, P. J. Scales and F. Sofra. *Rheological concepts, in Paste and Thickened Tails. A Guide.* (eds. Jewell, R., Fourie, A. & Lord, E.), UWA Press, Perth, 2002.

[16] F. Bossard, M. Sotiropoulou and G. Staikos. Thickening effect in soluble hydrogen-bonding interpolymer complexes. Influence of pH and molecular parameters. *Journal of Rheology*, 48(4): 927, 2004.

[17] R. Bürger. Phenomenonological foundation and mathematical theory of sedimentation-consolidation processes. *Chemical Engineering Journal*, 80: 177-188, 2000.

[18] R. Bürger and F. Concha. Mathematical model and numerical simulation of the settling of flocculated suspensions. *International Journal of Multiphase Flow*, 24: 1005-1023, 1998.

[19] R. Bürger, J. J. R. Damasceno and K. H. Karlsen. A mathematical model for batch and continuous thickening of flocculated suspensions in vessels with varying cross-section. *International Journal of Mineral Processing*, 73(2-4): 183, 2004.

[20] R. Bürger, S. Evje, K. H. Karlsen and K. A. Lie. Numerical methods for the simulation of the settling of flocculated suspensions. *Chemical Engineering Journal*, 80: 91-104, 2000.

[21] R. Bürger, K. H. Karlsen and J. D. Towers. Mathematical model and numerical simulation of the dynamics of flocculated suspensions in clarifiers-thickeners. *Chemical Engineering Journal*, 111(119-134): 2005.

[22] R. Bürger and W. Wendland. Sedimentation and suspension flows: Historical perspective and some recent developments. *Journal of Engineering Mathematics*, 41: 101-116, 2001.

[23] R. Bürger, W. L. Wendland and F. Concha. Model equations for gravitational sedimentation-consolidation processes. *ZAMM Z. Angew Math. Mech*, 80: 79-92, 2000.

[24] R. Buscall and L. R. White. The consolidation of concentrated suspensions. *J.Chem.Soc.Faraday Trans*, 83: 873-891, 1987.

[25] G. C. Bushell, Y. D. Yan, D. Woodfield, J. Raper and R. Amal. On techniques for the measurement of the mass fractal dimension of aggregates. *Advances in Colloid and Interface Science*, 95(1): 1, 2002.

[26] T. R. Camp and P. G. Stein. *J.Boston.Soc.Civ.Eng*, 30: 219, 1943.

[27] S. H. Chan, S. Kiang and M. A. Brown. One-dimensional centrifugation model. *AIChE Journal*, 49(4): 925-938, 2003.

[28] G. M. Channell. *Mechanics of aggregated alumina suspensions: behavior under shear and compression*. PhD Thesis, 1999.

[29] G. M. Channell, K. T. Miller and C. F. Zukoski. Effects of microstructure on the compressive yield stress. *AIChE Journal*, 46(1): 72-78, 2000.

[30] C. Chin, S. Yiacoumi and C. Tsouris. Shear-induced flocculation of colloidal particles in stirred tanks. *Journal of Colloid and Interface Science*, 206(2): 532, 1998.

[31] M. M. Clark and J. R. V. Flora. Floc-restructuring in varied turbulent mixing. *Journal of Colloid and Interface Science*, 147(2): 407-421, 1991.

[32] H. S. Coe and G. H. Clevenger. Methods for determining the capacities of slime settling tanks. *Trans AIME*, 55: 356, 1916.

[33] E. W. Comings, C. E. Pruiss and C. DeBord. Continuous settling and thickening. *Ind. Eng. Chem.*, 46: 1164-1172, 1954.

[34] F. Concha and M. C. Bustos. Settling velocities of particulate systems, 6. Kynch sedimentation processes: batch settling. *Int. J. Miner. Process.*, 32(3-4): 193-212, 1991.

[35] L. J. Connelly and P. F. Richardson. Coagulation and flocculation in the mining industry. *Solid/liquid separation and mixing in industrial practice*: 1984.

[36] C. Coufort, D. Bouyer and A. Line. Flocculation related to local hydrodynamics in a Taylor-Couette reactor and in a jar. *Chemical Engineering Science*, In Press, Corrected Proof:

[37] J. M. Coulson, J. F. Richardson, J. R. Backhurst and J. H. Harker. *Chemical Engineering*. Butterworth Heinemann, Oxford, 1998.

[38] R. F. Craig. *Craig's soil mechanics*. Spon Press, New York, 2004.

[39] R. G. De Kretser, S. P. Usher, P. J. Scales, D. V. Boger and K. A. Landman. Rapid filtration measurement of dewatering design and optimization parameters. *AIChE Journal*, 47(8): 1758-1769, 2001.

[40] S. Diehl. On boundary conditions and solutions for ideal clarifier-thickener units. *Chemical Engineering Journal*, 80(1-3): 119-133, 2000.

[41] S. Diehl. Operating charts for continuous sedimentation I: Control of steady states. *Journal of Engineering Mathematics*, 41(2-3): 117, 2001.

[42] L. G. Eklund. The working conditions in a continuous pilot thickener at optimal load. *Chemical Engineering Science*, 31(10): 881, 1976.

[43] L. G. Eklund and S. A. Barr. Influence of feed conditions on continuous thickening. *Chemical Engineering Science*, 34(8): 1061, 1979.

[44] L. G. Eklund and A. Jernqvist. Experimental study of the dynamics of a vertical continuous thickener. *Chemical Engineering Science*, 30(5-6): 597, 1975.

[45] J. B. Farrow, P. D. Fawell, R. R. M. Johnston, T. B. Nguyen, M. Rudman, K. Simic and J. D. Swift. Recent developments in techniques and methodologies for improving thickener performance. *Chemical Engineering Journal (Lausanne)*, 80(1-3): 149-155, 2000.

[46] J. B. Farrow, R. R. M. Johnston, K. Simic and J. D. Swift. Consolidation and aggregate densification during gravity thickening. *Chemical Engineering Journal (Lausanne)*, 80(1-3): 141-148, 2000.

[47] J. B. Farrow and L. J. Warren. The measurement of floc density - floc size distributions. *Flocculation Dewatering, Proc. Eng. Found. Conf.*: 153-165, 1989.

[48] B. Fitch. Current theory and thickener design. *Industrial and Engineering Chemistry*, 58(10): 18-28, 1966.

[49] J. C. Flesch, P. T. Spicer and S. E. Pratsinis. Laminar and turbulent shear-induced flocculation of fractal aggregates. *AIChE Journal*, 45(5): 1114, 1999.

[50] E. E. Free. The Phenomena of Flocculation and Deflocculation. *Journal of the Franklin Institute*, 169;170: 421-438;446-457, 1910.

[51] E. E. Free. Sedimentation and flocculation. *Engineering and Mining Journal*, 101: 509-513, 1916.

[52] P. Garrido, R. Burgos, F. Concha and R. Burger. Settling velocities of particulate systems: 13. A simulator for batch and continuous sedimentation of flocculated suspensions. *International Journal of Mineral Processing*, 73(2-4): 131, 2004.

[53] P. Garrido, F. Concha and R. Burger. Settling velocities of particulate systems: 14. Unified model of sedimentation, centrifugation and filtration of flocculated suspensions. *International Journal of Mineral Processing*, 72(1-4): 57, 2003.

[54] L. A. Glasgow and J. P. Hsu. An experimental study of floc strength. *AIChE Journal*, 28(5): 779-785, 1982.

[55] L. A. Glasgow and X. Liu. Response of aggregate structures to hydrodynamic stress. *AIChE Journal*, 37(9): 1411-1414, 1991.

[56] M. D. Green. *Characterisation of Suspensions in Settling and Compression.* PhD Thesis, Department of Chemical Engineering, University of Melbourne, 1997.

[57] M. D. Green and D. V. Boger. Yielding of suspensions in compression. *Ind.Eng.Chem.Res.*, 36: 4984-4992, 1997.

[58] M. D. Green, K. A. Landman, R. G. de Kretser and D. V. Boger. Pressure filtration technique for complete characterisation of consolidating suspensions. *Ind.Eng.Chem.Res.*, 37: 4152-4156, 1998.

[59] J. Gregory. Fundamentals of flocculation. *Critical Reviews in Environmental Control*, 19(3): 185-230, 1989.

[60] J. Gregory. The density of particle aggregates. *Water Science and Technology*, 36(4): 1-13, 1997.

[61] J. H. Hand and M. C. Williams. Effect of secondary polymer structure on the drag-reducing phenomenon. *Journal of Applied Polymer Science*, 13(11): 2499-2503, 1969.

[62] A. Hazen. On Sedimentation. *Trans. ASCE*, 53: 45-71, 1904.

[63] T. W. Healy and V. K. La Mer. The adsorption-flocculation reactions of a polymer with an aqueous colloidal dispersion. *Journal of Physical Chemistry*, 66: 1835-1838, 1962.

[64] A. R. Heath, P. A. Bahiri, P. D. Fawell and J. B. Farrow. Polymer flocculation of calcite: Experimental results from turbulent pipe flow. *AIChE J.*, 52(3): To appear, 2006.

[65] A. R. Heath, P. A. Bahiri, P. D. Fawell and J. B. Farrow. Polymer flocculation of calcite: Population balance model. *AIChE J.*, 52(3): To appear, 2006.

[66] L. L. Hoekstra, R. Vreeker and W. G. M. Agterof. Aggregation of colloidal nickel hydroxycarbonate studied by light scattering. *Journal of Colloid and Interface Science*, 151(1): 17, 1992.

[67] R. Hogg. The role of polymer adsorption kinetics in flocculation. *Colloids and Surfaces A: Physicochemical and Engineering Aspects*, 146(1-3): 253, 1999.

[68] R. Hogg. Flocculation and dewatering. *International Journal of Mineral Processing*, 58(1-4): 223, 2000.

[69] R. Hogg, T. W. Healy and D. W. Fuerstenau. Mutual coagulation of colloidal dispersions. *Transactions of the Faraday Society*, 62(6): 1638-1651, 1966.

[70] R. G. Holdich and G. Butt. Compression and channelling in gravity sedimenting systems. *Minerals Engineering*, 9(1): 115-131, 1996.

[71] R. G. Holdich and G. Butt. Gravity sedimentation including compression and channeling. In *Proceedings - World Filtration Congress, 7th, Budapest, May 20-23, 1996,* 136-140, 1996.

[72] F. A. Holland and F. S. Chapman. *Liquid mixing and processing in stirred tanks*. Reinhold Publishing Corporation, New York, 1966.

[73] J. Hulston. *Effect of Flocculation Conditions on the Dewaterability of Hematite and Red mud Suspensions*. PhD Thesis, Chemical and Biomolecular Engineering, University of Melbourne, 2005.

[74] J. Hulston, R. G. de Kretser and P. J. Scales. Effect of temperature on the dewaterability of hematite suspensions. *International Journal of Mineral Processing*, 73(2-4): 269, 2004.

[75] S. B. Johnson. *The Relationship Between the Surface Chemistry and the Shear Yield Stress of Mineral Suspensions.* PhD Thesis, Department of Chemistry, The University of Melbourne, 1998.

[76] S. B. Johnson, D. R. Dixon and P. J. Scales. The electrokinetic and shear yield stress properties of kaolinite in the presence of aluminium ions. *Colloids and Surfaces A*, 146(1-3): 281-292, 1999.

[77] S. B. Johnson, P. J. Scales, D. R. Dixon and M. Pascoe. Use of a superthickener device to concentrate potable water sludge. *Water Research*, 34(1): 288-294, 2000.

[78] R. Jullien and P. Meakin. Simple models for the restructuring of three-dimensional ballistic aggregates. *Journal of Colloid and Interface Science*, 127(1): 265-272, 1989.

[79] P. C. Kapur, S. Laha, S. Usher, R. G. de Kretser and P. Scales. Modeling of the consolidation stage in pressure filtration of compressible cakes. *Journal of Colloid and Interface Science*, 256(1): 216-222, 2002.

[80] J. R. Karl and S. A. Wells. Numerical model of sedimentation/thickening with inertial effects. *Journal of Environmental Engineering*: 792, 1999.

[81] R. C. Klimpel and R. Hogg. Effects of flocculation conditions on agglomerate structure. *Journal of Colloid and Interface Science*, 113(1): 121, 1986.

[82] R. C. Klimpel and R. Hogg. Evaluation of floc structures. *Colloids and Surfaces, A: Physicochemical and Engineering Aspects*, 55: 279, 1991.

[83] K. B. Krauskopf and D. K. Bird. *Introduction to Geochemistry*. McGraw-Hill, Inc., New York, 1995.

[84] I. M. Krieger. Shear rate in the couette viscometer. *Transactions of the Society of Rheology*, 12(1): 1968.

[85] L. L. M. Krutzer, A. J. G. van Diemen and H. N. Stein. The influence of the type of flow on the orthokinetic coagulation rate. *Journal of Colloid and Interface Science*, 171(2): 429, 1995.

[86] K. A. Kusters, J. G. Wijers and D. Thoenes. Aggregation kinetics of small particles in agitated vessels. *Chemical Engineering Science*, 52(1): 107, 1997.

[87] G. J. Kynch. A theory of sedimentation. *Trans. Far. Soc.*, 48: 166-177, 1952.

[88] V. K. La Mer and T. W. Healy. Adsorption-flocculation reactions of macromolecules at the solid-liquid interface. *Reviews of Pure and Applied Chemistry*, 13: 112-133, 1963.

[89] A. L. Lagvankar. *Size-density relations for chemical flocs*. PhD Thesis, 1968.

[90] H. Lamb. *Hydrodynamics*. Dover publications, New York, 1945.

[91] K. A. Landman, J. M. Stankovich and L. R. White. Measurement of the filtration diffusivity D([ϕ]) of a flocculated suspension. 45(9): 1875, 1999.

[92] K. A. Landman and L. R. White. Solid/liquid separation of flocculated suspensions. *Advances in Colloid and Interface Science*, 51: 175-246, 1994.

[93] K. A. Landman and L. R. White. Predicting filtration time and maximizing throughput in a pressure filter. *AIChE Journal*, 43(12): 3147-3160, 1997.

[94] K. A. Landman, L. R. White and R. Buscall. The continuous flow gravity thickener: steady state behaviour. *AIChE Journal*, 34(2): 239-252, 1988.

[95] K. A. Landman, L. R. White and M. Eberl. Pressure filtration of flocculated suspensions. *AIChE Journal*, 41(7): 1687-1700, 1995.

[96] K. A. Landman, White, L.R. Determination of the hindered settling factor for flocculated suspensions. *AIChE Journal*, 38(2): 184-192, 1992.

[97] D. R. Lester. *Colloidal Suspension Dewatering Analysis*. PhD Thesis, Department of Chemical and Biomolecular Engineering, The University of Melbourne, 2002.

[98] D. R. Lester, S. P. Usher and P. J. Scales. Estimation of the hindered settling function R(ϕ) from batch-settling tests. *AIChE Journal*, 51(4): 1158-1168, 2005.

[99] A. D. Martin. Optimisation of clarifier-thickeners processing stable suspensions for turn-up/turn-down. *Water Research*, 38(6): 1568, 2004.

[100] P. Meakin. Fractal aggregates. *Advances in Colloid and Interface Science*, 28(4): 249-331, 1988.

[101] P. Meakin and R. Jullien. Simple models for two and three dimensional particle size segregation. *Physica A: Statistical Mechanics and Its Applications*, 180(1-2): 1-18, 1992.

[102] A. S. Michaels and J. C. Bolger. Settling rates and sediment volumes of flocculated kaolin suspensions. *Industrial & Engineering Chemistry Fundamentals*, 1(1): 24-33, 1962.

[103] P. D. A. Mills, J. W. Goodwin and B. W. Grover. Shear field modification of strongly flocculated suspensions - aggregate morphology. *Colloid and Polymer Science*, 269(9): 949-963, 1991.

[104] R. T. Mishler. Relation of feed to tube mill efficiency. *Engineering and Mining Journal*, 98: 469-471, 1914.

[105] G. Moody. The use of polyacrylamides in mineral processing. *Minerals Engineering*, 5(3-5): 479, 1992.

[106] G. M. Moody. Role of polyacrylamides and related products in treatment of mineral processing effluent. *Transactions of the Institution of Mining and Metallurgy, Section C: Mineral Processing and Extractive Metallurgy*, 99: 137-141, 1990.

[107] G. M. Moody. Pre-treatment chemicals. *Filtration & Separation*, 32(4): 329-336, 1995.

[108] M. Mosquet, Y. Chevalier, P. L. Perchec, A. Foissy and J. P. Guicquero. The mechanism of fluidization of concentrated calcium carbonate slurries by poly(oxyethylene) diphosphonates. *Colloid & Polymer Science*, 277(12): 1162, 1999.

[109] P. Mpofu, J. Addai-Mensah and J. Ralston. Temperature influence of nonionic polyethylene oxide and anionic polyacrylamide on flocculation and dewatering behavior of kaolinite dispersions. *Journal of Colloid and Interface Science*, 271(1): 145, 2004.

[110] Q. D. Nguyen and D. V. Boger. Characterisation of yield stress fluids with concentric cylinder viscometers. *Rheologica Acta*, 26: 508-515, 1987.

[111] Q. D. Nguyen and D. V. Boger. Application of rheology to solving tailings disposal problems. *International Journal of Mineral Processing*, 54(3-4): 217-233, 1998.

[112] Novak J.T and Bandak N. The effect of shear on the dewatering of water treatment residuals. *AWWA*: 84-91, 1994.

[113] J. Y. Oldshue. *Fluid Mixing Technology*. 1983.

[114] R. H. G. Parry. *Mohr circles, stress paths and geotechnics*. Spon Press, New York, 2004.

[115] N. Pashias. *The Characterisation of Bauxite Residue Suspensions in Shear and Compression*. PhD Thesis, Department of Chemical Engineering, The University of Melbourne, 1997.

[116] M. J. Pearse and J. Barnett. Chemical treatments for thickening and filtration. *Filtration+Separation*, 17(5): 460-470, 1980.

[117] M. J. Pearse, S. Weir, S. J. Adkins and G. M. Moody. Advances in mineral flocculation. *Minerals Engineering*, 14(11): 1505, 2001.

[118] M. Perez, R. Font and C. Pastor. A mathematical model to simulate batch sedimentation with compression behavior. *Computers & Chemical Engineering*, 22(11): 1531-1541, 1998.

[119] O. C. Ralston. The control of ore slimes. I. *Engineering and Mining Journal*, 101: 763-769, 1916.

[120] C. Rattanakawin and R. Hogg. Aggregate size distributions in flocculation. *Colloids and Surfaces, A: Physicochemical and Engineering Aspects*, 177(2-3): 87-98, 2001.

[121] M. J. Rhodes. *Introduction to particle technology*. John Wiley, New York, 1998.

[122] R. A. Ruehrwein and D. W. Ward. Mechanism of clay aggregation by polyelectrolytes. *Soil Science*, 73: 485-492, 1952.

[123] P. J. Scales, T. W. Healy, D. V. Boger, R. de Kretser, K. Bremmel, S. Usher, J. Hulston and D. Lester. *Bayer Process Flocculants*. AMIRA P527 Final Report, The University of Melbourne, 2001.

[124] K. J. Scott. Experimental study of continuous thickening of a flocculated silica slurry. *Industrial & Engineering Chemistry Fundamentals*, 7(4): 582-595, 1968.

[125] K. J. Scott. Continuous thickening of flocculated suspensions. Comparison with batch settling tests and effects of floc compression using pyrophyllite pulp. *Industrial & Engineering Chemistry Fundamentals*, 9(3): 422-427, 1970.

[126] C. Selomulya, G. Bushell, R. Amal and T. D. Waite. Understanding the role of restructuring in flocculation: The application of a population balance model. *Chemical Engineering Science*, 58(2): 327, 2003.

[127] P. T. Shannon, R. D. Dehaas, E. P. Stroupe and E. M. Tory. Batch and continuous thickening. Prediction of batch settling behavior from initial rate data with results for rigid spheres. *Industrial & Engineering Chemistry Fundamentals*, 3(3): 250-260, 1964.

[128] P. T. Shannon and E. M. Tory. Analysis of continuous thickening. *Transactions of the Society of Mining Engineers of AIME*, 235(4): 375-382, 1966.

[129] A. H. P. Skelland. *Non-Newtonian Flow and Heat Transfer.* Wiley, New York, 1967.

[130] F. Sofra and D. V. Boger. Environmental rheology for waste minimization in the minerals industry. *Chemical Engineering Journal*, 86(3): 319-330, 2002.

[131] R. C. Sonntag and W. B. Russel. Structure and breakup of flocs subjected to fluid stresses: I. Shear experiments. *Journal of Colloid and Interface Science*, 113(2): 399, 1986.

[132] R. C. Sonntag and W. B. Russel. Structure and breakup of flocs subjected to fluid stresses. II. Theory. *Journal of Colloid and Interface Science*, 115(2): 378-389, 1987.

[133] P. T. Spicer, W. Keller and S. E. Pratsinis. The effect of impeller type on floc size and structure during shear-induced flocculation. *Journal of Colloid and Interface Science*, 184(1): 112-122, 1996.

[134] P. T. Spicer and S. E. Pratsinis. Shear-induced flocculation: The evolution of floc structure and the shape of the size distribution at steady state. *Water Research*, 30(5): 1049, 1996.

[135] P. T. Spicer, S. E. Pratsinis, J. Raper, R. Amal, G. Bushell and G. Meesters. Effect of shear schedule on particle size, density, and structure during flocculation in stirred tanks. *Powder Technology*, 97(1): 26, 1998.

[136] A. D. Stickland, R. G. de Kretser and P. J. Scales. Nontraditional constant pressure filtration behavior. *AIChE J.*, 51(9): 2481-2488, 2005.

[137] I. D. Sutalo, D. A. Paterson and M. Rudman. Flow visualization and computational prediction in thickener rake models. *Minerals Engineering*, 16(2): 93-102, 2003.

[138] L. Svarovsky. *Solid-Liquid Separation*. Butterworths, London, 1990.

[139] J. D. Swift, K. Simic, R. R. M. Johnston, P. D. Fawell and J. B. Farrow. A study of the polymer flocculation reaction in a linear pipe with a focused beam reflectance measurement probe. *International Journal of Mineral Processing*, 73(2-4): 103, 2004.

[140] W. P. Talmage and E. B. Fitch. Determining thickener unit areas. *Journal of Industrial and Engineering Chemistry (Washington, D. C.)*, 47: 38-41, 1955.

[141] N. Tambo and H. Hozumi. Physical characteristics of flocs. II. Strength of floc. *Water Research*, 13(5): 421-427, 1979.

[142] N. Tambo and X. C. Wang. Application of fluidized pellet bed technique in the treatment of highly colored and turbid water. *Aqua (Oxford)*, 42(5): 301-309, 1993.

[143] N. Tambo and X. C. Wang. Control of coagulation condition for treatment of high-turbidity water by fluidized pellet bed separation. *Aqua (Oxford)*, 42(4): 212-222, 1993.

[144] N. Tambo and X. C. Wang. The mechanism of pellet flocculation in a fluidized-bed operation. *Aqua (Oxford)*, 42(2): 67-76, 1993.

[145] N. Tambo and Y. Watanabe. Physical characteristics of flocs. I. The floc density function and aluminum floc. *Water Research*, 13(5): 409-419, 1979.

[146] K. Terzaghi and R. B. Beck. Soil mechanics in engineering practice. *Journal of the Franklin Institute*, 245(6): 566, 1948.

[147] A. Thill, S. Moustier, J. Aziz, M. R. Wiesner and J. Y. Bottero. Flocs restructuring during aggregation: experimental evidence and numerical simulation. *Journal of Colloid and Interface Science*, 243(1): 171, 2001.

[148] F. M. Tiller and W. Chen. Limiting operating conditions for continuous thickeners. *Chemical Engineering Science*, 43(7): 1695, 1988.

[149] F. M. Tiller and Z. Khatib. The theory of sediment volumes of compressible, particulate structures. *Journal of Colloid and Interface Science*, 100(1): 55-67, 1984.

[150] F. M. Tiller, C. S. Yeh, C. D. Tsai and W. Chen. Generalized approach to thickening, filtration, and centrifugation. *Filtration+Separation*, 24(2): 121-126, 1987.

[151] E. M. Tory and P. T. Shannon. Reappraisal of the concept of settling in compression. Settling behavior and concentration profiles for initially concentrated calcium carbonate slurries. *Industrial & Engineering Chemistry Fundamentals*, 4(2): 194-204, 1965.

[152] J. P. S. Turner and D. Glasser. Continuous thickening in a pilot plant. *Industrial & Engineering Chemistry Fundamentals*, 15(1): 23-30, 1976.

[153] S. P. Usher. *Suspension Dewatering: Characterisation and Optimisation*. PhD Thesis, Department of Chemical Engineering, University of Melbourne, 2002.

[154] S. P. Usher, R. G. De Kretser and P. J. Scales. Validation of a new filtration technique for dewaterability characterization. *AIChE Journal*, 47(7): 1561-1570, 2001.

[155] S. P. Usher, B. R. Gladman and P. J. Scales. New Techniques for Understanding Settler/Clarifier Behaviour. In *Proceedings of American Filtration and Separations Society, Atlanta, GA*, 2005.

[156] S. P. Usher and P. J. Scales. Steady state thickener modelling from the compressive yield stress and hindered settling function. *Chemical Engineering Journal*, 111: 253-261, 2005.

[157] P. A. Vesilind and G. N. Jones. Channelling in batch thickening. *Water Science and Technology*, 28(1): 59-65, 1993.

[158] M. J. Vold. A numerical approach to the problem of sediment volume. *Journal of Colloid Science*, 14: 168-174, 1959.

[159] T. D. Waite. Measurement and implications of floc structure in water and wastewater treatment. *Colloids and Surfaces A: Physicochemical and Engineering Aspects*, 151(1-2): 27, 1999.

[160] R. J. Wakeman. Modeling slurry dewatering and cake growth in filtering centrifuges. *Filtration+Separation*, 31(1): 75-81, 1994.

[161] X. C. Wang, P. K. Jin, H. L. Yuan, E. R. Wang and N. Tambo. Pilot study of a fluidized-pellet-bed technique for simultaneous solid/liquid separation and sludge thickening in a sewage treatment plant. *Water Science and Technology*, 49(10, Wastewater Sludge as a Resource): 81-88, 2004.

[162] S. E. Water. *Typical analysis of your water supply*. Data source: South East Water web site, http://www.southeastwater.com.au/sew/index, 2006.

[163] S. T. Wereley and R. M. Lueptow. Velocity field for Taylor--Couette flow with an axial flow. *Physics of Fluids*, 11(12): 3637, 1999.

[164] R. B. White, I. D. Sutalo and T. Nguyen. Fluid flow in thickener feedwell models. *Minerals Engineering*, 16(2): 145-150, 2003.

[165] Y. D. Yan, J. L. Burns, G. J. Jameson and S. Biggs. Viscosity effect on the structural compactness of latex flocs formed under weak depletion attractions. *Journal of Colloid and Interface Science*, 255(1): 91, 2002.

[166] A. K. C. Yeung and R. Pelton. Micromechanics: a new approach to studying the strength and breakup of flocs. *Journal of Colloid and Interface Science*, 184(2): 579-585, 1996.

[167] N. Yoshioka, Y. Hotta and S. Tanaka. Batch settling of homogeneous slurries. *Chem. Eng. (Japan)*, 19: 616-626, 1955.

[168] N. Yoshioka, Y. Hotta, S. Tanaka, S. Naito and S. Tsugami. Continuous thickening of homogeneous flocculated slurries. *Kagaku Kikai*, 21: 66-74, 1957.

[169] X. Yu and P. Somasundaran. Role of Polymer Conformation in Interparticle-Bridging Dominated Flocculation. *Journal of Colloid and Interface Science*, 177(2): 283, 1996.

[170] M. Yusa and C. Igarashi. Compaction of flocculated material. *Water Research*, 18(7): 811-816, 1984.

[171] Z. Zhou, M. J. Solomon, P. J. Scales and D. V. Boger. The yield stress of concentrated flocculated suspensions of size distributed particles. *Journal of Rheology*, 43: 651-671, 1999.